Universität Potsdam · Institut für Physik und Astronomie

Fluctuation-Mediated Interactions of Atoms and Surfaces on a Mesoscopic Scale

Dissertation zur Erlangung des akademischen Grades *doctor rerum naturalium (Dr. rer. nat.)* in der Wissenschaftsdisziplin *theoretische Physik*. Eingereicht an der Mathematisch–Naturwissenschaftlichen Fakultät der Universität Potsdam am 10. April 2012 von

Harald Richard Haakh

Betreuer
PD Dr. Carsten Henkel

Published online at the
Institutional Repository of the University of Potsdam:
URL http://opus.kobv.de/ubp/volltexte/2012/6181/
URN urn:nbn:de:kobv:517-opus-61819
http://nbn-resolving.de/urn:nbn:de:kobv:517-opus-61819

Zusammenfassung

Thermische und Quantenfluktuationen des elektromagnetischen Nahfelds von Atomen und makroskopischen Körpern spielen eine Schlüsselrolle in der Quantenelektrodynamik (QED), wie etwa beim Lamb-Shift. Sie führen z.B. zur Verschiebung atomarer Energieniveaus, Dispersionswechselwirkungen (Van der Waals-Casimir-Polder-Wechselwirkungen) und Zustandsverbreiterungen (Purcell-Effekt), da das Feld Randbedingungen unterliegt. Mikroelektromechanische Systeme (MEMS) und festkörperbasierte magnetische Fallen für kalte Atome ('Atom-Chips') ermöglichen den Zugang zu mesoskopischen Skalen, auf denen solche Effekte mit hoher Genauigkeit beobachtet werden können.

Eine Quantenfeldtheorie für Atome (Moleküle) und Photonen wird an Nichtgleichgewichtssituationen angepasst. Atome und Photonen werden durch vollständig quantisierte Felder beschrieben, während die Beschreibung makroskopischer Körper, ähnlich wie im Streuformalismus (*scattering approach*) der Resonator-QED, durch klassische Streuamplituden erfolgt. In diesem Formalismus wird das Nichtgleichgewichts-Zweiteilchenpotential diskutiert. Anschließend wird der Einfluss der Materialeigenschaften von normalen Metallen auf das elektromagnetische Oberflächenrauschen, das für magnetische Fallen für kalte Atome auf Atom-Chips und für Quantencomputer-Anwendungen von Bedeutung ist, sowie auf den Beitrag des magnetischen Dipolmoments zum Van der Waals-Casimir-Polder-Potential im thermischen Gleichgewicht und in Nichtgleichgewichtssituationen untersucht. In beiden Fällen sind die speziellen Eigenschaften von Supraleitern von besonderem Interesse. Beiträge von Oberflächenmoden, die die Feldfluktuationen im Nahfeld dominieren, werden im Kontext des (partiellen) dynamischen *Dressing* nach einer raschen Änderung eines Systemparameters sowie für die Casimir-Wechselwirkung zweier metallischer Platten diskutiert, zwischen denen in Nichtgleichgewichtssituationen Abstoßung auftreten kann.

Abstract

Thermal and quantum fluctuations of the electromagnetic near field of atoms and macroscopic bodies play a key role in quantum electrodynamics (QED), as in the Lamb shift. They lead, e.g., to atomic level shifts, dispersion interactions (Van der Waals-Casimir-Polder interactions), and state broadening (Purcell effect) because the field is subject to boundary conditions. Such effects can be observed with high precision on the mesoscopic scale which can be accessed in micro-electro-mechanical systems (MEMS) and solid-state-based magnetic microtraps for cold atoms ('atom chips').

A quantum field theory of atoms (molecules) and photons is adapted to nonequilibrium situations. Atoms and photons are described as fully quantized while macroscopic bodies can be included in terms of classical reflection amplitudes, similar to the scattering approach of cavity QED. The formalism is applied to the study of nonequilibrium two-body potentials. We then investigate the impact of the material properties of metals on the electromagnetic surface noise, with applications to atomic trapping in atom-chip setups and quantum computing, and on the magnetic dipole contribution to the Van der Waals-Casimir-Polder potential in and out of thermal equilibrium. In both cases, the particular properties of superconductors are of high interest. Surface-mode contributions, which dominate the near-field fluctuations, are discussed in the context of the (partial) dynamic atomic dressing after a rapid change of a system parameter and in the Casimir interaction between two conducting plates, where nonequilibrium configurations can give rise to repulsion.

Acknowledgments

I would like to thank PD Dr. Carsten Henkel, who supervised the research leading to this thesis, for sharing his outstanding intuition and profound knowledge of physics and research literature in many hours of fruitful discussions.

During the past three years, I had the chance to meet and work with many friends and colleagues and I would like to express my gratitude to all of them; especially to Francesco Intravaia, now at Los Alamos National Laboratory, for his friendship and reliable support. I would also like to thank Diego Dalvit and Ryan Behunin at Los Alamos National Laboratory, Roberto Passante, Lucia Rizzuto, and Salvo Spagnolo at Università degli Studi di Palermo, and Baruch Horovitz, Ron Folman, and Daniel Rohrlich at Ben Gurion University in Be'er Sheva for making it possible for me to visit these places and for many stimulating discussions. It is a pleasure to acknowledge the encouragement, help with all questions of physics and mathematics, and coffee steadily provided by my colleagues in Potsdam, Jürgen Schiefele, Gregor Pieplow, and Vanik Mkrtchian. Marlies Path was a great help with all administrative issues. Many useful numerical tricks were worked out by Benjamin D'Anjou during his *DAAD-RISE* internship.

The project received partial financial support from the *German-Israeli Foundation for Research and Development (GIF)*, from *Deutscher Akademischer Austauschdienst (DAAD)*, from the *Potsdam Graduate School*, and from *Los Alamos National Laboratory*.

There is a world beyond science and I thank my friends, Katharina, and my family for sharing it with me and making it so enjoyable.

Contents

Chapter 1

Introduction

1.1 Macroscopic Quantum Effects and Mesoscale Technology

It has been almost precisely a century since the first Solvay conference in 1911. Dedicated to "the theory of radiation and quanta", the meeting stands for the breakthrough of modern quantum physics, after a process that had started some ten years before with Planck's quantum hypothesis [Planck, 1901] and Einstein's interpretation of photoemission [Einstein, 1905]. Since then, the quantum world has not ceased to provide new discoveries and insights. In fact, much of the technological and scientific progress in the last century is due to a deeper understanding of quantum effects and to increased control over systems where quantum effects have become visible in the mesoscopic or macroscopic world (Figs. 1.1 and 1.2).

Among the important examples of *macroscopic quantum states* are the coherent light of a laser, superconductors, superfluids, and Bose-Einstein condensates (BECs) [Pitaevskii and Stringari, 2003], where many-body systems are described by a single macroscopic wave function. A different kind of large quantum systems has emerged in the field of atomic physics, where the preparation of highly excited Rydberg states [Gallagher, 1994] with atomic radii in the micron range is recently becoming a standard technique. In fact, even magnetic properties of solids should be considered a quantum effect, because classical theory does not predict a permanent magnetization, according to a fundamental theorem by Van Leeuwen [1921].

In this thesis we explore *mesoscopic length scales* (Fig. 1.1), where the advance of microprocessing and nanotechnology has opened up new ways to approach the quantum world (Fig. 1.2).

Much of the progress in miniaturization was boosted by the increasing complexity of microcircuitry, which, according to *Moore's law*, doubles roughly every two years. In fact, single atom circuitry has come into reach just recently [Fuechsle et al., 2012; Weber et al., 2012; Ferry, 2012]. Beyond chip fabrication, the possibility to image solid surfaces using atomic force microscopes (AFMs) and to manipulate them on an atomic scale has broad implications. As an example, this has led to the creation of *quantum dots*, where excitonic states are confined in tiny semiconductor structures that show many characteristics of an 'artificial atom'. Importantly, nanoscale processing allows for the construction of machinery known as *microelectromechanical systems* (MEMS).

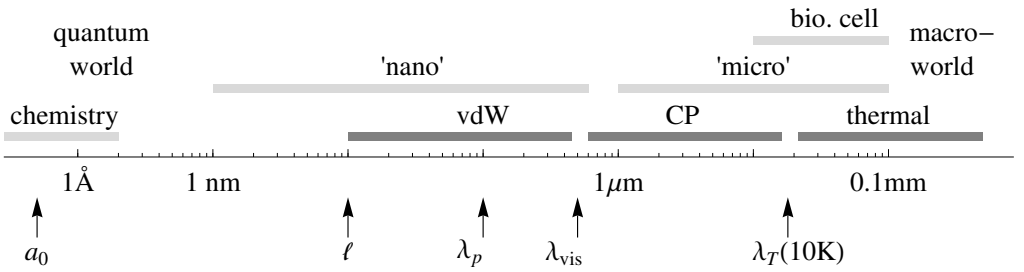

Figure 1.1: Overview of relevant length scales. The atomic scale is characterized by the Bohr radius a_0, while solid structures (crystal lattices, surface roughness, Bloch wavelengths) lie in the range of 1 Å. The mean free path of charge carriers in a metal is denoted by ℓ. The plasma wavelength $\lambda_{\rm p}$ describes collective excitations in a metal and is closely related to the Meißner penetration depth in a superconductor. Visible light has wavelengths $\lambda_{\rm vis}$, while thermal effects occur at distances larger than the thermal wavelength λ_T (*thermal* or *Lifshitz* regime of the dispersion interaction). Between these two scales, we have the *retarded Casimir-Polder* (CP) regime. There is a crossover to the nonretarded *van der Waals* (vdW) regime of the dispersion interaction at smaller distances. On very small lengthscales, physical vdW adsorption is replaced by chemical bonding.

At the small distances achievable in MEMS, the electromagnetical fluctuations at the quantum level give rise to mesoscale-range interactions. A prominent example is the interaction named after Casimir [1948]. In its stricter sense, this effect describes an interaction between two nonmagnetic, electrically neutral, yet polarizable objects. In the case of two parallel plane surfaces in vacuum, the potential depends on the surface distance as r^{-3}. Along with the Lamb shift of atomic spectra, the Casimir effect is commonly seen as one of the most striking pieces of evidence for the existence of vacuum fluctuations [Milonni et al., 1988; Milonni and Shih, 1992; Jaffe, 2005], claimed by Einstein and Stern [1913] on the basis of the blackbody law [Planck, 1912]. After first and rather indecisive experiments by Sparnaay [1957], the advance of nanotechnology and quantum optics has renewed interest in the Casimir effect [Lamoreaux, 1997] and high-precision measurements are now available, mainly based on MEMS technology and atomic force microscopy (AFM). For reviews, see [Klimchitskaya et al., 2009; Dalvit et al., 2011].

Similar to the Casimir interaction, vacuum fluctuations lead to an interaction potential between small neutral particles that scales as r^{-6} at short distances. Such an interaction had been introduced phenomenologically by Van der Waals [1873] in his equation of state and traced back to quantum fluctuations of the atomic dipoles by Eisenschitz and London [1930]. A quantum-electrodynamical calculation, including the effects of retardation, was given by Casimir and Polder [1948]. Today these interactions between two atoms and the closely related ones between atoms and a surface are known interchangeably as *van der Waals-Casimir-Polder (vdWCP) potential* or *London dispersion interaction*. Such noncoulombic interactions between atoms, molecules, or nanoparticles are well known in physical chemistry, where they lead, e.g., to the formation of noble gas clusters. Besides, they play an important role in fields reaching from adhesion in

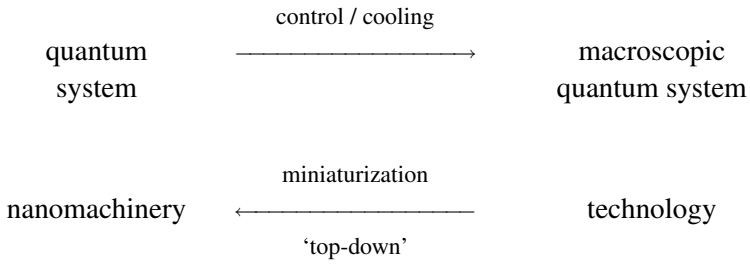

Figure 1.2: Strategies to approach the quantum world.

surface science [Israelachvili, 1992], colloids [Derjaguin and Landau, 1941; Verwey and Overbeek, 1946] (DLVO theory), granular matter [Johnson et al., 1971; Derjaguin et al., 1975] (JKR theory), and even in the formation of planetary bodies, e.g. [Blum and Wurm, 2008].

Atom-surface potentials are commonly encountered and measured with high precision in microscale magnetic traps for cold neutral atoms implemented on microchip surfaces [Harber et al., 2005]. The miniaturization possible in such *atom chips* brings about a number of advantages, e.g. stronger confinement and considerably smaller vacuum apparatus. This has led to implementations of atomic clocks [Treutlein et al., 2004] and interferometers for BECs [Schumm et al., 2005] on a microchip surface. Other recent experiments used trapped clouds of cold atoms to perform highly sensitive magnetometry with μm-resolution [David et al., 2008], and to take the role of the tip of an 'atomic cloud microscope' in analogy to the solid tip of an AFM [Gierling et al., 2011]. This underlines that these systems are the atom-optical equivalent of the MEMS of nanotechnology, and effort is put into the further integration of nanomechanics, atom optics and photonics [Hétet et al., 2011; Muschik et al., 2011].

When talking about micromachinery, one should not forget biological cells, whose structures are comparable in size to the systems manipulated in MEMS and atom chips (Fig. 1.1). The discipline of nanobiotechnology has emerged to study and manipulate these highly complex systems and it is now possible to trace and manipulate even single molecules inside a living cell [Deniz et al., 2008]. One can expect that these developments will lead not only to a deeper understanding of the field where molecular biology, chemistry, surface science, and quantum physics meet, but also to new applications, such as drug-releasing nanoparticles [LaVan et al., 2003; Zakrevskyy et al., 2012]. Many fundamental phenomena that play a role in a biological system, like resonant energy transfer and dispersion forces, can be studied in a complementary way in a setting known from quantum optics and nanotechnology.

As a common feature of all these fascinating developments, the quantum world is not as intangible any more as it used to be at the time of the first Solvay meeting. On the one hand, macroscopic quantum states are widely available and make it possible to witness 'quantumness' with your own eyes without removing any of its fascination. On the other

hand, applications of quantum systems have themselves led to the advent of technology that has provided access to the micro- and nanoscale, the natural habitat of quantum effects, cf. Fig. 1.2.

As quantum effects emerge, miniaturization becomes different from simple downsizing. The observation of the Casimir-Polder forces is an example of how the handling of atoms on a chip differs from previous experiments in free space. We have already seen that the advantages of nanoscale systems come hand in hand with new challenges. For example, increased spatial control of cold atoms brings along additional loss channels and MEMS allow for atomic force microscopy but are subject to Casimir forces and 'stiction'. However, what looks like a technological problem from one point of view may actually prove helpful in a different context. For example, Casimir forces in micromechanical oscillators can be used to tune the mechanical resonance frequency.

In this spirit, the major part of this thesis will deal with ways by which atom-surface interaction can be influenced through a careful choice of the surface material or – conversely – by which the observation of atom-surface interactions can tell us something about the processes inside matter. A number of the observables that play a role in this context will be reviewed in the rest of this introduction after a brief overview of some technological aspects of atom trapping.

1.2 Manipulation of Cold Atomic Gases in Atom Chips

1.2.1 Magnetic traps for neutral particles

Electrically neutral particles can be trapped in a minimum of an inhomogenous magnetic field[1], due to their magnetic moments, which lead to a Zeeman-like potential $\Delta E(\boldsymbol{r}) = -\boldsymbol{\mu}\cdot\boldsymbol{B}(\boldsymbol{r})$ [Migdall et al., 1985; Paul, 1990]. Suitable field configurations can be created by a careful arrangement of permanent magnets and/or current-carrying wires.

A very simple and commonly used configuration, called the *side guide*, is depicted in Fig. 1.3. The basic setup consists of a single straight conducting wire that carries a *trapping current* I. It is placed inside a homogenous *bias field* $\boldsymbol{B}_0$, which cancels the magnetic field created by the trapping current along a line of minimum magnetic field intensity at a distance $z = \mu_0 I/(2\pi B_0)$ from the wire. This side guide provides the the atom-optics analog of optical fibres in photonics.

A component of the bias field along the wire leads to a nonvanishing minimum field in the trap center. The resulting setup is known as a Ioffe-Pritchard trap [Gott et al., 1962; Pritchard, 1983; Bagnato et al., 1987] and provides a harmonic potential in the xz-plane transverse to the guide axis. The nonzero offset of the magnetic field in the trap center provides a quantization axis for the trapped atoms. As a side effect, Majorana [1932] losses due to nonadiabatic spin polarization can be suppressed if the magnetic

[1] From Maxwell's equations, all extrema of a static magnetic field in free space are minima [Wing, 1984; Ketterle and Pritchard, 1992]. This restricts magnetic trapping to weak-field seeking states, like the upper potential in Fig. 1.3b).

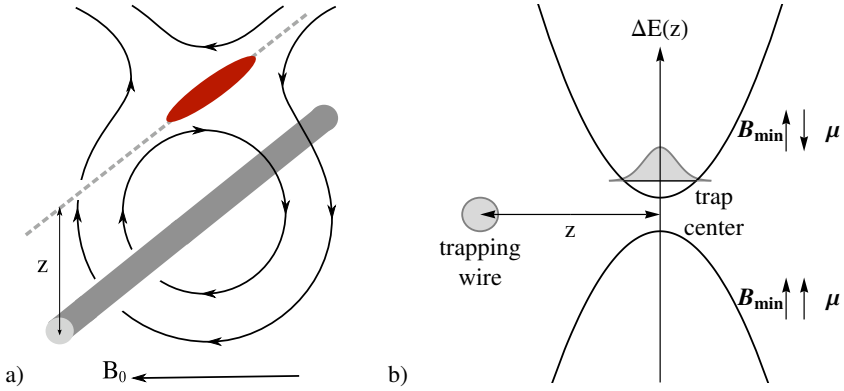

Figure 1.3: a) Typical scheme of a *side guide*. The magnetic field created by a current-carrying wire is cancelled at a distance z by a homogenous bias field $\boldsymbol{B}_0$. This creates a one-dimensional *side guide*, indicated by the dashed line, where a cloud of cold atoms can be trapped.
b) Trapping potential vs. distance from the trapping wire for different atomic states. For a weak-field-seeking state, the magnetic field in the trap center and the magnetic moments are anti-aligned ($\boldsymbol{B}_{\min} \uparrow\downarrow \boldsymbol{\mu}$), resulting in a potential minimum. The gray bell curve indicates a wave packet trapped in the ground state. A spin-flip transition connects trapped states with untrappable ones, for which the potential is repulsive ($\boldsymbol{B}_{\min} \uparrow\uparrow \boldsymbol{\mu}$).

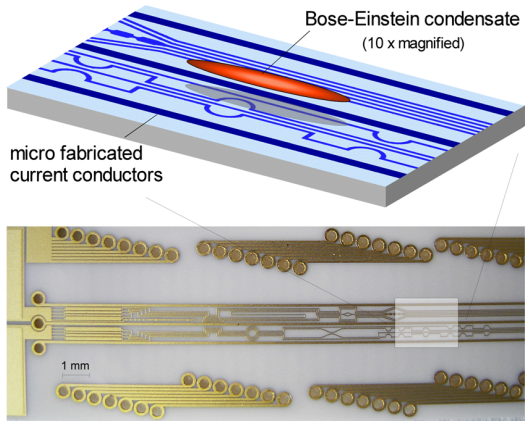

Figure 1.4: Top view onto the surface of an atom chip that implements a conveyor belt for a trapped cloud of cold atoms [Fortágh et al., 2004; Fortágh and Zimmermann, 2005]. Radial confinement is provided by the set of three thin conductors. The contact dots above and below connect to sets of conductors on the backface of the substrate (thickness $250\,\mu\mathrm{m}$), which provide the offset fields and axial confinement. (Image courtesy of J. Fortágh.)

field magnitude in the trap minimum is sufficiently high. The trap can be closed in the direction along the wire by bending the ends of the trapping wire to a Z- or U-shape.

While early magnetic traps made use of permanent magnets or freestanding wires, the use of microchip technology has led to a further miniaturization and integration of magnetic traps on a solid surface in so-called *atom chips*. For comprehensive reviews of physical and technological aspects of these systems, see Folman et al. [2002]; Fortágh and Zimmermann [2007]; and the recent book by Reichel and Vuletic [2011]. Solid-state-based traps offer a way of reducing the size of the apparatus by constructing a compact vacuum cell, one wall of which is formed by the atom chip itself [Du et al., 2004]. Besides, the use of on-chip circuitry has a number of advantages with respect to free-standing wires, e.g. the removal of Joule heat through the substrate. Importantly, steeper field gradients and, thus, stronger confinement can be achieved by using lower trapping currents. The resulting shift of the trap center towards the wire is limited by the finite wire size and, therefore, requires a miniaturization of the wires. Microfabrication also allows for a high degree of control over the shapes of magnetic fields. This has led, for example, to the construction of 'conveyor belts' [Hänsel et al., 2001; Fortágh et al., 2004] that transport atomic clouds across the chip surface by using an array of individually addressable trapping wires. A photo of a structure built in Tübingen is shown in Fig. 1.4.

Much interest is put in creating integrated atom optics that combines atom-optical, optical, and possibly mechanical elements. An important step towards a 'lab on a chip' is the on-chip creation and handling of BECs, where many atoms behave in a coherent manner, much like the photons of a laser [Pitaevskii and Stringari, 2003]. As an important result, matter-wave interference can be observed in split and recombined BECs with high signal and contrast [Mewes et al., 1996]. An atom-chip version of the setup that uses 'cloud splitters' [Folman et al., 2002; Reichel and Vuletic, 2011] to implement an atomic interferometer was presented by Schumm et al. [2005]. Further applications have led to atomic clocks on a chip [Treutlein et al., 2004], now commercially available. Chip-based traps for cold atoms are also considered a milestone towards the construction of a scalable quantum computer [Negretti et al., 2011; Nyman et al., 2011]. Here, stable traps and long coherence times are necessary, which requires precise knowledge of the fluctuation spectra and correlations of the electromagnetic fields above the chip.

1.2.2 Limitations

The application of magnetic traps is mainly limited by a finite trapping time of atoms. Losses of atoms from the trap occur, e.g., due to scattering with the background gas in the vacuum chamber and due to evaporation [Folman et al., 2002; Reichel and Vuletic, 2011]. The latter is well controllable with modern cooling techniques. The surface may even help to 'shave off' the hottest atoms (evaporative cooling), reaching cloud temperatures below $1\,\mu$K [Harber et al., 2003].

In atom-chip setups, the advantages of miniaturization come at a price. The close proximity to matter (i.e. the chip surface on which the wires are defined by etching) leads to enhanced levels of electromagnetic fluctuations as compared to free space. Most importantly, thermally excited currents in the conductors are the source of magnetic field fluctuations (Johnson noise) that can induce atomic transitions to untrapped (strong-field seeking) atomic states [Jones et al., 2003], see Fig. 1.3b). For a review of loss mechanisms in atom chips, see [Folman et al., 2002]. The noise intensity depends on material properties, more precisely on the conductivity [Henkel et al., 1999, 2003; Jones et al., 2003; Harber et al., 2003; Lin et al., 2004; Rekdal et al., 2004; Henkel, 2005; Scheel et al., 2005; Zhang et al., 2005]. A promising way to improve the trap stability involves superconducting trapping wires, where dissipation-free supercurrents reduce Johnson noise [Skagerstam et al., 2006; Nirrengarten et al., 2006; Hohenester et al., 2007; Cano et al., 2008; Dikovsky et al., 2009; Hufnagel et al., 2009; Emmert et al., 2009; Kasch et al., 2010]. Previous work has addressed technologically relevant questions, such as finite size effects [Zhang et al., 2005] and critical currents in superconducting atom chips [Zhang, 2008; Dikovsky et al., 2009]. Chapter 3 of the present thesis investigates the impact of a wave-vector-dependent conductivity, which arises due to small-scale ballistic charge transport, on the electromagnetic near-field noise of normal metals and superconductors.

A further limitation occurs when traps are operated at distances in the micron range from the surface. Here, van der Waals-Casimir-Polder potentials become dominant and tend to deform the trap, as is shown in Fig. 1.5 and discussed in the following section. In practice, this limits atom-chip experiments to distances above $1\,\mu\mathrm{m}$. Here, the trap breaks open towards the surface, giving rise to physical adsorption (without electron exchange) or chemical binding. Smaller distances down to $50\ldots150\,\mathrm{nm}$ can, however, be reached with evanescent wave mirrors [Landragin et al., 1996; Bender et al., 2010].

1.2.3 Measurement of atom-surface potentials with trapped atoms

Usually, the trap potential is well approximated by a harmonic potential. For simplicity we consider only the direction perpendicular to the surface, so that the trap potential is

$$V_\mathrm{t}(z) \approx \frac{m}{2}\Omega_\mathrm{t}^2 z^2 \tag{1.1}$$

with the atomic mass m and a trap frequency Ω_t. According to a theorem by Kohn [1961], the excitation of the *dipole mode*, a collective motional degree of freedom, results in a center-of-mass oscillation at the trap frequency Ω_t, even if the trapped particles interact, as in the case of a BEC surrounded by a thermal cloud. Center-of-mass oscillations are therefore very long-lived. The dipole mode can be excited by a periodic displacement of the trap [Japha and Band, 2002].

Any additional potential $U(z)$ acting on the trapped atoms leads to a deformation of the trap and to a change in the position and the shape of the trap minimum. This becomes

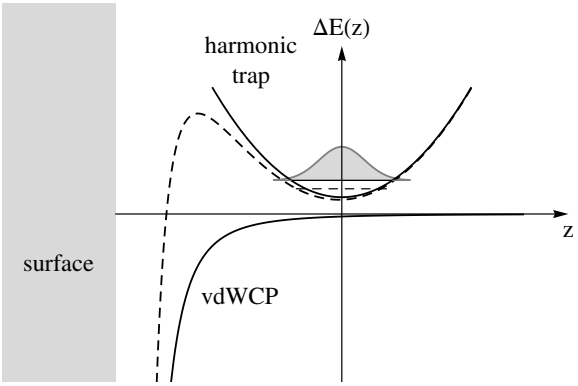

Figure 1.5: Deformation of the harmonic trapping potential due to van der Waals-Casimir-Polder (vdWCP) interactions. The effective potential (dashed curve) is characterized by a shifted trap frequency. The potential barrier towards the surface is lowered as the trap minimum is moved closer to the surface.

directly visible as a shift in the dipole-mode oscillation frequency [Antezza et al., 2004]

$$\Delta\Omega_t \approx \frac{1}{m}\int d^3\boldsymbol{r}\rho(\boldsymbol{r})\frac{\partial^2 U(z)}{\partial z^2} \qquad \text{if } \Delta\Omega_t \ll \Omega_t\,, \tag{1.2}$$

where the particle density of the cloud $\rho(\boldsymbol{r})$ limits the integration range. Fig. 1.5 illustrates the deformation of the trapping potential due to the van der Waals interaction. The small damping of the dipole-mode oscillations makes it possible to perform very precise frequency measurements. This has led to the characterization of the electric Casimir-Polder potential between a rubidium BEC and a surface [Harber et al., 2005] and its temperature dependence at distances as large as $5\,\mu\mathrm{m}$ [Obrecht et al., 2007].

Note that the dominant contribution to the van der Waals potentials is due electric dipole fluctuations (visible or near-IR transitions). In Chapter 4, we will, in contrast, consider magnetic dipole transitions (hyperfine or Zeeman levels), which involve much smaller Bohr frequencies, leading to a much stronger temperature dependence. The magnetic energy shift is too small to be resolved, at present, in the frequency-shift technique but might be accessed from measurements of the barrier height in quantum reflection experiments [Landragin et al., 1996; Druzhinina and DeKieviet, 2003], or in spectroscopic measurements similar to the approach by Failache et al. [1999]; Bloch and Ducloy [2005]. The merit of investigating the magnetic Casimir-Polder interaction of atoms with a (super)conducting surface lies in providing an alternative setting where current-damping (ohmic losses) in the surface play an important role, similar to the macroscopic Casimir interaction discussed below (Sec. 1.3). It turns out that the underlying physics might therefore, in principle, be tested in superconducting atom chips.

1.2.4 Transition rates and heat-transfer measurements

The previous section has underlined that a miniaturization of quantum optics experiments can be obtained on atom chips. But beyond that, the study of trapped atoms close to the surface provides new ways of probing surface properties with spatial resolution on a mesoscopic (subwavelength) scale, turning into virtues the same effects that put limits to the use of atom chips.

In magnetic microtraps, the direct observation of atomic transitions provides a 'microscope' for local static magnetic fields. From Fermi's Golden Rule we know that the probability for an atom to undergo a transition depends on the *local density of states (surface spectrum)* of the electromagnetic field at the respective transition frequency, cf. Chapters 2 and 3. Near a surface, this quantity differs from the blackbody prediction and depends on the material properties. In contrast to atom-surface potential measurements, the observation of atomic transition rates gives spectrally resolved information.

A well-known example is the spontaneous decay rate of an atom, which near a surface can be significantly enhanced with respect to the free space, or suppressed in a cavity [Purcell, 1946; Dalibard et al., 1982; Ford and Weber, 1984; Goy et al., 1983]. In atom-chip environments, the same mechanism leads to atomic loss from a trap due to magnetic transitions between trappable and untrappable states (Zeeman or hyperfine levels, cf. Fig. 1.3b). Measurements of how the number of trapped particles decays in time can, therefore, provide direct information about the magnetic surface spectrum. Previous work has shown the impact of the local conductivity on the magnetic near-field noise [Henkel et al., 1999, 2003; Henkel, 2005]. Chapter 3 discusses the role of ballistic charge transport in the material, relevant for the spin-flip loss channel in the 'extreme near field' of distances comparable to the mean free path of the charge carriers, typically $10 \ldots 100\,\mathrm{nm}$.

In an atom-chip setup, the trapped atoms are cooled down to less than $1\,\mu\mathrm{K}$, while the chip-surface has a much higher temperature ($4 \ldots 300\,\mathrm{K}$). Even in vacuum, the nonequilibrium situation gives rise to a radiative heat flux from the surface to the atomic cloud. The heat transfer rate is another possible observable that can reveal information about the material properties. As in the Casimir configuration, heat transfer can also be studied between any two objects at different temperatures, see [Volokitin and Persson, 2007] for a review. The impact of dissipation and ballistic charge transport was studied in these situations by Henkel et al. [1999]; Henkel and Wilkens [1999]; Chapuis et al. [2008b].

Of course, not only neutral atoms but also trapped ions can serve as probes for static electric fields and electric field noise near the surface. This provides information about the distribution of surface charges and adsorbates [Turchette et al., 2000; Dubessy et al., 2009]. In an atom-chip environment with neutral particles, patch potentials can still provoke a Stark shift in the electric dipole transitions of neutral particles. While this does not influence greatly the trap stability, it is relevant for applications such as quantum gates or atomic clocks that depend on exact tuning and accurate phase control.

We have already seen strong similarities between MEMS and trapped atom setups

in the case of surface force measurements. A highly interesting solid-state system that addresses the spectrally selective processes reviewed in this section is provided by a single nitrogen-vacancy (NV) center inside an AFM tip made of diamond. Its electric dipole has been used successfully in spatially resolved measurements of resonant energy transfer rates [Tisler et al., 2011].

1.3 Casimir Interactions in Microelectromechanical Systems

From a microscopic point of view, it is natural to think of the Casimir effect between macroscopic bodies as an effective dispersion interaction arising from the van der Waals-Casimir-Polder forces between the bodies' constituent atoms.

The resulting Casimir force is in fact large enough to be measured, e.g. in MEMS systems, see [Decca et al., 2011]. A typical setup used in precision measurements of the Casimir potential consists of a plane surface and a nanosphere attached to the tip of an atomic force microscope (AFM) [Chan et al., 2001; Iannuzzi et al., 2004; Lisanti et al., 2005]. Precisely as the trapped atoms in Sec. 1.2.3, the cantilever of the AFM provides a mechanical oscillator, the resonance frequency of which is shifted by the Casimir potential between the nanosphere and the surface below. Of course, any other potential affects the mechanical resonance, too, and the calibration of Casimir forces against electrostatic ones is a major topic in recent research [Lamoreaux, 2011; Decca et al., 2011; Behunin et al., 2012].

While the seminal article by Casimir [1948] assumed ideally reflecting plane surfaces, the Casimir potential is actually not universal but depends strongly on the specific properties of the cavity. A general description, based on an effective medium approach[2], goes back to Lifshitz [1956]. Still, the correct modelling of metals is an open question in the *thermal* Casimir effect [Milton, 2009; Klimchitskaya et al., 2009], because – counterintuitively – not all measurements are described best by a finite direct current (DC) conductivity, see [Decca et al., 2005; Sushkov et al., 2011]. From an 'anatomic approach', low-frequency modes most sensitive to ohmic damping can be shown to play an important role here [Intravaia and Henkel, 2009]. Valuable insights can therefore be expected from superconducting cavities, where a high degree of control over conductivity is possible [Bimonte et al., 2005, 2010; Bimonte, 2008].

Current research focuses on detailed descriptions of the objects involved, such as material, geometry, and roughness corrections [Golestanian, 2005; Emig et al., 2007; Lambrecht et al., 2011; Rahi et al., 2011; Johnson, 2011; van Zwol et al., 2011]. Another topic of interest is the search for Casimir repulsion [Pitaevskii, 2011; Capasso and Munday, 2011]. While the Casimir interaction results in attraction in many configurations

[2] See, e.g., the textbooks by Mahanty and Ninham [1976]; Milonni [1994]; Mostepanenko and Trunov [1997]; Milton [2001]; Parsegian [2006]; Dalvit et al. [2011] and the review articles by [Milton, 2009; Klimchitskaya et al., 2009]. For a review of density functional techniques in the dispersion interactions see [Dobson and Gould, 2012].

[Kenneth and Klich, 2006], a repulsive or switchable parameter might help to mitigate the *stiction forces* [Chan et al., 2001; Buks and Roukes, 2001] that lead to the jamming of movable parts in MEMS. Casimir repulsion occurs between bodies immersed in a dielectric liquid, due to 'optical buoyancy' [Dzyaloshinskii et al., 1961; Munday et al., 2009]. Other candidate systems involve an asymmetry between the surfaces [Boyer, 1974; Kenneth and Klich, 2006; Geyer et al., 2010] or systems out of thermal equilibrium [Antezza et al., 2005], where surface-mode contributions play an important role [Svetovoy, 2007]. One such example is discussed in Chapter 6.

1.4 Optical Surface Response

All the previous observables (Casimir and vdWCP potentials, heat transfer rates, fluorescence and transition rates) can be described in a common framework known as the *scattering approach* [Balian and Duplantier, 1977; Jaekel and Reynaud, 1991; Emig et al., 2007]. This approach is based on the fact that all interaction is mediated by light. This makes it possible to break down the description of the system to the knowledge of *optical linear response* functions of atoms and of matter, and of *correlation functions* of electromagnetic fields.

The field correlations in the presence of an atom or a small nanoparticle can be calculated perturbatively, based on the particle's electric or magnetic polarizability. This leads to the diagrammatic perturbation theory for atoms and photons exposed in detail in Chapter 2. In the case of a macroscopic object, the correlation function must describe both its geometry and the material properties. In this work, the object is always considered a continuous plane surface and all the necessary information is contained in a set of reflection amplitudes (or surface impedances, see App. B).

Historically, the model of an *ideally reflecting mirror* is very popular. A more thorough calculation of the reflection amplitudes involves the *bulk properties* of the material, described through a *conductivity* or *dielectric tensor* [García-Moliner and Flores, 1977; Dressel and Grüner, 2002]. One well-known example is the Drude model, giving the simplest description of a metal with a finite conductivity. Ballistic charge transport must be considered to describe the anomalous skin effect [Reuter and Sondheimer, 1948; Ford and Weber, 1984]. This leads to a wave-vector dependence of the conductivity (*spatial dispersion*). The *specific properties of the surface* must be taken into account, too. Especially in the case of spatial dispersion, responses to transverse and longitudinal fields differ and require a more careful treatment, e.g. through the introduction of boundary conditions that encode symmetries of the charge scattering at the inner metal surface [Reuter and Sondheimer, 1948; García-Moliner and Flores, 1977] (Apps. B.3, B.4). In general, also surface roughness, corrosion, or adsorbates may modify the response, e.g. [Toigo et al., 1977; Bedeaux and Vlieger, 2004]. Of course, the approach sketched out here is not the only one. Density functional theory, for instance, allows for a self-consistent calculation of the fields [Gross and Dreizler, 1995].

Due to the presence of charges in the material, the electromagnetic fields near a surface differ significantly from the dipole radiation (photons) in free space. Similar to the near field of a dipole, there are nonradiative (evanescent) fields confined to the interface. In fact, all the effects mentioned previously depend strongly on the fact that the near field of a body is dominated by these surface modes, such as the surface plasmon-polariton excitations in a metal [Raether, 1988; Joulain et al., 2005]. García-Moliner and Flores [1977] showed that the knowledge of the surface-mode dispersion relations is actually largely equivalent to the knowledge of reflection coefficients.

Surface modes can be well controlled in microstructured *plasmonic systems*, down to the quantum level [Bergman and Stockman, 2003], with applications such as near-field spectroscopy with sub-wavelength resolution [Brongersma and Kik, 2007; Maier, 2007], extraordinary transmission through structured media [Altewischer et al., 2002; Fasel et al., 2005; Garcia-Vidal et al., 2010], and heat-transfer control [van Zwol et al., 2012; Guérout et al., 2012]. The role of surface modes in the dispersion interactions is addressed specifically in Chapters 5 and 6.

1.5 Overview

This thesis investigates aspects of the interactions between surfaces and atoms on mesoscopic scales, comparable to the wavelength of light emitted by the atoms, but larger than the atomic structure of solids. This excludes length scales below $1\,\text{Å}$ (Fig. 1.1) and leads to the peculiar regime where the microscopic and the macroscopic manifestations of quantumness meet: Clearly, the quantum nature of atoms and photons is relevant, while solids appear as continua and can be described in terms of macroscopic electrodynamics. Light scattering from the surface, however, bears characteristics of the microscopic dynamics of charges near the surface, e.g. temperature-dependent relaxation rates due to phonon scattering, the anomalous skin effect connected with ballistic charge transport, or the resonant response of surface excitations.

Particular attention is paid to magnetic effects. Magnetic dipole transitions in atoms lie in the centimeter band of much smaller energies than typical electric dipole transitions, which leads to a strong impact of thermal occupation of the electromagnetic field modes. Surprisingly, this does not necessarily enhance the atom-surface interaction. Here, details of the current-transport in the material play a central role. It is therefore interesting to compare normal metals to superconductors, in which current-dissipation can be precisely controlled, with direct implications for the trap stability of superconducting atom chips and the atom-surface interaction.

The thesis is organized as follows. A nonequilibrium quantum field theory for atoms (or molecules) and light is developed in Chapter 2. It underlines that virtually all interactions are mediated by the electromagnetic field. The inclusion of light-scattering by macroscopic objects allows for addressing atom-surface interactions and provides a common framework for the rest of this thesis. Another important application is the potential

between two atoms or molecules, where the treatment of unstable excited states has led to apparently contradictory predictions in previous work.

Chapter 3 first considers how the magnetic noise spectrum near a surface is affected by nonlocal (spatially dispersive) charge transport in a metal, connected to the ballistic electron movement on the submicron scale. The noise spectrum is directly accessible through loss rates of trapped atoms. It turns out that at distances below the electronic mean free path in the conductor, the low-frequency magnetic near-field noise is less intense than predicted in earlier work. The discussion is complemented by a study of the impact of electric field noise on trapped Rydberg atoms. This has implications for the stability of qubit states used in quantum computing applications.

In Chapter 4, we study the magnetic dipole contribution to the Casimir-Polder interaction between an atom and a surface. We find that in contrast with the electric dipole coupling, ohmic losses are strongly relevant. It is therefore interesting to compare the atomic coupling to superconductors and normal metals. Ohmic dissipation leads to a regime of suppressed interaction despite the increased thermal occupation of the electromagnetic field. In the absence of dissipation, the potential features a temperature-independent regime. This makes the magnetic Casimir-Polder interaction of an atom with a normal metal strongly temperature dependent. A very similar behavior is known from the Casimir interaction between macroscopic bodies, so that open questions in this field might be addressed alternatively in the Casimir-Polder configuration.

In Chapter 5, we consider the Casimir-Polder potential in a system with time-dependent properties. The dynamic self-dressing approach illustrates how a cloud of virtual bosons is responsible for the surface-induced energy shift. This is studied in a system that evolves unitarily after an arbitrary nonadiabatic change of either atomic or surface properties. We find that the relaxation of surface-mode excitations becomes visible through the atomic dynamics in the near field.

Many of the previous observations can be directly connected to effects known from the Casimir interaction between two metallic surfaces. The impact of surface modes in such a Casimir cavity, including thermal field states and situations out of thermal equilibrium, is studied in Chapter 6.

The thesis concludes with a summary in Chapter 7. The Appendices give details on the nonequilibrium Green's functions of molecular field theory and the calculation of optical material response functions, especially in the cases of nonlocal metals and superconductors.

Chapter 2

The Coupling of Matter and Light

This section contains material from the article *Feynman diagrams for dispersion interactions out of equilibrium* by H. Haakh, J. Schiefele, and C. Henkel, *International Journal of Modern Physics Conference Series* **14**, 347 (2012).

In the long history of ideas and models used to describe the structure of matter on small scales, the observation of intermolecular and surface forces has always played a key role [Margenau and Kestner, 1971; Israelachvili, 1992]. We now understand that, except for gravity, virtually all the physics and chemistry of everyday life are based on interactions of electromagnetic nature. Even interactions between nonmagnetic and electrically neutral particles or even macroobjects have eventually been recognized to be mediated by electromagnetic fields arising from dipole fluctuations [Eisenschitz and London, 1930; London, 1930, 1937]. A treatment in the framework of quantum electrodynamics (QED) including the effects of field retardation was given by Casimir and Polder [1948].

Today, QED provides one of the most precisely tested physical theories available. While it was originally developed in the environment of particle physics at high energies, another important scenario where QED has been applied with great success deals with the interactions between atoms and molecules with the electromagnetic field at nonrelativistic energies. This limit is known as *molecular quantum electrodynamics* [Craig and Thirunamachandran, 1998; Salam, 2009]. There is a long tradition of perturbative treatments of such systems, typically based on a multipole coupling between the electromagnetic field and (hyper-)polarizable objects (atoms, molecules, nanoparticles, etc.).

We address molecular QED in the framework of a quantum field theory (QFT) [Schiefele and Henkel, 2010a,b; Schiefele, 2011], built on work by Lewenstein et al. [1994]; Zhang and Walls [1994]; Lewenstein and You [1996], see also [Cederbaum, 1975]. Here, the atoms and the electromagnetic fields are treated on 'equal footing', using fully quantized fields. A causal description of photons allows for a very efficient pictorial representation through Feynman diagrams. In this chapter, we present a generalization of the field theory of Schiefele [2011] to nonequilibrium configurations. Similar treatments were used previously by Sherkunov [2005, 2007, 2009]; Janowicz et al. [2003]. We use a connection to the classical electromagnetic Green's tensor provided by the fluctuation-dissipation theorem [Callen and Welton, 1951; Wylie and Sipe, 1984, 1985] instead of a mode decomposition of the electromagnetic field [Compagno et al., 1995b]. The advan-

tage is that external boundary conditions, such as the surfaces of macroscopic bodies, can be included in a very natural way.

After a review of the nonequilibrium perturbation theory, the calculation of the relevant observables (atomic energy shifts and lifetimes) is outlined in Section 2.1. Some aspects of the two-body potential are considered in Section 2.2 to illustrate the impact of nonequilibrium effects in a fundamental system. Finally, we outline the treatment of interactions between atoms and macroscopic objects (Sec. 2.3), aspects of which will be discussed in the following chapters.

2.1 Nonequilibrium QFT for Atoms and Photons

2.1.1 Electric and magnetic dipole coupling

Following the treatment by Lewenstein et al. [1994]; Lewenstein and You [1996]; Schiefele [2011], atoms are described in the Born-Oppenheimer approximation (heavy nucleus). The interaction with the electromagnetic field is included conveniently by the multipolar coupling Hamiltonian [Power and Zienau, 1957, 1959][1], which consists in the free Hamiltonians of the atom (A) and the field (F) and a coupling term (AF)

$$H = H_A + H_F + H_{AF}^{\mathrm{el}} + H_{AF}^{\mathrm{mag}} \,, \tag{2.1}$$

$$H_{AF}^{\mathrm{el}} = -\boldsymbol{E}(\boldsymbol{r}) \cdot \boldsymbol{d} \,, \qquad H_{AF}^{\mathrm{mag}} = -\boldsymbol{B}(\boldsymbol{r}) \cdot \boldsymbol{\mu} \,, \tag{2.2}$$

with electric and magnetic dipole moments $\boldsymbol{d}$ and $\boldsymbol{\mu}$. (Spin degrees of freedom can be included in $\boldsymbol{\mu}$.)

We neglect higher multipole moments that arise from expanding $\boldsymbol{E}$ and $\boldsymbol{B}$ around their value at the nucleus to higher orders. This is reasonable in cold dilute gases, because atoms are rather sharply localized on the scale of a few Bohr radii a_0 and will mostly be considered pointlike[2]. The nonzero width implies a UV cut-off on the scale $\omega \approx 2\pi c/a_0$, where the dipole approximation breaks down, e.g. [Compagno et al., 1995b].

A further simplification is possible, if the description of the internal level structure (electric or magnetic, corresponding to electronic or Zeeman transitions, respectively) can be limited to a few energy levels with the largest oscillator strength. For simplicity, we consider a two-level atom with a single transition between a ground-state $|g\rangle$ and an excited state $|e\rangle$, separated by the Bohr frequency $\omega_A = (E_e - E_g)/\hbar$. We introduce field

[1] See also Power and Thirunamachandran [1983]; Ackerhalt and Milonni [1984] and textbooks [Cohen-Tannoudji et al., 1987; Compagno et al., 1995b; Craig and Thirunamachandran, 1998; Scheel and Buhmann, 2008].

[2] Higher multipole contributions, most importantly the electric quadrupole transitions, can be relevant in Rydberg atoms [Crosse et al., 2010], resonant energy transfer [Salam, 2005], and surface-triggered transitions [Karam et al., 2002, 2006]. The impact on atom-surface interactions was reviewed by Bloch and Ducloy [2005]. When finite size effects and photon recoil are relevant in extended systems, e.g. BECs, a spatial wavefunction can be introduced in a natural way [Schiefele and Henkel, 2010a; Schiefele, 2011], see also [Rzazewski and Zakowicz, 1992].

operators $\psi^{a\dagger}$ that create a particle[3] in the state $|a\rangle = |e\rangle,\ |g\rangle$ at the position $\boldsymbol{r}$, see also App. A.1. The generalization to more involved level structures is obtained by summing over the the different excited states [Hinds and Sandoghdar, 1991] and will be considered in Sec. 4.1.

In the present chapter we consider, for definiteness, electric dipole coupling. From Eq. (2.2) the generalization to the magnetic case is straightforward. The interaction Hamiltonian of a two-level atom is given by, e.g. [Schiefele, 2011],

$$H_{AF}^{\mathrm{el}} = -E_i(\boldsymbol{r}) \left[d_i^{eg} \psi^e \psi^{g\dagger} + d_i^{ge} \psi^g \psi^{e\dagger} \right] , \tag{2.3}$$

where the Einstein sum over double spatial indices is implied. The dipole matrix elements $\boldsymbol{d}^{eg} = \boldsymbol{d}^{ge*} = e_0 \langle e|\boldsymbol{r}|g\rangle$ contain the electron charge and, hence, play the role of the coupling constant.

2.1.2 Perturbation series and nonequilibrium formalism

It is common to use stationary perturbation theory in H_{AF} [Craig and Thirunamachandran, 1998; Salam, 2009] to describe the interaction between polarizable objects mediated by the electromagnetic field. This works well at low order, e.g. in the atom-surface interaction, but gets increasingly complex when the summation over intermediate states involves a large number of terms, as in interatomic interactions, see, e.g., [Scheel and Buhmann, 2008]. Moreover, if a nonequilibrium system (e.g. an unstable excited atom) is prepared initially and left to evolve under the interaction, more care must be taken to cover all transitions to energetically allowed final states. We are therefore heading for a concise perturbative treatment based on the closed time-path contour formalism due to Schwinger [1960]; Kadanoff and Baym [1962]; Craig [1968]; Mills [1969], and – most prominently – Keldysh [1964], that helps both issues[4]. It also leads to a pictorial representation by Feynman diagrams.

The starting point of the perturbation theory is the time-evolution operator provided by the *scattering* or *S-matrix*. It can be expressed by the *Dyson expansion* [Dyson, 1949; Fetter and Walecka, 2003]

$$S(t',t) = 1 + \sum_{n=1}^{\infty} \frac{(-\mathrm{i}/\hbar)^n}{n!} \int_t^{t'} dt_1 \ldots dt_n \, T\left\{ H_{AF}(t_1) \ldots H_{AF}(t_n) \right\} , \tag{2.4}$$

where the interaction picture with respect to the unperturbed Hamiltonian $H_A + H_F$ is used. The time-ordering operator $T\{\ldots\}$ moves later time arguments to the left. Virtually all observables can be extracted from correlation functions (also known as propagators) of a product of field operators $\psi^{a\dagger}$ ($a = e, g$ for atoms; the electromagnetic field can be

[3] The operators $\psi^a, \psi^{a\dagger}$ may be either fermionic or bosonic. In the case of a two-level atom, the combinations $\psi^e \psi^{g\dagger}$ and $\psi^g \psi^{e\dagger}$ can always be identified with a fermion-like pseudospin algebra, cf. Sec. 5.1.1.

[4] The outline given in this section follows the presentation by Maciejko [2007]. See also [Danielewicz, 1984] and the extensive introductions by van Leeuwen et al. [2006]; Rammer [2007].

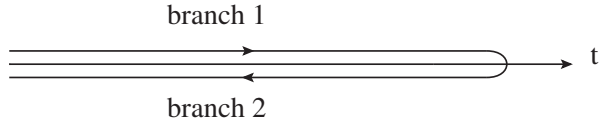

Figure 2.1: Schwinger-Keldysh contour or closed time contour.

treated in a similar way). Expectation values are taken with respect to an eigenstate of the noninteracting theory $|\Phi\rangle$, typically the ground state, so that

$$ia^{(\mathrm{full})}_{\alpha\beta}(x',x) \equiv \frac{\langle\Phi|T\{\psi^a_\alpha(x)\psi^{a\dagger}_\beta(x')\}|\Phi\rangle}{\langle\Phi|\Phi\rangle} \,. \tag{2.5}$$

Arguments $x = (\boldsymbol{r},t)$ denote four-dimensional coordinates, Greek indices are introduced for later use. The time-evolution operator S is used to map the expectation value to asymptotic states in the remote future and past, $|\Phi\rangle = S(0,\pm\infty)|\Phi(\pm\infty)\rangle$

$$ia^{(\mathrm{full})}_{\alpha\beta}(x',x) \equiv \frac{\langle\Phi(\infty)|T\{S(\infty,-\infty)\psi^a_\alpha(x)\psi^{a\dagger}_\beta(x')\}|\Phi(-\infty)\rangle}{\langle\Phi(\infty)|S(\infty,-\infty)|\Phi(-\infty)\rangle} \,. \tag{2.6}$$

Wick's theorem [Wick, 1950; Danielewicz, 1984] allows for a decomposition into products of single-particle correlation functions $a_{\alpha\beta} \equiv a^{(0)}_{\alpha\beta}$, corresponding to Feynman diagrams. Note that only nonfactorizing terms, i.e. *connected* Feynman diagrams, survive due to cancellations with the denominator. The notation can be simplified by introducing a 'connected expectation value' $\langle\ldots\rangle^{\mathrm{conn}}$ that keeps only these terms.

The Feynman formalism of Schiefele and Henkel [2010a]; Schiefele [2011] is valid when in- and out-states $|\Phi(\pm\infty)\rangle$ in the remote past and future, respectively, are known and differ at most by a complex phase [Maciejko, 2007]; the typical scenario in scattering processes of particle physics or in systems in global equilibrium. In contrast, it will break down when $|\Phi\rangle$ is unstable, i.e. out of equilibrium. The evolution of such a system can couple different basis states in a nontrivial way. The reference to an unknown future state can be avoided by applying the S-matrix on the initial state $|\Phi(\infty)\rangle = S(\infty,-\infty)|\Phi(-\infty)\rangle$, so that

$$\begin{aligned} ia^{(\mathrm{full})}_{\alpha\beta}(x,x') &= \langle\Phi(-\infty)|S^\dagger(\infty,-\infty)\ T\{S(\infty,-\infty)\psi^a_\alpha(x)\psi^{a\dagger}_\beta(x')\}|\Phi(-\infty)\rangle^{\mathrm{conn}} \\ &=: \langle\Phi(-\infty)|T_c\{S_2(-\infty,\infty)S_1(\infty,-\infty)\psi^a_\alpha(x)\psi^{a\dagger}_\beta(y)\}|\Phi(-\infty)\rangle^{\mathrm{conn}} \,. \end{aligned} \tag{2.7}$$

In the last step, the contour-ordering operator $T_c\{\ldots\}$ has been introduced to bring operators in that order, in which their time arguments are encountered on the Schwinger-Keldysh contour of Fig. 2.1. The Greek subscripts take the values 1 or 2, denoting the

branch of the contour, which extends from $t = -\infty$ to ∞ (branch 1) and back (branch 2). Note that the Greek indices of the correlation function can be used to generalize the previous concepts to arbitrary arrangements of the field operators. It will turn out that operators on the second branch are responsible to nonequilibrium effects. When the Feynman formalism holds, it is sufficient to use *Feynman propagators* of the type a_{11} with all fields on branch 1.

2.1.3 Field-mediated interaction: self-energy, level shifts, and lifetimes

It is a fundamental observation in quantum field theory that the full perturbation series of a Feynman-ordered response function[5] can always be rewritten in the form [Fetter and Walecka, 2003]

$$a_{11}^{(\mathrm{full})}(\omega, \boldsymbol{r}', \boldsymbol{r}) = a_{11}(\omega, \boldsymbol{r}', \boldsymbol{r}) + \int d^3\boldsymbol{r}_1 d^3\boldsymbol{r}_2 \; a_{11}(\omega, \boldsymbol{r}', \boldsymbol{r}_1)\Sigma_{11}(\omega, \boldsymbol{r}_1, \boldsymbol{r}_2)a_{11}(\omega, \boldsymbol{r}_2, \boldsymbol{r}) \, . \tag{2.8}$$

Here, $a_{11} \equiv a_{11}^{(0)}$ is the unperturbed (leading order) Feynman propagator for the (atomic or electromagnetic) field. The object Σ_{11} defines the *self-energy* and contains contributions from the interaction of the field with the rest of the system at all orders in the coupling. The real and imaginary parts of the single-particle self-energy,

$$\Sigma_{11} = \Delta E - \mathrm{i}\hbar\Gamma/2 \, , \tag{2.9}$$

can be identified as the energy shift and the inverse lifetime (decay width) of the particle [Fetter and Walecka, 2003].

An intuitive interpretation is provided by the closely related notion of *dressed states* [Compagno et al., 1995b]. In this picture, the *bare* object, i.e. the eigenstate of the non-interacting theory, is dressed by a cloud of virtual quanta, leading to a shift in the system energies. The actual physical object that can be addressed in experiments is the dressed state. We will come back to this picture later in Chapter 5.

By identifying self-energies for atoms, the perturbative analysis can be cast in a form that exposes very clearly the field-mediation of the interaction between polarizable objects. In what follows, we first calculate the self-energy of a single atom at next-to-leading order in the coupling to a generic photon. In a second step, the field-mediated interaction included by *dressing* the photons with other objects, e.g. another atom (Sec. 2.2) or a macroscopic surface (Sec. 2.3)[6].

The Hartree-Fock approximation provides an interpretation of ΔE as an effective potential acting on the atom [Kadanoff and Baym, 1962]. The approach sketched out here is especially useful to extract single-particle properties from a more complex system in a nonequilibrium environment.

[5] The consideration of self-energy insertions in Feynman propagators a_{11} is sufficient for the purposes of this work. General self-energy insertions in the Keldysh formalism are discussed in [Danielewicz, 1984].

[6] See Chapter 7 of Schiefele [2011] for a systematic discussion of the higher order radiative corrections to interatomic and atom-surface coupling in the self-energy approach.

2.1.4 The fluctuation-dissipation theorem and retarded response functions

A useful representation of the response functions $a_{\alpha\beta}$ can be obtained for (atomic or electromagnetic) fields in thermal equilibrium. For example, a_{12} must fulfill the fundamental *fluctuation-dissipation theorem* (FDT) [Callen and Welton, 1951; Agarwal, 1975a; Polevoi and Rytov, 1975]

$$a_{12}(x', x) = \mathrm{i} \int \frac{d\omega}{2\pi} e^{-\mathrm{i}\omega(t'-t)} 2\bar{n}(\omega) \,\mathrm{Im}\,[a_R(\omega, \boldsymbol{r}', \boldsymbol{r})] \,. \tag{2.10}$$

Here, $\bar{n}(\omega)$ denotes the Bose-Einstein distribution. In the Fourier domain, this connects a two-point correlation function (fluctuations) to the imaginary part of the *retarded response function*

$$\mathrm{i}a_R(x', x) = \Big\langle [\psi^a(x'), \psi^{a\dagger}(x)] \Big\rangle \, \theta(t'-t) \,, \tag{2.11}$$

where $\theta(t)$ is the Heaviside function. As a consequence, the Feynman propagator is related to the retarded response function by

$$a_{11}(\omega, \boldsymbol{r}', \boldsymbol{r}) = a_R(\omega, \boldsymbol{r}', \boldsymbol{r}) + a_{12}(\omega, \boldsymbol{r}', \boldsymbol{r}) \tag{2.12}$$

$$= a_R^*(\omega, \boldsymbol{r}', \boldsymbol{r}) + a_{21}(\omega, \boldsymbol{r}', \boldsymbol{r}) \,. \tag{2.13}$$

In a system at temperature T, the FDT can be used to express the Feynman propagator through the retarded response [Fetter and Walecka, 2003]

$$a_{11}(\omega, \boldsymbol{r}', \boldsymbol{r}) = \,\mathrm{Re}\,[a_R(\omega, \boldsymbol{r}', \boldsymbol{r})] + \mathrm{i}\coth\{\hbar\omega/2k_BT\} \,\mathrm{Im}\,[a_R(\omega, \boldsymbol{r}', \boldsymbol{r})] \,. \tag{2.14}$$

The previous relations also provide the connection to other formalisms, such as the fluctuation electrodynamics approach of Rytov et al. [1989] and the macroscopic electrodynamics of the Jena school, e.g. [Buhmann and Scheel, 2008], which are based on retarded response functions (Green's functions) of the electromagnetic fields.

The response functions can be classified according to their pole structure in the complex frequency plane. From Eq. (2.11), the retarded response

$$a_R(x', x) = \int \frac{d\omega}{2\pi} e^{-\mathrm{i}\omega(t'-t)} a_R(\omega, \boldsymbol{r}', \boldsymbol{r}) \tag{2.15}$$

must vanish for $t' < t$, so that $a_R(\omega, \boldsymbol{r}', \boldsymbol{r})$ must be analytic in the upper complex frequency halfplane ($\mathrm{Im}\,\omega > 0$). Besides, the imaginary and real part of $a_R(\omega, \boldsymbol{r}', \boldsymbol{r})$ are connected by Kramers-Kronig relations, see [Nussenzveig, 1972]. In contrast, the Feynman propagator a_{11} is an even function in ω and its pole structure depends on the quantum state. Eq. (2.12) relates the Feynman propagator to a *normally ordered response* function, e.g. $a_{12}(x', x) = \langle \psi^{a\dagger}(x') \psi^a(x) \rangle$. The latter quantity gives nonvanishing contributions only in excited systems and is often called a *density matrix* element [Kadanoff and Baym, 1962]. *Anti-normally ordered* quantities $a_{21}(\omega, \boldsymbol{r}', \boldsymbol{r}) = a_{12}^*(\omega, \boldsymbol{r}', \boldsymbol{r})$ will not appear in ground-state systems.

2.1.5 Single atom plus field: self-energy, spontaneous emission, and Lamb shift

We will first consider the radiative corrections to the free propagator of a ground-state atom B (transition frequency ω^B) at the one-loop level. This is a stable particle and all information is contained in the Feynman propagator with both times on the forward branch. Its series expansion is, from Eq. (2.7),

$$ig_{11}^{(\mathrm{full})}(x,y) = \langle T\{\psi^g(x)\psi^{g\dagger}(y)\}\rangle \tag{2.16}$$
$$-\frac{1}{2}\int dt_1 dt_2\, \langle T_c\{\sum_{\alpha,\beta=1}^{2}(-1)^{\alpha+\beta}H_{AF,\alpha}(t_1)H_{AF,\beta}(t_2)\psi_1^g(x)\psi_1^{g\dagger}(y)\}\rangle^{\mathrm{conn}} + \dots\ ,$$

where the first line is the ordinary (bare) Feynman propagator of the ground-state atom, specified in Eq. (A.1) of App. A.1. The excited state Feynman propagator e_{11} can be defined along the same lines [Eq. (A.2)]. In fact, it turns out that all processes with ground-state atoms in their external states can be entirely described in terms of Feynman propagators. The evaluation of Eq. (2.16) to second order in the coupling can be written as

$$g_{11}^{(2)}(x,x') = \int d^3\boldsymbol{r}_1 d^3\boldsymbol{r}_2 \int \frac{d\omega}{2\pi}\, e^{-i\omega(t-t')} g_{11}(\omega,\boldsymbol{r},\boldsymbol{r}_1)\Sigma_{11}^g(\omega,\boldsymbol{r}_1,\boldsymbol{r}_2)g_{11}(\omega,\boldsymbol{r}_2,\boldsymbol{r}')\ . \tag{2.17}$$

Here, the leading order self-energy contribution can be identified. Using the Feynman rules of App. A it can be expressed as

$$\Sigma_{11}^{gB}(\omega_{\mathrm{in}}) = \quad \underset{\omega_{\mathrm{in}}}{B} \overset{\omega}{\sim\!\sim} \underset{\omega_{\mathrm{in}}}{B} \quad = -\mathrm{i}\hbar d_j^B d_i^{B*}\int \frac{d\omega}{2\pi}\, G_{11,ij}(\omega,\boldsymbol{r}_B,\boldsymbol{r}_B)e_{11}(\omega_{\mathrm{in}}+\omega)\ , \tag{2.18}$$

where the $\boldsymbol{G}_{11}$ is the leading order photon propagator, i.e the tensor-valued Feynman correlation function of the electric fields. See Appendices A.3 and B for details and the explicit forms. For the self-energy Σ_{11}^e of an excited atom, replace e_{11} by g_{11} under the integral.

Eq. (2.18) can be brought into a more familiar form [Wylie and Sipe, 1985] by evaluating it on the mass shell, $\omega_{\mathrm{in}} = \epsilon_g^B$ (real particle), and writing the integral over positive frequencies only (recall that $\boldsymbol{G}_{11}(\omega)$ is even in ω):

$$\Sigma_{11}^{gB}(\epsilon_g^B) = \mathrm{i}\hbar\int_0^\infty \frac{d\omega}{2\pi}\, G_{11,ij}(\omega,\boldsymbol{r}_B,\boldsymbol{r}_B)\alpha_{11,ji}^{gB}(\omega)\ . \tag{2.19}$$

Here, we obtain the Feynman-ordered *polarizability tensor* of the ground-state atom B

$$\alpha_{11,ij}^{gB}(\omega) = \frac{d_i^B d_j^{B*}}{\hbar}\left[\frac{1}{\omega_B-\omega-\mathrm{i}0^+}+\frac{1}{\omega_B+\omega-\mathrm{i}0^+}\right]\ , \tag{2.20}$$

which is also discussed in App. A.2. (For the excited two-level atom A^*, replace $\omega_B \to -\omega_A$.) Note that this expression has poles in the upper left and lower right quadrant of the complex frequency plane (Feynman prescription). The analytic properties of the response functions depend on the pole with $\mathrm{Re}\,\omega < 0$, which in quantum optics is often neglected under the rotating wave approximation [Milonni and Boyd, 2004; Berman et al., 2006]. The other pole coindices with the one of the retarded response functions [Eq. (A.7)] at $\mathrm{Re}\,\omega > 0$, and only these appear in the complex self-energy (2.19).

For an atom in free space, substituting the bare photon propagator (see Apps. A.3 and B.1) into $\Sigma_{11}^{g/e}$ yields, according to Eq. (2.9), an infinite energy shift which is, of course, the unrenormalized Lamb shift of atom B [Bethe, 1947; Wylie and Sipe, 1985].

The imaginary part of the ground-state atom self-energy Σ_{11}^{g} is nonzero only if the electromagnetic field is at temperature $T > 0$ [see Eq. (A.12)]. In this case, it describes the absorption rate of thermal photons. At $T = 0$, an imaginary part is found for the excited atom A^*: this is due to a pole of $\boldsymbol{\alpha}_{11}^{eA}(\omega)$ in the upper right quadrant and gives the spontaneous decay rate, i.e. Einstein's A-coefficient

$$\Gamma_0^{eA} = \frac{2 d_i^B d_j^{B*}}{\hbar} \,\mathrm{Im}\, G_{11,ij}(\omega_A, \boldsymbol{r}_A, \boldsymbol{r}_A). \tag{2.21}$$

2.2 Basic Example: Nonequilibrium Two-Body Interaction

To underline the efficiency of the formalism exposed in the first part of this chapter, and to illustrate the impact of nonequilibrium processes, we will apply it a fundamental systems in atomic and molecular physics and consider the interaction between two electrically neutral yet polarizable particles, commonly named after J. D. van der Waals, F. London, H. Casimir, and D. Polder.

2.2.1 Photon propagation in the presence of a second atom

To evaluate the impact of a second atom (labeled A) on the self-energy of atom B, we only have to consider terms where photons are connecting the two atoms, provided we assume the transition frequencies to include the single-particle Lamb shift [Wylie and Sipe, 1985]. Hence, we take the diagram (2.18) and replace the photon propagator by its next-to-leading order correction:

where the lines depend on the state of atom A. This 'modular' strategy is in fact very close to the original calculation of Casimir and Polder [1948] and the treatment by Sherkunov [2005, 2007, 2009]. It is, of course, consistent with the fourth-order expansion of the atom propagator g_{11} in Eq. (2.7). The bare photon propagator $\boldsymbol{G}_{11}(x, x')$ is given in App. A.3,

and its correction to leading order recovers Eq. (28) of Sherkunov [2007]

$$\boldsymbol{G}_{11}^{(2)a}(x',x) = \frac{-i}{2\hbar^2}\int dt_1 dt_2 \times \langle a|T_c\big\{\sum_{l,l'=1}^{2}(-1)^{l+l'}H_{AF,l}(t_1)H_{AF,l'}(t_2)\boldsymbol{E}_1(x')\boldsymbol{E}_1(x)\big\}|a\rangle^{\rm conn}, \tag{2.22}$$

where $a = e, g$ denotes the state of atom A. For the moment we restrict the field to zero temperature, which simplifies the treatment in the frequency domain considerably, e.g. $\boldsymbol{G}_{12}(\omega > 0) = 0$ (see App. A.3 for the general expressions). We find from Wick's theorem [Danielewicz, 1984]

$$\begin{aligned} G_{11,il}^{(2)a}(\omega>0,\boldsymbol{r}',\boldsymbol{r}) &= G_{11,ij}(\omega,\boldsymbol{r}',\boldsymbol{r}_A)\alpha_{11,jk}^{aA}(\omega)G_{11,kl}(\omega,\boldsymbol{r}_A,\boldsymbol{r}) \\ &\quad - G_{11,ij}(\omega,\boldsymbol{r}',\boldsymbol{r}_A)\alpha_{12,jk}^{aA}(\omega)G_{21,kl}(\omega,\boldsymbol{r}_A,\boldsymbol{r})\ , \end{aligned} \tag{2.23}$$

with the atomic polarizabilities of App. A.2. Clearly, nonequilibriums effects are due to the second term in Eq. (2.23) that contains the Keldysh response functions $\boldsymbol{G}_{21}$ and $\boldsymbol{\alpha}_{12}^{aA}$, rather than Feynman propagators.

2.2.2 Interaction of two ground-state atoms

The two-body potential between two particles (atoms, molecules, nanoparticles) in their internal ground state is well known [Casimir and Polder, 1948; Power and Thirunamachandran, 1983; McLachlan, 1963; Craig and Thirunamachandran, 1998].

If atom A is in the ground state ($a = g$), the contribution from the second Keldysh branch vanishes because $\boldsymbol{\alpha}_{12}^{gA}(\omega > 0) = 0$. We obtain a two-atom self-energy by substituting the dressed photon propagator $\boldsymbol{G}_{11}^{(2)g}$ into Σ_{11}^{g},

$\Sigma_{11}^{gg} =$ 

$$= \mathrm{i}\hbar\int_0^\infty \frac{d\omega}{2\pi}\alpha_{11,ij}^{gB}(\omega)\alpha_{11,lk}^{gA}(\omega)G_{11,ki}(\omega,\boldsymbol{r}_A,\boldsymbol{r}_B)G_{11,jl}(\omega,\boldsymbol{r}_B,\boldsymbol{r}_A)\ . \tag{2.24}$$

Only Feynman-ordered quantities contribute, and indeed, this situation corresponds to the ground state of the noninteracting theory where no nonequilibrium formalism is needed. The integration lends itself to a rotation to imaginary frequencies and one sees that $\Sigma_{11}^{gg} = \Delta E^{gg}$ is a purely real two-body potential. If the two atoms are embedded in free space ($T = 0$), the Green's tensor of Eq. (B.2) gives the well-known Casimir-Polder potential that scales as r^{-6} at small separations $r = |\boldsymbol{r}_A - \boldsymbol{r}_B| \ll c/\omega_{A,B}$ and changes to a r^{-7} behavior when retardation sets in.

Note that the same calculation in traditional perturbation theory, e.g. in [Craig and Thirunamachandran, 1998, Sec. 7.4], involves 12 diagrams with time-directed photon lines rather than the two Feynman diagrams above.

The potential ΔE^{gg} can clearly be read as an atomic polarization energy in the field of the second atom. This might be what Casimir and Polder [1948] had in mind, when they suggested "that it might be possible to derive these expressions [...] by more elementary considerations. This would be desirable since it would also give a more physical background to our result [...]. So far we have not been able to find such a simple argument."

2.2.3 Interaction of a ground-state atom and an excited atom

While there is nothing unclear about the potential (2.24), apparently incompatible results have been obtained if one of the atoms is prepared in an excited state, while the second is in the ground state. Due to this initial excitation, the system is metastable and exhibits resonant energy transfer $|A^*\rangle \otimes |B\rangle \rightarrow |A\rangle \otimes |B^*\rangle$, where the asterisk denotes an excited state. Such processes give rise to a resonant long-range part of the potential that overwhelms the familiar van der Waals interaction: at interatomic distances $r \gg c/\omega_A$, large as compared to the atomic transition wavelength, some calculations found this part to oscillate spatially $\Delta E_{\rm res} \sim r^{-2}\sin(2r\omega_A/c + \text{const.})$ [McLone and Power, 1965; Philpott, 1966; Margenau and Kestner, 1971; Kweon and Lawandy, 1993], while later work found a monotonic power law $\Delta E_{\rm res} \sim r^{-2}$ [Power and Thirunamachandran, 1993, 1995; Sherkunov, 2007, 2009]. It is the aim of this section to understand these differences better. A comparison of the Feynman and Keldysh results suggests an interpretation of the apparent disagreement of earlier results: these may apply in different time regimes after preparation, separated by the time scale that characterizes energy transfer by an exchange of resonant photons.

The difference between the Feynman and Keldysh results are due to additional nonequilibrium term in the photon propagator (2.23). We find the following self-energy for the ground-state atom B in the presence of an excited atom A^*

$$\begin{aligned}\Sigma^{ge}_{11} = \quad & \mathrm{i}\hbar \int_0^\infty \frac{d\omega}{2\pi} \alpha^{gB}_{11,ij}(\omega) \{\, G_{11,jl}(\omega, \boldsymbol{r}_B, \boldsymbol{r}_A)\alpha^{eA}_{11,lk}(\omega) G_{11,ki}(\omega, \boldsymbol{r}_A, \boldsymbol{r}_B) \\ & - G_{11,jl}(\omega, \boldsymbol{r}_B, \boldsymbol{r}_A)\alpha^{eA}_{12,lk}(\omega) G_{21,ki}(\omega, \boldsymbol{r}_A, \boldsymbol{r}_B)\}\end{aligned} \tag{2.25}$$

$=$

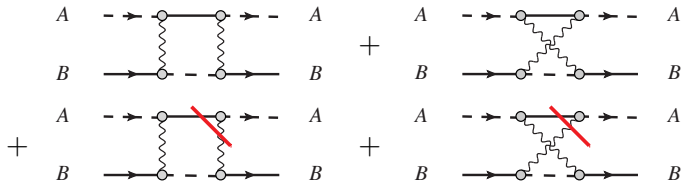

(2.26)

The first line is the result obtained by McLone and Power [1965]; Philpott [1966]; Margenau and Kestner [1971]; Kweon and Lawandy [1993]. In our formalism, this part contains only time-ordered (Feynman) quantities and is represented by the first two diagrams of

Eq. (2.26). We will argue in the next section under which conditions this line gives already the full result.

The second set of diagrams illustrates the terms that contain nonequilibrium response functions. There is one vertex beyond the (thick) bars that corresponds to an interaction operator $H_{AF,2}(x)$ on the second Keldysh branch. It will end *leftmost in an operator product* after the contour ordering T_c and can hence be interpreted as acting directly on the *outgoing* states. This modification of the out-state provides the off-diagonal channels that allow for the equilibration of the initial state (prepared at $t = -\infty$ and left to evolve under the interaction). The thick bar illustrates thus the split between the branches of the Keldysh contour: it corresponds, apart from a prefactor, to cutting the diagrams and putting the loose ends on the mass shell. The resulting two off-diagonal processes conserve energy (tree structure of the diagrams) and can be read as spontaneous emission from atom B after a resonant photon exchange (left diagram) and as emission from atom B stimulated by a photon from atom A (right diagram).

To provide a more transparent physical interpretation, we bring the above result into a form that involves only retarded electric Green's tensors $\boldsymbol{\mathcal{G}}$. At positive frequencies and at $T = 0$, we have $\boldsymbol{G}_{11}(\omega > 0) = \boldsymbol{\mathcal{G}}(\omega)$ and $\boldsymbol{\alpha}^g_{11}(\omega > 0) = \boldsymbol{\alpha}^g_R(\omega)$. Using the connections provided by Eqs. (2.12) and (2.13), see also App. A, we get

$$\begin{aligned}\Sigma^{ge}_{11} = \mathrm{i}\hbar \int_0^\infty \frac{d\omega}{2\pi} \alpha^{gB}_{R,ij}(\omega) \{ \quad & \mathcal{G}_{jl}(\omega, \boldsymbol{r}_B, \boldsymbol{r}_A) \alpha^{eA}_{R,lk}(\omega) \mathcal{G}_{ki}(\omega, \boldsymbol{r}_A, \boldsymbol{r}_B) \\ & + \mathcal{G}_{jl}(\omega, \boldsymbol{r}_B, \boldsymbol{r}_A) \alpha^{eA}_{12,lk}(\omega) \mathcal{G}_{ki}(\omega, \boldsymbol{r}_A, \boldsymbol{r}_B) \qquad (*) \\ & - \mathcal{G}_{jl}(\omega, \boldsymbol{r}_B, \boldsymbol{r}_A) \alpha^{eA}_{12,lk}(\omega) \mathcal{G}_{ki}(\omega, \boldsymbol{r}_A, \boldsymbol{r}_B) \qquad (*) \\ & + \mathcal{G}_{jl}(\omega, \boldsymbol{r}_B, \boldsymbol{r}_A) \alpha^{eA}_{12,lk}(\omega) \mathcal{G}^*_{ki}(\omega, \boldsymbol{r}_A, \boldsymbol{r}_B) \} \ . \end{aligned} \tag{2.27}$$

The two lines indicated by the asterisk $(*)$ cancel out exactly. Note that all nonequilibrium effects have now been traced back to the Keldysh function $\boldsymbol{\alpha}^{eA}_{12}$, connected with the excited atom.

In the first term, we can use that for a two-level atom $\boldsymbol{\alpha}^e_R = -\boldsymbol{\alpha}^g_R$, so that the first term is equal, up to a global sign, to the ground-ground self-energy Σ^{gg}_{11}. The integrand is regular in the upper right quadrant and can be rotated onto the imaginary axis; it does not yield any oscillating contributions.

The last line gives a purely resonant contribution because

$$\alpha^{eA}_{12,ij}(\omega) = 2\pi \mathrm{i} d^A_i d^{A*}_j \, \delta(\omega - \omega_A)/\hbar \, , \tag{2.28}$$

cf. App. A.2. Writing out the retarded polarizability (A.7), too, we find that the resonant

term contains the *square modulus* of the retarded Green's function,

$$\Sigma_{11}^{ge} = -\Sigma_{11}^{gg} - |d_i^A d_j^{B*} \mathcal{G}_{ij}(\omega_A, \boldsymbol{r}_B, \boldsymbol{r}_A)|^2 \frac{2\omega_B/\hbar}{\omega_B^2 - (\omega_A + \mathrm{i}0^+)^2} \tag{2.29}$$

$$= -$$

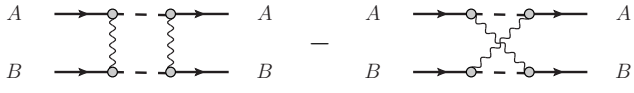

$$-$$

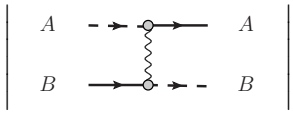

$$^2 \frac{2\omega_B/\hbar}{\omega_B^2 - (\omega_A + \mathrm{i}0^+)^2} \,. \tag{2.30}$$

From the imaginary part of this self-energy, we recover the rate of Förster resonant energy transfer (FRET[7])

$$\Gamma_{\mathrm{FRET}} = -\frac{2}{\hbar} \mathrm{Im}\big[\Sigma_{11}^{ge}\big] = \frac{2\pi}{\hbar} \delta(\omega_B - \omega_A) |d_i^A d_j^{B*} \mathcal{G}_{ij}(\omega_A, \boldsymbol{r}_B, \boldsymbol{r}_A)|^2 \,, \tag{2.31}$$

in full agreement with the Golden Rule. This gives a clear meaning to the resonant contribution to the self-energy. Rather than distinguishing absorption and emission, the above reordering has led to a separation of dispersion (nonresonant or virtual photons) and energy-transfer effects [Power and Thirunamachandran, 1983]. Note that the ground-state atom B has now acquired a finite lifetime, due to the resonant energy-exchange channel. The generalization of the expression for the FRET rate to molecular emission and absorption spectra of finite width is well known [Wu and Brand, 1994; Andrews and Demidov, 1999].

The FRET process comes along with a resonant two-body potential (the real part of Σ_{11}^{ge}) that has been discussed in [Power and Thirunamachandran, 1993; Cohen and Mukamel, 2003a,b; Sherkunov, 2007]. Since it contains the square modulus of the retarded Green's function [Eq. (B.2)], the interaction potential for two particles in free space does not oscillate spatially. Finally, it lends itself to a simple semiclassical picture: the polarization energy of atom B in the time-averaged field of a dipole source located at atom A, whose amplitude is fixed by the transition dipole [Power and Thirunamachandran, 1995].

2.2.4 Transient spatial oscillations of the resonant potential

It is instructive to evaluate the contribution that cancelled out in Eq. (2.27) [upper line marked $(*)$]. Using the explicit forms of $\boldsymbol{\alpha}_{12}^{eA}$ and $\boldsymbol{\alpha}_R^{gB}$, as before, this term gives a resonant contribution

$$\Delta\Sigma_{11}^{eg} = -\big[d_i^A d_j^{B*} \mathcal{G}_{ij}(\omega_A, \boldsymbol{r}_B, \boldsymbol{r}_A)\big]^2 \frac{2\omega_B/\hbar}{\omega_B^2 - (\omega_A + \mathrm{i}0^+)^2}, \tag{2.32}$$

[7] Förster transfer [Förster, 1949; Andrews, 1989] is discussed in the textbooks by Craig and Thirunamachandran [1998]; Andrews and Demidov [1999]; Salam [2009]. For forces connected with FRET processes, see [Cohen and Mukamel, 2003a,b]. Higher multipole contributions were considered by Salam [2005].

which contains the *square* of the electric Green's tensor (B.2) and therefore contains a term $\exp(2\mathrm{i}r\omega_A/c)$ that gives rise to spatial oscillations. Therefore, the first two (Feynman) diagrams in Eq. (2.26) give

$$= -\Sigma_{11}^{gg} + \Delta\Sigma_{11}^{eg}\,, \quad (2.33)$$

where the term $\Delta\Sigma_{11}^{eg}$ is responsible for the spatially oscillating potential found by some authors. This result is subtle, because considering only these terms corresponds to applying an equilibrium formalism in a nonequilibrium situation.

If, in contrast, all four diagrams in Eq. (2.26) are taken into account in the full nonequilibrium description, we have seen in the previous section that the resonant part of the self-energy Σ_{11}^{eg} does not give rise to any spatial oscillations. This is the result of Power and Thirunamachandran [1993, 1995].

We suggest the following scenario to understand the physical relevance of the two results, using the narrative of atom dressing [Compagno et al., 1995b]. The interchange of virtual (or nonresonant) photons responsible for the monotonous part of the potential is very fast. This short-time behavior is similar for both ground-state and excited atoms. The exchange of near-resonant photons takes a longer time due to the small frequency differences involved and it leads to the equilibration of the initial state. This happens on the scale $1/\Gamma_{\mathrm{FRET}}$ set by the Förster rate. This time appears as a lower limit for the validity of the equilibrated potential obtained from Σ_{11}^{eg}. An upper limit is set by the spontaneous lifetime $1/\Gamma_0^e$ of the atom A^* when photons appear in free-space modes [Sherkunov, 2009; Cohen and Mukamel, 2003a]. The two time scales are well separated at short distance (nonretarded range, typical for FRET experiments).

The spatial oscillations of the potential (2.33) may therefore appear as a transient effect after the preparation. We speculate that they remain visible if the excited state is continuously replenished with a sufficiently high rate (larger than Γ_{FRET}), which redefines the cut between 'system' and 'bath'. It would be interesting to consider a time-dependent perturbative calculation similar to the approach of Power and Thirunamachandran [1983] or the formalism presented in Chapter 5 in the context of atomic dressing near a surface. We note that a spatially oscillating dispersion potential has been found in the analogous situations of excited atoms near a surface [Hinds and Sandoghdar, 1991]. For molecules, it has been discussed as a transient effect [Ellingsen et al., 2009b].

In Chapter 4 we will consider the magnetic Casimir-Polder interaction between an atom and a surface. There, the main focus will be put on the impact of the surface properties rather than on the atomic dynamics. For simplicity, the analysis will assume slow equilibration, so that the Feynman formalism is applied.

2.2.5 State-selective directed diffusion in molecular biophysics

As a concluding example, we estimate the FRET force in the context of biological systems. Such a force might modify the motion of the molecules relative to undirected

Brownian diffusion which may help to understand unusually high reaction rates [Berg and von Hippel, 1985]. In fact, it has been discussed whether diffusion-limited reactions between an excited and a ground-state reactant are sped up by a state-selective force [Jordan, 1939; Pauling and Delbrück, 1940; Fröhlich, 1970, 1975], e.g. between proteins and DNA [Hillisch et al., 2001].

In the field of molecular physics, Förster broadening of atomic or molecular spectra is well known, but there is limited literature on the forces that come along with such resonant exchanges of energy [Mal'nev and Pekar, 1970]. The term *Förster force* was apparently coined by Cohen and Mukamel [2003a,b]. These forces may play an important role not only in the aforementioned reaction kinetics but also in a number of other systems that stand in the focus of recent research, such as cold atoms [Anderson et al., 1998; Mourachko et al., 1998] to quantum dots, NV centers [Tisler et al., 2011], and soft condensed matter [Zurita-Sánchez and Henkel, 2012].

We dare a very rough estimate of the recombination rate for a reaction of the type $A^* + B \to AB$, assumed to take place at first contact, cf. [Preto et al., 2012]. From the Smoluchovski equation for spherically symmetric reactands one finds a recombination rate $\gamma_{AB} = 4\pi D_{\rm eff} R_{\rm eff}$, cf. [Berg and von Hippel, 1985]. Here, $D_{\rm eff} = D_A + D_B$ is the sum of the single particle diffusion coefficients, that depend on the particle radii $r_{A,B}$ and the host-medium viscosity. In the so-called Smoluchovski limit of large viscosity, the effective interaction radius for two particles interacting via a two-body potential $U(r)$ takes the simple form

$$R_{\rm eff}^{-1} = \int_{r_A+r_B}^{\infty} dr\, \frac{\exp[U(r)/k_BT]}{r^2}\,. \tag{2.34}$$

For nondirected Brownian diffusion, we have $U(r) = 0$ and $R_{\rm eff} = R_0 = r_A + r_B$. In many cases, including the Coulomb potential and retarded dispersion interactions, it is sufficient to consider a power law $U(r) = -C_n r^{-n}$ (Hamaker ansatz), so that the integral can be expressed through the incomplete gamma function. Then, the speedup of the reaction due to the attractive potential is given by ratio

$$\frac{R_{\rm eff}}{R_0} = \frac{n[U(R_0)/k_BT]^{1/n}}{\Gamma[1/n] - \Gamma[1/n, U(R_0)/k_BT]}\,. \tag{2.35}$$

We neglect a possible temperature dependence of the potential for simplicity. (For a discussion of thermal effects in aqueous solutions at room temperature see [Pauling and Delbrück, 1940]. The two-body potential at nonzero temperature was given, e.g., by Sherkunov [2007, Eq. (70)].)

For distances $r > R_0$, we use asymptotes of the nonresonant Casimir-Polder dispersion potential and of the resonant radiative FRET potential in the retarded regime and include the medium permittivity $\varepsilon(\omega)$

$$U_{\rm CP}(r) \approx -\frac{3\hbar\alpha_A(0)\alpha_B(0)c}{32\pi^2\varepsilon_0^2[\varepsilon(0)]^{5/2}r^7}\,, \qquad U_{\rm FRET}(r) \approx \frac{|d^A|^2\alpha_B(\omega_A)\omega_A^4}{8\pi^2\varepsilon_0^2c^4r^2}. \tag{2.36}$$

At the distances considered, the two terms are ruled by different frequency regimes. Unlike the retarded dispersion term, which is ruled by low frequencies, the resonant term depends on the detuning between the donor and the acceptor. The sign of $\omega_A - \omega_B$ defines, whether atom A illuminates atom B with a red-shifted or a blue-shifted light field. As for an atom in a detuned laser field, this changes the sign of the force [Sherkunov, 2009].

Characteristic numbers can be obtained from systems of DNA molecules, in which the intensity of FRET is commonly used to measure intermolecular distances [Hillisch et al., 2001]. We consider a single dominant transition in the UV regime ($\lambda_A = 265\,\mathrm{nm}, \omega_A = 7.3 \times 10^{15}\,\mathrm{s}^{-1}, |d^{A,B}| = 1.2 \times 10^{-29}\,\mathrm{Cm}$, [Bouvier et al., 2002]), where water is transparent ($\sqrt{\varepsilon(\omega_A)} \approx 1.3$ [Dagastine et al., 2000]), and a typical molecular size of $r_A + r_B = 400\,\mathrm{nm}$. We neglect the nonzero width of the atomic spectra, which corresponds to ideal spectral overlap between the donor and the acceptor and provides an upper limit to the efficiency of FRET. Considering the actual spectral overlap would therefore result in a somewhat smaller FRET potential, e.g. [Cohen and Mukamel, 2003a; Zurita-Sánchez and Henkel, 2012]. In contrast to the resonant contribution, the Casimir-Polder (van der Waals) potential is sensitive to low frequency fields. In water, the static value $\sqrt{\varepsilon(0)} \approx 9$ results in a strong screening with respect to the free space result $U_{\mathrm{CP}}(R_0) \approx 4 \times 10^{-22}\,\mathrm{K}\ k_B$. At atomic separations beyond the medium wavelength, the FRET potential dominates the interaction,

$$\frac{U_{\mathrm{FRET}}(r)}{U_{\mathrm{CP}}(r)} \approx \frac{3}{2} \frac{\left(\sqrt{\varepsilon(0)} r \omega_A / c\right)^5}{1 - \omega_A^2/\omega_B^2} \,. \tag{2.37}$$

This hints at interesting and potentially important effects. From Eq. (2.35) they do, however, not seem sufficient to account for a speedup of reaction rates of several orders of magnitude [Berg and von Hippel, 1985], unless the interaction dipoles are greatly enhanced by some coherence effect. This was suggested by Fröhlich [1970, 1975], see also [Preto and Pettini, 2012].

In any case, a much more thorough consideration of the molecular properties is necessary, before any claims can be made. In biological systems in particular, the excited state may be pumped by an energy source (photoabsorption, chemical). Then, the energy flow through the system will determine to what extent the scenario involving equilibration after excitation actually applies.

The resonant potential can also be expected to play a role in the thermodynamic properties of cold gases (e.g. the virial coefficients [Margenau and Kestner, 1971; Mal'nev and Pekar, 1970]) and to affect solid state based systems such as quantum dots [Kagan et al., 1996]. Such questions certainly deserve further investigation. One should keep in mind that talking about unstable states as in dispersion interactions between atoms or molecules requires a careful characterization of the *excited state* in question.

2.3 Surface-Dressed Photons and the Atom-Surface Interaction

We will now discuss, how boundary conditions imposed by macroscopic bodies can be included in MQED calculations. Similar to the approach of Sec. 2.2.1, where a photon was 'dressed' by an atom, this involves a modified photon propagator. The photon propagator in free space can be calculated directly from a mode expansion of the field. In principle, the same can be done for a field subjected to boundary conditions, for example in the presence a nondispersive surface, but the mode functions become delicate in dispersive or even dissipative systems [Carniglia and Mandel, 1971; Balian and Duplantier, 1977; Dung et al., 1998; Eberlein and Robaschik, 2004]. A more useful approach is provided by the fundamental connection between the classical retarded electric (magnetic) Green's function $\boldsymbol{\mathcal{G}}$ ($\boldsymbol{\mathcal{H}}$) and the Keldysh response functions $\boldsymbol{G}_{\alpha\beta}$ ($\boldsymbol{H}_{\alpha\beta}$) due to the FDT of Sec. 2.1.4 [Agarwal, 1975a; Wylie and Sipe, 1984, 1985]. It is a nontrivial result that all correlation functions for the electromagnetic fields can thus be obtained from the solution of the boundary value problem in classical electrodynamics.

A general scheme for obtaining the Green's tensor in arbitrary configurations of (multiple) magnetodielectric objects is known as the *scattering approach* [Jaekel and Reynaud, 1991; Emig et al., 2007]. In the presence of a single object, the Green's tensor can be written as a sum $\boldsymbol{\mathcal{G}} = \boldsymbol{\mathcal{G}}^{\mathrm{free}} + \boldsymbol{\mathcal{G}}^{\mathrm{refl}}$of a free space part and a reflected part. The latter contains information about the position, geometry, and surface properties encoded in classical reflection amplitudes. This provides a connection to linear response functions of the surface. Such approaches are typical in surface science and condensed matter physics[8] [Flores and García-Moliner, 1979; Dressel and Grüner, 2002]. In this work, we will consider fields near a solid surface modeled by a semi-infinite half-space. A convenient expression for the reflected Green's tensor is due to Sipe [1981]. Here, s- and p-polarized fields form a basis in which the reflection amplitudes are well known [Jackson, 1975]. The explicit forms of the Green's tensor and the reflection coefficients are given in App. B.

The previous decomposition translates immediately to all other correlation functions. A suggestive diagrammatic representation of the surface-dressed photon can be obtained by replacing the free photon line by

Here, the reflected contribution appears as a correction to the free space result, visible e.g. in the Lamb shift and spontaneous emission rates. The correction may in fact be treated as a small perturbation for optically thin surfaces ('dilute limit', e.g. [Milton and Wagner,

[8] The use of classical reflection amplitudes is reasonable on mesoscopic length scales only. There are different approaches that can account for the microscopic structure of solids, most importantly *density functional theory* [Kohn and Sham, 1965; Gross and Dreizler, 1995].

2008]) but not in the case of the near field of a solid, due to the much higher local density of states [Joulain et al., 2003]. In this case, identifying the total correlation functions $\boldsymbol{\mathcal{G}}, \boldsymbol{G}_{\alpha\beta}$ with the reflected one $\boldsymbol{\mathcal{G}}^{\mathrm{refl}}, \boldsymbol{G}^{\mathrm{refl}}_{\alpha\beta}$ provides a simple way of renormalizing the (formally infinite) free-space Lamb shift encountered in Sec. 2.1.5. Then, one should consider Lamb-shift corrected effective atomic transition frequencies as in the work by Wylie and Sipe [1985].

Applying this approximation to the photon propagator in the single-atom self-energy of Eq. (2.19) gives the atom-surface interaction of a ground state atom (for an excited state: $g \to e$)

$$\Sigma^g_{11} = \quad = \mathrm{i}\hbar \int_0^\infty \frac{d\omega}{2\pi}\, G^{\mathrm{refl}}_{11,ij}(\omega, \boldsymbol{r}_B, \boldsymbol{r}_B)\alpha^{gB}_{11,ji}(\omega)\ . \tag{2.38}$$

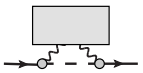

This will be the starting point for the investigation of the properties of atoms at small distances in the (sub-)micron regime from metallic surface. According to Eq. (2.9), the real part of Σ^g_{11} recovers immediately the Casimir-Polder potential of Wylie and Sipe [1985] and their interpretation as a surface correction to the Lamb shift [1984]. In Chapter 4 we will come back to this effect. The imaginary of part Eq. (2.38) describes surface-induced transitions to other atomic levels, which will be considered in Chapter 3. An interesting perspective is the study of surface-assisted FRET, when the surface-dressed photon line is used in the resonant process of Sec. 2.2.3. In this case surface modes can greatly enhance the resonant energy transfer between two particles [Reil et al., 2008; Dzsotjan et al., 2010].

2.4 Summary

In this chapter, we have reviewed a fully quantized formulation of molecular QED, similar to the approaches by Lewenstein et al. [1994]; Lewenstein and You [1996]; Zhang and Walls [1994]; Schiefele [2011] and its generalization to nonequilibrium situations. Note that extended wave functions and recoil shifts might also be included [Rzazewski and Zakowicz, 1992; Schiefele and Henkel, 2010a]. Starting from a modular combination of self-energies of atoms and photons, well-known QED results are recovered, such as the Lamb shift and spontaneous emission rates. Corrections due to the field-mediated interaction with other polarizable objects (macroscopic objects or other atoms) lead to general expressions for the van der Waals-Casimir-Polder potentials and result in changes of the atomic lifetimes. For illustration, the formalism has then been applied to the interaction of two atoms (molecules), either in the ground state or with one of them excited. In the second case, the apparently differing predictions for the resonant part of the two-body potential (spatially oscillating or not) have been a source of confusion for quite some time. From the viewpoint of a nonequilibrium description is seems plausible that contributions that oscillate spatially disappear in a stationary limit. The two different results may thus correspond to different physical setups or to situations separated by a characteristic

time scale, which we related to the rate of energy transfer (FRET). The oscillatory potential [McLone and Power, 1965; Philpott, 1966; Margenau and Kestner, 1971; Kweon and Lawandy, 1993] may apply on very short time scales, and eventually evolve into the nonoscillatory one [Power and Thirunamachandran, 1993, 1995; Sherkunov, 2007, 2009]. Finally, the impact of such resonant potentials on directed diffusion in the context of diffusion-limited chemical reactions has been considered.

Chapter 3

Atoms as Probes for the Electromagnetic Near Field

This chapter is based on material presented in the article *Magnetic near fields as a probe of charge transport in spatially dispersive conductors* by H. Haakh and C. Henkel, *European Physical Journal B*, **85**, 46 (2012). Sec. 3.4 contains material from the article *Prospects for fast Rydberg gates on an atom chip* by M. Müller, H. Haakh, T. Calarco, C. Koch, and C. Henkel, *Quantum Information Processing* **10**, 771 (2012).

Electromagnetic fluctuations have played a key role in physics ever since Planck discovered the blackbody spectrum. They have rather universal properties at distances from a body large compared to the thermal (Wien) wavelength. In contrast, the near-field noise spectrum can tell a lot about material properties due to the links provided by the Kirchhoff law and the fluctuation-dissipation theorem [Callen and Welton, 1951]. In practical applications like magnetic resonance imaging, this near-field noise is a limiting factor for detecting biological signals, see for example [Nenonen et al., 1996; Sidles et al., 2003]. In the case of a metallic body, electromagnetic fluctuations depend mainly on the conductivity and can reveal details about charge transport in the bulk. Our aim is to go beyond Ohm's local law. Therefore, we focus on a linear current-field relation in the general *nonlocal* form (Einstein sum over spatial indices is intended)

$$j_m(\boldsymbol{r},\omega) = \int d^3\boldsymbol{r'}\sigma_{mn}(\boldsymbol{r},\boldsymbol{r'},\omega)E_n(\boldsymbol{r'},\omega)\;, \tag{3.1}$$

where the dependence on both $\boldsymbol{r}$ and $\boldsymbol{r'}$ contains the crossover from ballistic to diffusive in the motion of charge carriers. This introduces the mean free path ℓ as a characteristic length scale. The conductivity (or dielectric) tensor now depends on both frequency and wave vector in Fourier space (*spatial dispersion*) [Reuter and Sondheimer, 1948; Dingle, 1953; Lindhard, 1954; Kliewer and Fuchs, 1968, 1969; Mermin, 1970; Ford and Weber, 1984]. Further nonlocal effects are introduced by the details of the surface and the surface scattering of charge carriers [Reuter and Sondheimer, 1948; Ford and Weber, 1984; Kliewer and Fuchs, 1968, 1970; Foley and Devaney, 1975; Flores and García-Moliner, 1979, 1977; García-Moliner and Flores, 1977; Feibelman, 1982].

The anomalous skin effect is a famous consequence of the nonlocal bulk response. It is typically discussed in the regime of high frequencies, where the classical skin depth $\delta(\omega)$ falls below the mean free path ℓ and does no longer correctly describe screening of magnetic fields in the surface layer of a thickness comparable to ℓ [Reuter and Sondheimer,

1948; Pippard, 1947; Chambers, 1952]. Here, the ballistic transport of charge must be considered and gives rise to a nonlocal response. Other relevant physical phenomena are Thomas-Fermi (Debye-Hückel) screening and Landau damping [Dressel and Grüner, 2002], connected to plasma screening due to mobile charges in the metal and electron-hole generation (internal photo effect), respectively. One can generally expect a reduction of field fluctuations close to the surface of a nonlocal metal as compared to local theory, because the bulk fields are better screened and escape less easily into the surrounding space.

The nonlocal response of surfaces has also been discussed for other observables outside the range of the anomalous skin effect. Its implications have been worked out for the dispersion relation of surface plasmon modes [Flores and García-Moliner, 1979; Feibelman, 1982], the transfer of heat via near-field radiation [Volokitin and Persson, 2007; Chapuis et al., 2008a], the van der Waals interaction across an electrolyte [Podgornik et al., 1987; Jancovici, 2006], and the Casimir interaction between two conducting half-spaces [Sernelius, 2005; Contreras-Reyes and Mochan, 2005; Esquivel-Sirvent et al., 2006; Dalvit and Lamoreaux, 2008].

A motivation for the work presented in this chapter is the observation that spin-flip transitions of ultracold atoms held in miniaturized chip-based magnetic traps (atom chips) are sensitive to magnetic fluctuations in the near field of a metal [Folman et al., 2002; Henkel et al., 2003; Fortágh and Zimmermann, 2007; Reichel and Vuletic, 2011]. Here, atoms probe surface properties at somewhat exotic frequencies in the radio or microwave band, much below the visible to ultraviolet frequency range of conventional metal spectroscopy. (Note, however, that the microwave band is routinely used in superconductor experiments.) At the same time, the corresponding wavelengths are in the micron range because atoms illuminate the surface with their near field. Modes characterized by these frequencies and wave vectors (parallel to the surface) lie in the evanescent sector, way below the light cone; in particular their in-plane wave vector p is not restricted as in propagating vacuum fields. Therefore values $p \sim 1/\ell$ cannot be excluded where spatial dispersion is clearly relevant. Previous work by Henkel and Wilkens [1999]; Henkel et al. [1999]; Jones et al. [2003]; Rekdal et al. [2004] has considered spin-flip transitions for the microtrap scenario in the local limit, identifying these as a relevant challenge to miniaturization below the micron scale. We also mention the results of Chklovskii and Lee [1992] on nuclear spin relaxation that are reproduced and generalized here, including the skin effect and covering a wider range of distances.

Another motivation is the study of spatial correlations of thermal near-field radiation. These differ strongly from the blackbody limit, where the wavelength provides a universal correlation (or coherence) length [Mandel and Wolf, 1995]. For an overview on the coherence of thermal radiation see [Greffet and Henkel, 2007; Dorofeyev and Vinogradov, 2011]. Electric field correlations were discussed previously by Gori et al. [1994]; Ponomarenko and Wolf [2001]; Blomstedt et al. [2007] for homogeneous media, and by Carminati and Greffet [1999]; Henkel et al. [2000]; Dorofeyev et al. [2002]; Henkel and Joulain [2006]; Lau et al. [2007]; Norrman et al. [2011] for the near field of bodies. Sur-

face charge and current correlations have been studied in the high-temperature limit by Boustani et al. [2006]; Jancovici [2006]; Samaj and Jancovici [2008]. In the electric case, the mean free path ℓ did not emerge as a characteristic length scale, neither in the distance dependence of the noise spectrum nor in the spatial autocorrelation function [Henkel and Joulain, 2006]. This may be related to sum rules and efficient screening at the surface. The magnetic field behaves differently because at distances around the mean free path there is a crossover in the noise spectrum [Chklovskii and Lee, 1992]. We show here that the field correlations in a plane parallel to the metal surface become more coherent at short distances and that the correlation length depends on the mean free path.

While the magnetic field noise is of great relevance for trap lifetimes, its electric counterpart has important impact on technological applications, too. A high degree of control over the electric dipole interaction between stored atoms is fundamental if these atoms serve as qubits in the register of a quantum computer [Schmiedmayer et al., 2002; Negretti et al., 2011; Treutlein et al., 2011]. Lately, much interest is put in Rydberg atoms, where a strong dipole interaction is possible. Electric noise leads to decoherence of the qubit states and puts fundamental limits to the operation times of quantum gates. A joint publication with M. Müller, C. Koch, T. Calarco, and C. Henkel recently discussed the possibility to implement a phase gate with trapped atoms using optimal control technology [Müller et al., 2011]. Although the technology and physics of quantum computation does not stand in the center of this thesis, we analyze the effects of electromagnetic noise on the typical scales of atom chips for quantum computation, applying the techniques developed in this chapter to a situation of interest. Note that quantum computation in atom chips requires a high trap stability and will preferably be operated in distance regimes where it is possible to neglect nonlocal effects. One should still consider the impact of patch charges due to surface adsorbates.

In this chapter, we first outline the calculation of magnetic spectra and spin-flip rates and give an overview on the length scales and effects that have an impact on these quantities in a system with nonlocality (Sec. 3.1). Then, a specific nonlocal model for the bulk and surface response is introduced and used to obtain the near-field asymptotes. Some technical details of the calculation are given in App. B. We also briefly discuss superconductors and semiconductors. In Sec. 3.3, field correlation functions above local and nonlocal metals are analyzed with respect to their correlation length. In a complementary way, important sources of electric field noise that may have an impact in trapped Rydberg atoms used for quantum computation are considered in Sec. 3.4. Sec. 3.5 summarizes the main results and reflects on their relevance for experimental setups.

3.1 The Impact of Nonlocal Transport on Magnetic Near-Field Noise

3.1.1 Surface noise spectrum and spin flips

Our main quantity of interest is the spectral density per unit frequency of the magnetic field cross-correlation, evaluated for a thermal state of the field ($i, j = x, y, z$)

$$S^B_{ij}(\boldsymbol{r}, \omega) = \int dt \langle : B_i(0,0) B_j(\boldsymbol{r}, t) : \rangle e^{\mathrm{i}\omega t} \, . \tag{3.2}$$

This spectrum can be calculated with Green's function techniques. According to the fluctuation-dissipation theorem (see Sec. 2.1.4 and App. A.3, note the normal ordering),

$$S^B_{ij}(\boldsymbol{r}, \omega) \;\; = \;\; 2\hbar\bar{n}(\omega) \, \mathrm{Im} \, \mathcal{H}_{ij}(\boldsymbol{r}, \boldsymbol{r}, \omega) \, , \tag{3.3}$$

where $\bar{n}(\omega) = \left(e^{\hbar\omega/k_B T} - 1\right)^{-1}$ is the Bose-Einstein distribution and $\mathcal{H}_{ij}$ the magnetic Green's tensor, cf. App. B. The spectrum can be probed by observing the atomic transition of atoms due to the fluctuating magnetic field. An expression for the atomic transition rate is obtained from Fermi's Golden Rule [Henkel et al., 2003] or a master equation approach [Henkel et al., 1999; Rekdal et al., 2004]. Alternatively, Eq. (2.9) relates the transition rate to the imaginary part of the (magnetic) self-energy in the framework of molecular QED, presented in Chapter 2. From there, Eq. (3.3) gives a natural connection between the spin-flip rate and the spectrum,

$$\Gamma_{a\to b}(\boldsymbol{r}) \;\; = \;\; -\frac{2}{\hbar} \, \mathrm{Im} \left[\quad \right] = \sum_{i,j} \frac{\mu_i^{ab} \mu_j^{ba}}{\hbar^2} S^B_{ij}(\boldsymbol{r}, -\omega_{ab}). \tag{3.4}$$

Here, a (b) labels a magnetic sublevel that is trapped (not trapped) in the static magnetic field of the atom chip, $\mu_i^{ab} = \langle a|\mu_i|b\rangle$ is the matrix element of the magnetic dipole operator, and ω_{ab} the resonant Bohr frequency. For magnetic moments in the order of a Bohr magneton μ_B, the prefactor in Eq. (3.4) translates a spectrum of $130\,\mathrm{pT}^2/\mathrm{Hz}$ to a transition rate of one per second. Rates in this low range have been in fact been measured near conducting surfaces using ultracold trapped atoms as a probe [Jones et al., 2003; Lin et al., 2004; Harber et al., 2003; Reichel and Vuletic, 2011]. The magnetic near-field noise flips the spin of trapped atoms, leading to loss from a magnetic trap and setting a fundamental limit to the coherence in these setups [Folman et al., 2002; Henkel et al., 2003]. Conversely, this process offers a way of probing material properties.

As in Sec. 2.3 we split the Green's tensor in two terms, i.e. the free-space contribution [blackbody spectrum, Eq. (B.4)] and the fields reflected from the surface. In the situations considered in this chapter, the latter term dominates the spectrum by far [Purcell, 1946]. For example, at a frequency of $100\,\mathrm{MHz}$ and at room temperature, the spectrum of a surface at a distance of $1\,\mu\mathrm{m}$ exceeds the blackbody noise spectral density by 15 orders

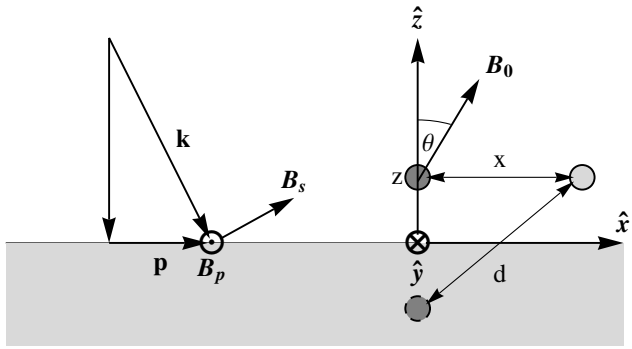

Figure 3.1: *Left*: Orientations of the magnetic field components of an incoming wave with vacuum wave vector $\boldsymbol{k}$ (projection $\boldsymbol{p}$ parallel to the surface). The magnetic field vectors $\boldsymbol{B}_\mathrm{s}$ and $\boldsymbol{B}_\mathrm{p}$ illustrate the two principal polarizations, with the labels s and p taken over from the electric field component of the respective mode.
Right: Coordinates and geometry of the setup. Magnetic noise is evaluated in the center of a magnetic trap (dark gray circle) situated at distance z from the surface. The trapping field $\boldsymbol{B}_0$ defines the quantization axis. In Sec. 3.3 we consider the magnetic field correlations between two points at the same height above the surface, but laterally separated by a distance x. The separation from the mirror image is d.

of magnitude. The reflected magnetic Green's tensor is conveniently expressed in the Weyl representation as a two-dimensional Fourier integral, see also App. B.2,

$$\mathcal{H}_{ij}(z,\omega) = \frac{\mu_0}{8\pi}\int_0^\infty dp\, p\kappa\, e^{-2\kappa z}\times \qquad (3.5)$$
$$\times\left[\left(r_\mathrm{s}(\omega,p)+\frac{\omega^2}{c^2\kappa^2}r_\mathrm{p}(\omega,p)\right)[\delta_{ij}-\hat{z}_i\hat{z}_j]+2\frac{p^2}{\kappa^2}r_\mathrm{s}(\omega,p)\hat{z}_i\hat{z}_j\right].$$

Here, s and p label the two principal polarizations, $\kappa^2 = p^2 - \omega^2/c^2$ is the propagation constant in vacuum, and $\hat{\boldsymbol{z}}$ the unit normal to the surface as shown in Fig. 3.1. Details on the reflection coefficients r_s, r_p are given in Appendix B.3. Note that the magnetic reflected Green's tensor can be obtained from its electric counterpart $\boldsymbol{\mathcal{G}}$ by interchanging $r_\mathrm{p} \leftrightarrow r_\mathrm{s}$ and $\mu_0 \leftrightarrow 1/\varepsilon_0$ [Eq. (B.8)].

Most of this chapter will consider near-field noise, where large values of the perpendicular wave vector $p \gg \omega/c$ (evanescent waves) dominate the response and nonlocal effects become relevant. In this regime, the p-polarization involving r_p is suppressed by the prefactor $\omega^2/(c\kappa)^2$ in the integrand of Eq. (3.5). The analysis can thus be restricted to s-polarization for our purposes (magnetic field vector in the plane of incidence, see Fig. 3.1).

For atoms trapped in their electronic ground state, the magnetic moment is dominated by the contribution of the electron spin. We evaluate the matrix elements in Eq. (3.4),

where the quantum number of the nuclear spin is neglected for simplicity. We consider two magnetic sublevels (spin-like system $J = 1/2$), one of which is magnetically trapped. For a static trapping field in the xz-plane that is tilted by an angle θ relative to the surface normal $\hat{\boldsymbol{z}}$ (cf. Fig. 3.1), the magnetic dipole matrix elements read (App. A.4)

$$\boldsymbol{\mu}^{ge} = \frac{\mu_B g_J}{2} \left(\cos\theta, -\mathrm{i}, -\sin\theta\right)^T \tag{3.6}$$

with the Landé factor g_J.

Above a planar surface, the noise correlations are diagonal, see Eq.(3.7) below, so that the spin-flip rate is proportional to $2 + \sin^2\theta$. The more general case including hyperfine structure can be found in App. A.4, see also [Henkel et al., 1999].

3.1.2 Distance regimes of the noise spectrum

Nonlocal effects can be expected to become visible on a length scale in the order of the mean free path ℓ of ballistic transport of charge carriers, as was already conjectured by Rytov and coworkers [1989]. Numerical calculations of the spin-flip rates for neutral atoms near a metal surface with and without a nonlocal response are shown in Fig. 3.2. Clearly, there are different asymptotic regimes of the distance between the atom and the surface, two of which involve distances much larger than ℓ, where the surface spectrum cannot be distinguished from a local one[1]. We shall find that in these regimes, the Green's tensor can be approximated by the scaling laws

$$\operatorname{Im}\mathcal{H}_{ij}(\omega,z) = \begin{cases} \dfrac{\mu_0[\delta_{ij}+\hat{z}_i\hat{z}_j]}{8\pi\delta^2(\omega)\ell}\left(\ln\left[\dfrac{\ell}{2z}\right]-0.077\right), & z\ll\ell & \text{(i)} \\ \dfrac{\mu_0}{32\pi\delta^2(\omega)z}[\delta_{ij}+\hat{z}_i\hat{z}_j], & \ell\ll z\ll\delta(\omega) & \text{(ii)} \\ \dfrac{3\mu_0\delta(\omega)}{64\pi z^4}[\delta_{ij}+\hat{z}_i\hat{z}_j], & \delta(\omega)\ll z\ll c/\omega & \text{(iii).} \end{cases} \tag{3.7}$$

Here, the skin depth of the normal skin effect is given by

$$\delta(\omega) = \sqrt{\frac{2}{\mu_0\sigma\omega}}\,, \tag{3.8}$$

where $\sigma = \sigma(0)$ is the local limit of the DC conductivity [Eqs. (3.13), (3.14) below]. The first line (i) in Eq. (3.7), obtained below in Sec. 3.1.4, is a central result of this chapter. The local regimes (ii) and (iii) were given already by Henkel and Wilkens [1999]; Henkel et al.

[1] Note for completeness that there is also a *retarded regime* (iv) at even larger distances $z \gg c/\omega$, where the finite speed of light is relevant, and the *thermal (Lifshitz) regime* (v), where thermal energy scales become relevant. These regimes are not shown in Fig. 3.2, but will be considered later, in Sec. 3.1.5 and in the following Chapter 4. An overview over the asymptotic expansions of the reflection coefficients and Green's tensors in the local regimes (ii), (iii) and in the retarded far field (iv) is given in Tables 3.1 and 4.1.

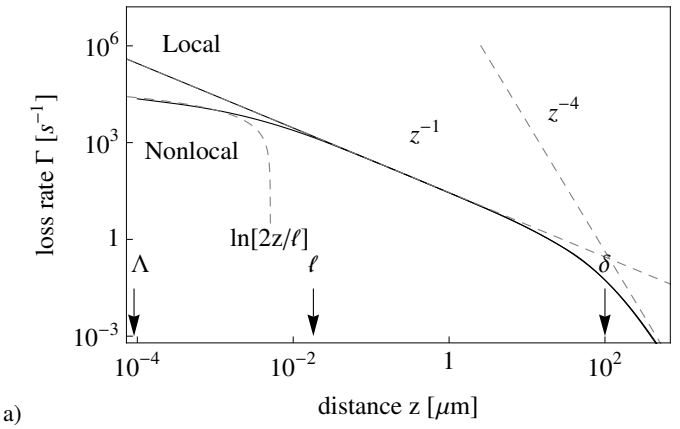

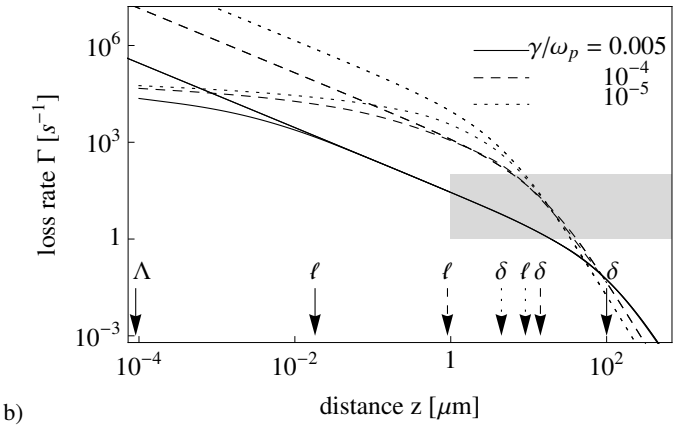

Figure 3.2: a) Spin-flip (loss) rate near a conducting half-space described by the nonlocal Boltzmann-Mermin model [Eqs. (3.9)–(3.12)]. The local description [Drude model (3.13)] and the asymptotic expressions of Eq. (3.7) (dashed) are shown for comparison. The length scales $\Lambda = v_F/\omega_\mathrm{p}$, $\ell = v_F/\gamma$, and δ [Eq. (3.8)] illustrate the Thomas-Fermi screening length, the mean free path, and the skin depth, respectively. The parameters are for gold at $T = 300\,\mathrm{K}$ ($\sigma = 2.5 \times 10^7\,\Omega^{-1}\mathrm{m}^{-1}$, $\ell = 18\,\mathrm{nm}$, $\gamma = 6.7 \times 10^{13}\,\mathrm{rad\,s}^{-1}$) and the surface impedance is calculated with a specular boundary condition [Eqs. (B.11), (B.12)]. Spin flips are driven by fields at the Larmor frequency $\omega/2\pi = 1\,\mathrm{MHz}$ and oriented parallel to the surface [$\theta = 0$ in Eq. (3.6)]. Losses due to the free-space blackbody spectrum are much smaller and not visible on this scale. b) Loss rates near gold surfaces with different purities. The local and nonlocal models are the the same as in a). We vary the ratio γ/ω_p between relaxation rate and plasma frequency in the conductivity. The lowest set of curves coincides with Fig. 3.2a). Note how the intermediate regime $\ell \ll z \ll \delta$ opens up in the 'dirty' limit. The leftmost arrow marks the Thomas-Fermi screening length Λ, δ is again the normal skin depth.

[1999]. To make the qualitative behavior understandable, we propose an interpretation in terms of an *active surface volume*:

When $z \gg \delta(\omega)$ [*nonretarded regime* (iii)], the normal skin effect screens noise from deep in the bulk so that only a skin layer of thickness $\delta(\omega)$ contributes to the noise. The noise is proportional to the squared nonretarded fields $\sim 1/r^3$ of current loops, integrated over the surface – this explains the power law $1/z^4$ and the proportionality to the skin depth $\delta(\omega)$ in Eq. (3.7), upper line.

At smaller distances $\ell \ll z \ll \delta(\omega)$ in the *sub-skin-depth regime* (ii), a medium-filled half-sphere of radius $\sim z$ effectively contributes to the noise. In addition, the probe particle now resolves individual current elements rather than loops. The noise then arises from the squared fields of these current elements ($\sim 1/r^2$), integrated over the volume of the half-sphere, as explained by Henkel and Joulain [2005]. The previous cases (iii) and (ii) have been observed experimentally in the kHz to MHz range with sensitive magnetometers [Varpula and Poutanen, 1984] and with trapped ultracold atoms [Harber et al., 2003], and will be considered in more detail in Ch. 4 in the context of atom-surface forces.

In the present chapter, we mainly address the regime (i) of the *extreme near field* in a nonlocal conductor, $z \ll \ell$: the ballistic (rather than diffuse) motion of charge carriers creates spatial correlations in the fluctuating current field. This reduces the number of mutually uncorrelated volume elements in the half-sphere introduced in (ii) above, and hence lowers the noise power. Note that the limiting value in Eq. (3.7) scales with $1/(\delta^2\ell)$, which is actually independent of the relaxation time in a Drude conductor. The magnetic noise is related to Landau damping, or equivalently to the thermal excitation of electron-hole pairs [Ford and Weber, 1984]. This regime is therefore quite universal and we show in Secs. 3.2.1 and 3.2.2 that semiconductors and even superconductors follow the same scaling law. The rest of this section will review the nonlocal response functions of the conductor and present calculations that confirm these arguments.

3.1.3 Bulk response of a (nonlocal) conductor

All information about the current-field relationship of the bulk is contained in the conductivity or the dielectric tensor. In what follows, different classes of materials, such as metals, semiconductors, superconductors, or dielectrics are modeled by an adequate choice of this quantity. Different mechanisms of current-dissipation will stand in the focus of Chapter 4, while the present one investigates the impact of nonlocality.

In the nonlocal regime, the current-field relationship of the bulk depends on the wave vector and it is necessary to distinguish longitudinal and transverse response functions. Very basic descriptions taking into account some nonlocal effects are hydrodynamic models, see, e.g., [Flores and García-Moliner, 1979; Barton, 1979]. These approaches are valid in a restricted momentum range. The simplest model does not lead to any change in the s-polarization with respect to the local limit, unless some phenomenological transverse response is introduced. A more substantial description of a metal is given by the

Boltzmann-Mermin (BM) model [Lindhard, 1954; Ford and Weber, 1984; Mermin, 1970]

$$\varepsilon_l(\omega, \boldsymbol{k}) = 1 + \frac{\omega_\mathrm{p}^2}{\omega + \mathrm{i}\gamma} \frac{3u^2 f_l(0,u)}{\omega + \mathrm{i}\gamma f_l(0,u)} \,, \tag{3.9}$$

$$\varepsilon_t(\omega, \boldsymbol{k}) = 1 - \frac{\omega_\mathrm{p}^2}{\omega(\omega + \mathrm{i}\gamma)} f_t(0,u) \,, \tag{3.10}$$

where ω_p is the plasma frequency and γ describes the broadening of the electronic states at the Fermi level due to scattering. The variable u contains the momentum dependence via the dimensionless functions

$$f_l(0,u) = 1 - \frac{u}{2} \ln\left[\frac{u+1}{u-1}\right] \,, \quad u = \frac{\omega + \mathrm{i}\gamma}{k v_F} \,, \tag{3.11}$$

$$f_t(0,u) = \frac{3}{2}u^2 - \frac{3}{4}u(u^2-1) \ln\left[\frac{u+1}{u-1}\right] \,, \tag{3.12}$$

where v_F is the Fermi velocity and the logarithm is taken with a branch cut along the negative real axis. These expressions are obtained in the limit $k/2k_F \ll 1$ from a more general model due to Lindhard [1954], hence the redundant first argument '0' [Ford and Weber, 1984]. This assumption is reasonable because for micron-scale chip setups, the relevant wave vectors are in the range $k \sim 1/z$, much smaller than the Fermi momentum $k_F \approx 10^{10}\,\mathrm{m}^{-1}$.

The relevant frequencies for magnetic transitions, typically in the rf- to microwave range, lie in the Hagen-Rubens regime $\omega \ll \gamma \ll \omega_\mathrm{p}$. In this case, spatial dispersion is obviously encoded by the parameter $u \approx \mathrm{i}/k\ell$, and the mean free path $\ell = v_F/\gamma$ sets the relevant scale. In the local limit $k\ell \ll 1$, both expressions reduce to the Drude form

$$\varepsilon_{l,t}(\omega, \boldsymbol{k}) \to \varepsilon_\mathrm{Dr}(\omega) = 1 - \frac{\omega_\mathrm{p}^2}{\omega(\omega + \mathrm{i}\gamma)} \,. \tag{3.13}$$

This is the regime of the normal skin effect where Eq. (3.8) applies. Note that the relation

$$\varepsilon(\omega) = 1 + \frac{\mathrm{i}\sigma(\omega)}{\varepsilon_0 \omega} \tag{3.14}$$

provides the connection to the AC conductivity in the local limit.

While the dielectric function describes the bulk response of the conductor, the specific properties of the surface have an impact on the nonlocality of response as well. The calculation of the reflectivities requires the solution of the electromagnetic scattering problem at the surface. If the bulk conductivity depends on the wave vector, Fresnel's equations do not hold any more, and one has to introduce additional boundary conditions for the current-density at the inner surface. The latter model the way charge carriers are scattered there.

The simplest assumption is that of specular reflection of charge carriers [Reuter and Sondheimer, 1948; Kliewer and Fuchs, 1968; Flores and García-Moliner, 1979; Ford

and Weber, 1984]. Diffuse scattering [Kliewer and Fuchs, 1970; Foley and Devaney, 1975; Flores and García-Moliner, 1979] or a general combination of both mechanisms can be included, but must be treated with care to ensure that charge conservation holds at the surface [Flores and García-Moliner, 1979]. Severe as it may be, this problem only occurs when electric fields have components perpendicular to the surface, i.e. in the p-polarization, while the nonlocal effects considered in this chapter involve the s-polarization. In addition, it is well known that the scattering mechanisms show little differences for the anomalous skin effect [Reuter and Sondheimer, 1948]. Much larger corrections occur, e.g. , due to surface roughness [Bedeaux and Vlieger, 2004]. A detailed calculation of the reflection coefficients at the surface of a nonlocal metal is given in Appendix B.4. It depends on integral equations for surface impedances, closed forms of which can be obtained only in some limiting cases. The resulting reflection amplitudes are shown in Fig. 3.3 for both polarizations. We plot the absorption $\operatorname{Im} r_{\mathrm{s,p}}$, which is proportional, by reciprocity, to the radiated noise power. In the s-polarization, all models converge to the local scenario as $p \ll 1/\ell$, as expected. Spatial dispersion leads to reduced noise for wave vectors $p \gg 1/\ell$. The impact of nonlocality is much more important in p-polarization. The increase of p-polarized absorption in the range $1/\ell < p < 1/\Lambda$ has been discussed previously by Ford and Weber [1984]; Larkin et al. [2004]; Henkel and Joulain [2006]; Chapuis et al. [2008a]; it is due to the internal photoeffect (creation of particle-hole pairs, Landau damping). The results with the diffuse boundary condition introduced by Foley and Devaney [1975] deviate from the local limit already in the range $p \gtrsim 1/\delta$, and become independent of the bulk conductivity. This is likely to be an artifact due to the violation of charge conservation, as discussed by Flores and García-Moliner [1977, 1979].

Note that the factor $(\omega/c\kappa)^2 \sim 10^{-16}$ is very small where the p-polarized absorption peaks so that it is a good approximation to neglect this part in the Green's tensor (3.5). This polarization is essential, on the contrary, for situations sensitive to surface charges and electric surface fields [Flores and García-Moliner, 1979], such as heat transport [Volokitin and Persson, 2007], heating of trapped ions [Henkel et al., 1999] or the electric dipole contribution to dispersion forces [Parsegian, 2006]. As an example, we will consider the impact of electric surface fields on a Rydberg atom in Sec. 3.4.

3.1.4 Surface response in the nonlocal near field

As a central result of this chapter, we derive here the asymptotic form of Eq. (3.7) in regime (i). Within the approximations introduced above, the Green tensor (3.5) can be calculated from

$$\mathcal{H}_{ij}(z,\omega) \approx \frac{\mu_0[\delta_{ij} + \hat{z}_i\hat{z}_j]}{8\pi} \int_0^\infty \mathrm{d}p\, p^2 r_{\mathrm{s}}(\omega,p)\, \mathrm{e}^{-2pz} \,. \tag{3.15}$$

The distance range is now $z \ll \ell$, so that the relevant wave vector range is $p \sim 1/z \gg 1/\ell$. We start from an expansion of the Boltzmann-Mermin model at small values of u. The limiting form of the reflection coefficients in this regime is calculated in Appendix B.4. For specular scattering of charge carriers we find

$$p \gg 1/\ell, \text{ spec. scatt.:} \quad \operatorname{Im} r_{\mathrm{s}}(p,\omega) \approx \frac{1}{p^3 \delta^2(\omega) \ell} , \tag{3.16}$$

while the diffuse boundary condition yields a result smaller by a factor $3/4$. This is similar to the findings of Reuter and Sondheimer [1948] for the anomalous skin effect. The following analysis assumes specular scattering. The power law of Eq. (3.16) illustrates the reduction of noise by spatial dispersion (the decay with momentum is $\sim p^{-2}$ in the local limit) and agrees well with a numerical calculation, as illustrated in Fig. 3.3.

We split the integration range in Eq. (3.15) at $p \sim 1/\ell$ and replace for $p \gg 1/\ell$ the reflection coefficient $r_{\mathrm{s}}(\omega, p)$ by the nonlocal approximation (3.16). The integral then gives

$$\begin{aligned} \int_{1/\ell}^{\infty} dp\, p^2 \operatorname{Im} r_{\mathrm{s}}(\omega,p)\, \mathrm{e}^{-2pz} &\approx \frac{1}{\delta^2(\omega)\ell} \int_{1/\ell}^{\infty} dp \frac{e^{-2pz}}{p} = \frac{\mathrm{E}_1(2z/\ell)}{\delta^2(\omega)\ell} \\ &\approx \frac{\ln(\ell/2z) - \gamma_E}{\delta^2(\omega)\ell} . \end{aligned} \tag{3.17}$$

Here, $\mathrm{E}_1(z) = \int_z^\infty \mathrm{d}t\, t^{-1} e^{-zt}$ is the exponential integral and $\gamma_E \approx 0.577$ is the Euler-Mascheroni constant. In the range $p \ll 1/\ell$, the s-polarized reflection coefficient is approximately equal to its local form $r_{\mathrm{s}}(\omega,p) \approx \mathrm{i}/(2p^2\delta^2)$, cf. Table 3.1 below. The integral becomes (we assume $\ell \ll \delta$)

$$\int_0^{1/\ell} p^2\, dp \operatorname{Im} r_{\mathrm{s}}(\omega,p) e^{-2pz} \approx \frac{1 + \mathcal{O}(\ell/\delta)}{2\delta^2(\omega)\ell} . \tag{3.18}$$

Summing the two contributions gives the approximate Green's tensor (always for $z \ll \ell$)

$$\operatorname{Im} \mathcal{H}_{ij}(z,\omega) \approx \frac{\mu_0[\delta_{ij} + \hat{z}_i \hat{z}_j]}{8\pi\delta^2(\omega)\ell} \left(\ln\left[\frac{\ell}{2z}\right] - \gamma_E + \frac{1}{2} \right) . \tag{3.19}$$

This is the first regime (i) of the Green's tensor (3.7) discussed in Sec. 3.1.2 and corroborates the statement that a nonlocal description predicts less noise at short distances compared to a local one. We have thus generalized a similar result reported by Chklovskii and Lee [1992] within the context of nuclear spin relaxation, where the normal skin effect was neglected. We conclude that for the miniaturization of atom-chip experiments, a large mean free path is advantageous. Crystalline metals may push ℓ into a range that is achievable with atom-chip traps. Another possibility may be chips based on pure semiconductor substrates that we discuss in Sec. 3.2.1.

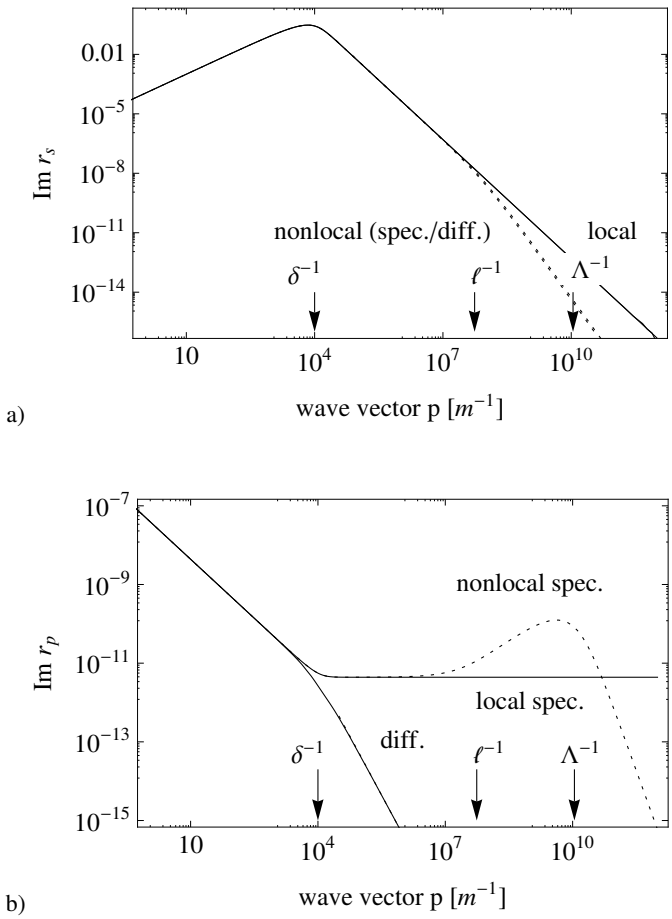

Figure 3.3: Reflection coefficients $\mathrm{Im}\, r_{s,p}$ vs. wave vector in the evanescent sector. a) s-polarization and b) p-polarization. The curves show specular and diffuse scattering at the boundary, and bulk responses given by the local Drude model (solid), and in the nonlocal Boltzmann-Mermin model (dotted). Parameters are for gold ($\sigma = 2.5 \times 10^7\,\Omega^{-1}\mathrm{m}^{-1}$, $\ell = 18\,\mathrm{nm}$, $\gamma = 6.7 \times 10^{13}\,\mathrm{rad\,s}^{-1}$). Frequency $\omega/2\pi = 1$ MHz.

3.1.5 Surface response in the local regimes

Similar asymptotic expansions are known for distances $z \gg \ell$ outside the *extreme near field* (i), where the impact of nonlocality is not visible in the surface response and the dielectric tensor coincides with the Drude model (3.13).

When $\varepsilon(\omega)$ does not depend on the wave vector, the reflection coefficients recover the well-known form of the Fresnel equations ([Jackson, 1975], see App. B.3 for details)

$$r_{\mathrm{s}}(\omega, p) = \frac{\kappa - \kappa_m}{\kappa + \kappa_m}, \quad r_{\mathrm{p}}(\omega, p) = \frac{\varepsilon(\omega)\kappa - \kappa_m}{\varepsilon(\omega)\kappa + \kappa_m}\,, \tag{3.20}$$

	Sub-skin depth (ii) $p \gg 1/\delta(\omega)$	Nonretarded (iii) $1/\delta(\omega) \gg p \gg \omega/c$	Retarded (iv) $\omega/c \gg p$
r_p	$\dfrac{\varepsilon(\omega)-1}{\varepsilon(\omega)+1}\left[1+\dfrac{\varepsilon(\omega)}{\varepsilon(\omega)+1}\dfrac{\omega^2}{c^2p^2}\right]$	$1+\mathrm{i}\dfrac{2}{\sqrt{\varepsilon(\omega)}}\dfrac{\omega}{cp}$	$1-\dfrac{2}{\sqrt{\varepsilon(\omega)}}$
r_s	$[\varepsilon(\omega)-1]\dfrac{\omega^2}{4c^2p^2}$	$-1+\mathrm{i}\dfrac{2}{\sqrt{\varepsilon(\omega)}}\dfrac{cp}{\omega}$	$-1+\dfrac{2}{\sqrt{\varepsilon(\omega)}}$
$\mathcal{H}_{xx}$	$-\dfrac{\mu_0\omega^2}{64\pi Lc^2}\dfrac{5-4\varepsilon(\omega)-\varepsilon^2(\omega)}{1+\varepsilon(\omega)}$	$-\dfrac{\mu_0}{32\pi L^3}\left[1-\dfrac{3\mathrm{i}c}{L\omega\sqrt{\varepsilon(\omega)}}\right]$	$-\dfrac{\mu_0 e^{2\mathrm{i}\omega L/c}}{32\pi L^3}\times$ $\times\left[1-\frac{2\mathrm{i}\omega L}{c}-\frac{4\omega^2L^2}{c^2}\right]$

Table 3.1: Limiting expressions for the Fresnel reflection coefficients for wave vectors relevant in the distance regimes beyond the nonlocal near field (i). From these, the approximation to the magnetic Green's tensor is obtained by performing the integration over p in Eq. (3.5). We have $\mathcal{H}_{xx} = \mathcal{H}_{yy} = \mathcal{H}_{zz}/2$, off-diagonal elements vanish [Spagnolo, 2009]. A comparison between the electric and magnetic Green's tensors obtained from specific models is given in Table 4.1 below.

with propagation constants $\kappa = \sqrt{p^2 - \omega^2/c^2}$ in vacuum and $\kappa_m = \sqrt{p^2 - \varepsilon(\omega)\omega^2/c^2}$ in the medium (roots with $\mathrm{Re}\,\kappa \geq 0, \mathrm{Im}\,\kappa \leq 0$). Approximations for the reflection coefficients appearing in the Green's function (3.5) can be made in characteristic distance regimes that depend on the physical length scales of the system, i.e. the photon wavelength $2\pi c/\omega$ and the normal skin depth $\delta(\omega)$ [Eq. (3.8)], as can be clearly seen in Fig. 3.3.

At relatively small magnetic resonance frequencies $\omega \ll \gamma \ll \omega_\mathrm{p}$ we are in the Hagen-Rubens regime, where $\varepsilon(\omega) \approx 2\mathrm{i}c^2/[\omega\ \delta(\omega)]^2$. We then have $\delta(\omega) \ll c/\omega$ and can distinguish between

(ii) the *sub-skin-depth region*, $z \ll \delta(\omega)$ and

(iii) the *nonretarded region*, $\delta(\omega) \ll z \ll c/\omega$, Besides, there is

(iv) the *retarded regime* $c/\omega \ll z$, mentioned in footnote 1, p. 37. Here, the finite value of the speed of light becomes relevant and leads to a change in the power law of the distance dependence. It is well known in the Casimir-Polder interaction considered in Chapter 4. Expansions of the Fresnel reflection coefficients for the relevant range of wave vectors ($pz \approx 1$) have been obtained and reviewed by Henkel et al. [1999, 2005]; Zhang [2008]. The results are not restricted to the Drude model but remain valid for materials with different dielectric functions, as long as $|\varepsilon(\omega)| \gg 1$. Using these forms, the p-integral in Eq. (3.5) lends itself to direct evaluation. Limiting forms of the reflection coefficients and the Green's tensor are collected in Table 3.1.

For the specific case of the Drude model in the low-frequency regime this gives the results reported in Eq. (3.7). Similar calculations for conductors with different mechanisms of current-damping will form the basis of Chapter 4; superconductors are considered in the upcoming Sec. 3.2.2.

3.2 Universality of the Nonlocal Response

3.2.1 Semiconductors

The previous analysis of near-field noise can be generalized to other classes of conducting materials. Strongly doped semiconductors (where the electron gas is degenerate like in a metal) may be described by the BM model [Eqs. (3.9)-(3.12)] with modifications only in the values of the parameters. For frequencies well below the gap, a background dielectric constant ε_b appears due to the static interband polarizability, but this does not play a role for magnetic near-field noise. In contrast, weakly doped semiconductors (nondegenerate electron gas) are not ruled by Fermi statistics but by a thermal distribution, with the characteristic velocity $v_T = (3k_BT/m)^{1/2}$ taking over the role of the Fermi velocity v_F. Here, Eqs. (3.11) and (3.12) should be replaced by the following expression [Landau et al., 1981; Melrose and McPhedran, 1991]

$$f_t(0,u) = 1 - \frac{3}{2} f_l(0,u) = -\frac{u}{\sqrt{\pi}} \int_{-\infty}^{\infty} dz \frac{\exp(-z^2)}{z-u} \,. \tag{3.21}$$

We observe that this is numerically very close to Eqs. (3.11), (3.12) in the local regime $k\ell \ll 1$ and differs only by a numerical factor in the deeply nonlocal regime. Up to this changed prefactor, the preceding calculations for the $r_{\rm s}$ coefficient and the Green's tensor carry through so that the physics is qualitatively the same.

Let us consider typical numbers that can be found from experiments on charge transport in silicon [Weber and Gmelin, 1991]. An n-type semiconductor with a rather low doping of $3 \times 10^{16}\,\mathrm{cm}^{-3}$ is characterized by a skin depth $\delta > 1\,\mathrm{cm}$ in the MHz range. At room temperature, $v_T = 1.2 \times 10^5\,\mathrm{m/s}$ and the mean free path $\ell \approx 60\,\mathrm{nm}$ is quite comparable to the value for gold. Since it is proportional to the DC conductivity, the magnetic near-field spectrum is smaller by orders of magnitude compared to a metal. Cooling the sample down to $100\,\mathrm{K}$ reduces phonon excitations and enhances the conductivity. Yet, the thermal velocity drops also to, say, $v_T = 6.7 \times 10^4\,\mathrm{m/s}$, so that the mean free path is barely larger, $\ell \approx 85\,\mathrm{nm}$. At even lower temperatures the conduction band occupation freezes out and the response becomes local.

3.2.2 Superconductors

The nonlocal response of superconductors in the microwave range was discussed by Pöpel [1989]; Miller [1960]. It was argued by Rickayzen [1959] that screening in a superconductor does not differ greatly from a normal metal. This is because all charge carriers contribute to screening, whereas the specific properties of a superconductor are determined by the states close to the Fermi level. We thus expect the noise spectrum to be characterized by the same logarithmic asymptote (3.17) found earlier. This is indeed confirmed by numerical calculations of magnetic noise near a niobium surface, the results of which are shown in Fig. 3.4. We have evaluated the nonlocal BCS conductivity

within the approach of Mattis and Bardeen [1958] including disorder scattering, using the expressions of Pöpel [1989], see App. C. The local limit recovers correctly the results of Zimmermann et al. [1991]; Berlinsky et al. [1993]. For comparison we also give the curves for a fictitious normal metal with the same parameters except that the gap is closed ($\Delta(0) = 0$). The description then agrees with the nonlocal BM model. The metallic plasma frequency was adjusted in order to take into account the redistribution of the spectral weight by disorder, as discussed in the articles by Berlinsky et al. [1993]; Bimonte et al. [2010].

In the local regime $z \gg \ell$, the superconductor indeed shows a strong reduction of magnetic noise. This happens because the relevant frequency is below the gap, $\hbar\omega \ll \Delta(T)$, and magnetic fields are screened efficiently by the Meißner effect. At large distances, we find good agreement with the expressions for the lossrate for a two-fluid model, if the same rescaled plasma frequency is taken into account (thin dashed asymptote in Fig. 3.4). This model superimposes a normally conducting Drude fraction and a dissipation-free *plasma* fraction (obtained from the Drude model by setting $\gamma = 0$)

$$\begin{aligned} \varepsilon_{\rm sc}(\omega,T) &= \eta(T)\varepsilon_{\rm pl}(\omega) + [1-\eta(T)]\varepsilon_{\rm Dr}(\omega)\,, & (3.22)\\ \eta(T) &= 1-(T/T_c)^4\,, & (3.23) \end{aligned}$$

where the relative weight is given by the Gorter-Casimir order parameter [Schrieffer, 1999]. No qualitative change occurs if the BCS gap is used instead, setting $\eta(T) \approx \Delta(T)/\Delta(0)$, see also the discussion in Sec. 4.2.1 below.

Inserting this model in the intermediate distance approximation from Table 3.1, the imaginary part of the Green's tensor recovers the result obtained by Skagerstam et al. [2006]. At low frequencies and well below T_c

$$\mathcal{H}_{xx}(z,\omega) \approx -\frac{\mu_0}{32\pi z^3}\left(1-\frac{3\delta(\omega)}{z\sqrt{\eta(T)}}\right) + {\rm i}\frac{3\mu_0\lambda_L}{32\pi\delta(\omega)z^4}\frac{1-\eta(T)}{[\eta(T)]^{3/2}}, \qquad (3.24)$$

where Meißner-London length $\lambda_L = c/\omega_{\rm p}$ determines the penetration depth for quasistatic fields, while the skin depth $\delta(\omega)$ describes the normal fluid fraction. The Meißner effect becomes inefficient, however, if the spatial scale $1/p$ of the noise field becomes comparable to or smaller than the penetration depth $\lambda_L(T)$. In this regime,

$$z \ll \lambda_L(T): \quad \mathcal{H}_{xx}(z,\omega,T) \approx \frac{\mu_0}{64\pi\lambda_L^2 z}\eta(T) + {\rm i}[1-\eta(T)]\frac{\mu_0}{32\pi z\delta^2(\omega)}\,, \qquad (3.25)$$

so that the loss rate follows the $1/z$ asymptote of a normal conductor, see Fig. 3.4. Obviously, the result for a local conductor is obtained as $T > T_c$ ($\eta = 0$).

At shorter length scales $z \ll \ell$, we recover numerically the logarithmic scaling law found before for the normal conductor (Fig. 3.4, thin dashed line). This illustrates the very general character of this regime that does not depend greatly on the material class.

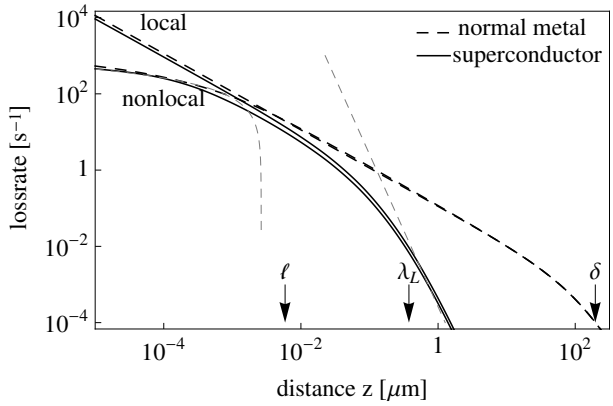

Figure 3.4: Spin flip (loss) rate near a surface made of superconducting niobium (solid curves) and a fictitious normal metal (dashed curves). Nonlocal effects are given for both cases as compared to the local limit. Parameters for niobium at $T = 0.5T_c$ follow Ashcroft and Mermin [1987] $\omega_\mathrm{p} = 1.33 \times 10^{16}\,\mathrm{rad\,s^{-1}}, \gamma = 2.38 \times 10^{-14}\,\mathrm{rad\,s^{-1}}, T_c = 9.2\,\mathrm{K}, \Delta(0) = 1.9\,k_B T_c = h \times 7.9\,\mathrm{GHz}$, $\ell = 5.7\,\mathrm{nm}$. We chose the Larmor frequency $\omega/2\pi = 1\,\mathrm{MHz}$ and $\theta = 0$. Note that Pöpel [1989] gives a mean free path larger by a factor of 4 and a smaller value of γ. For better comparison the normal metal is obtained by closing the superconducting energy gap and rescaling the plasma frequency. Gray dashed lines indicate the asymptotes to the superconductor. Losses due to the free space blackbody spectrum are not visible on this scale.

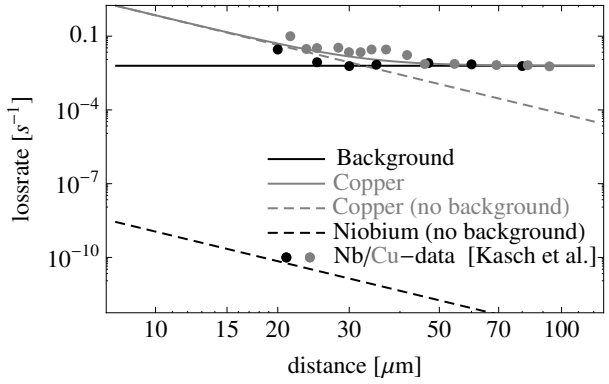

Figure 3.5: Atomic loss rate vs. distance. Data points for superconducting niobium at $T \approx 4.2\,\mathrm{K}$ and for normally conducting copper at the same temperature are taken from [Kasch et al., 2010]. The atomic transition frequency is $\Omega/(2\pi) = 1.71\,\mathrm{MHz}$. Sensitivity is limited by background losses due to imperfect vacuum (black solid line). We use a temperature-corrected conductivity [Poker and Klabunde, 1982] and a skin depth $\delta_\mathrm{Cu}(\Omega) \approx 8\,\mu\mathrm{m}$ (slightly different from $\approx 5\,\mu\mathrm{m}$ reported by Kasch et al. [2010]), so that the trap is operated in the $1/z^4$-regime. Data for copper is well explained by the theory curve (gray solid line, this curve includes the background losses). In the superconducting trap, Eq. (3.24) with parameters given by Ashcroft and Mermin [1987] fails to explain the observed losses. This indicates mixed states in the experiment.

Comparison with experimental data

We confront the previous discussion with experimental data of atomic loss rates near metallic and superconducting surfaces reported by Kasch et al. [2010]. Fig. 3.5 shows good agreement between measured data and the theory prediction in the case of normally conducting copper. Due to additional loss channels, loss rates of atoms near a copper surface lie slightly *above* the theory prediction based only on spin-flip losses. Note that in a superconducting trap, the data lie *below* the theory prediction for copper, indicating a reduction of noise with respect to the normal conductor, according to [Kasch et al., 2010]. However, the strong difference with the theory prediction for the superconductor (Eq. (3.24), see also the results of Skagerstam et al. [2006]; Hohenester et al. [2007]) indicates other sources of magnetic noise present in the experiment. In fact, the model considers a superconductor in the Meißner state. Since niobium is a type-II superconductor, this may not be the case in a trap working with rather large trapping currents and strong magnetic fields. An advanced description should therefore be adapted to nonuniform superconductors, where mixed states [Ketterson and Song, 1999; Tinkham, 2004] lead, e.g., to vortex noise [Dikovsky et al., 2009; Nogues et al., 2009; Horovitz, 2011] but might also be put to use in new trapping schemes [Müller et al., 2010].

3.2.3 Layered structures

So far, the metallic surface has been described as a half-space. However, in many applications it is interesting to consider structures consisting of layers of metals and insulators. The impact of the wire geometry and layered structures on magnetic near-field noise has been considered by Zhang et al. [2005]; Zhang [2008]; Dikovsky et al. [2009] in the context of normal and superconducting atom chips. The calculation of effective reflection coefficients for a layered structure is well-known and can be reduced to the reflection coefficients at the single interfaces [Landau and Lifshitz, 1960; Scheel et al., 2005; Zhang et al., 2005]. In the Casimir interaction between plates, work by Svetovoy and Esquivel [2005] has addressed the role of nonlocality in thin films, providing all the formalism necessary for the analysis of near-field noise. It turns out that the impedances of Eqs. (B.11), (B.12) can still be used, but the integrals must be replaced by sums over possible standing waves inside the layer, giving rise to peaks of the spectrum as a function of frequency. From there, one can expect the logarithmic near-field asymptote to hold even in the case of a thin metal layer, at least where the mean free path is small compared to the film thickness.

3.3 Lateral Coherence

A nonlocal conductivity creates spatial correlations in the current-fluctuations below the surface, which reduce the overall magnetic noise level. It is to be expected that this leaves also a signature in the correlations of the field. These correlations are universal for black-

body radiation [Mandel and Wolf, 1995] and have been studied by Gori et al. [1994]; Ponomarenko and Wolf [2001]; Blomstedt et al. [2007] for homogeneous media, and by Carminati and Greffet [1999]; Henkel et al. [2000]; Dorofeyev et al. [2002]; Henkel and Joulain [2006]; Lau et al. [2007]; Norrman et al. [2011] for the near field of bodies. The spatial correlation length can be much larger or much smaller than the wavelength, depending on the polariton modes that dominate the electromagnetic field noise.

We find in this section that the correlation length is connected to the mean free path as a direct consequence of the ballistic motion of the charge carriers. This is surprising from the contrast to electric fields near nonlocal solids, where the spatial correlations were found to differ from the local description only at distances comparable to the Thomas-Fermi length Λ, with the mean free path ℓ not playing any role [Henkel and Joulain, 2006]. Electric field correlations in the local limit are considered in Sec. 3.4.

We are interested in the correlation between fields at a fixed height z from the surface and laterally separated by a distance x, as shown in Fig. 3.1. The axes are chosen such that the x-axis points along the separation between the two observation points. We define the coherence function as the cross-correlation spectrum of the normally-ordered field operators in frequency space:

$$\mathcal{B}_{ij}(x,z,\omega) \;=\; \int dt \langle : B_i(x,z,t) B_j(0,z,0) : \rangle \mathrm{e}^{\mathrm{i}\omega t} \,. \tag{3.26}$$

The fluctuation-dissipation theorem for normally-ordered operator products (Sec. 2.1.4, [Agarwal, 1975a]) provides the link to the two-point Green's tensor

$$\mathcal{B}_{ij}(x,z,\omega) = 2\hbar\bar{n}\ \mathrm{Im}\ \mathcal{H}_{ij}(\boldsymbol{r},\boldsymbol{r}',\omega) \,, \tag{3.27}$$

where the points $\boldsymbol{r}$, $\boldsymbol{r}'$ are located at the same height and laterally separated by x. This generalizes Eq. (3.3). A general integral form for $\boldsymbol{\mathcal{H}}$ is given in Appendix B.2. We drop the frequency arguments for simplicity in the following.

3.3.1 Local limit

Where a local description of the metal is sufficient, the coherence function in the near field can be evaluated asymptotically by expanding all integrands for values $p \gg 1/\delta, \omega/c$. The resulting integrals involve Bessel functions $J_n(px)$ and can be evaluated exactly.

We find that at distances $\ell \ll z \ll \delta$, the magnetic coherence tensor depends on the distance $d = \sqrt{x^2 + (2z)^2}$ between one observation point and the mirror image of the other (Fig. 3.1). The tensor elements are approximated well by

$$\mathcal{B}_{ij}(x,z) = \frac{4z^2\,\mathcal{B}_{xx}(0,z)}{d(d+2z)} \begin{pmatrix} 2 & & x/z \\ & d/z & \\ x/z & & 2+d/z \end{pmatrix} , \tag{3.28}$$

as can be seen in Fig. 3.6. Here, the noise spectrum $\mathcal{B}_{xx}(0,z)$ for $x=0$ was introduced as a convenient scale, cf. Eq. (3.3). The remaining quantities are independent of the specific

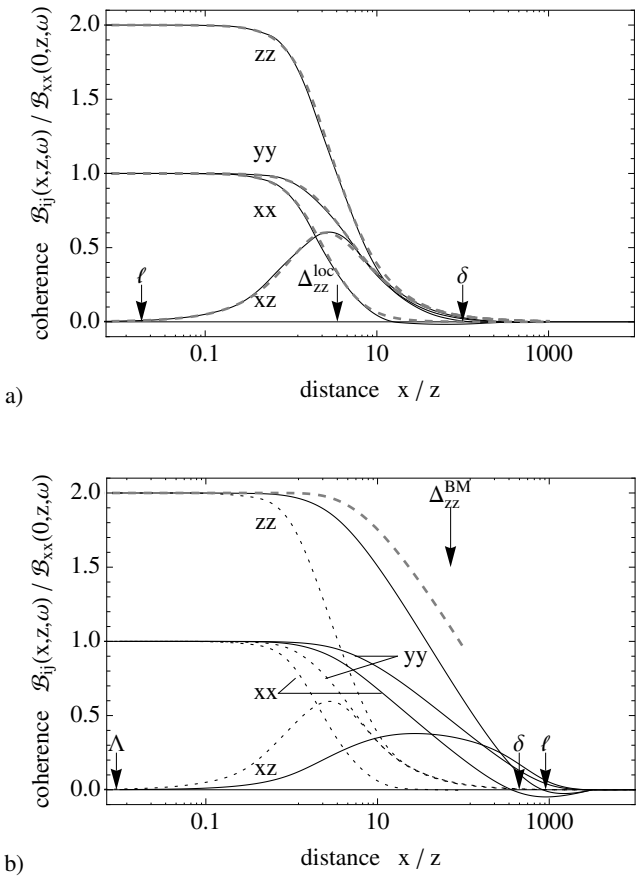

Figure 3.6: Components of the coherence tensor of the magnetic field near a gold surface. Solid (dotted) lines: Boltzmann-Mermin model with specular boundary condition (Drude model).
a) Distance $z = 1\,\mu$m much larger than mean free path $\ell = 18$ nm: all curves coincide with the local approximation (3.28) (dashed gray curves).
b) Nonlocality becomes important at short distances. For better visibility we set $\ell = 10\,\mu\text{m} \gg z = 10\,\text{nm}$ by lowering the scattering rate γ. The thick dashed line gives the rather coarse approximation from Eq. (3.34) (dashed gray curve). Frequency $\omega/2\pi = 1$ MHz.

material properties and depend only on the ratio x/z, i.e. the geometry of the system. An equivalent form for the xx-component was already given in Eq. (33) of Henkel et al. [2003], see also [Nenonen et al., 1996]. Note that the xz-cross-correlation was missed in [Lau et al., 2007].

The coherence functions decay on a typical length scale. For example, the zz-component (and similarly for the other ones) is characterized by the correlation length

$$\ell \ll z: \quad \Delta_{zz}^{\text{loc}} = 2\sqrt{3}\,z\,, \tag{3.29}$$

where $\mathcal{B}_{zz}(x,z)$ drops to half of its value at $x = 0$ [see Fig.3.6a)]. The approximate

forms of Eq. (3.28) are not valid far beyond the correlation length, where some correlation functions become negative as shown in Fig. 3.6a). The agreement with the asymptotes is so high, however, that the curves are hardly distinguishable. The peak in the crossed xz-correlation arises from light paths that are reflected from the surface at oblique angles and whose fields are polarized in the xz-plane ($\boldsymbol{B}_\mathrm{s}$ component in Fig. 3.1).

3.3.2 Nonlocal metal

In the near field $z \ll \ell$, nonlocality leads to a larger coherence length than predicted by the local scenario, as is clearly visible in Fig. 3.6b). In this section we extract the relevant scales by evaluating the two-point Green's tensor $\mathcal{H}_{zz}(x,z)$. It is necessary to interpolate the reflection coefficient $r_\mathrm{s}(p)$ between the local and the nonlocal limits to avoid an unphysical logarithmic divergence at the lower bound. The simplest choice is the Padé approximation

$$\operatorname{Im} r_\mathrm{s}(p) \approx \frac{\operatorname{Im} r_\mathrm{s}^\mathrm{loc}(p)}{1+p\ell/2} \approx \frac{1}{2\delta^2 p^2(1+p\ell/2)} , \tag{3.30}$$

where the last form is appropriate for $p \gg 1/\delta$ and the small-p divergence is removed by the factor p^2 under the integral [see, e.g., Eq. (3.15)]. The integrals then give

$$\mathcal{H}_{zz}(0,z) \approx \frac{\mu_0}{4\pi\delta^2\ell}\,\mathrm{E}_1(4z/\ell)\mathrm{e}^{4z/\ell} , \tag{3.31}$$

$$\mathcal{H}_{zz}(x,z) \approx \frac{\mu_0}{8\pi\delta^2}\int_0^\infty dp\,\frac{\exp(-2pz)J_0(px)}{1+p\ell/2} , \tag{3.32}$$

where E_1 is the exponential integral defined after Eq. (3.17). We split the integral at $p = x_0/x$, where $x_0 \approx 2.405$ is the first zero of the Bessel function $J_0(x)$. For $0 < p < x_0/x$, $J_0(px)$ is replaced by a spline $j(x) = 1 + bx^2 + ax^3$, while it is replaced by its asymptote $j(x) \approx \sqrt{2/\pi x}\cos(\pi/4 - x)$ for larger arguments. It turns out that the first interval gives the dominant contribution, since the oscillations beyond x_0/x provide a cut-off for the integrand. We obtain

$$\begin{aligned}\mathcal{H}_{zz}(x,z) \approx\ & \mathcal{H}_{zz}(0,z) - \frac{\mu_0}{16\pi\delta^2\ell}\Bigg[-4\,\mathrm{E}_1(2x_0z/x) \\ & + \frac{bx^2}{z^2}\left(1-(1+2x_0z/x)\,\mathrm{e}^{-2x_0z/x}\right) \\ & + \frac{ax^3}{z^3}\left(1-(1+2x_0z/x+2(x_0z/x)^2)\,\mathrm{e}^{-2x_0z/x}\right) + \mathcal{O}\left(\frac{x}{\ell},\frac{z}{\ell}\right)\Bigg] .\end{aligned} \tag{3.33}$$

A careful glance at this expression shows that in the regime $z \ll x \ll \ell$ the first line dominates. The decay of the lateral coherence is therefore logarithmic (see Fig. 3.6), as the small-argument approximation to the exponential integral illustrates [thick dashed

line in Fig.3.6b)]

$$\frac{\mathcal{B}_{zz}^{\mathrm{BM}}(x,z)}{\mathcal{B}_{xx}^{\mathrm{BM}}(0,z)} \approx 2 - \frac{2\,\mathrm{E}_1(2x_0z/x)}{\mathrm{E}_1(4z/\ell)} \approx 2 - \frac{\ln\left[(2x_0z/x)^2\right]}{\ln\left[4z/\ell\right]} \,. \tag{3.34}$$

This yields a coherence length

$$z \ll \ell: \quad \Delta_{zz}^{\mathrm{BM}} = x_0\sqrt{z\ell} \gg z \,, \tag{3.35}$$

much larger than its local counterpart of Eq. (3.29). The spatial correlations of magnetic near fields are therefore linked to the characteristic mean free path of ballistic transport. We recall that a similar discussion by Henkel and Joulain [2006] for electric correlations did not find Eq. (3.35) involving the mean free path ℓ, but rather the Thomas-Fermi screening length Λ, which is typically smaller. This may be attributed to the different frequency bands considered. The impact of spatial dispersion is therefore somewhat easier to reveal by analyzing magnetic fields.

3.4 Electric Field Noise, Patch Potentials, and Trapped Rydberg Qubits

We have so far investigated magnetic noise, which is the main source of atomic losses from magnetic traps implemented on atom chips. In this section, the discussion is complemented by estimations of the electric noise. The electric sector of the spectrum influences the behavior of trapped atoms and ions and may become relevant if stored atoms are used as qubits in quantum computation. We will consider the important case of a rubidium atom, whose hyperfine ground-state levels $|0\rangle = |5s_{1/2}, F = 2, M_F = 2\rangle$ and $|1\rangle = |5s_{1/2}, F = 1, M_F = -1\rangle$ provide a qubit robust with respect to noise, as has been discussed by Folman et al. [2002]; Fortágh and Zimmermann [2007]; Reichel and Vuletic [2011] and demonstrated experimentally [Treutlein et al., 2004]. The two states interact weakly, but strong interatomic interactions can be achieved by exciting the atoms to a so-called Rydberg state $|r\rangle = |58d_{3/2}, F = 3, M_F = 3\rangle$ [Gallagher, 1988]. The far-field coupling between two such Rydberg atoms A and B with dipole moment $\boldsymbol{d}^R$, placed in $\boldsymbol{r}_A, \boldsymbol{r}_B$, respectively, is then ruled by an effective dipole-interaction Hamiltonian

$$H_{\mathrm{Ryd}} = |r_A\ r_B\rangle\langle r_A\ r_B| \frac{|d^R|^2}{4\pi\varepsilon_0|\boldsymbol{r}_A - \boldsymbol{r}_B|^3} \,. \tag{3.36}$$

This offers the possibility to implement a phase gate: the two atoms are illuminated by laser pulses that selectively excite trapped atoms from the qubit state $|0\rangle$ to the Rydberg state and back, via a two-photon process involving an intermediate level $|i\rangle = |5p_{1/2}, F = 2, M_F = 2\rangle$, but not from $|1\rangle$. In this scheme, two atoms prepared in an initial state $|0_A\ 0_B\rangle$, will be transiently excited to the Rydberg state and gain a two-atom

phase $\phi = H_{\mathrm{Ryd}}\tau/\hbar$ from their dipole interaction, while other initial states remain uninfluenced. Importantly, the strong coupling allows for short interaction times in the order of $10\,\mathrm{ns}$, so that fast phase gates can be achieved. Besides, shaping the laser pulses helps to gain *optimal control* over the intermediate state occupation and motional degrees of freedom [Müller et al., 2011].

In this thesis, we do not go into the details of the technology and physics of quantum computation[2]. Rather, the focus is put on the specific sensitivity of the Rydberg state $|r\rangle$ to static and fluctuating fields typical for an atom-chip environment. Since Rydberg levels are populated only for a short time (some $10\,\mathrm{ns}$) and their angular momenta are relatively small ($J \leq 5/2$), we do not have to consider magnetic field noise that takes effect only on a time scale of $100\,\mathrm{ms}$ or longer [Reichel and Vuletic, 2011] and can concentrate on a number of relevant sources of electric field noise.

3.4.1 Surface impurities: DC Stark shifts

Previous work has shown that the surfaces of atom chips get contaminated with adsorbed atoms that lead to randomly placed charges or dipoles [McGuirk et al., 2004]. As a typical scenario, consider an alkali atom on a metal that gives off its electron into the surface so that an upright dipole moment remains. At a distance $z \approx 10\,\mu\mathrm{m}$ above it, this single impurity creates a tiny electric field of the order of

$$E_{\mathrm{imp}}(z) \sim \frac{2ea_B}{4\pi\varepsilon_0 z^3} = 0.15\,\frac{\mathrm{mV}}{\mathrm{m}}\,, \tag{3.37}$$

where a_B is the Bohr radius. But if 10^4 adatoms are distributed over an area of $(10\,\mu\mathrm{m})^2$, (corresponding to an average distance $\sim 100\,\mathrm{nm}$, i.e., much less than a monolayer), their electric fields roughly add up to $\mathcal{O}(1\,\mathrm{V/m})$. The corresponding Stark-Hamiltonian,

$$H_{\mathrm{S}} = -\hat{\boldsymbol{\mu}} \cdot \mathbf{E}_{\mathrm{imp}}(z)\,, \tag{3.38}$$

has matrix elements of the order $ea_B n^2 E_{\mathrm{imp}}(z) \approx 6.6\,\mathrm{MHz}$ for $n = 58$, just one order of magnitude below the Rydberg interaction Hamiltonian (3.36) for atomic separations in the micron range. The experiments of McGuirk et al. [2004] have actually revealed electric fields up to $1\,\mathrm{kV/m}$ at a distance of about $10\,\mu\mathrm{m}$. On an insulating surface, charges can be trapped and the fields would even be stronger. Note that the threshold for field ionization is of the order of $5\,\mathrm{kV/m}$ for the $n = 58$ level [Gallagher, 1988]. The Rydberg level considered here, $|r\rangle = |n\mathrm{d}_{3/2}\rangle$ ($n = 58$), is actually 'protected' from a linear Stark shift because its quantum defect ($\delta_{\mathrm{d}} \approx 1.34$) lifts the degeneracy with the opposite parity states $|n\mathrm{p}, \mathrm{f}, \ldots\rangle$, by an energy splitting of the order of $\Delta_n = 1/n^3\,\mathrm{a.u.} \approx 1.125\,\mathrm{cm}^{-1} = 33.7\,\mathrm{GHz}$ [see Fig. 3.7 (left)]. For this reason, the Stark

[2] For recent reviews of quantum information processing on atom chips, see [Negretti et al., 2011] and [Treutlein et al., 2011]. A comprehensive introduction to the theory of quantum information and quantum computing is given, e.g., in the book by Nielsen and Chuang [2011].

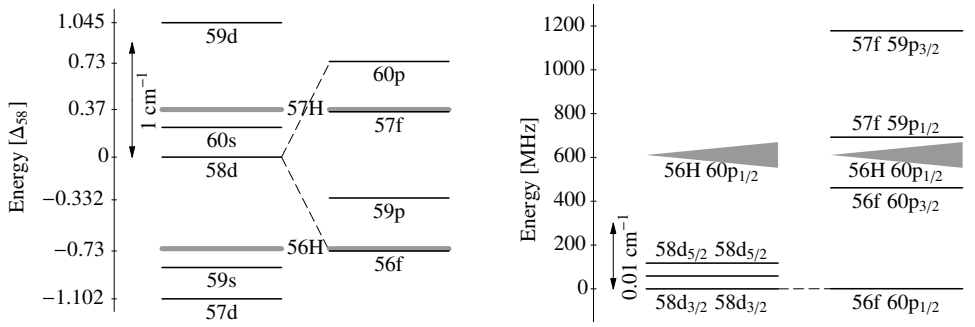

Figure 3.7: (left) Energy levels near the Rydberg state $|r\rangle = |58\mathrm{d}_{3/2}\rangle$. The strong Rydberg interaction arises from the near degeneracy of $|r\ r\rangle$ with the two-atom level $56\mathrm{f}_{5/2}\,60\mathrm{p}_{1/2}$ ("Förster resonance" [Walker and Saffman, 2005], dashed lines). The fine structure is not resolved on the scale $\Delta_{58} = 1/58^3$ a.u. $= 33.7\,\mathrm{GHz}$. The thick gray lines (label nH) give the hydrogen-like state manifold beyond the nf states (angular momenta $l > 3$). The left and right columns show even and odd orbital angular momentum states.
(right) Energy levels of the two-atom system. The levels in the Förster resonance are connected by the dashed line (detuning $\approx 7\,\mathrm{MHz}$ [Gaëtan et al., 2009]). At a distance $|\boldsymbol{r}_A - \boldsymbol{r}_B| \approx 4\,\mu\mathrm{m}$, the two levels hybridize and split by $\approx\ 50\,\mathrm{MHz}$, as described by the two-atom Hamiltonian (3.36). Note the difference in scale: the fine structure of the p and d levels is resolved (but not for the f levels). A quantum defect of order 10^{-2} splits off the level $56\mathrm{f}$ from the hydrogen-like manifold $56\mathrm{H} = 56\mathrm{g}, \mathrm{h}, \ldots$. The gray triangles illustrate the linear Stark splitting of $56\mathrm{H}$ in a weak static electric field between 0 and $1\mathrm{V/m}$ (shifts up to $\pm 60\,\mathrm{MHz}$). At slightly higher fields, also the levels $57\mathrm{f}\,59\mathrm{p}_{1/2}$ and $56\mathrm{f}\,60\mathrm{p}_{3/2}$ would be pushed away (avoided crossings). The quadratic Stark shift of the other levels is not visible on this scale.
The energy levels are calculated from quantum-defect data collected in [Lorenzen and Niemax, 1983; Li et al., 2003]. A precise localization of the Förster resonance (not attempted here) would require knowledge of the quantum defects at the 10^{-4} level. (Figure reproduced from [Müller et al., 2011].)

shift is quadratic in the field and inversely proportional to the detuning ($< \Delta_n$) from the nearest level with opposite parity. The nearest levels $57\mathrm{f}$ and $59\mathrm{p}$ give quadratic Stark shifts that partially cancel each other, leaving a polarizability for $58\mathrm{d}$ of the order of $50\,\mathrm{kHz(V/m)}^{-2}$. The $56\mathrm{f}$ state shows a much larger polarizability because the hydrogen manifold $56\mathrm{H} = 56\mathrm{g}, \mathrm{h}, \ldots$ is only about $0.02\,\mathrm{cm}^{-1}$ ($\approx 600\,\mathrm{MHz}$) away [Fig. 3.7 (right)] and its influence is not cancelled by another level. We estimate a quadratic Stark effect of the order of $2 \ldots 3\,\mathrm{MHz(V/m)}^{-2}$.

The two-atom states $|58\mathrm{d}_{3/2}\,58\mathrm{d}_{3/2}\rangle$ and $|56\mathrm{f}_{5/2}\,60\mathrm{p}_{1/2}\rangle$ whose energy mismatch is only $7\,\mathrm{MHz} \approx 2.3 \times 10^{-4}\,\mathrm{cm}^{-1}$ (see Fig. 3.7 (right) and [Walker and Saffman, 2005; Gaëtan et al., 2009]) are known to give rise to a Förster resonance. At fields above $1\,\mathrm{V/m}$, the Stark shift starts to detune the resonance. One then loses the strong $1/r^3$ scaling of the Rydberg interaction that turns into the weaker $1/r^6$ van der Waals scaling. In addition, at the level of $10\,\mathrm{V/m}$, the linear DC Stark shift of the hydrogen-like state manifold $|56\mathrm{H}\rangle$ exceeds $\approx 600\,\mathrm{MHz}$. By an avoided crossing, the state $|56\mathrm{f}_{5/2}\rangle$ is then pushed down, and the Förster resonance is detuned.

3.4.2 Fluctuating fields: dephasing

The one- and two-atom Rydberg states that we are considering do not feature a permanent electric dipole moment. This is because the quantum defects split them off the hydrogen-like manifolds of higher angular momentum states ($L > 3$). In weak fields, their Stark effect is therefore quadratic. We consider here the beating between a fluctuating field and a static impurity field $E_{\rm imp}(z)$ at the level of $1\,{\rm V/m}$, small enough not to perturb the dipole-dipole interactions, see previous section. The mixing of states with opposite parity is linear in the impurity field and translates into a dipole moment of the order of $d_R = \alpha_R E_{\rm imp}(z)$ where α_R is the quasistatic (scalar) polarizability. For the level $58{\rm d}_{3/2}$, the contributions to nearby levels above and below partially cancel, leading to the relatively small value $|d_R| \sim 4\,ea_B$. The level $56{\rm f}_{5/2}$ is much more polarizable, as found above, and $d_R \sim 200\,ea_B$. Note that this is still much smaller than expected from the average size of a Rydberg atom ($\approx a_B n^2$). The fluctuating phase shift due to the Rydberg polarizability α_R is then given by

$$\Delta\phi(\tau) = -\int_{t_1}^{t_2} {\rm d}t\, \frac{\alpha_R}{\hbar} \mathbf{E}_{\rm imp}(z)\cdot\mathbf{E}_{\rm fluct}(z,t)\,, \tag{3.39}$$

where the time integral is evaluated over that part of the pulse that the atom effectively spends in the Rydberg level.

Let us assume an electric field noise spectrum, defined in analogy to the magnetic one of Eq. (3.3), with a scaling

$$S^E_{ij}(z,\omega) = \frac{S^E_{ij}(z_0,\omega_0)}{(z/z_0)^4}\left(\frac{\omega_0}{\omega}\right)^\beta\,, \tag{3.40}$$

that arises from *patch-charge* fluctuations, as observed in experiments with miniaturized ion traps [Turchette et al., 2000; Labaziewicz et al., 2008; Dubessy et al., 2009] (exponent $\beta \approx 0.7\ldots1$). Different descriptions of patch spectra have recently been discussed by [Behunin et al., 2012]. The $1/z^4$ scaling actually only holds at heights z beyond a characteristic length scale for the patch size. This effect is taken into account in the plots shown, using the model of Dubessy et al. [2009]. The thermal electric fields that originate from the motion of charges in the chip material (Johnson-Nyquist noise) have a lower noise spectrum compared to the patch-charge model of Eq. (3.40) [Henkel et al., 1999; Turchette et al., 2000; Leibrandt et al., 2007], at least in the low-frequency range (up to a few MHz) relevant for dephasing. This is illustrated in Fig. 3.8, where the two noise spectra (at fixed distance $z = 10\,\mu{\rm m}$) are plotted vs. frequency.

The dephasing of the Rydberg state is now estimated by calculating the variance of the phase shift (3.39). Provided the interaction time $\tau = t_2 - t_1$ is large compared to the noise correlation time, the variance increases like

$$\overline{\Delta\phi^2(\tau)} \approx \tau \frac{d^R_i d^R_j S^E_{ij}(z_0,1/\tau)}{2\hbar^2(z/z_0)^4}\frac{1}{\cos(\pi\beta/2)\Gamma(2+\beta)}\,, \tag{3.41}$$

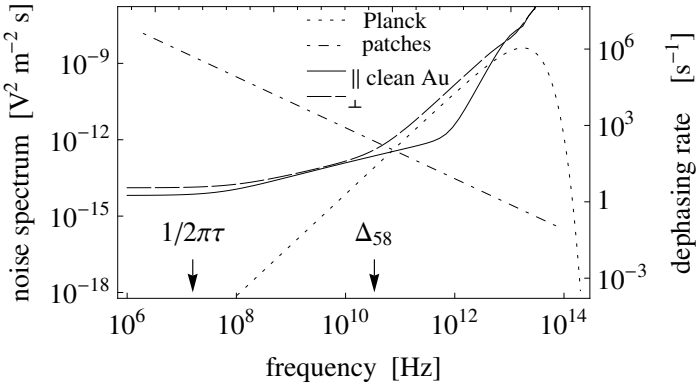

Figure 3.8: Electric field noise spectrum (in $(\mathrm{V/m})^2/\mathrm{Hz}$) due to patch-charge fluctuations (dot-dashed) and due to Johnson-Nyquist noise from a gold half-space (solid and dashed lines). Distance fixed to $z = 10\,\mu\mathrm{m}$, temperature 300 K. Patch fluctuations are calculated from [Dubessy et al., 2009] and extrapolate ion trap data (in the MHz range), assuming a $1/\omega$ scaling. The Johnson-Nyquist noise is calculated along the lines of [Henkel et al., 1999]. It includes blackbody radiation and free-space vacuum fluctuations and changes from a $\omega^{1/2}$ into a ω^2 power law near the typical Rydberg transition energy Δ_{58} (arrow). Solid (dashed) lines are for fields parallel (perpendicular) to the surface, respectively. The right scale gives the expected dephasing rate for a static dipole moment $\mathcal{O}(200\,ea_B)$ and a white spectrum. The arrow at $1/2\pi\tau$ marks the Fourier-limited band width for quasistatic noise over an effective interaction time $\tau = 10\,\mathrm{ns}$. The contribution of quantum fluctuations was subtracted in the Planck spectrum (dotted curve).

where the noise spectrum is evaluated at $\omega = 1/\tau$, roughly the Fourier-limited band width of the pulse, and $\Gamma(\cdot)$ is Euler's gamma function. For room-temperature microscopic ion traps [Deslauriers et al., 2006; Epstein et al., 2007; Labaziewicz et al., 2008; Dubessy et al., 2009], noise levels of $|S^E(75\,\mu\mathrm{m}, 1\,\mathrm{MHz})| \sim 10^{-11}\,(\mathrm{V/m})^2/\mathrm{Hz}$ and $\beta \approx 0.7 \ldots 0.8$ are typical. Note that a low-frequency cut-off must be applied for pure $1/f$ noise. Taking an effective time of $\tau \approx 20\,\mathrm{ns}$ spent in the Rydberg level, one gets at $z = 10\,\mu\mathrm{m}$ a dephasing rate of

$$D_\phi(56\mathrm{f}) = \overline{\Delta\phi^2(t)}/\tau = \mathcal{O}(10^6\,\mathrm{s}^{-1}) \tag{3.42}$$

for the highly polarizable Rydberg state. This affects in particular the two-Rydberg state via its admixture of $56\mathrm{f}\,60\mathrm{p}$ (Fig. 3.7). For the phase gate, we get a sizable decoherence error $\epsilon \approx 1 - \langle \mathrm{e}^{\mathrm{i}\Delta\phi(\tau)}\rangle \approx \frac{1}{2} D_\phi \tau \sim 1\%$ from the uncertainty in the two-atom phase ϕ. We recall that this number scales quadratically with the impurity field, assumed here to be $1\,\mathrm{V/m}$. The other Rydberg levels involved show a much smaller dephasing, in particular $D_\phi(58\mathrm{d}) = \mathcal{O}(400\,\mathrm{s}^{-1})$. This is insignificant over the effective pulse duration τ.

As for the magnetic field in Sec. 3.3, one may ask how far the fields seen by the two atoms are correlated. A differential phase would mix the even and odd states $|56\mathrm{f}_{5/2}\,60\mathrm{p}_{1/2}\rangle \pm |60\mathrm{p}_{1/2}\,56\mathrm{f}_{5/2}\rangle$ that are involved in the Förster resonance. This can be quantified from the cross-correlation spectrum of the patch fields $\boldsymbol{\mathcal{E}}(\boldsymbol{r}_A, \boldsymbol{r}_B; \omega)$, which is

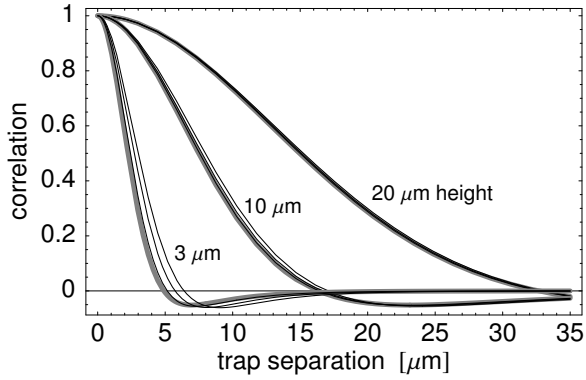

Figure 3.9: Normalized cross-correlation of electric field noise due to patch-charge fluctuations, evaluated at three different positions and normalized to the noise spectrum in one trap. If the correlation is weak, the relative phase of the Rydberg state in the two traps is randomized on the same time scale as the common phase. The correlations are calculated by generalizing the model of Dubessy et al. [2009]. Any group of three curves corresponds to patch correlation lengths 0.5, 1, and $1.5\,\mu$m. (Figure reproduced from [Müller et al., 2011].)

the electric counterpart of the two-point correlation function $\boldsymbol{\mathcal{B}}$ of Eq. (3.26), with $\boldsymbol{r}_A$ and $\boldsymbol{r}_B$ are the positions of the two traps. In Fig. 3.9, we plot the normalized cross-correlation for two atoms at the same distance z from the chip, but laterally separated by a length x (cf. Fig. 3.1). The two atoms are subject to the same noise (no differential dephasing) if the normalized correlation is unity. One notes that the fields decorrelate on a scale given by the height above the surface. The correlation is still quite strong for the parameters we considered here, i.e. a separation $x = 4\,\mu\mathrm{m}$ and height $10\,\mu\mathrm{m}$. Note, however, that a phase gate may be affected even by such long-ranged fluctuations.

3.4.3 Thermal radiation: lifetime and AC Stark shift

The radiative lifetime of an emitter is strongly modified in the vicinity of a macroscopic body, as discussed in the first part of this chapter. In addition, thermal radiation plays a significant role because the Bohr frequencies of Rydberg atoms are low, typically $\Delta_n \ll k_B T$. It is well known that this reduces the lifetime and coherence time of trapped particles, even to the level that magnetic dipole transitions become relevant [Reichel and Vuletic, 2011]. We estimate here surface-enhanced radiative loss and discuss that despite the large polarizabilities, thermal radiation gives rise to AC Stark shifts that are overall small, leaving only the zero-temperature van der Waals shift. A similar question has been addressed by Crosse et al. [2010]; Ellingsen et al. [2010].

Spontaneous emission in free space is dominated by the decay into the lowest states because of the cubic frequency dependence of the vacuum field spectrum. This leads to a lifetime of the Rydberg state of $210\,\mu$s at $T = 0$ [Theodosiou, 1984] and a decay probability, i.e., gate error, of the order of 10^{-4} given the Rydberg excitation time $\tau \approx 20\,\mathrm{ns}$.

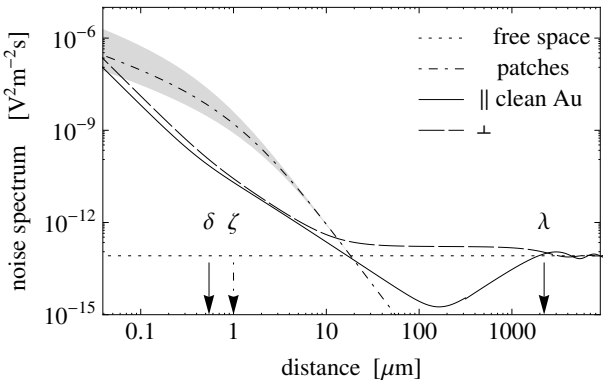

Figure 3.10: Electric field noise spectra (in $(\mathrm{V/m})^2/\mathrm{Hz}$) vs distance from the chip surface, evaluated at the level splitting Δ_{58} typical for Rydberg transitions, and 300 K. The patch-charge spectrum is extrapolated to this frequency assuming a $1/\omega$ scaling; the patch correlation length is in the range $\zeta = 1 \pm 0.5\,\mu\mathrm{m}$ (shaded area). The solid and dashed curves "clean Au" give the noise spectrum of thermal near-field radiation, the far-field limit is shown by the dotted line. The skin depth δ separates two power laws [Henkel et al., 1999], and for $z \gtrsim \lambda/2$, the spectrum oscillates due to interference by reflection from the surface. In this limit, a perfect conductor approach yields good agreement. Within the wide plateau betwen $10\,\mu\mathrm{m}$ and $1\,\mathrm{mm}$, a dipole perpendicular to the surface ($\perp$) is subject to near-field noise about five times as strong as the free space (Planck) level.

We therefore need to check that this error does not increase significantly in an atom-chip environment. The contribution of blackbody radiation reduces the lifetime considerably (absorption and emission), to a total figure of roughly $90\,\mu\mathrm{s}$ for the Rydberg level $58d$ where the effective quantum number is $n^* \approx 58 - 1.34$ [Theodosiou, 1984].

The chip surface enhances the mode density of the electromagnetic field [Wylie and Sipe, 1984; Failache et al., 2002; Crosse et al., 2010]. This leads to different scenarios, however, for transitions with large or small Bohr frequencies. For the decay into low states, the resonant wavelengths are typically in the visible and near UV, small compared to the atom-surface distance. These field modes form a shallow interference pattern due to reflection at the surface, enhancing or suppressing the decay by roughly a factor of 2. Destructive interference can be used to suppress certain decay channels, as suggested by Hyafil et al. [2004] in an application of the Purcell effect [Purcell, 1946].

At smaller Bohr frequencies, thermally stimulated emission and absorption are enhanced much more strongly in the near field [Wylie and Sipe, 1984; Crosse et al., 2010]. Eq. (2.21) gives the spontanous transition rate for an electric dipole transition $a \to b$

$$\Gamma_{a\to b} = \frac{2}{\hbar}[1 + \bar{n}(\omega_{ab})] d_k^{ab} d_l^{ba}\ \mathrm{Im}\left[\mathcal{G}_{kl}(z;\omega_{ab})\right] ,$$

analogous to the magnetic case of Eq. (3.4). In thermal equilibrium, this rate coincides also with the absorption rate of thermal photons ($\omega_{ab} = -\omega_{ba} < 0$), cf. Sec. 2.1.5. Summing over the final states $|b\rangle$ gives the total decay rate $\Gamma_a = \sum_b \Gamma_{a\to b}$. Fig. 3.8 can

be taken as an illustration of the terms in this sum due to the proportionality between the spectrum and the loss rate. The dependence on distance is shown in Fig. 3.10 for a Green's tensor calculated for a gold surface, cf. App. B.2. Compared to free space (Planck spectrum, dashed line), transitions among Rydberg levels are significantly enhanced at short distances, while the rates oscillate in the opposite limit (distance comparable to the transition wavelength) due to the interference pattern mentioned above. Note the quite strong destructive interference for a transition dipole parallel to the surface (solid curve) which can be understood from the image dipole at a perfectly conducting surface.

The transition rates scale with the electric dipole matrix elements of the Rydberg levels. We note that for a Bohr frequency $\hbar|\omega_{ab}| \gg \Delta_n$, the matrix elements are much smaller because a kind of radial selection rule suppresses changes in the principal quantum number by more than a few units, see also [Gallagher, 1988; Crosse et al., 2010]. For a typical final state among adjacent Rydberg levels, for example $\Delta n^* \lesssim 2$, we find an enhancement of the transition rate by a factor $\mathcal{O}(5)$ at $z = 10\,\mu\mathrm{m}$ compared to free space. The corresponding lifetime is reduced from $\sim 150\,\mu\mathrm{s}$ (free space) to $\sim 30\,\mu\mathrm{s}$, estimating the matrix element by $ea_B n^{*2}$. We note that the rate for this generic pair of levels essentially exhausts the thermal decay rate summed over all final states, including photoionization [Theodosiou, 1984]. We therefore expect a total lifetime somewhat below the $\sim 30\,\mu\mathrm{s}$ figure estimated above from a single bound-bound transition. While this is still three orders of magnitude longer than the Rydberg excitation pulse, it may pose a serious challenge to gate errors below the fault tolerance threshold of 10^{-4} assumed by Müller et al. [2011]. As a preliminary check, we have performed a calculation of the phase gate error when a finite lifetime $20\,\mu\mathrm{s}$ of the Rydberg level is included: an increase of the order of 10^{-3} is indeed found.

The radiation field also induces a van der Waals-Casimir-Polder shift on the Rydberg levels. We can estimate this in the London limit (transition wavelength large compared to the atom-surface distance) since the Rydberg spacing Δ_{58} corresponds to wavelengths in the centimeter range,

$$U_{\mathrm{vdW}}(z) = -\frac{\langle r|d_x^2 + d_y^2 + 2d_z^2|r\rangle}{8\pi\varepsilon_0(2z)^3}\,. \tag{3.43}$$

The expectation value of the squared dipole is of the order of $\frac{5}{2}(ea_B n^{*2})^2$ (e.g. [Courtois et al., 1996]) and gives a shift $\approx 1.6\,\mathrm{MHz}$ at $10\,\mu\mathrm{m}$, consistent with the findings of Crosse et al. [2010] where the electric quadrupole contribution is analyzed as well. This is not far from the dipole-dipole interaction (as it must from the scaling), but still small enough not to perturb it. The level shift changes only weakly across the levels shown in Fig. 3.7 and does not induce significant detunings. Its main impact is therefore to pull the Rydberg atoms towards the chip during the pulse. This effect which excites motional states in the trap, could be compensated for in the optimal-control approach by the exciting laser pulse in a similar way as the momentum exchange between the two Rydberg atoms, discussed in [Müller et al., 2011].

We finally turn to the question how thermal radiation is shifting the Rydberg levels. This could be significant since even room-temperature blackbody radiation produces a sizable electric field above $100\,\mathrm{V/m}$, albeit over a wide frequency range. It has been pointed out that the Casimir-Polder potential, discussed in Chapter 4, is essentially temperature-independent, due to cancellations between different transitions on the one hand, and between virtual and real photon exchange on the other [Ellingsen et al., 2010]. This holds, provided the typical transition wavelengths are large compared to the atom-surface distance, which is indeed the case for a Rydberg atom. We have checked that this result can be understood in a simple way starting from the dynamical polarizability of a free electron and integrating over the thermal radiation spectrum. For an analysis at zero temperature, see [Eberlein and Robaschik, 2004] and references therein. The Planck spectrum gives a free-space level shift, common to all weakly bound Rydberg levels, of the order of $\alpha_{\mathrm{fs}}(k_B T)^2/(m_e c^2) = \mathcal{O}(2\,\mathrm{kHz})$, where α_{fs} is the fine structure constant and $m_e c^2$ the electron's rest energy. This is consistent with the value given by Gallagher [1988]. Near the chip surface, the shift is modified by a factor $4\pi\Lambda_T/z$, where $\Lambda_T = \hbar c/4\pi k_B T \approx 0.6\,\mu\mathrm{m}$ is Wien's thermal wavelength (at room temperature). The result is still negligible on the energy scale set by the Rydberg dipole-dipole interaction, and we provide a detailed discussion elsewhere.

3.5 Summary and Discussion

In this chapter, we have considered the electromagnetic near fields of conductors. We found that the scattering mean free path of charge carriers sets the distance scale for the onset of nonlocal effects in the magnetic near-field noise. For evanescent modes that dominate the near field, the fraction of the metallic volume that contributes to noise is limited by more efficient screening as compared to the normal skin effect. The present calculation indicates, therefore, that loss rates at short distances are actually lower than predicted by local conductivity models (Ohm's law). This noise reduction sets in at atom-surface separations comparable to or below the mean free path. In a clean (crystalline) metal ℓ may take values in the order of $1\,\mu\mathrm{m}$, which is at the limits of the experimentally accessible region (cf. the gray box in Fig. 3.2): typical traps operate at distances of $1\ldots100\,\mu\mathrm{m}$ from the surface and can resolve lifetimes up to $10^{-2}\ldots1\,\mathrm{s}$. The data shown in Fig. 3.2 are calculated at room temperature. Since both the conductivity and the mean free path depend on temperature, it is worth investigating whether the lifetimes of magnetic levels may be tuned by cooling the atom-chip device. This strategy is hitting a limit in the extreme near field (distance $z \ll \ell$): the noise power becomes independent of the scattering rate of carriers (the Drude parameter γ), and also the details of the scattering mechanism of charge carriers at the inner surface become irrelevant. The near-field spectrum of Eq. (3.17) has a rather general character and is expected to apply to doped semiconductors and even to superconductors, as our numerical calculations show (Fig. 3.4).

We have also analyzed the asymptotic form of the magnetic noise correlations in the short-distance range and found that magnetic fields are laterally coherent on a scale $\sim \sqrt{(\ell + z)z}$. This implies for an atom-chip environment that fluctuating forces due to magnetic field gradients are smaller (their spectral density scales roughly with the inverse square of the correlation length). Also when matter-wave interferometry involves the spatial splitting of a thermal cloud or condensate, the increase in spatial coherence makes the device more robust against decoherence from magnetic noise [Cheng and Raymer, 1999; Henkel et al., 2003; Fermani et al., 2006]. The increase in spatial coherence intimately relates to the reduction of heat transfer via fluctuating near fields because the effective number of channels for heat transport is inversely proportional to the 'coherence area'. For a more detailed discussion of this link, see [Biehs et al., 2010; Ben-Abdallah and Joulain, 2010].

All of these results imply that nonlocality may be visible at the edge of what is feasible with atom chips. Still, operating a chip trap at short distances is fundamentally limited by the Casimir-Polder interaction that deforms and breaks the trapping potentials. Alternative setups might, therefore, address the broadening of magnetic transitions spectroscopically, e.g. using evanescent-wave based surface traps as in [Bender et al., 2010; Stehle et al., 2011] or optical tweezers. One may also think of muonic or nuclear magnetic moments, as used in the experiment of Suter et al. [2004] on spatial dispersion in superconductors.

Patch potentials due to adsorbates on the surface are known to add significantly to the electric field noise, relevant for ion traps [Turchette et al., 2000; Dubessy et al., 2009] and systems involving precisely tuned electric dipole transitions, such as Rydberg states [Tauschinsky et al., 2010; Carter and Martin, 2011; Müller et al., 2011]. Yet they will not affect the magnetic case. Static patches have no impact on the magnetic noise spectrum and magnetic surface dipoles due to adsorbed atoms have only a minor effect: A static charge trapped at a distance of $1\,\mu\mathrm{m}$ from an atomic-scale electric dipole results in an interaction energy in the order of $20\,\mathrm{MHz}$, while the interaction between two such dipoles gives only $1\,\mathrm{kHz}$, and the magnetic counterpart for two magnetic dipoles of one Bohr magneton μ_B at the same distance gives $1\,\mathrm{mHz}$. More prominent sources of magnetic noise might involve diffusive currents confined to a surface layer. Their effect may still be negligible, however, as the analysis of Henkel and Horovitz [2008] has found.

To decide whether a Rydberg phase gate [Müller et al., 2011] can be implemented on an atom chip to yield a universal quantum computer in a scalable setting, all relevant noise sources specific to the chip environment need to be considered. To summarize the estimates on sensitivity to noise due to the chip environment, we have found serious issues for Rydberg atoms held at a distance of the order of $10\,\mu\mathrm{m}$, due to linear and quadratic Stark shifts. The reason is the contamination by impurity atoms of the chip surface at densities higher than $100\,\mu\mathrm{m}^{-2}$, still much less than a monolayer. This would create, above a metallic surface, electric fields exceeding $\mathcal{O}(1\,\mathrm{V/m})$, and reduce significantly the strong dipole-dipole interaction between the Rydberg atoms. This slows down the quantum gate, and a sizable dephasing rate arises from the beating between stray fields

and fluctuating patch potentials, in particular for the highly polarizable $56\mathrm{f}$ state. Operating the chip at lower temperatures would reduce the patch-charge noise [Deslauriers et al., 2006; Labaziewicz et al., 2008]. The radiative decay of the Rydberg state is also enhanced by nearly an order of magnitude compared to free space at zero temperature: we estimate a lifetime in the $20 \ldots 30\,\mu\mathrm{s}$ range. As it stands, this could provide a fundamental lower limit around 10^{-3} to the gate error. Possible improvements may exploit a Purcell effect to suppress, by destructive interference, radiative transitions for certain orientations of the transition dipole, similar to the suggestion of Hyafil et al. [2004]. This may be achieved with suitably polarized laser pulses. We therefore estimate that reaching errors below the fault tolerance threshold for a Rydberg phase gate on an atom chip is challenging but possible.

Chapter 4

Thermal Effects in the Magnetic Casimir-Polder Potential

This chapter is based on the articles *Temperature dependence of the magnetic Casimir-Polder interaction*, Physical Review A **80**, 062905 (2009) by H. Haakh, F. Intravaia, C. Henkel, S. Spagnolo, R. Passante, B. Power, and F. Sols, and *Thermal effects in the magnetic Casimir-Polder interaction* by H. Haakh, F. Intravaia, and Carsten Henkel, in M. Bordag and K. Milton (eds.), *Proceedings of QFExt '09*, pages 194–198 (World Scientific, Singapore, 2010)[1].

Ever since the work of Lennard-Jones [1932] has the interaction between atoms and surfaces been of interest in many fields of physics, chemistry and technology. The seminal work by Casimir and Polder [1948] demonstrated that the shift in atomic energy levels close to a conductor is a probe for the quantum fluctuations of the electromagnetic field[2], a key concept of quantum electrodynamics (QED). In this context, a nonzero temperature becomes relevant for several aspects of the atom-surface interaction: thermally excited motion of the surface (phonons) and inelastic scattering of atomic beams [Zangwill, 1988; Desjonquères and Spanjaard, 1996; Farias and Rieder, 1998], occupation of excited atomic energy levels, and enhancement of field fluctuations due to thermal photons [Barton, 1972]. The latter aspect is usually associated with distances from the surface larger than the thermal wavelength $\Lambda_T = \hbar c/4\pi k_B T$, approximately $0.6\mu\mathrm{m}$ at room temperature. The free energy of interaction typically shows a change in power law with distance around this point: generally, it is enhanced with respect to zero temperature and becomes proportional to T. This is the classical limit where the interaction is mainly entropic in character [Balian and Duplantier, 1977, 1978; Feinberg et al., 2001].

Experimental progress in recent years has achieved the sensitivity required to detect the small energy shifts that occur at distances on the order of Λ_T. One approach makes use of the exquisite control over the motion of atomic beams (beam deflection [Sandogh-

[1] Part of the research leading to Secs. 4.1–4.3 has previously been reported in my diploma thesis *Cavity QED with Superconductors and its application to the Casimir effect*, Universität Potsdam (2009) and in Ch. 4 of the doctoral thesis [Spagnolo, 2009]. Some textual coincidence among the two theses, the present one, and the publications [Haakh et al., 2009, 2010] is acknowledged but not indicated sentence by sentence.

[2] See [Milonni et al., 1988]. Note, however, that it is also possible to take a complete 'matter point of view', considering the field fluctuations a result of fluctuations in charge degrees of freedom [Milonni and Shih, 1992; Jaffe, 2005].

dar et al., 1992; Sukenik et al., 1993], quantum reflection [Shimizu, 2001; Druzhinina and DeKieviet, 2003], see also the reviews [Aspect and Dalibard, 2003; DeKieviet et al., 2011]). Another one is based on clouds of ultracold laser-cooled atoms [Lin et al., 2004; Obrecht et al., 2007], which can be handled precisely at micron distances from a solid surface in atom chips, as discussed in Sec. 1.2. Here, the atom-surface interaction manifests itself typically as a distortion of the trapping potential, leading to loss of atoms through evaporation to the surface [Harber et al., 2003] and to the change in the trap oscillation frequency of Eq. (1.2) [Antezza et al., 2004]. Therefore, the design of magnetic microtraps requires exact knowledge of atom-surface interactions and, conversely, theory predictions can be tested experimentally with high precision [Obrecht et al., 2007].

In this chapter, we address the magnetic dipole contribution to the atom-surface (Casimir-Polder) interaction including nonzero temperature. One might expect this to be a small correction to the electric dipole coupling [McLachlan, 1963; Zaremba and Kohn, 1976; Sols and Flores, 1982; Wylie and Sipe, 1985; Milonni, 1994; Gorza and Ducloy, 2006; Buhmann and Welsch, 2007; Bezerra et al., 2008] because of the smallness of the transition matrix elements [Bimonte et al., 2009; Skagerstam et al., 2009]. Yet, a reconsideration of the magnetic contribution is called for by the strong magnetic mode density close to a metallic surface [Jackson, 1975; Joulain et al., 2003; Henkel et al., 2005] and by experimental evidence for magnetic spin flips, that arise from thermally excited currents in the material of the chip (Johnson noise related to ohmic dissipation) and are mainly responsible for the atomic loss from the trap, as discussed in Chapter 3. In addition, the thermal occupation of photonic modes is quite relevant because magnetic transitions occur at much lower frequencies than electric ones, leading to a stronger temperature dependence. Finally, it is well known that dispersion forces between dielectric and magnetic materials can be repulsive [da Silva et al., 2001], as was shown for the magnetic Casimir-Polder interaction at $T = 0$ by Henkel et al. [2005]. We were thus led to investigate whether at distances beyond Λ_T the total atom-surface interaction might be reduced due to the magnetic contribution.

Most experimental setups involve distances where nonlocal charge transport, investigated in Chapter 3, plays a minor role. Rather, since ohmic losses are crucial for the thermal behavior, it is highly interesting to compare normal metals with superconductors. Thus, the present chapter focusses on different mechanisms of energy dissipation, included in the magnetic Casimir-Polder free energy of interaction through a few well-known models for the electromagnetic response of the surface. Superconductors are described here in the frame of the two-fluid model and Bardeen-Cooper-Schrieffer (BCS) theory [Bardeen et al., 1957; Schrieffer, 1999].

We demonstrate that the magnetic atom-surface coupling has very peculiar features unknown from its electrical equivalent and find that for normal conductors at nonzero temperature, the magnetic dipole contribution to the interaction is reduced, while it is enhanced for superconductors and in certain nonequilibrium situations. This resembles the macroscopic Casimir interaction between two metallic plates. Here, however, the correct calculation of the force at large distances and nonzero temperatures has been the sub-

ject of debate [Boström and Sernelius, 2000; Milton, 2009; Klimchitskaya et al., 2009; Decca et al., 2011] because some experimental results suggest unexpectedly a disagreement with models featuring a finite DC conductivity, cf. [Decca et al., 2005; Sushkov et al., 2011].

This chapter is organized as follows. In Section 4.1, we give a brief review of the formalism used to calculate atom-surface interactions and present the specific forms of the atomic response functions and the experimental setups they describe. Section 4.2 collects expressions for the Green's tensor in different asymptotic regimes of the distance between the atom and the surface. The magnetic Casimir-Polder free energy and entropy of an atom near metallic or superconducting surfaces at global thermal equilibrium is calculated in Section 4.3, with special attention paid to the role of the ohmic dissipation. Nonthermal (out-of-equilibrium) states of the atoms that occur typically in experimental setups are investigated in Section 4.4.

4.1 Atom-Surface Potential

4.1.1 Treatment in molecular quantum electrodynamics

In the formalism of Chapter 2, the magnetic level shift for an atom prepared in a state $|a\rangle$ is related, according to Eq. (2.9), to the real part of the lowest order self-energy correction [Schiefele and Henkel, 2010a,b; Schiefele, 2011] in the magnetic dipole-coupling Hamiltonian. Until now, only a single transition has been considered, but generally there is of course a number of allowed transitions $|a\rangle \to |b\rangle$ with transition dipoles $\boldsymbol{\mu}^{ab}$, which must be summed over. Including thermal states of the electromagnetic field, the real part of the self-energy (2.9) becomes a free energy

$$\mathcal{F}(L,T) = \text{ Re } \left[\quad \right] = \text{ Im } \sum_b \mu_i^{ab}\mu_j^{ba} \int \frac{d\omega}{2\pi} \frac{H^T_{11,ji}(\omega,\boldsymbol{r},\boldsymbol{r})}{\omega-\omega_{ba}+i0^+} \tag{4.1}$$

$$= -\text{ Im } \hbar \int_0^\infty \frac{d\omega}{2\pi} H^T_{11,ji}(\omega,\boldsymbol{r},\boldsymbol{r})\beta^a_{R,ij}(\omega)\,, \tag{4.2}$$

where Einstein summation is intended for spatial tensor indices and we used that $\boldsymbol{H}_{11}$ is even in ω, to introduce the state-specific retarded magnetic polarizability (see Eq. (A.7) and [McLachlan, 1963; Wylie and Sipe, 1985])

$$\beta^a_{R,ij}(\omega) = \sum_b \frac{\mu_i^{ab}\mu_j^{ba}}{\hbar} \frac{2\omega_{ba}}{\omega_{ba}^2-(\omega+i0^+)^2}\,. \tag{4.3}$$

Here, $\mu_i^{ab} = \langle a|\mu_i|b\rangle$ are the dipole matrix elements, ω_{ba} is the frequency of the virtual transition $|a\rangle \to |b\rangle$ ($\omega_{ba} < 0$ for a transition to a state of lower energy). Only retarded response functions are considered in the following so that the subscript $_R$ is dropped. The

photon propagator can be expressed through the retarded magnetic Green's tensor $\boldsymbol{\mathcal{H}}$, including the thermal occupation of field modes [cf. Eq. (2.14) and App. B.2]:

$$\boldsymbol{H}_{11}^{T}(\omega,\boldsymbol{r},\boldsymbol{r}) = \text{ Re } \boldsymbol{\mathcal{H}}(L,\omega) + i \text{ Im } \boldsymbol{\mathcal{H}}(L,\omega)\coth[\hbar\omega/2k_BT] \,. \tag{4.4}$$

As before (Secs. 2.3 and 3.1.1) a divergent free-space contribution (Lamb shift) is removed naturally, if only the reflected part of the magnetic Green's tensor near a boundary is considered [Wylie and Sipe, 1985]. In writing the arguments of the propagator (4.4) we used that from the symmetry of a planar cavity, the result can only depend on the dipole-surface distance L. The explicit expression for $\boldsymbol{\mathcal{H}}$ is well-known and was given earlier in Eq. (3.5), see also App. B.2. Note that the Green's tensor can also depend on temperature implicitly through the surface reflectivity.

By parity, and using contour integration in the upper half-plane, where $\boldsymbol{\mathcal{H}}$ is analytic, the free energy can be expressed as a sum over poles in the form given by Wylie and Sipe [1985]

$$\mathcal{F}(L,T) = -\text{ Im }\frac{\hbar}{2\pi}\sum_b \int d\omega \beta_{ij}^a(\omega)\mathcal{H}_{ji}(L,\omega)\frac{1}{2}[1+\coth(\hbar\omega/2k_BT)] \tag{4.5}$$

$$= -k_BT{\sum_{n=0}^{\infty}}' \beta_{ij}^a(\mathrm{i}\xi_n)\mathcal{H}_{ji}(L,\mathrm{i}\xi_n) + \sum_b \mu_i^{ba}\mu_j^{ab}\bar{n}(\omega_{ba})\text{ Re }\mathcal{H}_{ji}(L,\omega_{ba})\,. \tag{4.6}$$

The thermal kernel gives rise to a number of poles at the so-called *Matsubara frequencies* $\xi_n = 2\pi n k_BT/\hbar$ [Matsubara, 1955] in the first term of Eq. (4.6). The dashed sum symbol indicates that the term $n = 0$ is weighted by a factor $1/2$. Both $\boldsymbol{\beta}^T(\mathrm{i}\xi)$ and $\boldsymbol{\mathcal{H}}(L,\mathrm{i}\xi)$ are real expressions for $\xi > 0$. The second term in Eq. (4.6) contains the atomic pole at ω_{ba} and depends on the thermal occupation of photon modes $\bar{n}(\omega) = 1/\left(e^{\hbar\omega/k_BT}-1\right)$ given by the Bose-Einstein distribution. At $T = 0$ the atomic pole can contribute only for excited states, for which $\bar{n}(\omega_{ba}) \to -1$ for $\omega_{ba} < 0$ (see Eqs. (4.3) and (4.4) of Wylie and Sipe [1985]). The real part of the Green's tensor can be given an interpretation from the radiation reaction of a classical dipole oscillator [Wylie and Sipe, 1985]. This term is practically absent for the electric Casimir-Polder interaction of ground-state atoms because $\bar{n}(\Omega_e) \approx 0$ at the higher frequencies of electric transitions, $\Omega_e \approx (k_B/\hbar)\,10^3 \ldots 10^5\,\mathrm{K}$ as compared to magnetic transition frequencies $\Omega_m \approx (k_B/\hbar)5 \ldots 500\,\mathrm{mK}$, see Sec. 4.1.3 below.

In the following, we call the Matsubara sum (first term) in Eq. (4.6) the *nonresonant* contribution, and the second term the *resonant* one, because it involves the field response at the atomic transition frequency.

When the atom is not in a pure state $|a\rangle$ but in thermal equilibrium, we have to sum the polarizability over the states $|a\rangle$ with a Boltzmann weight:

$$\beta_{ij}^T(\omega) = \sum_a \frac{e^{-E_a/k_BT}}{Z}\beta_{ij}^a(\omega)\,, \tag{4.7}$$

where Z is the partition function. In the limit $T \to 0$, we recover the polarizability for a ground-state atom. For a two-level system with transition frequency Ω_m, the previous expression takes a simple form and can be expressed in terms of the ground-state polarizability [Eq. (4.3), where $a = g$]:

$$\boldsymbol{\beta}^T(\omega) = \tanh\left(\frac{\hbar\Omega_m}{2k_BT}\right)\boldsymbol{\beta}^g(\omega)\ . \tag{4.8}$$

This polarizability shows a rather strong T-dependence because of a Fermi-Dirac-like statistics [Callen and Welton, 1951]. Note that the thermal dependence can compensate with the one from the Green's tensor, if $\boldsymbol{\beta}^g$ is peaked around $\omega = \Omega_m$, which is the case for the radiation reaction $\operatorname{Im}\boldsymbol{\beta}^g$. From the previous expression and the Green's function identities given in App. A.3 it is possible to recover the general formula

$$\mathcal{F} = -\frac{\hbar}{2\pi}\int_0^\infty \mathrm{d}\omega\coth\left(\frac{\hbar\omega}{2k_BT}\right)\operatorname{Im}[\beta_{ij}^T(\omega)\mathcal{H}_{ji}(L,\omega)] \tag{4.9}$$

found previously from perturbation theory with respect to the multipolar atom-field coupling [McLachlan, 1963]. For a proof of the connection between Eqs. (4.9) and (4.6) that uses only retarded response functions see [Spagnolo, 2009]. Eq. (4.9) is often expressed in an equivalent form using the analyticity of $\boldsymbol{\beta}^T(\omega)$ and $\boldsymbol{\mathcal{H}}(L,\omega)$ in the upper half of the complex frequency plane. Performing a rotation onto the imaginary frequency axis as in Eq. (4.3) gives the Matsubara series

$$\mathcal{F}(L,T) = -k_BT{\sum_{n=0}^{\infty}}'\,\beta_{ij}^T(\mathrm{i}\xi_n)\mathcal{H}_{ji}(L,\mathrm{i}\xi_n)\ . \tag{4.10}$$

4.1.2 Treatment in fluctuation electrodynamics

Another simple and general derivation of Eq. (4.9) can be given following Henkel et al. [2002]; Novotny and Henkel [2008]; Intravaia et al. [2011]. The effective interaction potential between a polarizable particle and the (magnetic or electric) field $\boldsymbol{B}$ is given by [Jackson, 1975]

$$\mathcal{F} = -\frac{\langle\boldsymbol{\mu}\cdot\boldsymbol{B}(\boldsymbol{r}_0)\rangle_T}{2}. \tag{4.11}$$

The expectation value $\langle\cdots\rangle_T$ is taken in an equilibrium state of the noncoupled system at temperature T and implicitly evaluates symmetrically ordered operator products; $\boldsymbol{\mu}$ is the (magnetic or electric) dipole operator and $\boldsymbol{B}$ the corresponding field operator, evaluated at the atom position $\boldsymbol{r}_0$. The factor $1/2$ arises from a coupling constant integration (excluding a permanently polarized atom). Within first-order perturbation theory, both the dipole moment $\boldsymbol{\mu}(t)$ and the field $\boldsymbol{B}(t)$ can be split into fluctuating (fl) and induced (in) parts: the fluctuating part describes the intrinsic equilibrium fluctuation, while the

induced part arises in perturbation theory from the dipole coupling [Mandel and Wolf, 1995]. Eq. (4.11) becomes

$$\mathcal{F} = -\frac{\langle \boldsymbol{\mu}^{\mathrm{in}}(t) \cdot \boldsymbol{B}^{\mathrm{fl}}(\boldsymbol{r}_0, t)\rangle_T}{2} - \frac{\langle \boldsymbol{\mu}^{\mathrm{fl}}(t) \cdot \boldsymbol{B}^{\mathrm{in}}(\boldsymbol{r}_0, t)\rangle_T}{2} \,. \tag{4.12}$$

Here, we assume the fluctuating parts of the dipole and of the field to be decorrelated at this order. This assumption would break down at higher orders of perturbation theory. Note that while in Eq. (4.11), the total dipole and field operators (Heisenberg picture) commute at equal times, this is no longer true for their 'in' and 'fl' constituents in Eq. (4.12). The induced quantities are given, in frequency space, by the retarded response functions [Jackson, 1975], cf. Apps. A.2, B.2,

$$\mu_i^{\mathrm{in}}(\omega) = \beta_{ij}(\omega) B_j^{\mathrm{fl}}(\boldsymbol{r}_0, \omega) \,, \quad B_i^{\mathrm{in}}(\boldsymbol{r}, \omega) = \mathcal{H}_{ij}(\boldsymbol{r}, \boldsymbol{r}_0, \omega) \mu_j^{\mathrm{fl}}(\omega) \,, \tag{4.13}$$

where the frequency dependence allows for the description of absorption and dispersion. The equilibrium fluctuations follow from the fluctuation-dissipation theorem [Callen and Welton, 1951], cf. Sec. 2.1.4,

$$\langle B_i^{\mathrm{fl}}(\boldsymbol{r}, \omega) B_j^{\mathrm{fl}}(\boldsymbol{r}, \omega')\rangle_T = \frac{\hbar}{2\pi} \delta(\omega + \omega') \coth\left(\frac{\hbar\omega}{2k_B T}\right) \mathrm{Im}[\mathcal{H}_{ij}(\boldsymbol{r}, \boldsymbol{r}, \omega)] \,, \tag{4.14}$$

$$\langle \mu_i^{\mathrm{fl}}(\omega) \mu_j^{\mathrm{fl}}(\omega')\rangle_T = \frac{\hbar}{2\pi} \delta(\omega + \omega') \coth\left(\frac{\hbar\omega}{2k_B T}\right) \mathrm{Im}[\beta_{ij}^T(\omega)] \,. \tag{4.15}$$

Combining Eqs. (4.12)–(4.15), we recover Eq. (4.9), setting $\mathcal{H}_{ij}(\boldsymbol{r}_0, \boldsymbol{r}_0, \omega) = \mathcal{H}_{ij}(L, \omega)$. One uses the fact that the imaginary part of both Green's tensor and polarizability tensor are odd in ω (retarded response functions). The field correlations are needed at the same position $\boldsymbol{r}_0$ and, as already stated, the Lamb-shift is removed by considering only the reflected part of the field.

Note that the generalization to systems with a temperature unbalance between atoms and the field can be achieved very naturally in this scheme. Since expectation values are taken only for either fields or dipoles alone, the global equilibrium temperature T in Eqs. (4.14) and (4.15) may be simply replaced by the respective subsystem temperatures.

4.1.3 Polarizabilities and interaction potentials in optical and magnetic traps

The formalism presented in the previous section is quite general and $\boldsymbol{\beta}$ [$\boldsymbol{\mathcal{H}}$] could, in principle, represent either the magnetic or electric polarizability [Green's tensor], respectively. It is, in fact, well known that the potential of Eq. (4.9) has the same form for electric or magnetic dipole couplings [Boyer, 1974; Buhmann and Welsch, 2007]. This is a direct consequence of the similarities between the electric and the magnetic interaction Hamiltonian in the multipolar coupling scheme [Eq. (2.2)].

The magnetic and electric polarizabilities of atoms are determined by the transition dipole matrix elements and the resonance frequencies. We are interested in the retarded response function, which for a pure atomic state $|a\rangle$ is given by Eq. (4.3) above and for a thermal state by Eq. (4.7).

We now compare the electric and magnetic polarizabilities of atoms[3]. The magnetic transition moment among states with zero orbital angular momentum scales with $\mu_B g_s$ where g_s is the Landé factor for the electron spin and μ_B is the Bohr magneton. Electric dipoles are on the order ea_0 with a_0 the Bohr radius. Introducing factors ε_0 and μ_0 to obtain the same dimensions, we find that the ratio of the dipole moments gives

$$\frac{(ea_0)^2/\varepsilon_0}{(\mu_B g_s)^2 \mu_0} \sim \frac{1}{\alpha_{\rm fs}^2} \,, \tag{4.16}$$

where $\alpha_{\rm fs} \approx 1/137$ is the fine-structure constant.

The magnetic interaction is thus expected to be a small correction. It is, however, connected with much lower transition frequencies than the electric dipole coupling, which makes it much more sensitive to the influence of temperature. The resonance frequencies relevant for the magnetic Casimir-Polder potential depend on the trapping scheme. We focus here on alkali atoms that are typically used in ultracold gases and distinguish between optical and magnetic traps.

In an *optical trap*, we may consider the magnetic sublevels degenerate and subject to the same trapping potential (proportional to the intensity of a far-detuned laser beam). Magnetic dipole transitions can then occur between hyperfine levels whose splitting is on the order of $\Omega_m/2\pi \approx 10^8 \ldots 10^{10}\,\mathrm{Hz}$, corresponding to temperatures of $5 \ldots 500\,\mathrm{mK}$ (see Appendix A.4 for more details). In contrast, electric dipole transitions of single atoms occur in the visible range $\Omega_e/2\pi \approx 10^{15}\mathrm{Hz}$ or $\sim 50\,000\,\mathrm{K}$. Note also that electric dipole transitions between Rydberg states [Crosse et al., 2010] or vibronic transitions in molecules [Ellingsen et al., 2011] can be comparable to the magnetic Bohr frequencies considered here.

In an optical trap, all magnetic sublevels are trapped and we obtain an isotropic magnetic polarizability by averaging. We write $\beta_{ij}^T = \beta_{\rm iso}^T \frac{1}{3}\delta_{ij}$, so that in Eq. (4.9) or (4.10)

$$\beta_{ij}^T \mathcal{H}_{ji} = \beta_{\rm iso}^T \frac{2\mathcal{H}_{xx} + \mathcal{H}_{zz}}{3} \,. \tag{4.17}$$

The setup we will consider in most of our examples is an atom in a *magnetic trap*. In these traps, one uses the interaction of a permanent magnetic dipole with an inhomogeneous, static magnetic field $\boldsymbol{B}$, as discussed in Sec. 1.2.1. Let us consider for simplicity a spin-$1/2$ manifold: in weak fields, the linear Zeeman effect leads to a splitting of the magnetic sublevels by the Larmor frequency, $\Omega_m = \mu_B g_s |\boldsymbol{B}|/\hbar$. To give an order of magnitude, $\Omega_m/2\pi \approx 280\,\mathrm{MHz} \approx (k_B/2\pi\hbar)\,13.5\,\mathrm{mK}$ at $B = 10\mathrm{mT}$. Atoms in those magnetic sublevels where $\Delta E = -\boldsymbol{\mu}\cdot\boldsymbol{B} > 0$ are weak-field seekers and

[3] For a discussion of the magnetic and electric response of nanospheres see [Haakh et al., 2009, Sec. III C].

can be trapped in field minima. We consider a surface mounted magnetic trap where the trap center is characterized by a nonzero field component perpendicular to the surface. This may be achieved in a two-wire trap. Magnetic dipole transitions are then generated by the parallel components μ_x, μ_y of the dipole moment, see App. A.4. In this anisotropic scenario, the components of the magnetic polarizability tensor are given by $\beta^T_{xx}(\mathrm{i}\xi) = \beta^T_{yy}(\mathrm{i}\xi) = \beta^T_{\rm an}(\mathrm{i}\xi)$ and $\beta^T_{zz}(\mathrm{i}\xi) = 0$. The relevant components of the Green's tensor are, therefore,

$$\beta^T_{ij}\mathcal{H}_{ji} = \beta^T_{\rm an}\, 2\mathcal{H}_{xx} \,. \tag{4.18}$$

We should mention that many experiments do not realize a global equilibrium situation, as assumed in Eq. (4.9). In typical atom-chip setups, atoms are laser cooled to μK temperatures or prepared in a well-defined state, whereas the surface is generally at a much higher temperature, even when superconducting. For the description of such situations, an approach *à la* Wylie and Sipe [Eqs. (4.6) and (4.3)] is more suitable and we discuss the results in Sec. 4.4. Before addressing such systems, we start with thermal equilibrium free energies. This may be not an unrealistic assumption in spectroscopic experiments where Casimir-Polder energies are measured with atoms near the window of a vapor cell [Failache et al., 1999]. From the theoretical viewpoint, thermal equilibrium provides an unambiguous definition of the entropy related to the atom-surface interaction. We shall see that this quantity shows remarkable features depending on the way dissipation and conductivity is included in the material response. This closely parallels the issue of the thermal correction to the macroscopic Casimir interaction, a subject of much interest lately, cf. [Intravaia and Henkel, 2008; Milton, 2009; Klimchitskaya et al., 2009; Pitaevskii, 2010].

To summarize, in an optical (isotropic) trap, the equilibrium Casimir-Polder free energy (4.10) is given by the Matsubara sum

$$\mathcal{F}_{\rm iso}(L,T) = -k_B T {\sum_{n=0}^{\infty}}' \beta^T_{\rm iso}(\mathrm{i}\xi_n) \frac{2\mathcal{H}_{xx}(L,\mathrm{i}\xi_n) + \mathcal{H}_{zz}(L,\mathrm{i}\xi_n)}{3} \,, \tag{4.19}$$

while in a magnetic (anisotropic) trap, we have

$$\mathcal{F}_{\rm an}(L,T) = -2k_B T {\sum_{n=0}^{\infty}}' \beta^T_{\rm an}(\mathrm{i}\xi_n)\mathcal{H}_{xx}(L,\mathrm{i}\xi_n) \,. \tag{4.20}$$

4.2 Surface Properties

4.2.1 Dielectric functions for local metals and superconductors

We have argued before (Secs. 1.4 and 3.1) that all information about the optical properties of the bulk is encoded in the dielectric function $\varepsilon(\omega)$. While in Chapter 3 the focus was put on the impact of ballistic charge transport (nonlocal conductivity) on the surface response, we will now consider a number of widely used local models, each of which

includes ohmic dissipation (Joule heating due to the scattering of charge carriers) in a very characteristic way. As it turns out, the magnetic Casimir-Polder interaction is much more sensitive to this type of current-dissipation in the material than the electric one. This is due to the fact that the resonance frequencies in the magnetic polarizability $\boldsymbol{\beta}(\omega)$ are much lower (see Sec. 4.1.3) and that the boundary conditions for quasistatic magnetic and electric fields differ significantly.

The first model considered is the *Drude metal* of Eq. (3.13) [Jackson, 1975]

$$\varepsilon_{\mathrm{Dr}}(\omega) = 1 - \frac{\omega_{\mathrm{p}}^2}{\omega(\omega + \mathrm{i}\gamma)} ,$$

where ω_{p} is the plasma frequency and $\gamma > 0$ is a phenomenological dissipation rate. This is the simplest description for a metal with a finite conductivity and has been found in Sec. 3.1.3 as the local limit (mean free path $\ell \to 0$) of the nonlocal Boltzmann-Mermin model. When the finite conductivity can be attributed to impurity scattering in the medium, γ is a constant (independent of temperature).

In contrast, in a very clean metal, dissipation is dominated by electron-electron or electron-phonon scattering rather than impurity scattering. In this case, the dissipation rate in the Drude formula depends on temperature and follows a characteristic power law

$$\gamma(T) \sim T^n, \qquad n > 1 \tag{4.21}$$

at the rather low temperatures considered in the following. At higher temperatures, the temperature dependence differs from the simple power law (Bloch-Grüneisen law, e.g. [Ashcroft and Mermin, 1987]). It is reasonable to call this system the *perfect crystal* model.

Another important model is the lossless *plasma model* $\varepsilon_{\mathrm{pl}}(\omega)$: here, one sets $\gamma = 0$ in the right-hand side the Drude model. This corresponds to a purely imaginary conductivity and provides, on one hand, a high-frequency limit to the Drude model. On the other, it is well known as the current-field relation deduced by London and London [1935] in an early model for a *superconductor* that described correctly the expulsion of low-frequency magnetic fields from a (type-I) superconductor (Meißner-Ochsenfeld effect). In the light of the ongoing debate about these fields in the macroscopic Casimir interaction at nonzero temperature [Boström and Sernelius, 2000; Milton, 2009; Klimchitskaya et al., 2009; Intravaia and Henkel, 2009; Sushkov et al., 2011; Decca et al., 2011], where some experimental data seem to favor a lossless model over a lossy one, measurements of dispersion interactions with superconductors provide a promising perspective [Bimonte et al., 2005, 2010; Bimonte, 2008].

It has become clear already in the previous chapters that superconductors are also particularly interesting in the context of atom chips, because resistive losses are suppressed as the temperature T drops below the critical temperature T_c. Going beyond London theory, we adopt here a description in terms of the two-fluid model, which has already

been briefly discussed in Sec. 3.2.2. Recall that it consists in a weighted sum of a lossless supercurrent response (plasma model) and a normal conductor response

$$\varepsilon_{\rm sc}(\omega,T) = \eta(T)\varepsilon_{\rm pl}(\omega) + [1-\eta(T)]\varepsilon_{\rm Dr}(\omega)\,, \tag{4.22}$$

$$\eta(T) = 1-(T/T_c)^4\,, \tag{4.23}$$

where Eq. (4.22) for the *order parameter* $\eta(T)$ is known as the Gorter-Casimir relation [Schrieffer, 1999]. At $T=0$ the order parameter $\eta\to 1$, so that two-fluid superconductor coincides with the plasma model. Note that more involved descriptions of superconductors (including BCS theory) also reproduce the plasma behavior at low frequencies (ω well below the BCS gap) and temperature close to absolute zero. The full BCS theory of superconductivity[4] can be applied in this context, too, using the optical conductivity given in App. C. However, we shall see in Sec. 4.3.3 that the two-fluid model and BCS theory agree well for realistic choices of the physical parameters.

Note that in both the perfect crystal and the superconductor, dissipation is switched on by temperature, but in completely different ways[5]. It turns out that this can be distinguished in the atom-surface interaction potential.

4.2.2 Electric and magnetic Green's tensors

We will build the further analysis of atom-surface forces on asymptotic expansions of Green's tensors and reflectivities, similar to the approach of Ch. 3.

As in Sec. 3.1.5, we discuss here material models that do not contain spatial dispersion (nonlocality), so that the relevant scales are the photon wavelength in vacuum, $\lambda_\omega = 2\pi c/\omega$, the skin depth in the medium $\delta(\omega)$ [Eq. (3.8)], and the plasma wavelength $\lambda_{\rm p} = 2\pi c/\omega_{\rm p}$. Thermal energies introduce the *thermal wavelength* $\Lambda_T = \hbar c/(4\pi k_B T)$ as a further characteristic length scale. These scales limit the different regimes in the atom-surface distance identified in Sec. 3.1.2:

(ii) the *sub-skin-depth region*, $L \ll \delta(\omega)$,

(iii) the *nonretarded region*, $\delta(\omega) \ll L \ll \lambda_\omega$, and

(iv) the *retarded region*: $\lambda_\omega \ll L$, limited by the onset of

(v) a *thermal regime* $L \gg \Lambda_T$, also known as *Lifshitz regime*.

The *nonlocal extreme near field* (i) $L \ll \ell$ (distances smaller than the electronic mean free path) of Sec. 3.1.4 does not occur for the local metals considered here. In zones (i)-(iii), retardation can be neglected (van der Waals zone), while in zone (iv), it leads to a different power law (Casimir-Polder zone) for the atom-surface interaction.

Since the boundaries of the distance zones (ii) – (iv) depend on frequency, the respective length scales differ by orders magnitude between the magnetic and the electric case [Spagnolo, 2009]. For electric dipole transitions, the Hagen-Rubens regime

[4] See also [Mattis and Bardeen, 1958; Zimmermann et al., 1991; Berlinsky et al., 1993; Bimonte et al., 2010] and the textbooks by Schrieffer [1999]; Ketterson and Song [1999]; Tinkham [2004].

[5] Mind that the use of temperature-dependent parameters in a Hamiltonian approach is a subtle issue [Barton, 2012].

		Sub-skin depth (ii)	Nonretarded (iii)	Retarded (iv)
$\mathcal{H}_{xx}$	Drude	$\dfrac{\mathrm{i}\mu_0}{32\pi\delta^2(\omega)L}$	$-\dfrac{\mu_0}{32\pi L^3}\left[1-\dfrac{3(1+\mathrm{i})\delta(\omega)}{2L}\right]$	$-\dfrac{\mu_0 e^{2\mathrm{i}\omega L/c}}{32\pi L^3}\times$
	plasma	$-\dfrac{\mu_0\pi}{16\lambda_\mathrm{p}^2 L}$	$-\dfrac{\mu_0}{32\pi L^3}\left[1-\dfrac{6\pi\lambda_\mathrm{p}}{L}\right]$	$\times\left[1-\frac{2\mathrm{i}\omega L}{c}-\frac{4\omega^2L^2}{c^2}\right]$
$\mathcal{G}_{xx}$		$\dfrac{1}{32\pi\varepsilon_0 L^3}\left[1-\dfrac{(1+\mathrm{i})\omega^2\delta(\omega)L}{c^2}\right]$		$\dfrac{e^{2\mathrm{i}\omega L/c}}{32\pi\varepsilon_0 L^3}\times$ $\times\left[1-\frac{2\mathrm{i}\omega L}{c}-\frac{4\omega^2L^2}{c^2}\right]$

Table 4.1: Magnetic and electric Green's tensors at a planar surface in terms of the skin depth $\delta(\omega)$ and the plasma wavelength λ_p. The Hagen-Rubens regime ($\gamma \gg \omega$) can be applied only in the magnetic case. The other elements have the asymptotes $\mathcal{H}_{yy}=\mathcal{H}_{xx}$, $\mathcal{H}_{zz}=2\mathcal{H}_{xx}$, and similarly for $\mathcal{G}_{ii}$. The off-diagonal elements vanish, cf. [Spagnolo, 2009]. At the order given here, the expressions of the retarded regime coincide with the perfect reflector limit.

($\omega \ll \gamma \ll \omega_\mathrm{p}$) cannot be applied because the Bohr frequency Ω_e is much larger. The role of the skin depth is then taken by the plasma wavelength λ_p. This implies that the Casimir-Polder zone (iv) for the electric dipole interaction occurs in a range of distances, where magnetic retardation is still negligible [zones (ii) and (iii)]. We compare the limiting forms of the electric and magnetic Green's tensors obtained from the plasma and the Drude model in these regimes in Table 4.1. Already in Chapter 3, asymptotic expansions of the reflection coefficients and the magnetic Green's tensor have been given for a general dielectric function (Table 3.1), and have been used there to obtain limiting expressions for the Drude model [Eq. (3.7)] and for the two-fluid model [Eqs. (3.24), (3.25)]. From the construction of the two-fluid model it is clear that the plasma and Drude asymptotes are also recovered for a superconductor as $\eta \to 1,\ \ \eta \to 0$, respectively.

One notes that the zz-component is larger by a factor 2 compared to the xx- and yy-components. Recalling that the Green's tensor describes the field of a test dipole (App. B.1), this difference between the normal and parallel components can be understood by the method of images [Jackson, 1975]. Furthermore, the magnetic response for a normally conducting metal in the sub-skin-depth regime is purely imaginary and scales linearly with the frequency ω – the reflected magnetic field is generated by induction. Only the superconductor or the plasma model can reproduce a significant low-frequency magnetic response, via the Meißner-Ochsenfeld effect. In contrast, the electric response is not sensitive to the skin effect, i.e. ohmic dissipation. Rather, it is strong for all conductors [Bezerra et al., 2008] because surface charges screen the electric field efficiently.

The imaginary part of the Green's functions determines the local mode density (per frequency) for the magnetic or electric fields [Joulain et al., 2003]. These can be compared directly after multiplying by $1/\mu_0$ (or ε_0), respectively. Joulain et al. [2003]; Henkel et al. [2005] have discussed that in the sub-skin-depth regime near a metallic surface, the field fluctuations are mainly of magnetic nature. This can be traced back to electric screening

by surface charges, that efficiently decouples the interior of the metal from the vacuum above. Magnetic fields, however, cross the surface much more easily as surface currents are absent except for superconductors. It has been the goal of Chapter 3 to understand in detail how this reveals, in the vacuum outside the metal, the thermally excited currents from the bulk.

4.3 Temperature Dependence

The (free) energy vs. distance has been calculated numerically for an anisotropic magnetic dipole in front of a half-space filled with a normal conductor [Fig. 4.1a)] or described by the plasma model [Fig. 4.1b)]. The thick black curves give the zero-temperature result (see the caption for parameters). The dashed asymptotes are discussed in this section. All energies are normalized to the L^{-3} power law of the nonretarded Van der Waals interaction between an atom and a perfectly reflecting surface. The scale factor $\mathcal{F}_{\rm pl}(1\mu{\rm m})$, given in the caption, is just Eq. (4.27) below. For these and the following results, the Matsubara sum has been evaluated numerically in a self-consistent way, see [Haakh et al., 2009, App. A] for details and an estimate of the numerical error.

As a striking feature, the magnetic Casimir-Polder potential is always repulsive. This could have been expected from the interaction between an oscillating magnetic dipole and its image at the conducting surface. The sign is also consistent with the macroscopic Casimir interaction between a conducting and a permeable surface ('mixed' Dirichlet-von Neumann boundary conditions), see e.g. [Boyer, 1974]. To understand this argument, one may think of the isolated magnetic dipoles as a dilute limit of a permeable medium.

The curves in Fig. 4.1 make manifest the crossovers between the distance regimes introduced in Sec. 4.2.2 above. The relevant length scales are here the skin-depth $\delta_m = \delta(\Omega_m)$, evaluated at the transition frequency [Fig. 4.1a)], the plasma wavelength $\lambda_{\rm p} = 2\pi c/\omega_{\rm p}$ [Fig. 4.1 b)], and the transition wavelength $\lambda_m = \lambda(\Omega_m)$. Superconductors are discussed in Sec. 4.3.3 below (Fig. 4.2).

4.3.1 Zero-temperature interaction potential

The zero-temperature case [black curves in Fig. 4.1b)] for a Drude model has been discussed earlier by Henkel et al. [2005]; we give details on the asymptotes (dashed curves). Taking the limit $T \to 0$ in Eq. (4.10) recovers the well-known expression

$$\mathcal{F}(L,0) = E(L) = -\frac{\hbar}{2\pi}\int_0^\infty d\xi \beta_{ij}({\rm i}\xi)\mathcal{H}_{ji}(L,{\rm i}\xi)\ . \tag{4.24}$$

In the *sub-skin-depth regime* $L \ll \delta_m$, the distance dependence in the anisotropic case (4.18) for the Drude model becomes

$$\mathcal{F}_{\rm an}^{\rm Dr}(L,0) \approx \frac{|\mu_x|^2\mu_0}{8\pi^2\delta_m^2}\frac{1}{L}\ln\left(\frac{\delta_m}{L}\right)\ , \tag{4.25}$$

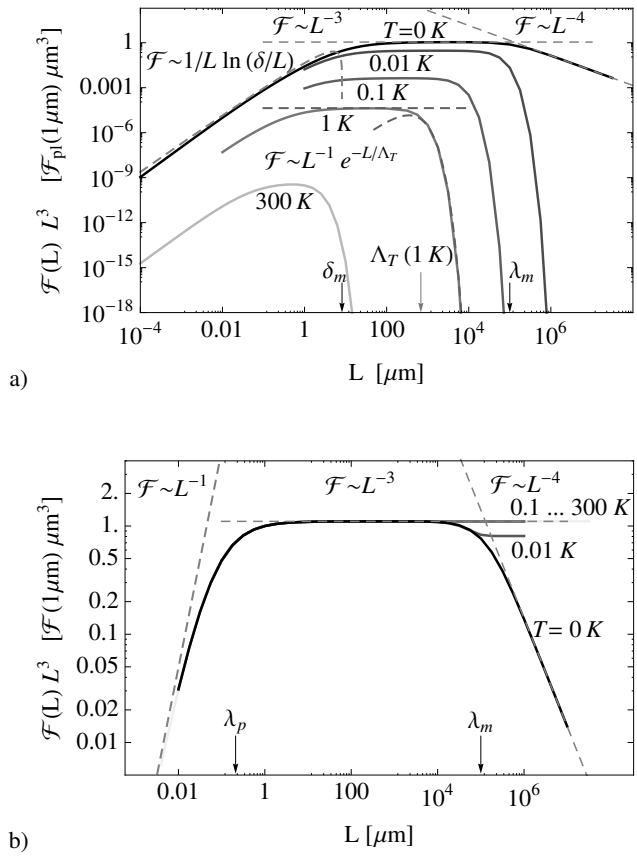

Figure 4.1: Casimir-Polder free energy vs. distance L for an anisotropic magnetic dipole (transition moment parallel to the surface). a) Drude model and b) plasma model, with plasma frequency $\omega_{\rm p}/2\pi \approx 1.42\times10^{15}$Hz ($\lambda_{\rm p}\approx 210\,$nm) and $\gamma = 0.01\omega_{\rm p}$ for better visibility. The transition frequency is $\Omega_m/2\pi \approx 480\,$MHz $\approx (k_B/2\pi\hbar)\,0.023\,$K ($\lambda_m = 63\,$cm). In both plots, the free energy scale $\mathcal{F}(1\mu{\rm m}) = (2\pi\hbar)1.48\,$mHz is the value at $T=0, L=1\mu$m obtained in the plasma model. Dashed lines indicate the asymptotic laws at zero temperature Eqs. (4.26)–(4.28), or including thermal corrections according to Eqs. (4.33), (4.34).

where $|\mu_x|^2$ is the magnetic transition dipole matrix element, cf. Appendix A.4. This expression is obtained by using the sub-skin-depth asymptote of the magnetic Green's tensor (first column of Table 4.1) under the ξ-integral (4.24) and cutting the integral off at the border of this regime where $L\sim\delta(\xi_{\rm max})$, i.e. at $\xi_{\rm max}\approx D/L^2$ with the diffusion constant for magnetic fields $D = 2\gamma c^2/\omega_{\rm p}^2$.

The small-distance calculation for the plasma model can be done in a similar way. In both the sub-skin-depth and the nonretarded regime, the Green's tensor becomes independent of ξ (see Table 4.1), and the frequency integral depends only on the polarizability. Therefore, the distance dependence is not logarithmic as in the dissipative case, but

follows [see Fig. 4.1a)]

$$\mathcal{F}_{\rm an}^{\rm pl}(L,0) = \frac{|\mu_x|^2\mu_0\pi}{16\lambda_{\rm p}^2}\frac{1}{L}\,. \tag{4.26}$$

In the *nonretarded regime* (intermediate distances), the interaction energy in the Drude model and in the plasma model behave alike

$$\mathcal{F}_{\rm an}(L,0) \;\approx\; \frac{|\mu_x|^2\mu_0}{32\pi}\frac{1}{L^3}\,, \tag{4.27}$$

This is calculated as outlined above for the plasma model. The energy (4.27) is identical to the interaction of the magnetic dipole μ_x with its image, calculated as for a perfectly conducting surface. Indeed, the L^{-3} power law is consistent with the dipole field of a static (image) dipole.

In the *retarded region* (not discussed by Henkel et al. [2005]) $L \gg \lambda_m, \delta_m, \lambda_{\rm p}$ and from the expressions of Table 4.1 the results for the Drude and the plasma model coincide. In this regime the field penetration into the surface is actually negligible and the asymptotic Green's tensor of Table 4.1 agrees with the assumption of perfect reflection. Retardation leads to a change in the power law with respect to shorter distances, identical to the electric Casimir-Polder interaction:

$$\mathcal{F}_{\rm an}(L,0) = \frac{|\mu_x|^2\mu_0\lambda_m}{16\pi^3}\frac{1}{L^4}\,. \tag{4.28}$$

The calculation of this asymptote follows the same lines as in the electric dipole case, see Wylie and Sipe [1985]. Comparing different transition wavelengths λ_m (e.g., Zeeman vs. hyperfine splitting): the smaller the transition energy, the larger the retarded interaction. The numerical data displayed in Fig. 4.1 agree very well with all these asymptotes.

Eqs. (4.27) and (4.28) illustrate that the magnetic atom-surface interaction is reduced relative to the electric one by the fine-structure constant $\alpha_{\rm fs}^2$, as anticipated earlier in Eq. (4.16). One should bear in mind, of course, that the length scales for the crossovers into the retarded regime are very different. A crossing of the nonretarded magnetic and the retarded electric potentials would be expected for a distance of order $\lambda_e\alpha_{\rm fs}^{-2} \sim 1\,\mathrm{mm}$, where it is clear that both energies are already extremely small, cf. [Spagnolo, 2009, Figs. 4.2 and 4.3]. In addition, the temperature should be low enough so that the crossing occurs at distances smaller than the thermal wavelength (ξ_1 is the first Matsubara frequency)

$$\Lambda_T = \frac{c}{2\xi_1} = \frac{\hbar c}{4\pi k_B T} \approx \frac{0.18\mathrm{mm\,K}}{T}\,, \tag{4.29}$$

where the thermal regime sets in. Indeed, Fig. 4.1a) shows clearly that a nonzero temperature can significantly reduce the magnetic Casimir-Polder potential.

4.3.2 Temperature dependence

In this section, we consider the temperature dependence of the Casimir-Polder interaction at *global* equilibrium, in particular using the temperature-dependent polarizability $\boldsymbol{\beta}^T$ of Eq. (4.8). This provides also a well-defined calculation of the atom-surface entropy, see Sec. 4.3.4. Scenarios with atoms prepared in specific magnetic sublevels are discussed in Sec. 4.4.

The set of curves in Fig. 4.1 illustrates the strong impact of a nonzero temperature for the Drude (normally conducting) metal: its magnitude is reduced for any distance L. In the plasma model (no dissipation), the main effect is the emergence of a different long-distance regime: the *thermal regime* $L \gg \Lambda_T$ [Eq. (4.29)], where the interaction becomes stronger than at $T = 0$. This kind of behavior could have been expected from the thermal occupation of photon modes within the thermal spectrum.

Temperature independent regime

Note that the large distance behavior of the plasma model becomes temperature independent even at moderate temperatures. It is sufficient that $k_B T \gg \hbar\Omega_m$. This is a significant difference compared the electric dipole interaction: it is quite common to have temperatures much larger than the magnetic resonance energies. In this case, there is an inversion of length scales $\Lambda_T \ll \lambda_m$. Thermal effects thus start to play a role already in the nonretarded regime, and can be pronounced at all distances. A very similar effect occurs in the electric Casimir-Polder interaction if small polarizable molecules are considered instead of single atoms. Here, vibronic degrees of freedom with small transition frequencies Ω_e, rather than electronic (optical) ones, are relevant and give rise to a similar temperature independent regime, as recently discussed by Ellingsen et al. [2010]. Rydberg atoms are another system with comparably small electric Bohr frequencies.

The usual description of the high-temperature (or Keesom [Parsegian, 2006]) limit is based on the term $n = 0$ in the Matsubara sum (4.10)

$$\mathcal{F}(L,T) \approx -\frac{k_B T}{2}\beta_{ij}^T(0)\mathcal{H}_{ji}(L,0)\,. \tag{4.30}$$

Indeed, the higher terms are proportional to the small factor $\exp(-2\xi_n L/c) = \exp(-nL/\Lambda_T)$ that appears in the Green's function $\mathcal{H}_{ji}(L, \mathrm{i}\xi_n)$. The qualitative details now depend on the low frequency response functions and differ among the material models.

In the plasma model and more generally, for all materials where the reflection coefficient $r_{\mathrm{s}}(\omega, k)$ goes to a nonzero static limit, the magnetic Green's tensor $\mathcal{H}_{ji}(L, \omega \to 0)$ is nonzero as well. Here, Eq. (4.30) gives the leading order potential. At thermal energies $k_B T \gg \hbar\Omega_m$, we have from Eq. (4.8) that $\boldsymbol{\beta}^T \sim 1/k_B T$, so that the temperature dependence of the free energy drops out. We find from a glance at Table 4.1, and assuming the

anisotropic polarizability of Eq. (4.18)

$$\mathcal{F}_{\rm an}^{\rm pl}(L \gg \Lambda_T, T) = -|\mu_x|^2 \mathcal{H}_{xx}(L,0) = \frac{\mu_0 |\mu_x|^2}{32\pi L^3} \tag{4.31}$$

(assuming $L \gg \lambda_{\rm p}$). Quite amusingly, this is identical to the zero-temperature result in the nonretarded regime (4.27), as can be seen in Fig. 4.1b). If the temperature is lower, $k_B T < \hbar\Omega_m$ but the distance is still in the thermal regime, the factor $\tanh(\hbar\Omega_m/2k_BT) < \hbar\Omega_m/2k_BT$ in the static polarizability (4.8) reduces the interaction slightly [$T = 0.01\,\mathrm{K}$ in Fig. 4.1b)].

Thermal decoupling

In the Drude model, the Green's tensor $\mathcal{H}_{ij}(L, \mathrm{i}\xi) \to 0$ at zero frequency in the normal conducting state. The leading order potential (4.30) vanishes, and one has to consider the next term $\xi = \xi_1$ in the Matsubara sum (4.10), so that the exponentially small factor $\exp(-L/\Lambda_T)$ governs the thermal (large distance) regime. The new asymptote explains the strong suppression at large distances found in the Drude model and the superconductor around the critical temperature. [Fig. 4.1a)]. We call this the *thermal decoupling* of the atom from the (normal) metal. This phenomenon is related to low-frequency magnetic fields that penetrate the (nonmagnetic) surface.

Indeed, the vanishing of $\mathcal{H}_{ij}(L, \omega \to 0)$ could have been expected from the Bohr-van Leeuwen theorem [Van Leeuwen, 1921; Bimonte, 2009] that states that for any classical system, the magnetization response to static fields must vanish. Both conditions apply here: the zeroth term in the Matsubara series involves static fields, and a normal conductor is a "fluid of classical charged particles" [Jancovici and Samaj, 2005], see also [Buenzli and Martin, 2005]. Indeed, Eq. (4.30) does no longer involve $\hbar$ (except implicitly through the material and coupling constants $\mu_B, \varepsilon(\omega), \omega_{\rm p}, \gamma$), while the next Matsubara terms do (via Λ_T). The Bohr-van Leeuwen theorem does not apply to a superconductor, whose response is a quantum effect (illustrated, for example, by the macroscopic wave function of Ginzburg-Landau theory), and by extension, not to the plasma model, as recently discussed by Bimonte [2009]. As a further consequence, a permanent magnetic dipole can couple only to a superconductor (or plasma) but not to a normal (Drude) metal.

These features are specific to the magnetic atom-surface interaction. Unlike magnetic fields, low frequency electric fields are screened effectively by surface charges, which behave very similarly in all good conductors, independent of dissipation [Bezerra et al., 2008]. Because of this screening, the electric Casimir-Polder potential resembles qualitatively the magnetic one obtained in the presence of the Meißner effect (superconductor, plasma model). All this holds even if the thermal occupation of photonic modes is relevant, as in the molecule-surface interaction [Ellingsen et al., 2010]. Thermal decoupling, therefore, does not occur in the electric Casimir-Polder interaction.

We now calculate the next order in the Matsubara series to understand the temperature dependence of the Casimir-Polder shift near a metal. For simplicity, we consider again

the limiting case $k_BT \gg \hbar\Omega_m$ which simplifies the polarizability to the Keesom form

$$\beta_{\rm an}(\mathrm{i}\xi_n) \approx \frac{|\mu_x|^2\Omega_m^2}{k_BT\xi_n^2}\,, \qquad n \geq 1. \tag{4.32}$$

In the thermal regime, $L \gg \Lambda_T$, we use the large-distance limit of the Green's tensor (cf. the retarded regime of Table 4.1). The Matsubara frequency $\omega = \mathrm{i}\xi_1$ then yields the mentioned exponential suppression

$$\mathcal{F}_{\rm an}^{\rm Dr}(L,T) \approx \frac{\pi\mu_0|\mu_x|^2}{\lambda_m^2 L}e^{-L/\Lambda_T}\,, \tag{4.33}$$

where λ_m is the magnetic resonance wavelength (cf. Fig. 4.1).

At shorter distances, we have to perform the Matsubara summation. In the regime $L \ll \Lambda_T \ll \lambda_m$, we consider the nonretarded approximation to the Green's tensor and make the approximation $\exp(-nL/\Lambda_T) \approx 1$. The sum over the polarizability $\beta_{\rm an}(\mathrm{i}\xi_n)$ can then be done with the approximation (4.32), and we get

$$\mathcal{F}_{\rm an}^{\rm Dr}(L,T) \approx \frac{\mu_0|\mu_x|^2}{384\pi L^3}\left(\frac{\hbar\Omega_m}{k_BT}\right)^2\,. \tag{4.34}$$

The scaling T^{-2} is in good agreement with Fig. 4.1. The crossover into the sub-skin-depth regime is now temperature-dependent and occurs where the skindepth $\delta(\xi_1) \sim L$ at the energy scale characteristic for the diffusive transport of electromagnetic radiation in the metal at wavevectors $\sim 1/L$, cf. Sec. 4.3.1. The corresponding temperature is $k_BT_D \sim \hbar D/L^2 = \gamma\lambda_{\rm p}^2/(2\pi L)^2$.

In the sub-skin-depth regime, the leading order approximation to the Matsubara sum involves terms up to some frequency $\xi_n \sim \xi_L$. This leads to an asymptote similar to Eq. (4.25), but with the ratio $\hbar\xi_L/k_BT$ in the argument of the logarithm and an additional factor $\hbar\Omega_m/k_BT$.

4.3.3 Interaction with a local superconductor

The atom-superconductor interaction shows an even richer behavior compared to the plasma model, as illustrated in Fig. 4.2.

At $T = 0$, it strictly coincides with the plasma model, as it must for the two-fluid description adopted here. The large-distance (thermal) asymptotes are the same as in the plasma model for $T < T_c$. The reasoning leading to Eq. (4.31) can be applied here as well: the response of the superconducting surface to a static magnetic field is characterized by a nonzero value for $r_{\rm s}(\omega \to 0, k)$ because of the Meißner-Ochsenfeld effect. Although the superconducting fraction decreases to zero, proportional to the product $\eta(T)\omega_{\rm p}^2$, the interaction potential Eq. (4.31) stays constant because it does not depend on this 'effective plasma frequency'.

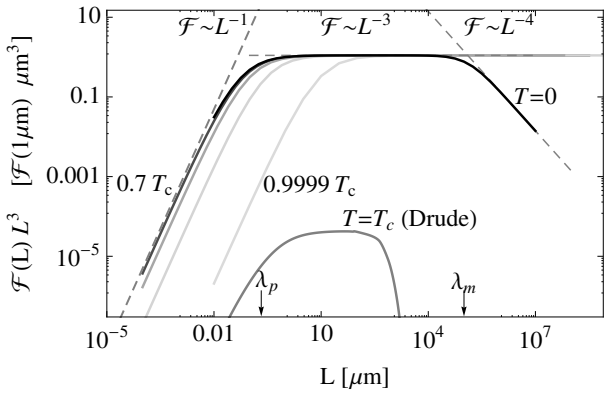

Figure 4.2: Casimir-Polder free energy vs. distance for an anisotropic magnetic dipole above a superconductig surface. Parameters $\omega_{\rm p}$, γ, Ω_m and normalization $\mathcal{F}(1\,\mu{\rm m})$ as in Fig. 4.1, critical temperature $T_c = 1\,{\rm K} \approx 43\,T_m$ (aluminum). Temperatures are $T/T_c \in \{0, 0.7, 0.9, 0.99, 0.9999, 1.0\}$.

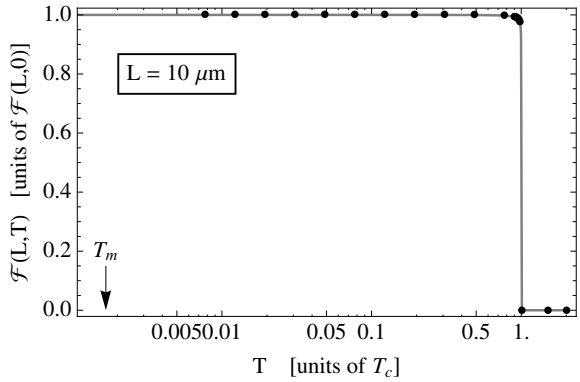

Figure 4.3: Casimir-Polder free energy for a superconducting surface, in the two-fluid model (solid line) and the BCS theory (dots). Parameters $\omega_{\rm p}$, Ω_m as in Fig. 4.1. Scattering rate $\gamma = 5 \times 10^{-4}\omega_{\rm p}$, critical temperature $T_c = 12\,{\rm K} = 520\,T_m$ (niobium), atom-surface distance $L = 10\,\mu{\rm m}$. Energies normalized to $\mathcal{F}_{\rm pl}(L, T \to 0) = (2\pi\hbar)1.65 \times 10^{-6}\,{\rm Hz}$.

This picture also explains the lowering of the sub-skin-depth asymptotes in Fig. 4.2: from Eq. (4.26), the Casimir-Polder potential is proportional to $1/\lambda_{\rm p}^2 \mapsto \eta(T)(\omega_{\rm p}/c)^2$. This gives scale factors $\mathcal{F}_{\rm sc}(L)/\mathcal{F}_{\rm pl}(L, 0\,{\rm K}) \approx 0.5 \ldots 2 \times 10^{-4}$ for the cases $T = 0.7 \ldots 0.9999\,T_c$, in quite good agreement with the numerical data.

At $T \geq T_c$, the superconductor crosses over to a completely different behavior, identical to the Drude metal. This is of course expected for a superconductor from the two-fluid model (4.22). Of course, BCS theory coincides with the Drude model, as soon as the gap parameter $\Delta \to 0$.

It is worth mentioning that the full BCS theory can give results in close agreement

with the simple two-fluid model used here. In Fig. 4.3, we show the temperature dependence of the Casimir-Polder potential (at fixed distance L) for the two cases. We choose here a damping parameter $\gamma = 5 \times 10^{-4}\omega_{\rm p}$ in the same order of the zero-temperature gap $\Delta(0) = 3.5 \times 10^{-4}\hbar\omega_{\rm p} \approx 1.76 k_B T_c$. The BCS calculations have been performed using an efficient expression for the optical conductivity at imaginary frequencies, see App. C.2 and [Bimonte et al., 2010]. This approach is based on [Mattis and Bardeen, 1958; Zimmermann et al., 1991; Berlinsky et al., 1993] and an approximative form of the gap equation [Thouless, 1960; Townsend and Sutton, 1962]. Calculations over a larger parameter range, but restricted to $T = 0$, have been reported by Skagerstam et al. [2009].

Recall finally that both models apply for type-I superconductors, which feature complete expulsion of static magnetic fields from the bulk (Meißner regime). However, measurements of the trapping lifetime in atom chips [Nogues et al., 2009; Kasch et al., 2010] indicate that quantized flux filaments present in type-II superconductors may change the field distribution significantly, cf. Sec. 3.2.2. This might, in turn, also influence the atom-surface potential.

4.3.4 Atom-surface entropy and Casimir analogy

It is well known that at high temperatures, where the free energy scales linearly in T [Eq. (4.30)], the dispersion interaction is mainly of entropic origin [Parsegian, 2006]. More precisely, the interaction is proportional to the *change in entropy* of the system 'atom plus field plus metallic surface', as the atom is brought slowly from infinity to a distance L from the surface, maintaining the thermalization. We calculate in this section the atom-surface entropy according to

$$S(L,T) = -\frac{\partial \mathcal{F}}{\partial T} \,. \tag{4.35}$$

This entropy definition is unambiguous for the global equilibrium setting of the present section.

The behavior seen in the previous figures implies significantly different entropies for the individual surface models. The strong dependence on the presence of dissipation (conductivity) at low frequencies, connected with the zeroth term of the Matsubara sum, parallels the discussion of the macroscopic Casimir entropy for the dispersion interaction between two plates. This quantity has been the subject of controversy, because the Drude and the plasma model give different answers, with the Casimir entropy obtained from the Drude model changing its sign at low temperatures [Bezerra et al., 2004; Boström and Sernelius, 2004; Svetovoy and Esquivel, 2005; Sernelius, 2006; Intravaia and Henkel, 2008; Klimchitskaya et al., 2009]. The results that follow indicate that the magnetic Casimir-Polder interaction provides an alternative scenario to investigate this point.

The atom-surface entropy (4.35) is plotted in Fig. 4.4 for surfaces of different materials. In all models, the entropy vanishes at high temperatures because to leading order, the free energy (4.30) becomes independent of T, and higher orders vanish exponentially with T. This feature is specific to the thermal polarizability of a two-level system.

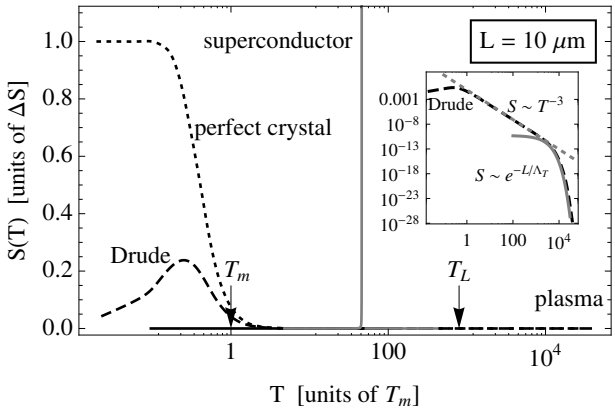

Figure 4.4: Casimir-Polder entropy of an anisotropic magnetic dipole with a plasma (solid), Drude metal (dashed), perfect crystal (dotted) and two fluid superconductor (gray). Parameters chosen as in Figs. 4.1 and 4.2. $k_B T_m = \hbar\Omega_m$ is the energy of atomic transition, while $T_L = \hbar c/4\pi k_B L$ is the 'geometric scale'. The superconducting transition leads to the pronounced peak at T_c. The unit of entropy ΔS is defined in Eq. (4.36). The inset shows a the data for the Drude model and its asymptotics obtained from Eqs. (4.33) and (4.34) in logarithmic scaling.

One notes in Fig. 4.4 very small values for a plasma and a superconductor, about three orders of magnitude smaller than the Drude model entropy. These are two cases where the conductivity provides ideal DC (Meißner) screening. The superconductor shows a narrow, pronounced entropy peak at T_c: we interpret this as the participation of the atomic dipole in the phase transition. Indeed, the electromagnetic waves near the surface are slightly shifted in phase due to the interaction of the evanescent wave tails with the magnetic dipole moment. The atom-surface interaction can be thought of a sum over all these phase shifts, similar to Feynman's interpretation of the Lamb shift [Feynman, 1961; Power, 1966], cf. Sec. 2.3.

It is another remarkable feature of Fig. 4.4 visible in the Drude curve is that the entropy decays at temperatures already much smaller than the *geometrical scale* $k_B T_L = \hbar c/4\pi L$ (i.e. $T/T_L = L/\Lambda_T$). This points towards another characteristic energy scale in the atom-surface system: In the Drude model, we observe a broad peak around a temperature $T_m = \hbar\Omega_m/k_B$. Comparable to this scale for our parameters is the *diffusive energy scale* $k_B T_D \sim \hbar D/L^2 \approx 3.3\,\hbar\Omega_m$, encountered already earlier. We thus attribute the atom-surface entropy to the phase shifts the atom acquires due to the thermally activated diffusive motion of charges and fields below the metal surface (Johnson-Nyquist noise). At the relevant low energies, this motion involves mainly eddy currents, whose contribution to the Casimir entropy (in the plate-plate geometry) has been discussed by Intravaia and Henkel [2009]; Intravaia et al. [2010]. As T drops below the diffusive scale T_D, the eddy currents 'freeze' to their ground state and the entropy vanishes linearly in T.

The dotted curve in Fig. 4.4 corresponds to the 'perfect crystal' that has not been discussed so far. We recall that in this model, the Drude parameter $\gamma(T)$ depends on tem-

perature, because resistive losses are attributed not to impurities scattering but, e.g., to the interaction with phonons. It gives rise to a nonzero atom-surface entropy in the limit $T \to 0$ which is an apparent violation of the Nernst heat theorem (third law of thermodynamics). This has also been discussed for the two-plate interaction [Bezerra et al., 2004; Intravaia and Henkel, 2008; Ellingsen et al., 2009a], but the entropy defect here has a different sign (it is *negative* for two plates, cf. [Pitaevskii, 2010]). The sign can be attributed to our atomic polarizability being paramagnetic, while metallic plates show a diamagnetic response. Using the technique exposed by Intravaia and Henkel [2008], the limit of the atom-surface entropy as $T \to 0$ can be calculated. For an anisotropic dipole we find [Haakh, 2009]

$$\text{'perfect crystal':} \quad \frac{\Delta S}{k_B} = -\beta^0_{\rm an}(0)\mathcal{H}^{\rm pl}_{xx}(L,\omega\to 0) \approx \frac{\mu_0|\mu_x|^2}{16\pi\,\hbar\Omega_m}\frac{1}{L^3}\,. \tag{4.36}$$

The second expression applies in the nonretarded limit $L \gg \lambda_{\rm p}$. This expression was used to normalize the data in Fig. 4.4 and provides good agreement for $T \ll T_m$.

One can argue along the lines of Intravaia and Henkel [2009]; Intravaia et al. [2010] that the Nernst theorem is actually not applicable for this system, since the perfect crystal cannot reach equilibrium over any finite time in the limit of vanishing dissipation, $\gamma \to 0$. The entropy ΔS then describes the modification that the atom imposes on the ensemble of field configurations that are 'frozen' in the perfectly conducting material.

In the two-plate scenario considered by Svetovoy and Esquivel [2005]; Sernelius [2006] it has been shown that not only dissipation, but also nonlocality of the response has strong implications for the entropy. In particular, the residual entropy $\Delta S = 0$ vanishes, because at very low temperatures, the anomalous skin effect and Landau damping, discussed earlier in Sec. 3.1.3, play the role of Drude damping. Though we have not considered nonlocality in this chapter explicitly, one can expect the same thing to happen in the magnetic Casimir-Polder interaction.

4.4 Nonequilibrium Systems

We have mentioned in the last section that many realistic setups involve nonequilibrium situations. Atom chips are a typical example where independent phenomenological temperatures can be introduced for the atom (or a sample of atoms), the surface, and/or the electromagnetic field. This temperature unbalance is metastable on experimentally relevant time scales because the weak interaction between the subsystems makes thermalization very slow. This type of nonequilibrium configurations has been considered by Henkel et al. [1999, 2002]; Antezza et al. [2005]; Spagnolo [2009].

We now analyze the case where the surface is described by a temperature T and the atom is prepared in an eigenstate $|a\rangle$. More complex configurations can be studied starting from this simple case. We first consider two-level atoms and then multilevel atoms, including hyperfine transitions as they occur for the alkali group.

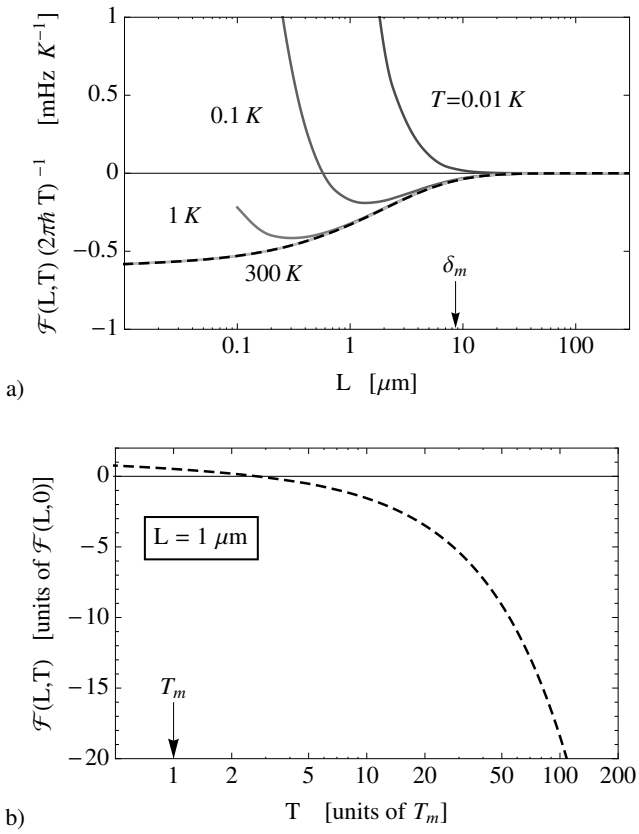

Figure 4.5: a) Casimir-Polder free energy vs. distance for a two-level atom in its ground state, transition dipole parallel to the surface. The surface is described by a Drude metal at different temperatures. Parameters $\omega_{\rm p}$, γ, Ω_m as in Fig. 4.1. Note the scale factor $1/T$ to show the classical limit $\mathcal{F} \sim T$. The limiting curve at high temperatures (black dashed line) can be inferred from the second line of Eq. (4.37).
b) Casimir-Polder free energy vs. temperature for the same system. Distance $L = 1\,\mu$m. The energy scale $\mathcal{F}(0)/(2\pi\hbar) = 3.9 \times 10^{-5}$ Hz is the value at $T = 0$K.

4.4.1 Two-level atom in a pure state

For a two-level atom characterized by the single resonance frequency Ω_m the free energy is given by Eq. (4.6). Its first term now contains the state-dependent polarizability $\boldsymbol{\beta}^a$ [Eq. (4.3)], rather than the thermal one. Note that for the two-level atom $\boldsymbol{\beta}^g = -\boldsymbol{\beta}^e$. The resonant second term of the free energy, not present in thermal equilibrium, involves the thermal occupation number, which we approximate by its classical value $\bar{n}(\pm\Omega_m) \approx \pm k_B T/(\hbar\Omega_m)$. This is sufficiently accurate at room temperature and typical magnetic resonances. In this limit, we obtain a simple expression for the magnetic Casimir-Polder

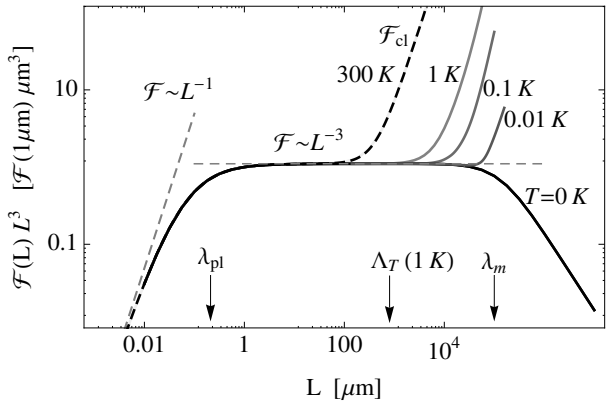

Figure 4.6: Casimir-Polder free energy vs. distance for a two-level atom near a plasma surface. Atom in the ground state and transition dipole parallel to the surface. Parameters $\omega_{\rm p}$, Ω_m and scale factor $\mathcal{F}(1\mu{\rm m})$ as in Fig. 4.1. At high temperatures, the curve can be well approximated by the classical contribution ($\mathcal{F}_{\rm cl}$, black dashed line). The oscillating part of Eq. (4.39) sets in at distances $L \gtrsim \lambda_m$ and is not visible in this plot.

free energy (anisotropic case, argument $a = e, g$ for the atomic state)

$$\begin{aligned}\mathcal{F}_{\rm an}(L,a,T) \approx \quad & -2k_BT\sum_{n\geq 1}\beta^a(\mathrm{i}\xi_n)\mathcal{H}_{xx}(L,\mathrm{i}\xi_n) \\ & +k_BT\beta^a(0)\left\{\mathrm{Re}\left[\mathcal{H}_{xx}(L,\Omega_m)\right]-\mathcal{H}_{xx}(L,0)\right\}\ . \end{aligned} \tag{4.37}$$

The first line is similar to the equilibrium result in the Drude model because of the separated zeroth Matsubara term. In this form, the second term gives a measure of the frequency dependence of the Green's tensor. From this expression, we now discuss the differences between the Drude and the plasma model.

For the Drude model, the resonant contribution involving $\mathrm{Re}\,\mathcal{H}(L,\Omega_m)$ becomes significant in the nonretarded regime. In particular, combined with the nonresonant contribution, it changes the sign of the Casimir-Polder potential already at short distances, resulting no longer in repulsion but in an *attractive interaction* as soon as $T \gtrsim T_m$, see Figs. 4.5a) and b).

In contrast, the second line of Eq. (4.37) nearly vanishes in the plasma model because the magnetic Green's function $\mathcal{H}_{xx}(L,\omega)$ is approximately independent of frequency, at least in the nonretarded regime, see Table 4.1. We thus get a situation where the zeroth Matsubara term is nearly removed from the Casimir-Polder potential. The resonant term still gives the leading order contribution, once the expansion of the occupation number is pushed to the next order, i.e. $\bar{n}(\Omega_m) \approx k_BT/\hbar\Omega_m - 1/2$. We then get

$$\mathcal{F}^{\rm pl}_{\rm an}(L,g,T) \approx -|\mu_x|^2\mathrm{Re}\,\mathcal{H}_{xx}(L,\Omega_m) \approx \frac{\mu_0|\mu_x|^2}{32\pi L^3}\ , \tag{4.38}$$

where the last expression applies in the nonretarded regime. As a striking result, again a high-temperature limit recovers the $T = 0$ case [cf. Eq. (4.27), Fig. 4.6]. At larger distances (retarded regime), the difference between the Green's functions in the second line of Eq. (4.37) is nonzero and becomes the leading term:

$$\mathcal{F}_{\rm an}^{\rm pl}(L,g,T) \approx \frac{k_B T}{\hbar\Omega_m}\frac{\mu_0\pi|\mu_x|^2}{\lambda_m^2\, L} \times \left[\cos\left(\frac{4\pi L}{\lambda_m}\right) - \frac{\lambda_m}{4\pi L}\sin\left(\frac{4\pi L}{\lambda_m}\right)\right] . \qquad (4.39)$$

Note that this has a longer range than the $1/L^3$ power law (4.38). The oscillations set in outside the range given in Fig. 4.6. This effect is well known from the electric dipole interaction of excited atoms [Hinds and Sandoghdar, 1991] and consistent with the classical interpretation of the resonant term (frequency shift of an antenna).

4.4.2 Trapped rubidium atom

Rubidium is the element most commonly used in atom-chip experiments, which makes it interesting to assess the observability and some details of the magnetic Casimir-Polder potential in this case. This requires a consideration of the level structure beyond the approximation of a two-level atom. Also it has become clear from the effects discussed in Ch. 3 and Sec. 4.1.3 that only certain levels are trappable. Therefore, the expression for the atom-surface potential involves in general transitions $|a\rangle \leftrightarrow |b\rangle$ to both higher and lower-lying energy levels. Eq. (4.6) yields the following form of the free energy

$$\begin{aligned}\mathcal{F}(L,a,T) \approx &- k_B T \sum_{n\geq 1,j} \beta_{jj}^a(\mathrm{i}\xi_n)\mathcal{H}_{jj}(L,\mathrm{i}\xi_n) \\ &+ k_B T \sum_{b,j} \frac{|\mu_j^{ab}|^2}{\hbar\omega_{ba}} \left\{\mathrm{Re}\left[\mathcal{H}_{jj}(L,\omega_{ba})\right] - \mathcal{H}_{jj}(L,0)\right\} , \end{aligned} \qquad (4.40)$$

where we assume again that $k_B T \gg \hbar|\omega_{ba}|$ which is valid in many experiments. The sign of the interaction depends on the oscillator strengths of virtual transitions to lower and higher energy levels (Fig. 4.7). From Eq. (4.3), a virtual level $E_b > E_a$ gives a positive contribution to the polarizability and a positive prefactor for the second line in Eq. (4.40), these terms being negative for levels $E_b < E_a$. We can interpret this sign change from the difference between stimulated emission into the thermal radiation field (for the excited atom) and photon absorption (for the ground state). Generally, these contributions do not cancel each other because the matrix elements $|\mu_j^{ab}|^2$ are not the same.

In the case of ^{87}Rb, the hyperfine state $|a\rangle = |F = 1, m_F = -1\rangle$ of the $5s$ ground-state configuration (Fig. 4.7) is magnetically trappable. This atom has vanishing orbital momentum $L = 0$, nuclear spin $I = 3/2$, and a single valence electron so that $J = S = 1/2$. The splitting between the hyperfine levels $F = 1$ (lower) and $F = 2$ is $\Omega_{\rm hf}/2\pi \approx 6.8\,\mathrm{GHz}$, to which the Zeeman splitting in the magnetic trap must be added with the correct Landé factor. We use the same Larmor frequency as before for the two-level atom; because of $\Omega_m/\Omega_{\rm hf} \approx 0.07$, we are still in the weak-field regime. Assuming

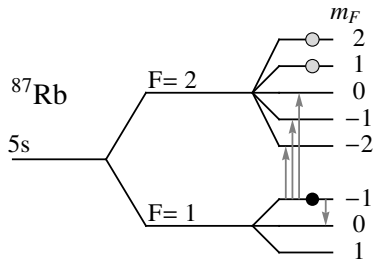

Figure 4.7: Energy scheme for $^{87}\mathrm{Rb}$ in the linear Zeeman regime (weak magnetic field outside the Breit-Wigner regime). The energy difference between hyperfine levels $F = 1$ and $F = 2$ is $\Omega_{\mathrm{hf}}/2\pi \approx 6.8\,\mathrm{GHz} \approx (k_B/2\pi\hbar)\,0.3\,\mathrm{K}$. Dots indicate magnetically trappable states. The arrows denote the transitions to higher and lower energy levels that contribute to the polarizability of an atom prepared in state $|F = 1, m_F = -1\rangle$ (black dot), considered here.

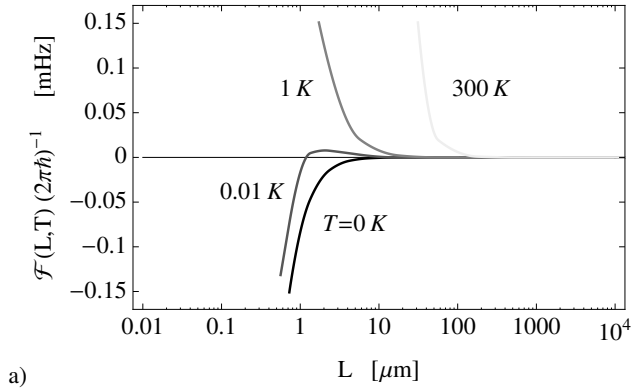

a)

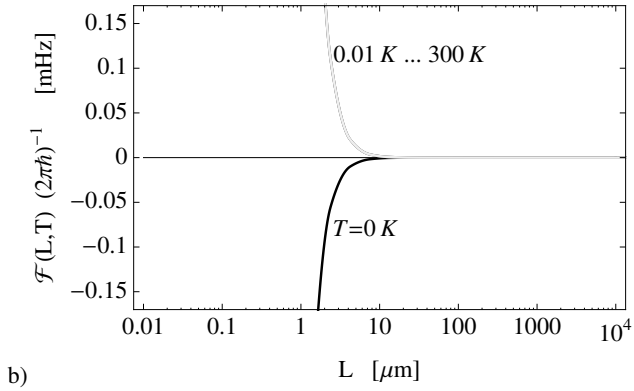

b)

Figure 4.8: a) Magnetic Casimir-Polder free energy near a Drude metal for a $^{87}\mathrm{Rb}$ atom in a given hyperfine state $|F = 1, m_F = -1\rangle$. Parameters ω_{p}, γ as in Fig. 4.1. The Larmor frequency (for virtual transitions between neighboring Zeeman levels) has the same value $\Omega_m/2\pi = (k_B/2\pi\hbar)\,23\,\mathrm{mK}$ as before, and the hyperfine splitting is $\Omega_{\mathrm{hf}}/2\pi \approx 6.8\,\mathrm{GHz} \approx (k_B/2\pi\hbar)\,0.3\,\mathrm{K}$.

b) The same for the plasma model. The numerical calculations for extremely low temperatures $0 < T \ll T_m$, where the potential changes sign, could not be performed with sufficient precision.

a quantization axis perpendicular to the surface, see Sec. 4.1.3, we get an anisotropic polarizability. The necessary matrix elements are calculated in Appendix A.4.

Numerical results for the Casimir-Polder interaction according to Eqs. (4.3) and (4.6), are shown in Figs. 4.8a) and b) for the Drude and plasma models, respectively. Near a normally conducting surface described by the Drude model, the interaction for $T = 0$ is attractive at all distances. We associate the sign reversal (compared to the absolute ground state considered so far) to the coupling to the lower-lying Zeeman levels. At high temperatures, the interaction becomes dominated by the resonant contribution that grows linearly with T and is repulsive. Again, we find the opposite sign as for the ground-state atom in Fig. 4.5. Thus, the sum of both contributions leads to a maximum of the free energy at a nonzero, T-dependent distance.

In the plasma model, the potential crosses over globally (for all distances) from attractive to repulsive. For all practical temperatures, $T > T_m$, and the interaction will be repulsive as shown in Fig. 4.8a). The results illustrate that the magnetic dipole interaction of an excited atom will be repulsive in all practical realizations.

To summarize, the strong dependence of the thermal correction on dissipation in the surface occurs in both nonequilibrium situations considered here: two-level or multilevel atoms prepared in a given energy state. The magnetic Casimir-Polder potential thus offers an opportunity to distinguish between the two models on the basis of experimental data taken at low surface temperatures and small distances. Though the magnetic potential is small (Fig. 4.8), a measurement seems within the possibilities of today's experiments [Druzhinina and DeKieviet, 2003; DeKieviet et al., 2011].

4.5 Summary and Discussion

We have considered the interaction of a magnetically polarizable particle with a metallic or superconducting surface including the effects of nonzero temperature and out-of-equilibrium situations. Previous work had considered mostly the case of electric polarizability, e.g. [Bezerra et al., 2008], or was limited to a static magnetic dipole [Bimonte et al., 2009] or zero temperature [Henkel et al., 2005; Skagerstam et al., 2009].

The magnetic atom-surface interaction is repulsive over a large range of parameters and – unlike its electric counterpart – turns out to be highly sensitive to both thermal fluctuations and dissipation. In this respect, the magnetic atom-surface interaction shows striking similarities with the Casimir interaction between metallic or magnetodielectric plates. The $T = 0$ results of Henkel et al. [2005] suggested that the magnetic interaction might be enhanced by raising the temperature, possibly creating a regime where it dominates over the electric contribution. In fact, thermal enhancement occurs only near a superconductor at distances beyond the thermal wavelength, where the material response is governed by the Meißner effect. In normal conductors, field penetration prevents such a regime – in accordance with the Bohr-van Leeuwen theorem – and the Casimir-Polder energy is exponentially suppressed in global equilibrium.

This behavior can be understood qualitatively from the competition between attractive and repulsive contributions to the force. Repulsion arises from the fluctuations of the magnetic dipole, coupled to its mirror image. This is similar to the interaction between electric currents (Lenz rule). Field fluctuations, on the other hand, produce attractive forces, due to the paramagnetic character of the atomic polarizability. Both contributions differ in their temperature dependence and depend on the state of the atom (thermalized or spin polarized). For example, attractive forces arise between a ground-state atom and a normal conductor, as the temperature scale exceeds the magnetic transition energy. Under realistic conditions, this flips the sign of the interaction in the regime accessible to experiments (Fig. 4.5).

Considering the Casimir-Polder entropy, we found that atoms probe the fluctuations in the material: for instance, at the superconducting phase transition a pronounced peak appears. In most situations, the entropy vanishes at absolute zero in agreement with Nernst's theorem. The only exception we found was the particular case of a 'perfect crystal' [Drude dissipation rate $\gamma(T) \sim T^n,\ n > 1$], already discussed thoroughly in the context of the two-plate Casimir interaction [Boström and Sernelius, 2004; Bezerra et al., 2004; Intravaia and Henkel, 2008; Henkel and Intravaia, 2010]. Here, the entropy takes a (positive) nonzero value at zero temperature and can be understood as the participation of the atom in the disorder entropy of currents frozen below the surface [Intravaia and Henkel, 2009; Intravaia et al., 2010]. Indeed, the magnetic dipole moment mimics the current-response of a second plate, except for the sign (paramagnetic rather then diamagnetic response).

In the analogous case of an electric dipole, the temperature dependence of the Casimir-Polder interaction becomes important only deep in the retarded regime ($\lambda \ll \Lambda_T$). This is due to the larger value of the (electronic) transition frequency so that for realistic temperatures, there is no difference between the ground-state and the thermalized polarizability. This was assumed by Bezerra et al. [2008], where it was also stated that all good conductors behave very similarly. In fact, the electric dipole coupling is dominated by p-polarized modes which cannot penetrate into the bulk due to screening by surface charges. This observation agrees with the results by Ellingsen et al. [2010, 2011] for the contribution of vibronic transitions to the interaction of small molecules with a metal surface. The frequencies involved are small enough that thermal excitation leads to a similar temperature independent regime, but the thermal decoupling does not occur for an electric dipole.

We have shown here that the Casimir-Polder interaction between a metal and a fluctuating magnetic dipole resembles in many respects the Casimir interaction between two metallic plates: In both scenarios, the thermal dependence is much more pronounced for a normally conducting surface compared to a description without ohmic losses, e.g. the plasma model. The role of the DC conductivity in the two-plate scenario is still an open question at nonzero temperature [Milton, 2009; Klimchitskaya et al., 2009; Decca et al., 2011]. The atom-surface interaction may thus provide an alternative way to investigate the temperature dependence of the Casimir effect, e.g. in atom-chip experiments.

The main challenge is the small value of the interaction energy as compared to the electric one. Future measurements of the magnetic Casimir-Polder interaction may involve high precision spectroscopy on the shift in hyperfine or Zeeman levels [Bloch and Ducloy, 2005]. In order to separate effects of the magnetic and the electric dipole coupling it will be important to find control parameters that affect exclusively the magnetic contribution. This may include the variation in external fields, isotope shifts, and states like Rydberg atoms with a large orbital momentum. For these systems it could also be interesting to compare the magnetic dipole interaction to the higher electric multipole contributions. These have been found to dominate for certain Rydberg states [Crosse et al., 2010].

Chapter 5

Dynamic Dressing of Atoms Near a Surface

So far, this work has considered the stationary interaction between a polarizable particle and a surface in the framework of molecular QED. In the present chapter we will go beyond the stationary scenario and discuss the dynamics of the atomic self-dressing near a surface using time-dependent perturbation theory. Already in the calculation of self-energies, the physical atom was identified[1] with a *dressed atomic state* that differs from the *bare atom* (eigenstate of the noninteracting theory) because it is surrounded by a *cloud of virtual photons*. Often, the difference between bare and dressed quantities leads to renormalization schemes, as in the Lamb shift of Sec. 2.1.5. For a thorough presentation of the dressing approach see [Compagno et al., 1995a,b].

The fundamental quantity we will consider is the time-dependent atom-surface potential. It was argued in Sections 2.1.5 and 2.3 that such potentials can be interpreted as a surface-induced energy shift of the atomic levels, generalizing the Lamb shift in free space [Bethe, 1947; Feynman, 1961]. In fact, we will see how some of our previous results can be recovered in the limit of long times. This is the equilibrium case, where the Feynman description of Chapter 2 holds.

Time-dependent approaches are well known in quantum optics [Mandel and Wolf, 1995]. They have been used to describe, for instance, interatomic interactions [Power and Thirunamachandran, 1983; Passante and Persico, 2003] or the relaxation of initially excited particles near a surface, e.g. [Knöll et al., 2001; Buhmann et al., 2008; Ellingsen et al., 2009c]. Previous work on dynamic self-dressing near a surface by Shresta et al. [2003]; Vasile and Passante [2008] considered an ideally reflecting surface and initially bare atoms, i.e. a sudden onset of the coupling. A more realistic scenario is known as *partial dressing* [Compagno et al., 1995a]. Here, the atom is initially dressed, i.e in the interacting ground state. After an abrupt (nonadiabatic) change of the interaction Hamiltonian, the system state is no longer stationary but evolves towards a new stationary (dressed) state. Messina et al. [2010] considered such partial atomic dressing near an ideally reflecting surface after a rapid shift in the atomic transition frequency induced by an external electric field (Stark shift). Fearn et al. [1995] investigated the sudden displace-

[1] The mapping between elements of two distinct Hilbert spaces is actually quite remarkable. Note that the interaction picture can only be defined in nonrelativistic quantum mechanics. In a relativistic quantum field theory its mere existence is questionable, according to Haag's theorem [Haag, 1955; Earman and Fraser, 2006].

ment of the atom relative to the surface with respect to causality constraints on virtual photons and the role of dressed atoms in photodetection theory.

The relaxation towards the stationary state takes place on the short time scale connected with the atomic transition frequencies. Also, the time of light propagation between the surface and the atom must be relevant, as it puts causality constraints on the information exchange. From the stationary atom-surface interaction it is known that surface excitations, such as plasmon polaritons on a metal surface, play an important role [Wylie and Sipe, 1984; Henkel et al., 2002; Failache et al., 2002; Gorza and Ducloy, 2006; Stehle et al., 2011]. They also have a strong impact on the transient atomic dynamics. In principle, atoms can therefore probe surface physics in the time-domain, such as the damping of surface modes. For example, a time-dependent dressing potential following a perturbation of the system could result in a center-of-mass motion of trapped atoms, i.e. the excitation of the dipole mode. But not only can the surface influence the atoms, but also the other way round. From this point of view, it would be very interesting to see how atom-surface interactions can modify the electronic density of states in a thin metal film, cf. [Judd et al., 2011].

In this chapter we generalize previous work on dynamic atomic self-dressing from ideally reflecting surfaces to rather arbitrary materials, using the matter-assisted field method elaborated by Welsch and coworkers, e.g. [Buhmann and Welsch, 2007; Scheel and Buhmann, 2008]. It turns out that all necessary information for the dressing calculation is encoded in the retarded response functions encountered earlier, in Chapter 2. We then consider the dynamic self-dressing of a bare atom near a plane surface as well as the partial dressing dynamics after a nonadiabatic transition in the system, which might affect either properties of the atom (transition frequencies, dipole moments, orientation), material properties of the surface (reflectivity), or the system geometry (shape or position of the surface).

All these systems are closely related to setups in which time-dependent boundary conditions lead to the creation of real photons due to the so-called *dynamic Casimir effect* [Yablonovitch, 1989; Schwinger, 1992]. This effect, originally predicted in cavity QED setups, has very recently been observed by Wilson et al. [2011] in an experiment based on circuit QED. Here, oscillating circuits take the role of cavities, while superconducting flux qubits replace atoms and can be described by a Jaynes-Cummings Hamiltonian [Blais et al., 2004], providing a precise analogy to the quantum systems typically studied in cavity QED. The resonance frequencies of the circuits lie in the microwave range, much lower than optical frequencies. This makes it possible to change the boundary condition on the timescale of the cavity resonance frequency, necessary for the creation of Casimir photons.

A sufficiently fast change in the boundary conditions is in fact the main obstacle in cavity QED experiments on the dynamic Casimir effect and partial dressing. Recently, interest has shifted from 'physically oscillating' mirrors (moving nuclei) towards setups in which the optical properties can be controlled (moving electrons). For a review of different experimental proposals see Dodonov and Dodonov [2006]; Dodonov [2010]. One

of them involves the injection of additional free carriers in a semiconducting surface illuminated by short laser pulses, cf. also [Chen et al., 2007]. Similarly, the superconducting phase transition may be employed to realize switchable mirrors.

5.1 Dynamic Dressing of an Initially Bare Atom

5.1.1 Spin-algebra analogy and operator evolution

We start from the multipolar coupling scheme introduced in Chapter 2. The atom is described by a two-level system. For the present calculation it is convenient to use the algebra of a set of pseudospin operators

$$S_z = \frac{1}{2}\left(\psi^{e\dagger}\psi^e + \psi^{g\dagger}\psi^g\right) , \quad S_+ = \psi^{e\dagger}\psi^g , \quad S_- = \psi^{g\dagger}\psi^e , \tag{5.1}$$

and to denote $|g\rangle = |\downarrow\rangle$, $|e\rangle = |\uparrow\rangle$ and the single Bohr frequency $\omega_{eg} = \Omega$. The dipole operator is then

$$\hat{\boldsymbol{d}} = \boldsymbol{d}(S_+ + S_-) , \tag{5.2}$$

where the vector $\boldsymbol{d}$ contains the transition matrix elements (assumed real) and takes the role of a coupling constant. The Hamiltonian of a polarizable particle interacting with the *matter-assisted* electromagnetic field in the dipole coupling approximation [Eqs. 2.1, 2.2] is now written

$$H = H_F + H_A + H_{AF} = \int_0^\infty d\omega\, \hbar\omega \boldsymbol{f}^\dagger(\omega)\boldsymbol{f}(\omega) + \hbar\Omega S_z - \hat{\boldsymbol{d}}\cdot\boldsymbol{E} . \tag{5.3}$$

In the presence of a body made of arbitrary dispersive and dissipative material, the excitations of the electromagnetic field cannot be separated from the excitations of the matter. The matter-assisted field approach [Safari et al., 2006; Buhmann and Welsch, 2007; Scheel and Buhmann, 2008] takes this into account in terms of generalized bosonic operators $\boldsymbol{f}$, $\boldsymbol{f}^\dagger$. For simplicity, the surface is described by a purely dielectric, nonmagnetic response[2] $\mu(\omega) = 1$. The generalized field is then expressed through the electric Green's tensor (see Appendices B.1 and B.2)

$$E_m(\boldsymbol{r},t) = \int_0^\infty d\omega \int d^3\boldsymbol{r}' \sqrt{\frac{\hbar}{\pi}\varepsilon_0\, \mathrm{Im}\,\varepsilon(\boldsymbol{r}',\omega)}\left[\mathrm{i}\mathcal{G}_{mn}(\boldsymbol{r},\boldsymbol{r}',\omega) f_n(\boldsymbol{r}',t;\omega) + h.c.\right] . \tag{5.4}$$

As before, Einstein sums over spatial indices are always implied. This expression generalizes a mode decomposition, necessary for the time-dependent perturbation theory which will now employ.

[2] This approximation neglects possible E-B-cross-correlations. The generalization to arbitrary magnetodielectrics is straightforward, e.g. [Safari et al., 2006], but leads to a more involved notation.

As in the preceding works by Vasile and Passante [2008]; Messina et al. [2010], the equation of motion for a general atomic or field operator A is calculated from the Heisenberg equation. This leads to series expansion $A(t) = \sum_n A^{(n)}(t)$, where n indicates the power of the coupling constant. Up to the first order in the coupling, this gives the pseudospin operator

$$S_+^{(0)}(t) = S_+^{(0)}(0)e^{\mathrm{i}\Omega t}\,, \qquad S_+^{(1)}(t) = \frac{2\mathrm{i}}{\hbar}e^{\mathrm{i}\Omega t}\int_0^t dt' S_z^{(0)}(0)\boldsymbol{d}\cdot\boldsymbol{E}^{(0)}(t')e^{-\mathrm{i}\Omega t'}\,. \quad (5.5)$$

The field operator, too, is needed to first order

$$\boldsymbol{f}^{\dagger(0)}(\boldsymbol{r},t;\omega) = \boldsymbol{f}^{\dagger}(\boldsymbol{r},0;\omega)e^{\mathrm{i}\omega t} \quad (5.6)$$

$$f_n^{\dagger(1)}(\boldsymbol{r},t;\omega) = e^{\mathrm{i}\omega t}\sqrt{\frac{\varepsilon_0}{\hbar\pi}\,\mathrm{Im}\,\varepsilon(\omega)}d_m\mathcal{G}_{mn}(\boldsymbol{r},\boldsymbol{r}_A,\omega)\times \quad (5.7)$$
$$\times\left[S_+^{(0)}(0)F(\Omega-\omega,t)+S_-^{(0)}(0)F(-\Omega-\omega,t)\right]\,.$$

We do not impose the rotating wave approximation (RWA) so that Eq. (5.7) contains both resonant (first term) and antiresonant (second term) contributions. The time-dependence is abbreviated by

$$F(\omega,t) = \int_0^t dt' e^{\mathrm{i}\omega t'} = \frac{e^{\mathrm{i}\omega t}-1}{\mathrm{i}\omega}\,. \quad (5.8)$$

5.1.2 Time-dependent atom-surface potential

For simplicity, we restrict the analysis to a ground-state atom and to zero temperature. The time-dependent Casimir-Polder potential is obtained from the energy shift $U(r_A,t) = \frac{1}{2}\langle H_{AF}(t)\rangle$. Analysis is restricted to leading order in the coupling and mean values are taken with respect to the global ground state $|\mathrm{vac},\downarrow\rangle$, so that

$$U^{(LO)}(r_A,t) \approx -\frac{1}{2}\langle\hat{\boldsymbol{d}}^{(0)}\cdot\boldsymbol{E}^{(0)}\rangle - \frac{1}{2}\langle\hat{\boldsymbol{d}}^{(0)}\cdot\boldsymbol{E}^{(1)}\rangle - \frac{1}{2}\langle\hat{\boldsymbol{d}}^{(1)}\cdot\boldsymbol{E}^{(0)}\rangle\,. \quad (5.9)$$

It is clear that the first term is off-diagonal in the spin basis and does not contribute. The remaining terms can be evaluated using the following 'magic formula'

$$\int d^3\boldsymbol{r}'\varepsilon_0\,\mathrm{Im}\,[\varepsilon(\omega,\boldsymbol{r}')]\mathcal{G}_{ik}(\boldsymbol{r}_1,\boldsymbol{r}',\omega)\mathcal{G}_{jk}(\boldsymbol{r}',\boldsymbol{r}_2,\omega) = \mathrm{Im}\,\mathcal{G}_{ij}(\boldsymbol{r}_1,\boldsymbol{r}_2,\omega)\,, \quad (5.10)$$

which is a property of the Green's tensors already hidden in the electrodynamics [Eckhardt, 1984; Dung et al., 1998; Knöll et al., 2001]. Besides, from the reciprocity principle we have $\mathcal{G}_{ij}(\boldsymbol{r},\boldsymbol{r}',\omega) = \mathcal{G}_{ji}(\boldsymbol{r}',\boldsymbol{r},\omega)$ and for real-valued fields $\mathcal{G}_{ij}(\boldsymbol{r},\boldsymbol{r}',-\omega) =$

$\mathcal{G}^*_{ij}(\boldsymbol{r},\boldsymbol{r}',\omega)$ (if $\omega \in \mathbb{R}$). From there,

$$-\frac{1}{2}\langle \hat{d}_m^{(0)} E_m^{(1)}(\boldsymbol{r}_A,t)\rangle = -\mathrm{i}d_m d_p \int_0^\infty \frac{d\omega}{2\pi}\,\mathrm{Im}\,\mathcal{G}_{mp}(\boldsymbol{r}_A,\boldsymbol{r}_A,\omega)\times \times\left[e^{-\mathrm{i}(\Omega+\omega)t}F(\Omega+\omega,t) - e^{-\mathrm{i}(\Omega-\omega)t}F(\Omega-\omega,t)\right] \tag{5.11}$$

$$-\frac{1}{2}\langle \hat{d}_m^{(1)} E_m^{(0)}(\boldsymbol{r}_A,t)\rangle = \mathrm{i}d_m d_p \int_0^\infty \frac{d\omega}{2\pi}\,\mathrm{Im}\,\mathcal{G}_{mp}(\boldsymbol{r}_A,\boldsymbol{r}_A,\omega)\times \times\left[e^{\mathrm{i}(\Omega+\omega)t}F(-\Omega-\omega,t) - e^{-\mathrm{i}(\Omega-\omega)t}F(\Omega-\omega,t)\right]\,. \tag{5.12}$$

Summing up Eqs. (5.11) and (5.12), the both resonant terms with a pole in the denominator cancel out and the energy shift to second order in $\boldsymbol{d}$ becomes

$$U(\boldsymbol{r}_A,t) = -d_m d_n \int_0^\infty \frac{d\omega}{2\pi}\,\mathrm{Im}\,\mathcal{G}_{mn}(\boldsymbol{r}_A,\boldsymbol{r}_A,\omega)\frac{2-2\cos\left[(\Omega+\omega)t\right]}{\Omega+\omega}. \tag{5.13}$$

This is the equivalent of Eq. (13) in [Vasile and Passante, 2008] and is manifestly real. It is convenient to consider the two terms of Eq. (5.13) individually, which separates the static contribution from the time-dependent term:

$$U(\boldsymbol{r}_A,t) = U_{\mathrm{stat}}(\boldsymbol{r}_A) + \Delta U_{\mathrm{dyn}}(\boldsymbol{r}_A,t)\,. \tag{5.14}$$

The system is unperturbed at $t = 0$ and must be continuous so that $U(\boldsymbol{r}_A,0) = 0$. The correction ΔU_{dyn} describes the transient dressing dynamics and averages to zero in the stationary limit $t \to \infty$, due to the oscillatory integrand. In this limit, we recover the stationary Casimir-Polder potential U_{stat} (derived already in Sec. 4.1) in the form given by Wylie and Sipe [1985, Eq. (2.14)].

Note that expression (5.13) does not depend any more explicitly on $\mathrm{Im}\,\varepsilon(\boldsymbol{r},\omega)$ (sources inside the material, cf. Eq. 5.4), but only on the total Green's tensor above the surface. This allows for the calculation of the time-dependent energy shift of an atom in a rather general setting and remains valid even in cases where the microscopic details of the surface response are completely ignored, as in the following case of a perfect reflector.

In what follows, the atom is placed near a planar surface described by a dielectric or metallic halfspace. As discussed earlier in this work, the free-space contribution to the electromagnetic Green's tensor can be separated from a surface term. Again, we focus on the reflected fields, which can be expressed through s- and p-polarized reflection amplitudes (see Sec. 2.3 and App. B).

5.1.3 The perfect reflector limit

Atomic dressing near a perfectly reflecting wall has been investigated previously by Vasile and Passante [2008]; Messina et al. [2010] and provides a convenient cross-check. The two-level atom is now assumed to be isotropically polarizable, so that $d_m d_n =$

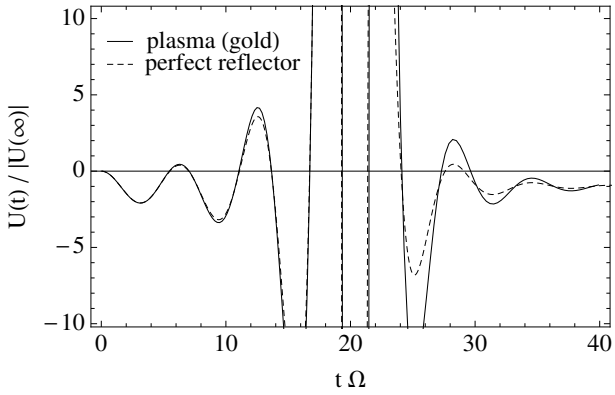

Figure 5.1: Time dependent energy shift for a perfect reflector and a dissipationless gold surface (plasma model) without the surface mode contribution. Parameters are $\omega_\mathrm{p} = 8.9\,\mathrm{eV}/\hbar = 1.4 \times 10^{16}\,\mathrm{rad\,s^{-1}}$, $\gamma \to 0$. The atomic transition corresponds to the $780\,\mathrm{nm}$ line of rubidium 85 between states $D_2(5^2S_{1/2} \to 5^2P_{3/2})$, and the atom-surface separation is $z = 10c/\Omega = 1.2\,\mu\mathrm{m}$. At the signal-transit time $\Omega t = 20$, the reflected light cone reaches the atom.

$\frac{1}{3}|d|^2\delta_{mn}$. (To describe more than two energy levels, excited states must be summed over). In the limit of a perfect reflector, the reflection coefficients are $r_\mathrm{p} = -r_\mathrm{s} = 1$ and the Green's tensor may be expressed through a spatial differential operator $\mathcal{D}$:

$$d_m d_n \mathcal{G}_{mn}(\boldsymbol{r},\boldsymbol{r},\omega) \mapsto \frac{|d|^2}{3}\mathcal{D}e^{2\mathrm{i}\frac{\omega}{c}rx}\,, \quad \mathcal{D} = \lim_{x\to 1}\frac{1}{4\pi\varepsilon_0 r^3}\left(2 - 2\frac{\partial}{\partial x} + \frac{\partial^2}{\partial x^2}\right). \tag{5.15}$$

The operator can be taken out of the integral and Eq. (5.13) becomes

$$U(z,t) \;=\; \frac{|d|^2}{3}\mathcal{D}\int_0^\infty \frac{d\omega}{2\pi}\sin(2xz\omega/c)\frac{2-2\cos\left[(\Omega+\omega)t\right]}{\Omega+\omega}\,. \tag{5.16}$$

This corresponds to Eq. (13) of Vasile and Passante [2008]. In this work, an explicit expression for the force was obtained in terms of cosine and sine integral functions.

A numerical evaluation of the time-dependent energy shift of an atom near a perfect reflector is shown in Fig. 5.1 together with the results obtained in the following Sec. 5.2 for a dissipationless metal (plasma model). Clearly, the dependence on the material properties is relatively weak. This is because in the retarded regime ($z \gg c/\Omega$) chosen here, the electromagnetic field is mediated by propagating photonic modes of low frequency for which the perfect reflector provides a reasonable boundary condition for electric fields even for a real material. The coincidence can also be understood by comparing the previous Green's tensor with the far-field asymptotes of Table 4.1.

The main features of Fig. 5.1 have already been discussed by Shresta et al. [2003]; Vasile and Passante [2008]: Initially, at $t < 2|z|/c$, the bare atom evolves freely in the field of the plate. Strong effects set in when the atom begins to 'see' its own mirror image, precisely at the signal-transit time $t = 2|z|/c$ when the reflected light cone reaches the

atom. The authors remarked that there is in fact a nontrivial divergence in the radiation reaction at this moment, which can be traced back to the dipole approximation [Milonni, 1976] and to assuming the atom initially bare [Passante and Vinci, 1996]. At later times, both the field and the atom will adapt to the new configuration until they reach a stationary state after a couple of signal-transit times.

5.2 Material Properties and Surface Mode Excitations

5.2.1 Imaginary frequency representation

We will now consider the dressing problem for a general surface. Already in the static Casimir-Polder interaction in Chapter 4, analytic continuations to imaginary frequencies have proved to be useful. Expressing the static Casimir-Polder potential as an integral along the positive imaginary axis, we recover an expression reported by Wylie and Sipe [1985],

$$U_{\rm stat}(\boldsymbol{r}_A) \;=\; -d_m d_n \int_0^\infty \frac{d\xi}{2\pi} \mathcal{G}_{mn}(\boldsymbol{r}_A,\boldsymbol{r}_A,\mathrm{i}\xi) \frac{2\Omega}{\Omega^2+\xi^2}\,, \tag{5.17}$$

which is obviously the counterpart of Eq. (4.24) for an electric dipole.

The analytic properties of the dynamic part are more subtle. Expressing the cosine in Eq. (5.13) as a real part, we find

$$\begin{aligned}
\Delta U_{\rm dyn}(\boldsymbol{r}_A,t) \;&=\; d_m d_n \,\mathrm{Re}\, \frac{e^{\mathrm{i}\Omega t}}{2\mathrm{i}} \int_0^\infty \frac{d\omega}{2\pi} \left[\mathcal{G}_{mn}(\boldsymbol{r}_A,\boldsymbol{r}_A,\omega) - \mathcal{G}_{mn}(\boldsymbol{r}_A,\boldsymbol{r}_A,-\omega)\right] \frac{e^{\mathrm{i}\omega t}}{\omega+\Omega} \\
&=\quad d_m d_n \,\mathrm{Re}\, \frac{e^{\mathrm{i}\Omega t}}{2\mathrm{i}} \int_0^\infty \frac{d\omega}{2\pi} \mathcal{G}_{mn}(\boldsymbol{r}_A,\boldsymbol{r}_A,\omega) \frac{e^{\mathrm{i}\omega t}}{\omega+\Omega} \\
&\quad -d_m d_n \,\mathrm{Re}\, \frac{e^{\mathrm{i}\Omega t}}{2\mathrm{i}} \int_{-\infty}^0 \frac{d\omega}{2\pi} \mathcal{G}_{mn}(\boldsymbol{r}_A,\boldsymbol{r}_A,\omega) \frac{e^{-\mathrm{i}\omega t}}{-\omega+\Omega}\,.
\end{aligned} \tag{5.18}$$

While the first integral converges in the upper complex half-plane and can be expressed through an integral along the positive imaginary axis, two cases must be considered for the second one, connected with times before and after the signal transit time. The asymptotic behavior of the Green's tensor at large values of $|\omega|$ is of the form $\mathcal{G}(\boldsymbol{r}_A,\boldsymbol{r}_A,\omega)e^{-\mathrm{i}\omega t} = e^{\mathrm{i}\omega(2z/c-t)}g(z,\omega)$ and converges in the upper complex plane if $2z > ct$ (before the signal transit time) but in the lower complex plane if $2z < ct$ (afterwards). The integrals can therefore be evaluated using the contours given in Fig. 5.2. For ground-state atoms, the poles in Ω are never inside of contour so that there are no

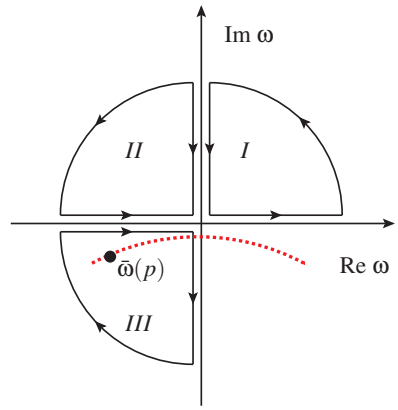

Figure 5.2: Integration contours for the analytic continuation. In the range $\mathrm{Re}\,\omega > 0$ convergence is always guaranteed in the upper half-space (I). Outside the reflected light cone ($ct < 2|z|$), the integration contour $\mathrm{Re}\,\omega < 0$ is closed in the upper complex plane (II), inside the light cone, contour (III) applies. The dotted line symbolizes the surface-plasmon resonances at $\bar{\omega}(p)$.

contributions from atomic resonances. The time-dependent potential is

$$\begin{aligned}\Delta U_{\mathrm{dyn}}(\boldsymbol{r}_A,t) \;=\; -d_m d_n\,\mathrm{Re}\,\frac{e^{\mathrm{i}\Omega t}}{2}\Bigg[&\int_0^\infty \frac{d\xi}{2\pi}\mathcal{G}_{mn}(\boldsymbol{r}_A,\boldsymbol{r}_A,\mathrm{i}\xi)\frac{e^{-\xi t}}{\mathrm{i}\xi+\Omega} \\ +\theta(2z-ct)\quad&\int_0^\infty \frac{d\xi}{2\pi}\mathcal{G}_{mn}(\boldsymbol{r}_A,\boldsymbol{r}_A,\mathrm{i}\xi)\frac{e^{\xi t}}{-\mathrm{i}\xi+\Omega} \\ +\theta(ct-2z)\quad&\int_{-\infty}^0 \frac{d\xi}{2\pi}\mathcal{G}_{mn}(\boldsymbol{r}_A,\boldsymbol{r}_A,\mathrm{i}\xi)\frac{e^{\xi t}}{-\mathrm{i}\xi+\Omega} \\ +\theta(ct-2z)\quad&i\oint_{III}\frac{d\omega}{2\pi}\mathcal{G}_{mn}(\boldsymbol{r}_A,\boldsymbol{r}_A,\omega)\frac{e^{-\mathrm{i}\omega t}}{\omega+\Omega}\Bigg]\,.\end{aligned} \tag{5.19}$$

This expression is sufficiently well-behaved to be evaluated numerically using a general Green's tensor. The last term will be denoted by ΔU_{res} and includes the transient contribution due to material excitations, i.e. poles of the Green's tensor, which will now be discussed in detail.

5.2.2 Resonant surface-plasmon contribution

In real materials, surface excitations play an important role [Flores and García-Moliner, 1979; Ford and Weber, 1984]. A simple scenario that allows for studying these effects is provided by a plane metal surface described by the plasma model, obtained by setting the dissipation rate $\gamma \to 0$ in the Drude model (3.13). As in the previous chapters, reflection coefficients given by Fresnel's equations (3.20) (see also App. B.3) are used to obtain the general form of the reflected surface Green's tensor (App. B.2).

From the analytic structure of retarded response functions, all poles of the Green's tensor (and of the reflection coefficients) must lie in the lower half of the complex frequency plane ($\mathrm{Im}\,\omega < 0$, cf. Sec. 2.1.4). From Fig. 5.2 and Eq. (5.19) it is therefore clear that material excitations can contribute only at $ct > 2z$. We now assume $\Omega \ll \omega_{\mathrm{p}}$ and focus on the surface-mode excitations. A surface described by the plasma model carries

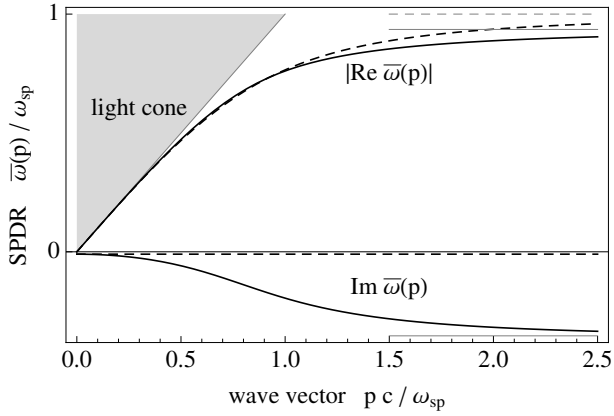

Figure 5.3: Surface-plasmon dispersion relation in the Drude model (solid lines) and the plasma limit $\gamma \to 0$ [dashed lines, cf. Eq. (5.20)]. Horizontal asymptotes give the respective limits at large values of p.

a single surface plasmon (plasmon-polariton) given by a pole of the $r_{\rm p}$-reflectivity. The relevant branch of the surface-plasmon dispersion relation (SPDR) inside the contour III of Fig. 5.2 is given by [Raether, 1988]

$$\bar{\omega}(p) = -\sqrt{\omega_{\rm sp}^2 + c^2p^2 - \sqrt{\omega_{\rm sp}^4 + c^4p^4}} - {\rm i}0^+ \,, \tag{5.20}$$

where the surface-plasmon frequency $\omega_{\rm sp} = \omega_{\rm p}/\sqrt{2}$. The surface plasmon-polariton is an evanescent wave, i.e. its dispersion relation lies below the light cone [$pc < \bar{\omega}(p)$] as is shown in Fig. 5.3 (dashed curves). Therefore, $\bar{\kappa}(p) = \sqrt{p^2 - \bar{\omega}^2(p)/c^2}$ is real (apart from the infinitesimal shift).

Using the explicit forms of the electric Green's tensor (App. B.2) as an integral over in-plane wave vectors p and the previous expression for the SPDR, it is possible to calculate separately the resonant contribution in Eq. (5.19). The integrals over wave vectors and the frequency are interchanged and the atom is assumed to be isotropically polarizable, so that

$$\begin{aligned} \Delta U_{\rm res}(z,t) &= -d_m d_n \,{\rm Re}\, \frac{{\rm i}e^{{\rm i}\Omega t}}{2} \oint_{III} \frac{d\omega}{2\pi} \mathcal{G}_{mn}(\boldsymbol{r},\boldsymbol{r},\omega) \frac{e^{-i\omega t}}{-\omega+\Omega} \qquad (5.21) \\ &= -\frac{|d|^2}{12\pi\varepsilon_0} \,{\rm Re}\, \frac{{\rm i}e^{{\rm i}\Omega t}}{2} \int_0^\infty dp \oint_{III} \frac{d\omega}{2\pi} \frac{e^{-i\omega t - 2\kappa z}}{-\omega+\Omega} \frac{p}{\kappa} \times \\ &\quad \times \left[\frac{\omega^2}{c^2} r_{\rm s}(\omega,p) + r_{\rm p}(\omega,p) \left(\frac{\omega^2}{c^2} + 2\kappa^2 \right) \right] . \qquad (5.22) \end{aligned}$$

In the absence of dissipation, the single isolated pole given by Eq. (5.20) is located inside the contour by the infinitesimal imaginary part. We calculate the residue from a series

expansion of the denominator of the $r_{\rm p}$ coefficient,

$$R_{\rm p}(\omega,p)=\frac{\varepsilon(\omega)\kappa-\kappa_m}{\frac{d}{d\omega}[\varepsilon(\omega)\kappa+\kappa_m]}\,. \tag{5.23}$$

Using the residue theorem, the contribution due to the surface plasmon, present at $t>2z/c$, is

$$\begin{aligned}\Delta U_{\rm res}(z,t) &= -\frac{|d|^2}{12\pi\varepsilon_0}\,{\rm Re}\,\frac{e^{{\rm i}\Omega t}}{2}\int_0^\infty dp\frac{e^{-{\rm i}\bar\omega(p)t-2\bar\kappa(p)z}}{-\bar\omega(p)+\Omega}\frac{p}{\bar\kappa(p)}\times\\ &\quad\times\left(2p^2-\frac{\bar\omega^2(p)}{c^2}\right)R_{\rm p}(\bar\omega(p),p)\,.\end{aligned} \tag{5.24}$$

Fig 5.4a) shows the resonant surface-plasmon contribution $\Delta U_{\rm res}$ for a plasma frequency corresponding to gold. A numerical evaluation of the total time-dependent energy shift obtained from the imaginary frequency formulation of Eqs. (5.18) and (5.19) is compared in Fig. 5.1 to the results for a perfect reflector. Note that $\Delta U_{\rm res}$ is much smaller than the total dressing potential at the distance considered, which lies in the retarded regime $z\gg c/\Omega$.

Clearly, the surface-mode contribution to the dressing potential is a transient effect and decays quickly in time, as could be expected from the discussion following Eq. (5.14). In the far field, where small values of p contribute and where the SPDR approaches the light cone, even a dissipative medium provides very little damping (cf. Fig. 5.3). The relaxation is, therefore, clearly not a dissipative effect but rather a result of the limited bandwidth of the SPDR $|\bar\omega(p)|<\omega_{\rm sp}$.

The time scale of the decay can be estimated from the exponential in Eq. (5.24), the rest of the integrand being a well-behaved function that vanishes as $p\to 0$ and is polynomial at infinity. From the distance dependent part of the integrand, only those values of p are relevant where $\bar\kappa(p)z<1$, so that $p<\hat p=(z^{-4}+\omega_{\rm p}^2/c^2z^2)^{1/4}$. If the oscillating exponential covers much more than half a period in this range of p, both the real and imaginary part of the integral will eventually be small on average. The typical timescale on which the resonant contribution decays is, therefore, given by $\hat t=\tau\pi/\bar\omega(\hat p)$, where $\tau\approx 1$. For atom-surface separations beyond the plasma wavelength, the decay time is

$$\hat t\approx\tau\pi\sqrt{\frac{z}{\omega_{\rm p}c}}\,, \tag{5.25}$$

which averages between the plasma wavelength and the signal-transit time. Fig. 5.4b) shows good agreement of this expression with the numerical solution.

In general, the conductivity of a metal is finite ($\gamma>0$, Drude model). This leads to a shift and broadening (imaginary part) of the SPDR, as depicted by the solid curves in Fig. 5.3. Besides, the system features material excitations other than the single surface plasmon. Diffusive *eddy-current modes*, corresponding to a branch cut of $r_{\rm s}$ along the

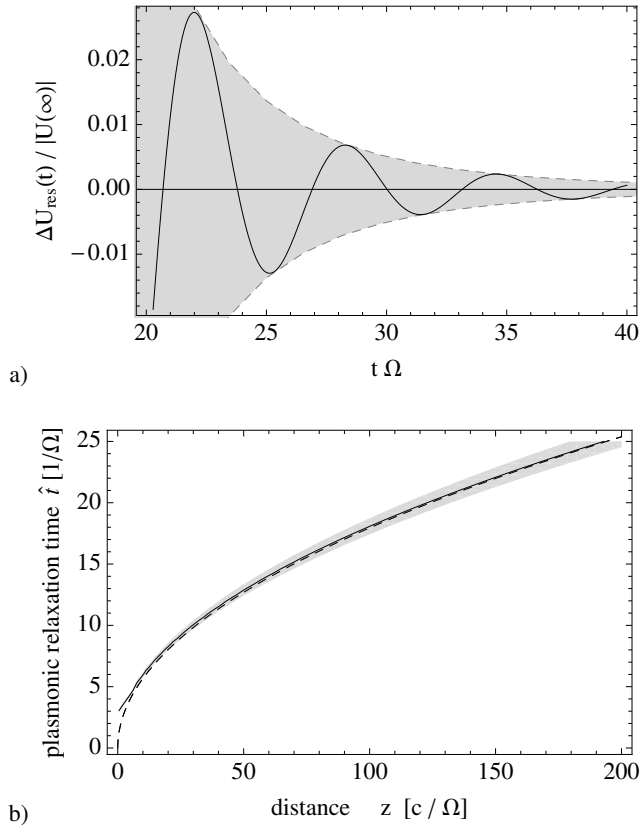

Figure 5.4: a) Resonant surface mode contribution $\Delta U_{\rm res}$ [Eq. (5.24)] to the atom-surface dressing. The atom-surface separation is $z = 10c/\Omega$. The contribution sets in only after the signal-transit time $t = 2z/c$ (signal-transit time). Dashed curves show the absolute value obtained from Eq. (5.24) without the leading exponential.
b) Surface mode relaxation time vs. distance. Parameters for a rubidium atom near a gold surface as in Fig. 5.1. Numerical solution (solid line, grey shaded area indicates 5% error margin) and asymptotic expression [dashed line, $\tau = 1.1$ in Eq. (5.25)] for a decay to half of the initial value.

negative imaginary axis, are known to play an important role in the thermal Casimir interaction [Intravaia and Henkel, 2009; Intravaia et al., 2010]. They are connected with low frequencies in the order of γ, and do not occur in the limit $\gamma \to 0$ considered here (Meißner effect, cf. Chapter 4). For completeness, one should also mention *bulk plasmon excitations*, which are connected with a branch cut of the $r_{\rm s}$-coefficient and with frequencies $\geq \omega_{\rm p}$ far from the atomic resonance, see Fig. 6.1 in the following chapter.

5.2.3 Near-field dressing

We consider now the near field, $z \ll c/\omega_{\rm p} \ll c/\omega$, where the surface-mode contribution is dominant. At frequencies connected with electric dipole transitions, this regime lies below the skin depth and reflection coefficients given in Table 3.1 can be applied for an asymptotic expansion of the electric Green's tensor. A near field asymptote of the reflected electric Green's tensor is obtained from an expansion for large in-plane wave vectors p

$$\text{Im}\, \mathcal{G}_{ij}(z,\omega) \approx \frac{1}{4\pi\varepsilon_0 z^3} \frac{\text{Im}\, \varepsilon(\omega)}{[1+\varepsilon(\omega)][1+\varepsilon^*(\omega)]} [\delta_{ij} + \hat{z}_i \hat{z}_j] \,. \tag{5.26}$$

In the near field, dissipative properties of the surface are crucial and we assume a Drude metal, allowing for a finite damping rate γ. There is no contribution from eddy currents in this distance regime and the only relevant surface excitation is the surface plasmon. At the wave vectors considered, the SPDR is flat (cf. Fig. 5.3), so that the plasmon resonances correspond to isolated poles of $\text{Im}\, \boldsymbol{\mathcal{G}}$ in all sectors of the complex frequency plane at $\pm\bar{\omega}(\infty), \pm\bar{\omega}^*(\infty)$, where

$$\bar{\omega}(\infty) = \sqrt{\omega_{\rm sp}^2 - \gamma^2} - \mathrm{i}\frac{\gamma}{2} \,. \tag{5.27}$$

In the near field, retardation is neglected and the signal-transit time coincides with $t = 0$. From the above expression, the analytical continuation of the time-dependent part of the potential can be performed in the upper half-plane (contour I of Fig. 5.2). This gives

$$\begin{aligned} \Delta U_{\rm dyn}(z) \;\; = \;\; & d_m d_n \,\text{Re}\, \mathrm{i} \int_0^\infty d\xi \,\text{Im}\, [\mathcal{G}_{mn}(i\xi, z)] \frac{e^{\mathrm{i}(\omega+\Omega)t}}{\mathrm{i}\xi + \Omega} \\ & + d_m d_n \,\text{Re}\, \left[\mathrm{i}\,\text{Im}\, [\mathcal{G}_{mn}(\bar{\omega}(\infty), z)] \frac{e^{\mathrm{i}(\bar{\omega}(\infty)+\Omega)t}}{\bar{\omega}(\infty) + \Omega} \right] \,. \end{aligned} \tag{5.28}$$

The second term corresponds to the resonant surface-plasmon contribution $U_{\rm res}(t)$. Numerical results are given in Fig. 5.5. From the structure of Eq. (5.28) it is clear that the resonant contribution is only damped by bulk dissipation with the rate $\gamma/2$. This is in strong contrast with the result in the far field, where the finite width of the SPDR provided the relaxation time scale. In the near field, the surface plasmon has basically a monochromatic spectrum [Joulain et al., 2005]. An immediate consequence is that the resonant potential oscillates with a frequency $\Omega + \bar{\omega}(\infty)$. This differs completely from the far-field result, where the potential oscillation is basically given by the atomic transition frequency [see the $e^{\mathrm{i}\Omega t}$ in Eq. (5.24)].

5.3 Partial Dressing After a Nonadiabatic Transition

5.3.1 Partially dressed states

In the absence of coupling, the ground state is given by the tensor product of the eigenstates of the free atom and field Hamiltonians, $|\text{vac}, \downarrow\rangle$. In the previous Sections 5.1 and

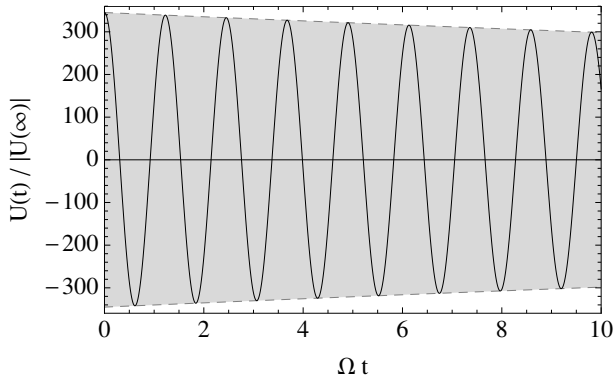

Figure 5.5: Dynamic dressing potential after the signal-transit time in the near field ($z = 0.1c/\Omega$) for an initially bare atom. The surface is described by a Drude metal with parameters $\omega_\mathrm{p} = 1.4 \times 10^{16}\,\mathrm{rad\,s^{-1}}, \gamma = 5 \times 10^{-3}\omega_\mathrm{p}$, and the atomic transition corresponds to the $780\,\mathrm{nm}$ line of rubidium. The grey envelope shows the exponential damping with a rate $\gamma/2$.

5.2, we considered the somewhat artificial situation where such a bare atom approaches the stationary configuration after the coupling is switched on instantaneously. It seems more convincing to consider the dynamics of an already fully-dressed atom, once the external conditions change nonadiabatically. This transition can act either on the atom or change the properties of the walls, resulting in a change of the Hamiltonian. The stationary state of the old configuration is then no longer an eigenstate, so that the system will relax to a new state in a process that resembles closely the previous dressing. Such a scenario has is known as *partial dressing*. Messina et al. [2010] considered partial dressing of an atom near a perfect reflector after a sudden change of the atomic transition frequency. For the related situation of a system consisting in two atoms, see [Passante and Persico, 2003].

We consider a fully-dressed system in a state $|G\rangle$. This is the stationary solution obtained in the Schrödinger picture by perturbation expansion in the basis of the uncoupled Hamiltonian at first order in the coupling constant

$$|G\rangle = |\mathrm{vac},\downarrow\rangle + |\{1\},\uparrow\rangle\,, \tag{5.29}$$

$$|\{1\},\uparrow\rangle = \sum_{|\Psi\rangle\neq|\mathrm{vac},\downarrow\rangle} \frac{\langle\Psi|H_{AF}|\mathrm{vac},\downarrow\rangle}{E_\Psi - E_0}|\Psi\rangle \tag{5.30}$$

$$= -\mathrm{i}d_m \int_0^\infty d\omega \int d^3\boldsymbol{r} \sqrt{\frac{\varepsilon_0}{\pi\hbar}\,\mathrm{Im}\,\varepsilon(\boldsymbol{r},\omega)}\frac{\mathcal{G}^*_{mn}(\boldsymbol{r}_A,\boldsymbol{r},\omega)}{\omega+\Omega} f_n^\dagger|\mathrm{vac},\uparrow\rangle\,. \tag{5.31}$$

The sum over possible elements $|\Psi\rangle = \boldsymbol{f}^\dagger(\boldsymbol{r},0;\omega)|\mathrm{vac},\uparrow\rangle$ contains a superposition of bare one-boson states. Note that $\langle G|G\rangle = 1+\mathcal{O}(d_m d_n)$, so that normalization corrections result subleading and the dressed state may be considered normalized in the following.

We now suppose the system to have relaxed to the stationary state $|G\rangle$ at $t = 0$. At this point, the external conditions change nonadiabatically and the new interaction

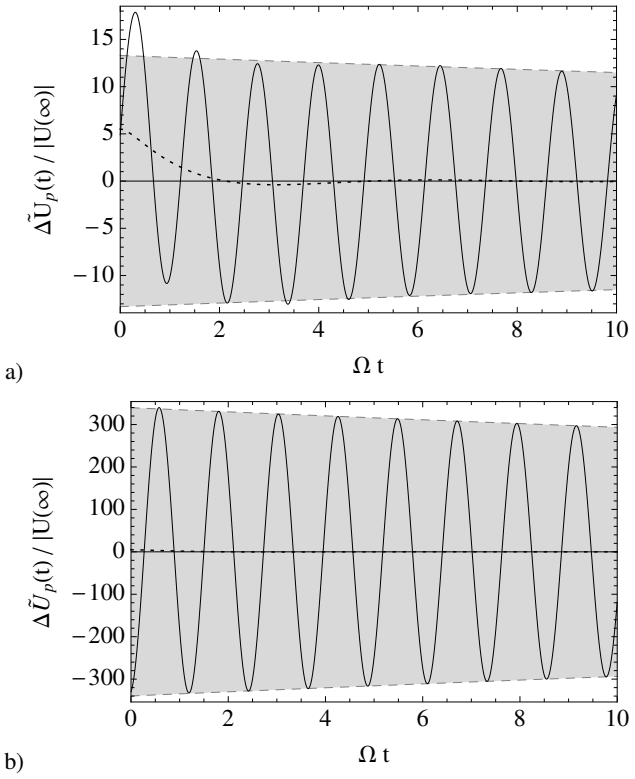

Figure 5.6: Partial dressing correction $\Delta\tilde{U}_{\rm p}(t)$ in the near field ($z = 0.1c/\Omega$). After the transition ($t > 0$), the surface is described by a Drude metal with parameters $\tilde{\omega}_{\rm p} = 1.4 \times 10^{16}\,{\rm rad\,s^{-1}}, \gamma = 5 \times 10^{-3}\omega_{\rm p}$. The atomic transition wavelength is $\lambda = 780\,{\rm nm}$.
a) Correction for a large change $\tilde{\omega}_{\rm p} = 1.2\omega_{\rm p}$, where Eq. (5.34) is dominated by the bare atom dressing-like contribution. The parameters are chosen such that the latter coincides with the curve of Fig. 5.5.
b) In the case of a small change $\tilde{\omega}_{\rm p} = \omega_{\rm p} + \gamma/4$, the two contributions compensate to a great extent. The dotted curves shows a short-lived nonresonant contribution, barely visible in Fig. 5.6b). The resonant surface-mode contribution is exponentially damped on the scale of bulk dissipation, $\gamma/2$, indicated by the grey envelopes.

Hamiltonian is $\tilde{H}_{AF}$. We assume that it has the same form as the old one, but since any system parameter may have changed, we replace $\Omega \to \tilde{\Omega}, \mathcal{G} \to \tilde{\mathcal{G}}, d \to \tilde{d}, \varepsilon \to \tilde{\varepsilon}$. The dynamic Casimir-Polder potential[3] is calculated in the Heisenberg picture

$$\tilde{U}(r_A,t) = \tfrac{1}{2}\langle G|\tilde{H}_{AF}(t)|G\rangle \tag{5.32}$$

$$= \tfrac{1}{2}\langle {\rm vac},\downarrow|\tilde{\rm H}_{\rm AF}({\rm t})|{\rm vac},\downarrow\rangle - \tfrac{1}{2}\langle\{1\},\uparrow|\tilde{\rm H}_{\rm AF}({\rm t})|\{1\},\uparrow\rangle + \tfrac{1}{2}\left(\langle {\rm vac},\downarrow|\tilde{\rm H}_{\rm AF}({\rm t})|\{1\},\uparrow\rangle + {\rm c.c.}\right). \tag{5.33}$$

[3] A change of the external conditions will also change the mean value of $H_A + H_F$ which, however, does not influence the distance-dependent Casimir-Polder potential.

Evaluation up to second order in $\boldsymbol{d}$ is again sufficient. The first term is exactly the potential (5.9), given by Eq. (5.13), where the old quantities are replaced by the new ones. The second term is a fourth-order contribution and, hence, neglected. Finally, the last term yields a correction $\Delta\tilde{U}_{\rm p}$, unique to the partial-dressing scenario. The partial dressing dynamics is hence described by the total time-dependent potential

$$\tilde{U}(\boldsymbol{r}_A,t) \;=\; U(\boldsymbol{r}_A,t)|_{\Omega\to\tilde{\Omega},\boldsymbol{\mathcal{G}}\to\tilde{\boldsymbol{\mathcal{G}}},\boldsymbol{d}\to\tilde{\boldsymbol{d}}} + \Delta\tilde{U}_{\rm p}(\boldsymbol{r}_A,t)\;, \tag{5.34}$$

where the partial dressing correction is

$$\Delta\tilde{U}_{\rm p}(\boldsymbol{r}_A,t) \;=\; -\,\mathrm{Re}\,\langle \mathrm{vac},\downarrow|\tilde{\hat{\boldsymbol{d}}}^{(0)}\cdot\tilde{\boldsymbol{E}}^{(0)}|\{1\},\uparrow\rangle \tag{5.35}$$

$$\;=\; -d_m\tilde{d}_n\,\mathrm{Re}\int_0^\infty d\omega\frac{e^{-\mathrm{i}(\omega+\tilde{\Omega})t}}{\omega+\Omega}\times \tag{5.36}$$

$$\times\int d^3\boldsymbol{r}\varepsilon_0\sqrt{\mathrm{Im}\;\varepsilon(\boldsymbol{r},\omega)\;\mathrm{Im}\;\tilde{\varepsilon}(\boldsymbol{r},\omega)}\tilde{\mathcal{G}}_{ml}(\boldsymbol{r}_A,\boldsymbol{r},\omega)\mathcal{G}^*_{nl}(\boldsymbol{r}_A,\boldsymbol{r},\omega)\;.$$

5.3.2 Relaxation to Stark-shifted levels

Messina et al. [2010] calculated the dynamic energy shift for an atom near a perfectly conducting wall, whose transition frequency is modified after the system has reached its stationary state, e.g. by the sudden onset of an external electric field (at $t=0$). The resulting Stark shift changes the atomic transition frequency, but leaves the structure of the Hilbert space unaltered. The matter-assisted field part of the system is assumed not to change at all. In this particular scenario, we have $\tilde{\Omega}\neq\Omega, \tilde{\boldsymbol{\mathcal{G}}}=\boldsymbol{\mathcal{G}}, \tilde{\boldsymbol{d}}=\boldsymbol{d}$, so that Eq. (5.36) can be evaluated using Eq. (5.10). The total time-dependent potential is then

$$\begin{aligned}\tilde{U}(\boldsymbol{r}_A,t) \;=\; &-d_md_n\int_0^\infty\frac{d\omega}{2\pi}\,\mathrm{Im}\,[\mathcal{G}_{mn}(\boldsymbol{r}_A,\boldsymbol{r}_A,\omega)]\frac{2-2\cos[(\tilde{\Omega}+\omega)t]}{\tilde{\Omega}+\omega}\\ &-d_md_n\int_0^\infty\frac{d\omega}{2\pi}\,\mathrm{Im}\,[\mathcal{G}_{mn}(\boldsymbol{r}_A,\boldsymbol{r}_A,\omega)]\frac{2\cos[(\tilde{\Omega}+\omega)t]}{\Omega+\omega}\;.\end{aligned} \tag{5.37}$$

In the limit of a perfect reflector, this recovers the last of Eqs. (9) of Messina et al. [2010].

5.3.3 Relaxation after a change of the surface properties

As a generalization, we want to consider the case where the wall has undergone a nonadiabatic transition, i.e. a change in the system properties that is fast on the scale $1/\Omega$. Here, we have that $\tilde{\Omega}=\Omega, \tilde{d}=d, \tilde{\boldsymbol{\mathcal{G}}}\neq\boldsymbol{\mathcal{G}}$, so that Eq. (5.36) becomes (arguments suppressed)

$$\Delta\tilde{U}_{\rm p}(\boldsymbol{r}_A,t)=-d_md_n\,\mathrm{Re}\int_0^\infty d\omega\frac{e^{-\mathrm{i}(\omega+\Omega)t}}{\omega+\Omega}\int d^3\boldsymbol{r}\varepsilon_0\sqrt{\mathrm{Im}\;[\varepsilon]\;\mathrm{Im}\;[\tilde{\varepsilon}]}\,\tilde{\mathcal{G}}_{mk}\mathcal{G}^*_{nk}\;. \tag{5.38}$$

The expression involves the Green's tensors (boundary conditions) before and after the transition. Eq. (5.10) cannot be used for further simplification but numerical evaluation is, in principle, possible.

As a basic example, we consider a rapid change of the plasma frequency in the Drude model $\omega_\mathrm{p} \to \tilde{\omega}_\mathrm{p}$. This can be realized, e.g., in semiconductors [Dodonov and Dodonov, 2006; Dodonov, 2010] or graphene [Koppens et al., 2011]. From the explicit form of the *transmitted* Green's tensor inside the material, see, e.g., [Scheel and Buhmann, 2008], the spatial integral can be performed using a near-field approximation for the Green's tensors as in Sec. 5.2.3. This gives

$$\int d^3\boldsymbol{r}' \varepsilon_0 \sqrt{\mathrm{Im}\,[\varepsilon]\,\mathrm{Im}\,[\tilde{\varepsilon}]}\,\tilde{\mathcal{G}}_{ik}\mathcal{G}_{jk} = \frac{1}{4\varepsilon_0 \pi z^3} \frac{\sqrt{\mathrm{Im}\,\varepsilon(\omega)\,\mathrm{Im}\,\tilde{\varepsilon}(\omega)}}{[1+\varepsilon(\omega)][1+\tilde{\varepsilon}^*(\omega)]}[\delta_{ij} + \hat{z}_i\hat{z}_j]\,, \quad (5.39)$$

which describes the correlation between the electric fields before and after the transition, generalizing Eq. (5.26). The partial dressing potential can then be calculated by analytic continuation along the lines of Eq. (5.28). This gives again an integral along the imaginary axis (nonresonant contribution) as well as a resonant surface-mode contribution, taken at the new value $\tilde{\tilde{\omega}}(\infty)$.

A numerical evaluation of the partial dressing correction $\Delta\tilde{U}_\mathrm{p}(t)$ is shown in Fig. 5.6. Here, we considered a sudden increase of the plasma frequency by two different values. The resonant contribution oscillates at $\tilde{\tilde{\omega}}(\infty)+\Omega$. In the case of a significant change of ω_p [Fig. 5.6a)] the contribution $\tilde{U}_p$ is rather small so that the nonresonant part of the integral is visible in the modulations at short times. However, the total partial dressing potential of Eq. (5.34) is clearly dominated by the first term, which coincides with the curve shown in Fig. 5.5 for the parameters chosen. As a result, the partial-dressing scenario resembles closely the case of an initially bare atom. If the change in the plasma frequency is small ($|\omega_\mathrm{p} - \tilde{\omega}_\mathrm{p}| < \gamma/2$), the two terms in Eq. (5.34) are comparable in amplitude and partly compensate [cf. Figs. 5.5 and 5.6b)], resulting in a total dynamic atom-surface potential that oscillates with a reduced amplitude.

5.4 Summary and Discussion

The dynamic atom-surface interaction has been investigated from the perspective of atomic self-dressing for initially bare atoms, as well as for the more realistic scenario in which the system relaxes after a sudden change in the boundary conditions or atomic properties. We have generalized previous work by Vasile and Passante [2008]; Messina et al. [2010] and used the approach of matter-assisted fields to include boundaries with arbitrary dielectric properties.

The limit of perfectly reflecting surfaces can be considered a reasonable approximation in the radiative zone of distances (far beyond the atomic transition wavelength and in electric dipole coupling). However, some interesting phenomena can be studied if more general surfaces are included in the model. For example, surface excitations are known to dominate the response in the near-field [Henkel et al., 2002; Failache et al., 2002; Gorza and Ducloy, 2006], see also [Ford and Weber, 1984; Stehle et al., 2011]. Their role in a two-plate Casimir cavity is discussed in the following chapter. We have isolated

the resonant surface-mode contributions to the time-dependent atom-surface potential in different distance regimes. Far from the surface, this contribution is a minor correction and gives a relatively short-lived contribution to the dynamic atom-surface potential. In contrast, in the near-field the surface-mode contribution dominates the response by orders of magnitude and decays on a much slower time scale related to the Drude parameter, which describes the characteristic dissipation rate of the bulk.

Finally, we have studied partial dressing, where a nonadiabatic (instantaneous) change of some system parameter changes the stationary state, which the system must approach. The generalized description of surfaces through reflection amplitudes made it possible to consider changes in the surface properties. As a proof of principle, we have considered a change in the charge-carrier density, similar to what might be realized by shining a short laser pulse on a semiconductor [Dodonov, 2010] or in graphene sheets [Koppens et al., 2011]. Conceptually, such partial-dressing scenarios are closely related to systems considered in the dynamic Casimir effect, where a change in the boundary conditions results in the creation of cavity photons.

Another system that seems very promising for both the dynamic dressing and the dynamic Casimir effect is a superconductor, in which a phase transition can be induced, e.g. by a supercritical current-pulse or by a strong laser pulse. Superconductivity breaks down on the scale of $1 \ldots 100\,\mathrm{ns}$ [Geier and Schön, 1982], rather slow as compared to atomic electronic transition periods, but comparable or smaller than the ones relevant in Rydberg atoms or small molecules. This system is potentially relevant for experiments with superconducting atom chips. From the results in the near field, the change in bulk dissipation during the superconducting transition should affect the life time of the transiently excited surface resonances. The two-fluid model does not provide sufficient information about fluctuations in the superconducting phase, cf. Sec. 3.2.2. A theoretical investigation of such effects should thus be based on a more detailed description, such as the BCS theory (App. C) or the model by Ginzburg and Landau [1956]. The dynamic interaction of atoms and vortex matter is an interesting aspect that might be addressed in the future.

Besides, the impact of the thermal occupation of field modes on the dynamic dressing should be included. Thermal photons can be absorbed by the atom, giving rise to additional resonant contributions. Thermal effects in the dressing dynamics are likely to be connected with a characteristic time scale $\hbar/k_B T \approx 1\,\mathrm{ps} \times (T/1\,\mathrm{K})^{-1}$.

Chapter 6

Plasmonic Casimir Interaction In and Out of Equilibrium

This chapter is based on the article *Temperature dependence of the plasmonic Casimir interaction* by H. Haakh, F. Intravaia, and C. Henkel, *Physical Review A* **82**, 012507 (2010).

The interaction between two parallel plates due to the fluctuations of the electromagnetic field is commonly known as the Casimir effect [Casimir, 1948]. The interaction resembles in many respects the van der Waals-Casimir-Polder interactions that arise when small polarizable particles (atoms, molecules, or nanoparticles) are placed near a solid surface, which were discussed in the previous chapters. In fact, also the seminal paper by H. Casimir was motivated by earlier work on such systems [Casimir and Polder, 1948]. As an important result, the role of surface-plasmon modes in the (dynamic) atom-surface interaction was underlined in the previous Chapter 5.

For metallic plates, too, it is well known that at short distance, the interaction can be attributed to surface-plasmon modes [Economou, 1969; Raether, 1988] that hybridize across the vacuum between the interfaces [Van Kampen et al., 1968; Schram, 1973; Gerlach, 1971]. Surface plasmons have been attracting much interest in the last years in connection with a broad range of topics such as near-field spectroscopy with sub-wavelength resolution [Brongersma and Kik, 2007; Maier, 2007], extraordinary transmission through subwavelength metallic hole arrays [Altewischer et al., 2002; Fasel et al., 2005; Garcia-Vidal et al., 2010], or heat transfer [Joulain et al., 2005; Guérout et al., 2012]. The electromagnetic field associated with these modes is evanescent, i.e. confined to the metal-vacuum interface. It therefore came as a surprise that they also give a significant contribution at large distances, and even a repulsive one [Intravaia, 2005; Intravaia and Lambrecht, 2005; Intravaia et al., 2007]. These papers have been restricted to the Casimir effect at zero temperature. The present chapter generalizes these results by including nonzero temperature and situations out of thermal equilibrium. One might expect that the thermal excitation of surface plasmons is irrelevant, since their typical energies are comparable to the plasma frequency of the metal, much larger than experimentally relevant thermal energies. As retardation is taken into account, however, the surface-plasmon dispersion relation approaches the light cone and includes much lower frequencies. For two parallel plates separated by a distance L, these frequencies are comparable to the lowest cavity resonance $\sim c/L$. We find indeed a significant thermal component to the Casimir

interaction between surface-plasmon modes when the cavity-mode energy meets the thermal energy scale $\hbar c/L \sim k_B T$. By selectively exciting a class of plasmonic modes, we even get an overall repulsive Casimir force. This parallels the evanescent-field force acting on atoms near a single surface used in atom trapping, e.g. [Stehle et al., 2011].

In this chapter, we first recall the dispersion relations for coupled surface-plasmon modes on two metallic plates [Economou, 1969] and obtain a general expression for the corresponding Casimir free energy. This is expanded asymptotically in different regimes of distance L and temperature T in Sec. 6.1.2. In Sec. 6.2, the plasmonic Casimir entropy is discussed. We then compare the results to the 'full' Casimir interaction between metal plates in Sec. 6.3, including all electromagnetic modes, consider situations in which the plasmonic modes are not at the same temperature as the rest of the system, and conclude with a short summary.

6.1 Plasmonic Casimir Free Energy

The Casimir energy and force (both per unit area) in a cavity formed by perfectly reflecting mirrors is well known [Casimir, 1948]

$$E_{\mathrm{C}} = -\frac{\hbar c}{4\pi \aleph L^3}, \quad F_{\mathrm{C}} = -\frac{3\hbar c}{4\pi \aleph L^4}\,, \tag{6.1}$$

where $\aleph = 180/\pi^3$. In the following the ideal reflector limit will be referred to as a useful scale. In realistic cavities, the material properties lead to corrections to these expressions. A general theoretical description based on dielectric functions of the plates is due to Lifshitz [1956], see also the recent books by Parsegian [2006]; Dalvit et al. [2011].

We adopt for simplicity the lossless, local dielectric function (cf. Sec. 4.2.1)

$$\varepsilon(\omega) = 1 - \frac{\omega_{\mathrm{p}}^2}{\omega^2}\,, \tag{6.2}$$

where ω_{p} is the plasma frequency. For this model, analytic calculations can be pushed very far. An intrinsic physical length scale of the system is the plasma wavelength $\lambda_{\mathrm{p}} = 2\pi c/\omega_{\mathrm{p}}$ (Meißner-London penetration depth, cf. Sec. 3.2.2). It is convenient to use the latter as a unit of length, switching to a dimensionless plate distance $\lambda = L/\lambda_{\mathrm{p}}$. We introduce also a reduced temperature $\tau = T/T_{\mathrm{p}} = (2\pi k_B T)/\hbar\omega_{\mathrm{p}}$, where T_{p} is the plasma temperature. This choice makes the numerical results independent of the specific material and gives universal scaling laws. Note that $1/\tau$ is proportional to the ratio between the thermal wavelength (a few microns at room temperature) and the plasma wavelength, and that the product $\lambda\tau = k_B T L/(\hbar c)$ is independent of the plasma wavelength. A parameter set used frequently in related work is the one for gold: $\hbar\omega_{\mathrm{p}} = 8.96$ eV, $\lambda_{\mathrm{p}} = 136$ nm and $T_{\mathrm{p}} = 1.66 \times 10^4$ K. Room temperature then corresponds to $\tau \approx 1.8 \times 10^{-2}$.

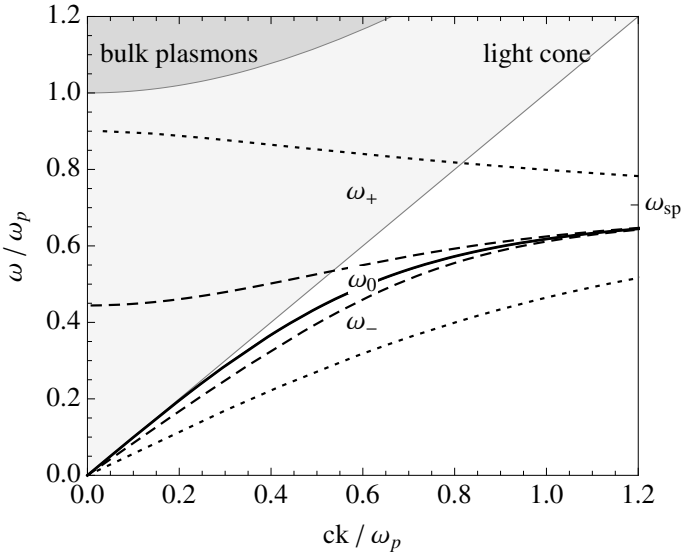

Figure 6.1: Dispersion relation of the surface-plasmon modes at plate separation $L = c/\omega_{\rm p}$ (dotted curves) and $L = 2c/\omega_{\rm p}$ (dashed curves); k is the wavevector parallel to the surface. The solid black curve $\omega_0(k)$ corresponds to the surface plasmon on an isolated plate ($L \to \infty$). The branch $\omega_+(k)$ crosses the light cone (light gray). The asymptotic value at large k is $\omega_{\rm sp} = \omega_{\rm p}/\sqrt{2}$.

6.1.1 Surface-plasmon contributions to the Casimir free energy

The Casimir free energy of two metallic plates is obtained by summing the free energy (per mode) over the electromagnetic modes vibrating inside the cavity [Casimir, 1948; Van Kampen et al., 1968; Schram, 1973]. This expression is suitably regularized, namely by subtracting the limit of large distances between the plates. Since the modes of the electromagnetic field are formally equivalent to harmonic oscillators, the free energy of a single mode of frequency ω in thermodynamical equilibrium at temperature T is

$$f(\omega) \;=\; \frac{\hbar\omega}{2} + k_B T \ln\left[1 - e^{-\frac{\hbar\omega}{k_B T}}\right] . \tag{6.3}$$

In what follows, we sum Eq. (6.3) over the dispersion relations for the surface-plasmon modes.

It was argued in Sec. 5.2.2 that isolated surfaces (at infinite distance) carry a single surface-plasmon mode of frequency $\omega_0(k)$, as illustrated in Fig. 6.1 (cf. also Fig. 5.3). If the plates are brought together, the electromagnetic fields of the modes overlap, breaking the degeneracy and splitting the dispersion relation in two branches, whose frequencies we label $\omega_\pm(k)$. The modes $\omega_-(k)$ and $\omega_0(k)$ are both entirely evanescent and lie below the light cone. The mode $\omega_+(k)$, however, crosses the light cone and connects smoothly with the lowest propagating mode (with p-polarization) within the cavity [Economou, 1969] (Fig. 6.1). Adding the free energies of the coupled modes and subtracting their

corresponding values at infinite distance, the integral over the dispersion relations gives the plasmonic Casimir free energy in the form (coefficients $c_\pm = 1$, $c_0 = -2$)

$$\mathcal{F}(L,T) = \int_0^\infty \frac{k\,\mathrm{d}k}{2\pi} \sum_{a=\pm,0} c_a\, f\left(\omega_a(k)\right) \tag{6.4}$$

which is convergent at large k [Intravaia, 2005]. The thermal part of the free energy [second term in Eq. (6.3)] naturally cuts off modes above $k_B T/\hbar$. Different choices of the lower integration boundary, related to the subtraction procedure, are possible and have been discussed before [Intravaia and Lambrecht, 2005; Intravaia et al., 2007; Bordag, 2006; Lenac, 2006; Lambrecht and Pirozhenko, 2008]. They are connected with the way the evanescent and propagating contributions of the mode $\omega_+(k)$ are split. By applying the convention of Intravaia and Lambrecht [2005]; Intravaia et al. [2007] and setting the lower bound equal to zero for all modes, we include both propagating and evanescent branches of the 'plasmonic mode' $\omega_+(k)$.

The calculation of the integral (6.4) is challenging because the surface-plasmon dispersion relations $\omega_a(k)$ are solutions of a transcendental equation, except in the nonretarded limit $k \gg \omega_\mathrm{p}/c$ where $\omega_a^2(k) = \omega_\mathrm{sp}^2(1 + a\, e^{-kL})$ with $\omega_\mathrm{sp} = \omega_\mathrm{p}/\sqrt{2}$, $a = 0, \pm 1$. Progress can be made with the parametric form described in [Intravaia, 2005; Intravaia and Lambrecht, 2005; Intravaia et al., 2007]. Adopting the notation of [Intravaia and Lambrecht, 2005], we get the dispersion relations $\omega_a(k)$, $a \in \{0, \pm\}$, from

$$\omega_a(z) = \frac{c}{L} g_a(z), \qquad k_a^2(z) = \frac{z + g_a^2(z)}{L^2} \quad \text{with } -z_a \le z < \infty \tag{6.5}$$

and the dimensionless functions

$$g_a^2(z) \;=\; \frac{(2\pi\lambda)^2 \sqrt{z}}{\sqrt{z} + \sqrt{z + (2\pi\lambda)^2}\,[\tanh(\sqrt{z}/2)]^a}\,. \tag{6.6}$$

(The exponents are ± 1 for $a = \pm$.) The range of z starts at $-z_a$ with $z_0 = z_- = 0$. The value of z_+, plotted in Fig. 6.2 as a function of λ, is the solution of the transcendental equation $\sqrt{z_+} = 2\pi\lambda \cos(\sqrt{z_+}/2)$ [Intravaia and Lambrecht, 2005]. The propagating branch of the mode $\omega_+(k)$ corresponds to the interval $z \in [-z_+, 0]$ (with $\sqrt{z} = +\mathrm{i}\sqrt{|z|}$); evanescent modes (below the light cone) have $z > 0$. Changing the integration variable in Eq. (6.4) from k to z, the plasmonic Casimir free energy is given by

$$\begin{aligned} \mathcal{F} \;=\; \frac{\hbar c}{8\pi L^3} \sum_{a=\pm,0} c_a \Bigg[& \int_{-z_a}^{\infty} \left(g_a(z) + 2\lambda\tau \ln\left[1 - e^{-\frac{g_a(z)}{\lambda\tau}}\right]\right) \mathrm{d}z \\ & + 2 \int_{g_a(-z_a)}^{g_a(\infty)} \left(g_a^2 + 2 g_a \lambda\tau \ln\left[1 - e^{-\frac{g_a}{\lambda\tau}}\right]\right) \mathrm{d}g_a \Bigg]\,. \end{aligned} \tag{6.7}$$

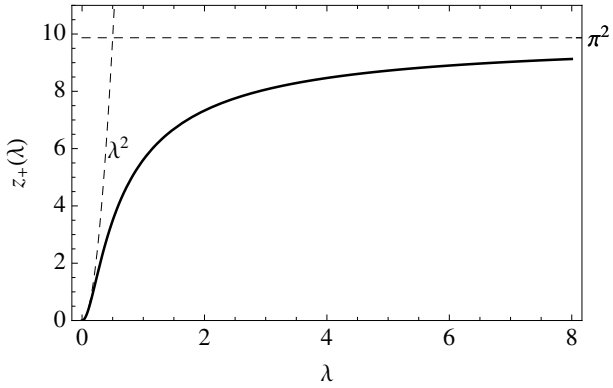

Figure 6.2: $z_+(\lambda)$ vs. the plate separation λ and its asymptotes at small and large distances. The limiting cases are $z_+ \approx (2\pi\lambda)^2$ and $\approx \pi^2$ for $\lambda \to 0$ and $\to \infty$, respectively.

For all plasmonic modes, the second integral has a common upper limit $g_a(\infty) = \sqrt{2}\,\pi\lambda = \omega_{\rm sp}L/c$ that coincides with the nonretarded surface plasmon frequency; their contributions cancel in the sum over a. The lower boundaries are $g_0(-z_0) = g_-(-z_-) = 0$, and $g_+(-z_+) = \sqrt{z_+}$. The first integral in Eq. (6.7) can only be evaluated approximately (see Sec. 6.1.2), but a closed form can be given for the second one [see Eq. (6.12)].

In the following, we scale the plasmonic free energy to the zero-temperature Casimir value, Eq. (6.1),

$$\mathcal{F}(L,T) = E_{\rm C}(L)\varphi(\lambda,\tau) \tag{6.8}$$

and split the correction factor in two terms

$$\varphi(\lambda,\tau) = \eta(\lambda) + \vartheta(\lambda,\tau)\,, \tag{6.9}$$

where the first is the plasmonic Casimir energy at zero temperature [Intravaia and Lambrecht, 2005; Intravaia et al., 2007]:

$$\eta(\lambda) \;=\; -\frac{\aleph}{2}\sum_a c_a \int_{-z_a}^{\infty} g_a(z)\mathrm{d}z + \frac{\aleph}{3} z_+^{3/2}\,. \tag{6.10}$$

The second term in Eq. (6.9) gives the temperature-dependent part for which Eq. (6.7) gives

$$\vartheta(\lambda,\tau) = -\,\aleph\,\lambda\tau \sum_a c_a \int_{-z_a}^{\infty} \ln\left[1 - e^{-\frac{g_a(z)}{\lambda\tau}}\right]\mathrm{d}z - 2\aleph\,(\lambda\tau)^3\,\mathcal{L}\left(\frac{\sqrt{z_+}}{\lambda\tau}\right)\,, \tag{6.11}$$

where the following combination of polylogarithmic functions appears

$$\mathcal{L}(x) = \zeta(3) - \mathrm{Li}_3(e^{-x}) - x\mathrm{Li}_2(e^{-x}) \tag{6.12}$$

with $\mathrm{Li}_n(x) = \sum_{k=1}^{\infty} x^k/k^n$. We note that $\mathcal{L}(x) \sim \frac{1}{4}x^2(1 - 2\log x)$ for small x, and $\mathcal{L}(x) \to \zeta(3)$ exponentially fast for large x. Eq. (6.11) does not depend only on the

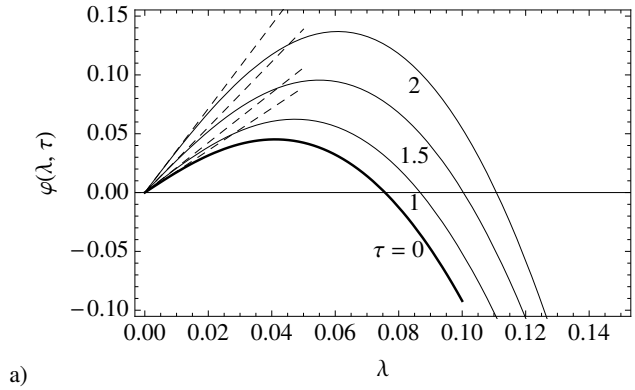

a)

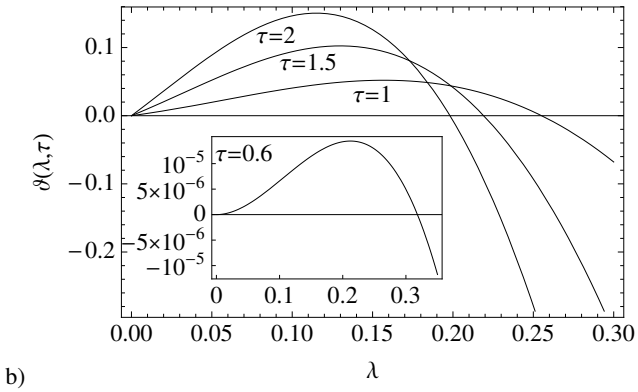

b)

Figure 6.3: a) Plasmonic contribution to the Casimir free energy vs. distance at different temperatures, normalized to the perfect mirror case at $T = 0$ (energy correction factor $\varphi(\lambda, \tau)$ in Eq. (6.8)). Solid curves: numerical evaluation of Eqs. (6.10, 6.11) for different temperatures; dashed curves: short-distance limit Eqs. (6.16, 6.17). $\lambda = L\omega_\mathrm{p}/2\pi c$ and $\tau = T/T_\mathrm{p} = k_B T/\hbar\omega_\mathrm{p}$ are the distance and temperature scaled to the plasma wavelength and temperature, respectively. Negative values correspond to a *repulsive* interaction energy.
b) Thermal correction to the plasmonic free energy at short distance for different temperatures [energy correction factor $\vartheta(\lambda, \tau)$ in Eq. (6.9)]. The behavior qualitatively differs from the complete free energy (Fig. 6.3), as a quadratic (rather than linear) distance dependence emerges at low temperatures, cf. Eq. (6.17).

product $\lambda\tau$ because the material-dependent parameter λ enters via the lower limit z_+ and the functions $g_a(z)$ [Eq. (6.6)].

The Casimir free energy is shown in Figs. 6.3 and 6.6 for different distance ranges. Qualitatively, a nonzero temperature does not modify the behavior of the plasmonic contribution – we still get a sign change at a distance of order $\lambda_\mathrm{p}/2\pi$, with the interaction becoming repulsive at large distances. We plot in Fig. 6.4 the inversion distance where the plasmonic Casimir pressure, $-\partial\mathcal{F}/\partial L$, changes sign: a weak increase is found as the temperature is raised. Much larger changes will be found in Sec. 6.3.3, where configura-

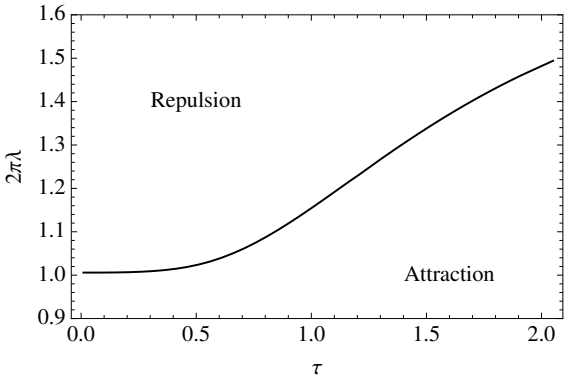

Figure 6.4: Repulsive and attractive regimes of the plasmonic Casimir pressure in the (λ, τ)-plane. A nonzero temperature slightly increases the distance for which the plasmonic contribution to the Casimir force becomes repulsive.

tions out of thermal equilibrium are discussed.

In the following, we analyze the thermal correction $\vartheta(\lambda, \tau)$ in different regimes of distance and temperature. The zero-temperature Casimir energy $\eta(\lambda)$ depends only on one physical scale provided by the plasma wavelength and leads to two regimes $\lambda \ll 1$ and $\lambda \gg 1$. For $\vartheta(\lambda, \tau)$ we discuss three regimes. In all situations of practical interest, it is safe to assume $\tau \ll 1$ for the scaled temperature and we can distinguish between: short distances $\lambda \ll 1$, intermediate distances, $1 \ll \lambda \ll 1/\tau$, and large distances (beyond the thermal wavelength) $1/\tau \ll \lambda$.

6.1.2 Asymptotic regimes of the Casimir free energy

The calculation of asymptotic expressions requires some care already at zero temperature as was shown by Intravaia et al. [2007]. When performing approximations on the integrals in Eqs. (6.10) and (6.11), one must bear in mind that the functions $g_a(z)$ cover a wide range of values, from very small to large, depending on z and λ. Their characteristic scale in the variable z is given by the distance parameter λ. For $-z_a < z \ll (2\pi\lambda)^2$ we may use $(a = 0, \pm)$

$$g_a(z) \approx \sqrt{2\pi\lambda\sqrt{z}\left[\coth\left(\frac{\sqrt{z}}{2}\right)\right]^a}\,, \tag{6.13}$$

while for $z \gg (2\pi\lambda)^2$ the (nonretarded) approximations

$$g_a(z) \approx \frac{2\pi\lambda}{\sqrt{2}}\sqrt{1 + a\, e^{-\sqrt{z}}} \tag{6.14}$$

hold. It is therefore convenient to split the integration range in Eqs. (6.10) and (6.11) as follows

$$\int_{-z_a}^{\infty} \mathrm{d}z = \int_{-z_a}^{0} \mathrm{d}z + \int_{0}^{(2\pi\lambda)^2} \mathrm{d}z + \int_{(2\pi\lambda)^2}^{\infty} \mathrm{d}z\,. \tag{6.15}$$

The first integral concerns only the mode $\omega_+(k)$ because $z_-, z_0 = 0$. We can use Eq. (6.13) in the first two integrals and Eq. (6.14) in the third. Depending on distance and tempera-

ture, and on the desired accuracy, these have to be compared with the integrated terms in Eq. (6.1.1) [proportional to $z_+^{3/2}$ or $\mathcal{L}(\sqrt{z_+}/\lambda\tau)$].

Short distance

At short distance, the zero-temperature energy correction was already analyzed earlier [Intravaia et al., 2007]. It turns out that it is dominated by large values of z [third integral of Eq. (6.15)]. At the leading order, we get

$$\eta(\lambda) \xrightarrow{\lambda\ll 1} 1.790\lambda\,. \tag{6.16}$$

Higher order terms take the form $\lambda^3(a + b\log\lambda)$ with numerical coefficients a and b given in the same reference.

By considering the thermal correction for $\lambda \ll 1$, the thermal scale becomes important, too. For realistic temperatures, we also have $\lambda\tau \ll 1$, and the main contribution arises from the second and the third integral in Eq. (6.15). Indeed, it can be shown that the first integral and the polylogarithmic term (involving $\mathcal{L}$) are beyond the order $\mathcal{O}(\lambda^2)$. In addition, the main contribution to the second integral arises from the mode $\omega_-(k)$. This is not surprising since the thermal correction selects frequencies $\omega_a(k) \lesssim T$ and the mode $\omega_-(k)$ is the one that vanishes most quickly as $k \to 0$. The corresponding exponent in k determines the power law in τ, as we discuss at the end of this section. The opposite case $\lambda\tau \gg 1$ is physically irrelevant at short distances, because one would need $\tau \gg 1$. Mathematically, this regime contains a divergence from the term proportional to $\mathcal{L}$ in Eq. (6.11) that is exactly balanced by the first integral in Eq. (6.15). It follows that the asymptotic form given in Eq. (6.17) remains valid.

All told, up to the second order in λ we find

$$\vartheta(\lambda,\tau) \xrightarrow{\lambda\ll 1} \aleph\lambda\tau\left[2\frac{\lambda\tau^2}{\pi}\mathcal{L}(2\pi\sqrt{\pi\lambda/\tau^2}) + \beta(\tau)\right]\,, \tag{6.17}$$

where the function $\mathcal{L}(x)$ defined in Eq. (6.12) appears with a different argument. The temperature-dependent function $\beta(\tau)$ is

$$\beta(\tau) = \int_0^\infty \ln\left[\frac{1-e^{-\pi\sqrt{2}/\tau}}{1-e^{-\pi\sqrt{2(1+e^{-\sqrt{z}})}/\tau}}\right]\mathrm{d}z + \int_0^\infty \ln\left[\frac{1-e^{-\pi\sqrt{2}/\tau}}{1-e^{-\pi\sqrt{2(1-e^{-\sqrt{z}})}/\tau}}\right]\mathrm{d}z. \tag{6.18}$$

This is plotted in Fig. 6.5 together with its asymptotes in the limits of high and low temperatures,

$$\beta(\tau) \xrightarrow{\tau\ll 1} 6\zeta(5)\left(\frac{\tau}{\pi}\right)^4, \quad \beta(\tau) \xrightarrow{\tau\to\infty} \frac{\zeta(3)}{4}. \tag{6.19}$$

We observe the emergence of the characteristic ratio λ/τ^2 that determines which of the two terms in Eq. (6.17) dominates. This illustrates that the limits $\lambda \to 0$ and $\tau \to 0$

do not commute for the temperature-dependent Casimir energy. If $\lambda \ll \tau^2$ [extremely short distances or high temperatures, Fig. 6.3a) and main plot of Fig. 6.3b)], the function $\beta(\tau)$ governs the thermal correction ϑ which scales as $\vartheta \sim \lambda\tau^5$ if $\lambda \ll \tau^2 \ll 1$. We recover here the same linear distance dependence as at zero temperature, Eq. (6.16). The opposite regime $\tau^2 \ll \lambda \ll 1$ emerges at low temperatures, where the term involving $\mathcal{L}$ in Eq. (6.17) dominates: we get a behavior $\vartheta \sim \lambda^2\tau^3$ [inset of Fig. 6.3b)]. This crossover from a quadratic to a linear scaling with distance can be seen in Fig. 6.3b).

This discussion also illustrates the failure of the nonretarded approximation. This leads to surface-plasmon dispersion relations $\omega_\pm^2(k) = \omega_{\rm sp}^2(1 \pm e^{-kL})$ and $\omega_0 = \omega_{\rm sp}$, and extrapolates a free energy $\vartheta \sim \tau^5$ down to low temperatures, while the correct power is τ^3. This is of course crucial for the low-temperature expansion of a thermodynamic quantity like the entropy (see Section 6.2).

Intermediate distance

Parameters for typical experiments are $\tau \approx 10^{-2}$, $\lambda \approx 1 \ldots 10^2$, way beyond short distances. They lie inside an intermediate regime $1 \ll \lambda \ll 1/\tau$, where the plate distance is between the plasma and the thermal wavelength. Here, the thermal correction to the free energy is still small compared to zero temperature, as for short distances.

In the scaled Casimir energy $\eta(\lambda, \tau)$, the main contribution to the integral (6.10) arises for $z \sim 1$ and we have to consider the first two integrals in Eq. (6.15), where, approximately, $z_+ \approx \pi^2$. The energy correction factor at zero temperature then becomes [Intravaia et al., 2007]

$$\eta(\lambda) \xrightarrow{\lambda \gg 1} -74.57\sqrt{\lambda} + 60. \,, \tag{6.20}$$

the offset arising from the second term in Eq. (6.10).

For the thermal correction, we find the leading order from the polylogarithmic $\mathcal{L}$ in Eq. (6.11). The z-integral gives a contribution which is dominated by the interval $z = -z_+ \ldots (2\pi\lambda)^2$. Combining the two,

$$\vartheta(\lambda, \tau) \approx -2\aleph(\lambda\tau)^3\zeta(3)\left(1 - \frac{1}{\lambda\pi}\right) \,. \tag{6.21}$$

This gives a small correction that scales as τ^3. Both Eqs. (6.20) and (6.21) are plotted in Fig. 6.6a), illustrating the weak impact of temperature. It is interesting to note that in this range of distances, the thermal plasmonic contribution is opposite in sign to the free energy of the full electromagnetic Casimir effect (see Sec. 6.2), and increases the plasmonic repulsion.

Large distance

Let us finally consider the regime $\lambda \gg 1/\tau \gg 1$, corresponding to a plate separation larger than both the plasma and the thermal wavelength. The zero-temperature contribution can still be approximated by Eq. (6.20), but now the thermal contribution dominates

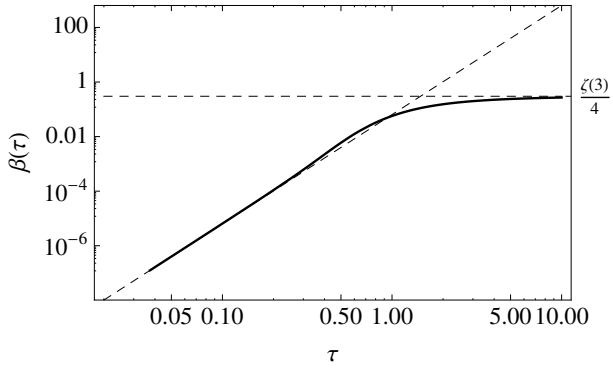

Figure 6.5: The function $\beta(\tau)$ vs. τ and its asymptotes [Eq. (6.19)] at low and high temperatures.

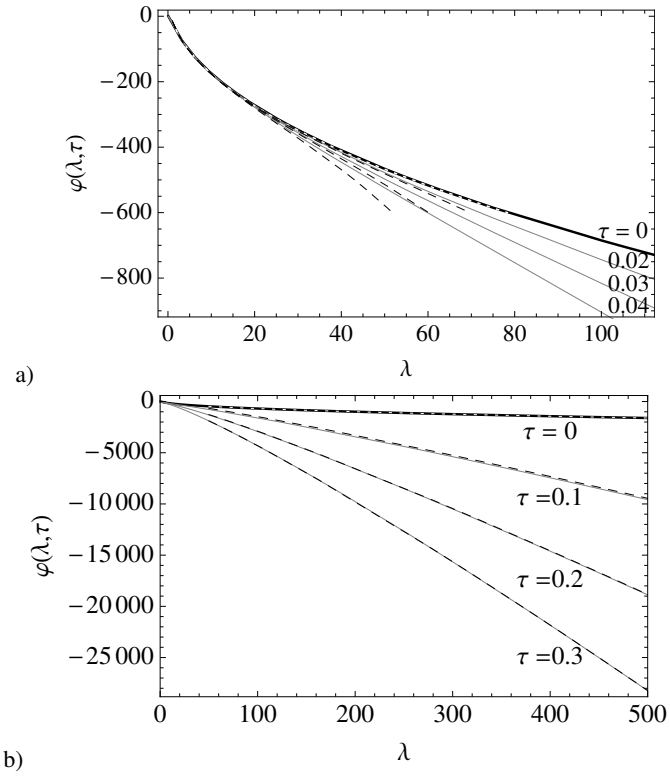

Figure 6.6: a) Thermal plasmonic Casimir free energy [reduction factor $\varphi(\lambda,\tau)$ in Eq. (6.8)] at intermediate distances and different temperatures. Exact numerical calculation (solid curves) and the approximation of Eq. (6.20) at zero temperature (short-dashed white) and sum of Eqs. (6.20) and (6.21) in the intermediate regime $\lambda\tau \ll 1$ (long-dashed) respectively.
b) Plasmonic Casimir free energy (correction factor $\varphi(\lambda,\tau)$) at large distances and different temperatures. Numerical calculation (solid curves) and large-distance approximations given in Eq. (6.20) at zero temperature (white dotted line) and in Eq. (6.23) at nonzero temperature (dashed curves).

the free Casimir energy. The asymptotic behavior of the integrals in Eq. (6.11) is obtained by expanding the logarithms for small $g_a(z)/(\lambda\tau)$, since the functions $g_a(z)$ are bounded:

$$-\lambda\tau \ln\left[1-e^{-\frac{g_a(z)}{\lambda\tau}}\right] \approx -\lambda\tau \ln\left[\frac{g_a(z)}{\lambda\tau}\right] + \frac{g_a(z)}{2} + \cdots \tag{6.22}$$

Using this expansion under the integral in Eq. (6.11), we note that the second term balances exactly with the zero-temperature contribution from Eq. (6.10). As for the first term, we perform the z-integration by splitting the integration range as in Eq. (6.15). It is easy to see that in the second interval, the sum over the mode branches gives zero. The leading contribution now comes from negative z, while the third interval in Eq. (6.15) gives an exponentially small contribution $\sim e^{-4\pi\lambda}$. The polylogarithmic term $\mathcal{L}$ can be expanded for small argument, which gives eventually

$$\begin{aligned}\varphi(\lambda,\tau) \xrightarrow[\lambda\gg 1]{\lambda\tau\gg 1} &-\frac{\aleph\lambda\tau}{2}\int_{-\pi^2}^{0} \ln\left[\frac{2\pi}{\lambda\tau^2}\sqrt{z}\coth\left(\frac{\sqrt{z}}{2}\right)\right]\mathrm{d}z - 2\aleph\,(\lambda\tau)^3\,\mathcal{L}\left(\frac{\pi}{\tau\lambda}\right) \\ &\approx -\frac{\aleph\pi^2\lambda\tau}{2}\left(\ln(2\lambda) - \frac{7\zeta(3)}{\pi^2} + \frac{1}{2}\right),\end{aligned} \tag{6.23}$$

where the dependence on $\ln\tau$ cancels to leading order. The validity range of this asymptotic formula is illustrated in Fig. 6.6 (dashed lines) where the full free energy is plotted at large distances.

Summarizing this section, we have generalized a result known from the zero-temperature case [Intravaia and Lambrecht, 2005; Intravaia et al., 2007] to $T > 0$: only the branch of the plasmonic mode $\omega_+(k)$ that crosses into the propagating sector contributes to the (repulsive) plasmonic Casimir interaction at large distances in a significant way.

6.2 Plasmonic Casimir Entropy

The Casimir entropy can be obtained from the Casimir free energy by differentiation with respect to the temperature T,

$$S(L,T) = -\frac{\partial\mathcal{F}}{\partial T}\,. \tag{6.24}$$

A related quantity the was already discussed for the atom-surface interaction in Sec. 4.3.4 with respect to the difference between lossless (superconductors, plasma model) and normal metals [Milton, 2009; Klimchitskaya et al., 2009; Intravaia and Henkel, 2008], especially at low T.

We recall the result for perfect reflectors, where the entropy per unit area can be expressed through the product $\lambda\tau = k_B T L/\hbar c$ (this includes two transverse photon polarizations) [Feinberg et al., 2001]

$$S_{\mathrm{C}} = \frac{\zeta(3)}{8\pi}\frac{k_B}{L^2} \times \begin{cases} 12(\lambda\tau)^2, & \lambda\tau \ll 1 \\ 1, & \lambda\tau \gg 1. \end{cases} \tag{6.25}$$

A convenient scale is provided by the high-temperature limit, and we define an entropy correction factor through

$$S(L,T) = \frac{\zeta(3)}{8\pi}\frac{k_B}{L^2}\sigma(\lambda,\tau)\,. \tag{6.26}$$

It is connected to the dimensionless thermal correction $\vartheta(\lambda,\tau)$ by a derivative (mind that $E_{\rm C} < 0$)

$$\sigma(\lambda,\tau) = \frac{2}{\zeta(3)\aleph\lambda}\frac{\partial}{\partial\tau}\vartheta(\lambda,\tau)\,. \tag{6.27}$$

The Casimir entropy due to surface plasmons is obtained from the plasmonic Casimir free energy, Eq. (6.7) and can be represented as the integral

$$\begin{aligned}\sigma(\lambda,\tau) &= -\frac{4}{\zeta(3)}\left[\sum_a \frac{c_a}{2}\int_{-z_a}^{\infty}\left(\ln\left[1-e^{-\frac{g_a(z)}{\lambda\tau}}\right] - \bar{n}_a(z)\frac{g_a(z)}{\lambda\tau}\right)\mathrm{d}z\right. \\ &\quad \left. +3(\lambda\tau)^2\mathcal{L}\left(\frac{\sqrt{z_+}}{\lambda\tau}\right) + z_+\ln\left[1-e^{-\frac{\sqrt{z_+}}{\lambda\tau}}\right]\right]\,,\end{aligned} \tag{6.28}$$

where $\bar{n}_a(z) = [\exp(g_a(z)/\lambda\tau) - 1]^{-1}$ is the Bose-Einstein mean photon number. Fig. 6.7 shows the temperature dependence of $\sigma(\lambda,\tau)$ for several distances λ, small and large. The strong qualitative differences between these cases could be anticipated from the free energy of Fig. 6.3b): at short distances, temperature makes $\vartheta(\lambda,\tau)$ increase towards positive values, leading to a positive σ from Eq. (6.27), while the trend is reversed at larger distances.

Note from Fig. 6.7 that the plasmonic Casimir entropy fulfills Nernst's heat theorem ($\sigma \to 0$ as $T \to 0$) at all distances. Though the same is known for the entropy of the complete plasma model [Bezerra et al., 2002a] including photonic modes, the result is not trivial because surface plasmons are only a subsystem of the two-plate system.

As before one can distinguish three characteristic distance regimes for the plasmonic Casimir entropy. The expression for $\lambda \ll 1$ can be easily obtained from the approximation (6.17) to $\vartheta(\lambda,\tau)$. At low temperatures (regime $\tau^2 \ll \lambda \ll 1$), we must include a subleading term in the small-λ expansion to get the right prefactor of the temperature power law. This is done by adding to Eq. (6.17) the polylogarithmic term with $\mathcal{L}$ of Eq. (6.11) that becomes $-2\aleph(\lambda\tau)^3\zeta(3)$. Differentiation leads to

$$\sigma(\tau,\lambda) \xrightarrow[\tau\ll 1]{\lambda\ll 1} 12(\lambda\tau)^2\left[\frac{1}{\pi\lambda} + \frac{5}{\pi^2}\frac{\zeta(5)}{\zeta(3)}\left(\frac{\tau}{\pi\lambda}\right)^2 - 1\right]. \tag{6.29}$$

The entropy approaches zero quadratically as $\tau \to 0$, as for perfect reflectors [Eq. (6.25)], but the prefactor is larger by a factor $1/(\pi\lambda)$. The good agreement with the exact result can be seen in the inset of Fig. 6.7a).

At high temperature, $\sigma(\lambda,\tau)$ becomes a constant that coincides at short distances with the perfect reflector limit for one polarization

$$\sigma(\lambda,\tau) \xrightarrow[\tau\gg 1]{\lambda\ll 1} \frac{1}{2}\,. \tag{6.30}$$

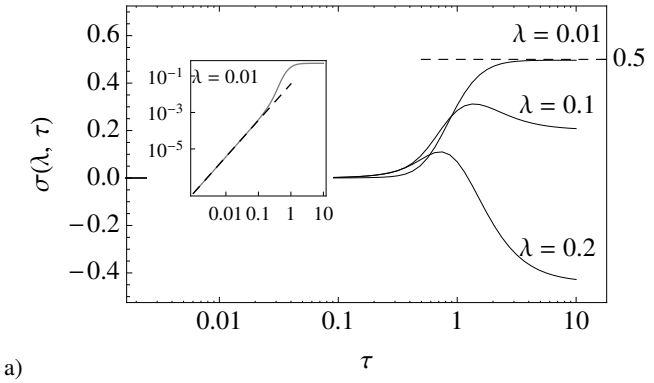

a)

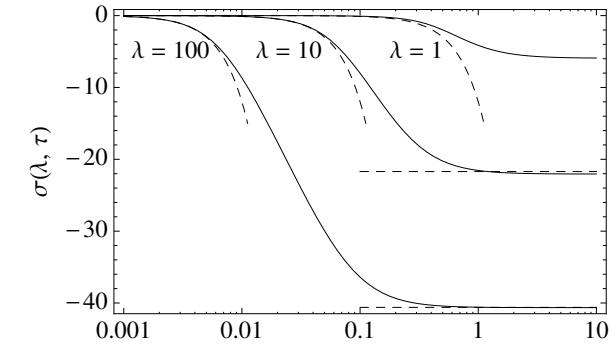

b)

Figure 6.7: a) Temperature dependence of the Casimir entropy from plasmonic modes [correction factor $\sigma(\lambda,\tau)$ relative to perfectly conducting mirrors, Eq. (6.24)] for short distances and high-temperature limit (6.30) (dashed). Inset (double logarithmic scale): low-temperature behavior at short distance and the asymptotic τ^2 power law from Eq. (6.29) (dashed line).
b) Plasmonic Casimir entropy in the scaled form $\sigma(\lambda,\tau)$ [Eq. (6.24)], vs. temperature for intermediate and large distances (solid lines). Dashed: low- and high-temperature asymptotes [Eqs. (6.31), (6.32)].

This can be seen from Eq. (6.17) taking into account the function $\beta(\tau)$.

Intermediate ($1 \ll \lambda \ll 1/\tau$) and large ($1, 1/\tau \ll \lambda$) distances can be treated with Eqs. (6.21), (6.23) that give, respectively,

$$\sigma(\lambda,\tau) \xrightarrow[\lambda\gg 1]{\lambda\tau\ll 1} 12(\lambda\tau)^2\left(-1+\frac{1}{\lambda\pi}\right). \tag{6.31}$$

$$\sigma(\lambda,\tau) \xrightarrow[\lambda\gg 1]{\lambda\tau\gg 1} -\frac{\pi^2}{\zeta(3)}\left(\ln(2\lambda)-\frac{7\zeta(3)}{\pi^2}+\frac{1}{2}\right). \tag{6.32}$$

The validity range of these formulas can be seen from Fig. 6.7 (dashed lines). Note that for intermediate and large distances, the entropy approaches zero from below as $\tau \to 0$.

6.3 Plasmonic and Photonic Modes In and Out of Equilibrium

6.3.1 Plasmonic vs. Photonic Modes in the Casimir free Energy

We now compare the plasmonic Casimir contribution to the full interaction, where all electromagnetic modes of the cavity are included. The knowledge of the surface-plasmon sector can in fact provide some physical interpretation for the whole interaction. For example, it is well known [Van Kampen et al., 1968; Schram, 1973; Gerlach, 1971] that the full Casimir interaction (zero temperature) at small plate separations is well described by taking only the electrostatic interaction between surface plasmons. We now show that this remains valid at nonzero temperature. The fundamental reason is that at short distances ($\lambda \ll 1$), the lowest cavity modes [above the plasmonic one, $\omega_+(k)$] have a characteristic frequency in the order of $2\pi c/L$ that already falls in the transparency band of the mirrors ($\omega > \omega_\mathrm{p}$).

The full Casimir free energy $\mathcal{F}_\mathrm{Lif} = \varphi_\mathrm{Lif}(\lambda,\tau)E_\mathrm{C}$ can be obtained from the Lifshitz formula [Lifshitz, 1956; Bezerra et al., 2002a]. In our scaled units,

$$\varphi_\mathrm{Lif}(\lambda,\tau) = -2\aleph\lambda\tau \sum_P {\sum_{n=0}^{\infty}}' \Gamma_P(2\pi n\lambda\tau)\,, \tag{6.33}$$

$$\Gamma_P(X) = \int_X^\infty \mathrm{d}\kappa\, \kappa \log[1-\tilde{r}_P^2(\mathrm{i}X,\kappa)e^{-2\kappa}]\,. \tag{6.34}$$

The index $P = \mathrm{s},\mathrm{p}$ denotes the polarization. The numbers $X_n = 2\pi n\lambda\tau$ are scaled Matsubara frequencies. We need expressions for the Fresnel reflection coefficients [cf. Eq. (3.20), App. B.3] in terms of the rescaled variables κ and X

$$\tilde{r}_\mathrm{s}(\mathrm{i}X,\kappa) = \frac{\kappa-\kappa_m}{\kappa+\kappa_m}, \quad \tilde{r}_\mathrm{p}(\mathrm{i}X,\kappa) = \frac{\tilde{\varepsilon}(\mathrm{i}X)\kappa-\kappa_m}{\tilde{\varepsilon}(\mathrm{i}X)\kappa+\kappa_m} \tag{6.35}$$

with $\kappa_m = \sqrt{\kappa^2+(2\pi\lambda)^2}$ and the dielectric function of the plasma model [cf. Eq. (6.2)] $\tilde{\varepsilon}(\mathrm{i}X) = 1+(2\pi\lambda/X)^2$.

Fig. 6.8 shows the scaled free energies for both the full Casimir interaction (dashed curves) and the plasmonic contribution alone (solid curves). A good asymptotic agreement is visible at short distances even at nonzero temperature. In this regime, we can, therefore, obtain detailed information on the thermodynamics of the Casimir effect by just considering the plasmonic contribution which can be worked out in analytic form quite easily. For example, we can immediately conclude that the (full) Casimir entropy at $\lambda \ll 1$ is given by Eq. (6.29) at low temperatures ($\tau \ll 1$) and by Eq. (6.30) for $\tau \gg 1$.

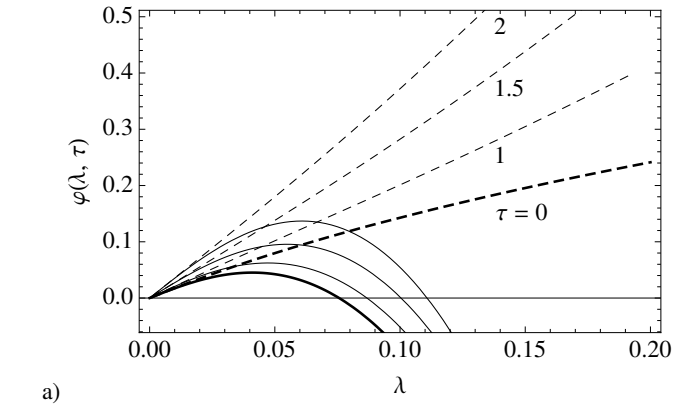

a)

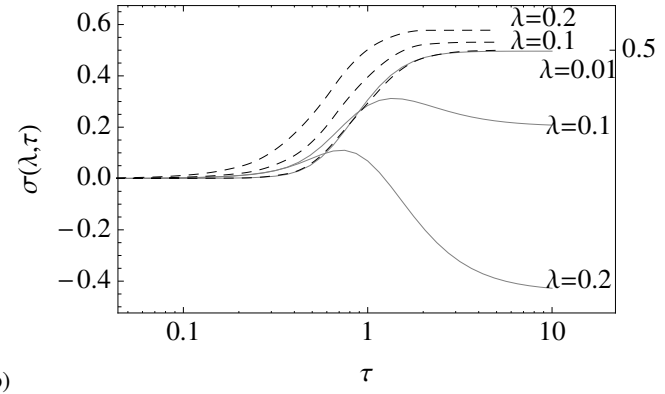

b)

Figure 6.8: a) Casimir free interaction energy including all modes (Lifshitz theory with the plasma model, dashed lines), compared to its plasmonic counterpart (solid). All energies are expressed relative via the correction factor $\varphi(\lambda, \tau)$.
b) Casimir entropy vs. temperature for all modes (plasma model, dashed), compared to the contribution of plasmonic modes only (solid). Entropies expressed via the correction factor $\sigma(\lambda, \tau)$.

6.3.2 Casimir entropy at low temperatures

With respect to the Casimir entropy, Figs. 6.8a) and b) illustrate that the Lifshitz expression deviates significantly from the plasmonic contribution when $\lambda \gtrsim 0.1$. It is obvious that propagating (photonic) modes then become relevant.

The dimensionless correction factor for the Casimir entropy of the plasma model can be written as the following integral over (scaled) real frequencies

$$\sigma_{\mathrm{Lif}}(\lambda, \tau) = -\frac{4}{\pi\zeta(3)} \int_0^\infty \frac{x \, \mathrm{d}x}{\sinh^2 x} \mathrm{Im} \sum_P M_P(2x\lambda\tau) \, , \tag{6.36}$$

where $P = \mathrm{s},\ \mathrm{p}$ indicates again the polarization and

$$M_P(\Omega) = \int_0^\infty \mathrm{d}\kappa\ \kappa \ln\left[1 - \tilde{r}_P^2(\Omega,\kappa)e^{-2\kappa}\right] + \int_0^\Omega \mathrm{d}y\ y \ln\left[1 - \tilde{r}_P^2(\Omega,-\mathrm{i}y)e^{2\mathrm{i}y}\right]\ . \tag{6.37}$$

The first (second) integral in Eq. (6.37) corresponds to the evanescent wave (propagating wave) sector, respectively. For s-polarization, the argument of the logarithm is always positive in the first integral, hence its imaginary part vanishes. This does not happen for the p-polarization, where the first integral gives the contribution of surface plasmons (evanescent branch) which has been evaluated before. At present, we are interested here in the propagating contribution only.

The function $x/\sinh^2 x$ significantly differs from zero only for $x \lesssim 1$. In the limit $\lambda\tau \ll 1$, we can therefore expand the integrands in $M_P(\Omega)$ for small y and Ω since $y \leq \Omega \ll 1$. This yields

$$\mathrm{Im}\, M_\mathrm{s}(\Omega) \approx -\frac{\pi}{4}\Omega^2 + \frac{\Omega^3}{3\pi\lambda}\,(1+\pi\lambda)\ ,\quad \mathrm{Im}\, M_\mathrm{p}(\Omega) \approx -\frac{\pi}{4}\Omega^2 + \frac{\Omega^3}{3\pi\lambda}\,(3+\pi\lambda)\ . \tag{6.38}$$

Performing the x-integral in Eq. (6.36),

$$\sigma(\lambda,\tau) \xrightarrow[\tau\ll 1]{\lambda\tau\ll 1} 12(\lambda\tau)^2\left[1 - \frac{8\pi^2\tau}{45\zeta(3)}\frac{2+\pi\lambda}{3}\right]\ . \tag{6.39}$$

Note, however, that this result contains the propagating branch of the plasmonic mode $\omega_+(k)$. It contributes a free energy

$$\begin{aligned}\vartheta_+^{\mathrm{pr}}(\lambda,\tau) = &-2\aleph\,(\lambda\tau)^3\left[\mathcal{L}\left(\frac{g_+(-z_+)}{\lambda\tau}\right) - \mathcal{L}\left(\frac{g_+(0)}{\lambda\tau}\right)\right] \\ &-\aleph(\lambda\tau)\int_{-z_+}^0 \ln\left[1 - e^{-\frac{g_a}{\lambda\tau}}\right]\mathrm{d}z,\end{aligned} \tag{6.40}$$

where $g_+(-z_+) = \sqrt{z_+}$ as noted before, and $g_+(0) = 2\pi\lambda/\sqrt{1+\pi\lambda}$ gives the (dimensionless) wavevector for which the dispersion relation $\omega_+(k)$ crosses the light cone. Reviewing the analysis from Sec. 6.1.2, it is easy to see that in the limit $\lambda\tau \ll 1$ considered here, the polylogarithmic term dominates in Eq. (6.41) and becomes $\mathcal{L}(\sqrt{z_+}/\lambda\tau) \approx \zeta(3)$. According to Eq. (6.27) this corresponds to an entropy contribution

$$\sigma_+^{\mathrm{pr}}(\lambda,\tau) \xrightarrow[\tau\ll 1]{\lambda\tau\ll 1} -12(\lambda\tau)^2\ . \tag{6.41}$$

Subtracting this contribution from Eq. (6.39), we find the entropy of the propagating photonic modes:

$$\sigma_{\mathrm{ph}}(\lambda,\tau) \xrightarrow[\tau\ll 1]{\lambda\tau\ll 1} 12(\lambda\tau)^2\left[2 - \frac{8\pi^2\tau}{45\zeta(3)}\frac{2+\pi\lambda}{3}\right]\ , \tag{6.42}$$

where the first term is twice the value obtained for perfect mirrors. This is precisely compensated by the plasmonic contribution. Indeed, for intermediate distances $1 \ll \lambda \ll 1/\tau$, both Eqs. (6.31) and (6.42) are valid, and their sum reproduces the entropy of the full Casimir effect calculated in [Bezerra et al., 2002a,b, 2004; Brevik et al., 2006]. Evaluating Eq. (19) of [Bezerra et al., 2004] in the regime of intermediate distances, we have

$$\sigma_{\rm Lif}(\lambda,\tau) \xrightarrow[\lambda\gg 1]{\lambda\tau\ll 1} 12(\lambda\tau)^2\left[1+\frac{1}{\pi\lambda}-\frac{8\pi^2\tau}{45\zeta(3)}\frac{\pi\lambda+2}{3}\right] . \tag{6.43}$$

6.3.3 Beyond thermal equilibrium

Until now, we have assumed both metallic slabs to be at the same temperature T. The previous results enable us to deal in a simple way with a more general situation, too, where each of the (otherwise identical) slabs is described by a local temperature T_1 and T_2. The general theory in this case was investigated by Dorofeyev [1998]; Antezza et al. [2008]: the nonequilibrium Casimir interaction for a symmetric cavity is obtained by simply averaging over the equilibrium free energies of the two mirrors

$$\mathcal{F}^{\rm neq}(L,T_2,T_1) = \frac{1}{2}\left[\mathcal{F}^{\rm eq}(L,T_2)+\mathcal{F}^{\rm eq}(L,T_1)\right] . \tag{6.44}$$

(Antezza et al. [2008] derived this result for the pressure, but the same reasoning can be applied for the free energy.) This Casimir pressure would fall right between the lower curves a) in Fig. 6.9, for example. Combining this formalism with the previous results of this chapter, it is straightforward to calculate the plasmonic contribution to the nonequilibrium Casimir free energy. Using the split (6.9) of the plasmonic free energy into a zero-temperature and a thermal part, Eq. (6.44) gives for two slabs at different temperatures

$$\varphi^{\rm neq}(\lambda,\tau_2,\tau_1) = \eta(\lambda)+\frac{1}{2}\left[\vartheta(\lambda,\tau_2)+\vartheta(\lambda,\tau_1)\right] . \tag{6.45}$$

From the results given above, we conclude that qualitatively, the behavior of $\varphi^{\rm neq}(\lambda,\tau_2,\tau_1)$ is similar to the equilibrium configuration, including a change in sign of the force with the distance. This is also confirmed by the asymptotic expressions for long/short distance and low/high temperature that can be easily extracted from the above results. The total Casimir force between identical plates, however, is always attractive, as is known from Dorofeyev [1998]; Antezza et al. [2008] for all temperatures.

Let us now consider a slightly different nonequilibrium scenario where temperature is still raised locally (in one plate), but only for a subclass of modes. If it were possible to increase the mean excitation of the plasmonic modes on one plate, above the equilibrium level of the propagating (photonic) modes, the total Casimir free energy would read

$$\varphi^{\rm neq}_{\rm Lif}(\lambda,\tau_2,\tau_1) = \varphi_{\rm Lif}(\lambda,\tau_1)+\frac{1}{2}\left[\vartheta(\lambda,\tau_2)-\vartheta(\lambda,\tau_1)\right] , \tag{6.46}$$

where the first term is the total Casimir free energy at equilibrium. The set of curves b) in Fig. 6.9 illustrates that this scenario can create a regime where the *total* Casimir force

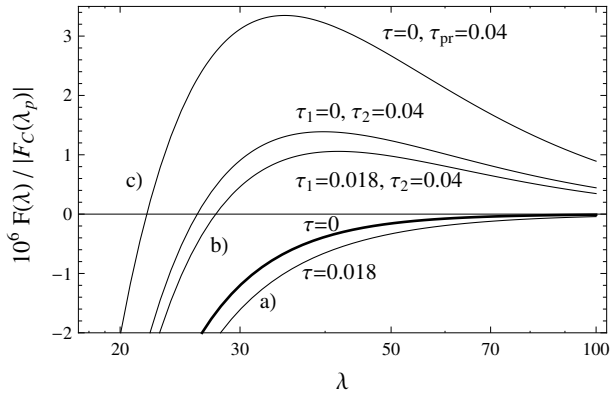

Figure 6.9: Total Casimir force (per unit area) in thermal equilibrium (thick line) and in different nonequilibrium scenarios. The force is normalized to $10^{-6}|F_{\rm C}(\lambda_{\rm p})|$, approximately $3.65\,\mu\,$Pa for gold ($\lambda_{\rm p} = 136\,$nm). In these units, $T = 300\,$K ($665\,$K) corresponds to $\tau \approx 0.018$ (0.04), respectively. a) Total equilibrium at temperature τ: attractive pressure at all distances. b) Surface-plasmon modes of one plate out of equilibrium at temperature τ_2, all other modes at temperature τ_1. c) All modes at τ, except for the propagating branch of the plasmonic mode [$\omega_+(k)$] which is at temperature $\tau_{\rm pr}$. The sign change to repulsion (positive pressure) would occur for gold at distances between $\approx 2.7\,\mu$m and $3.7\ \mu$m.

becomes repulsive, and this over a fairly large range of distances. We plot the Casimir pressure (nonequilibrium force per unit area) when the photonic modes are either at the scaled temperature τ_1 (zero or room temperature), and the plasmonic modes on plate 2 at $\tau_2 > \tau_1$. It appears that this setting breaks the delicate balance between photonic and plasmonic modes we found in Sec. 6.3.1. A similar interpretation has been put forward by Pitaevskii [2005] for the change in distance dependence of the atom-surface interaction out of equilibrium. The two values for τ_1 give close results because in the intermediate distance range, the effect of the temperature is still moderate for the equilibrium case. As could be expected, the inversion distance increases and the maximal repulsion becomes weaker as τ_1 increases towards τ_2.

We have also included in Fig. 6.9 a scenario where only a limited range of the surface-plasmon spectrum is selectively excited. For simplicity, we consider the propagating part of the plasmonic mode $\omega_+(k)$ to be populated at a temperature different from the rest of the system. From the free energy connected with this contribution, given in Eq. (6.41), the nonequilibrium free energy becomes

$$\tilde{\varphi}^{\rm neq}_{\rm Lif}(\lambda,\tau_{\rm pr},\tau) = \varphi_{\rm Lif}(\lambda,\tau) + \vartheta^{\rm pr}_{+}(\lambda,\tau_{\rm pr}) - \vartheta^{\rm pr}_{+}(\lambda,\tau)\,, \tag{6.47}$$

where $\tau_{\rm pr}$ is the temperature of the propagating plasmons and τ is the temperature of all other modes. The corresponding pressure [curve c) in Fig. 6.9] increases with respect to the previous nonequilibrium scenario by approximately a factor of 2, and repulsion sets in at a somewhat shorter distance. This is because, firstly, the – otherwise attractive – mode

$\omega_-(k)$ is less excited and, secondly, because the propagating branch of $\omega_+(k)$ dominates the interaction at these distances and excites the electron plasma on both plates rather than a single one. Clearly, even the excitation of a limited part of the surface-plasmon spectrum is sufficient to reach a repulsive regime.

The selective excitation of surface-plasmon modes is a well-studied problem, e.g. [Renger et al., 2009] and references therein. Most of the setups have to cope with the fact that the corresponding electromagnetic field is evanescent and, therefore, cannot be excited directly by laser photons incident from free space. A Kretschmann or Otto configuration [Raether, 1988] together with a wide-angle light source could provide an interesting starting point for an experimental implementation of the nonequilibrium Casimir setup. In fact, Fig. 6.9 [curve c)] shows that the most significant change can be achieved by exciting propagating modes. These couple to free-space light fields and can be excited by shining a laser [Povinelli et al., 2005] from the side onto the gap between the mirrors. (See [Ovchinnikov, 2000] for a related discussion.) This option has the drawback of a very limited optical access in a typical Casimir setup (large plates at short distance). One can also use, however, a thin metal plate and illuminate it from the back side. The surface-plasmon modes in this geometry are still very similar to the situation considered so far, if the plate thickness is large enough (no coupling between the surface modes on both sides, see [Economou, 1969]).

Due to the large number of photons present in a laser, a repulsive regime can be reached even if only a limited angular range ($\mathbf{k}$-range) is covered. Corrugated surfaces are of some help, if a broader range of wave vectors is to be excited in an experimental setup: not only do they convert plasmons into far-field radiation [Greffet et al., 2002] and vice-versa, but also a single plasmon mode excited by a laser on a rough surface is spread over a large angular range by surface scattering [Raether, 1988].

6.4 Summary and Discussion

We have calculated the contribution to the thermal Casimir effect due to surface plasmons, which are hybrid field-matter eigenmodes of metallic surfaces. The expression we found for the free energy of interaction is valid at any distance and temperature, and we have derived its asymptotics at small, intermediate, and large distances. Thermal effects become significant when the distance is larger than the thermal wavelength λ_T, similar to perfectly conducting plates, and below λ_T for nonequilibrium configurations. The other length scale of the system (plasma wavelength) determines the detailed behavior of the free energy.

We have found that at short distances and temperatures the thermal correction is small, and that the plasmonic Casimir interaction changes sign with distance, leading to a repulsive regime, as has been known from zero temperature [Intravaia and Lambrecht, 2005; Intravaia et al., 2007]. This goes hand in hand with a change of sign of the plasmonic Casimir entropy. In the short-distance regime, we found that the complete Casimir inter-

action between metallic plates (described by the plasma dielectric function) is completely dominated by the surface-plasmon contribution. The asymptotic scaling laws explain why $T = 0$ is a good approximation in most experimentally relevant situations (intermediate distance regime, low temperature). In this regime the known result for the complete plasma model is recovered in a simple way by adding propagative photonic modes.

Things are different at high temperatures and large distances. Here, it was shown that the plasmonic Casimir interaction is determined by a branch of the surface-plasmon dispersion relation corresponding to propagating modes, resulting in a large repulsive contribution that is enhanced by the temperature. This effect is probably one of the best illustrations of Casimir repulsion that arises from the radiation pressure of a standing wave mode. The pressure is repulsive, because the travelling photons are bouncing off the cavity walls, while the reference mode, a single-interface plasmon, has an evanescent field with zero radiation pressure.

The balance between plasmonic and photonic modes was emphasized by considering two configurations out of global thermal equilibrium where plasmonic modes are selectively excited to a higher temperature. These configurations show a crossover to a total Casimir force that becomes repulsive at plate distances $L \approx 20\,\lambda_\mathrm{p} \ldots 25\,\lambda_\mathrm{p}$ (a few microns for gold). This can be understood qualitatively in terms of radiation pressure due to the propagating branch of the plasmonic mode. We emphasize that this happens at distances shorter than the thermal wavelength where the Casimir pressure is stronger.

In conclusion, it seems in principle possible to tune the sign of the Casimir force by the selective excitation of the surface plasmons. Still, future research must address experimentally relevant questions for such a scheme, e.g. how to avoid exciting photonic modes just above the plasmonic one and how to populate plasmonic modes over a sufficiently wide angular range.

Chapter 7

Summary and Outlook

In this thesis, the main focus was put on ways in which atoms and solid surfaces influence each other on mesoscopic length scales, giving rise to, e.g., the dispersion interactions (vdWCP forces, energy shifts), surface-induced transitions (state broadening), or the dynamic dressing of atoms by virtual surface-mode quanta. Aspects of interatomic (or intermolecular) and surface-surface interactions were presented complementarily. All these phenomena have as their common origin the electromagnetic field fluctuations that surround polarizable bodies.

This observation provides the foundation of a quantum field theoretical description of atoms (molecules), electromagnetic fields, and macroscopic objects known as *molecular quantum electrodynamics (MQED)*. We have generalized a fully quantized field theory to initial nonequilibrium states in Chapter 2. As an example, this has allowed for a reconsideration of the interaction potential between two atoms, one of which is initially excited; a problem which has been controversally discussed in the past.

Another result recovered from MQED is the rate of surface-noise-induced atomic transitions between magnetic sublevels (Chapter 3). This has direct implications for atom chips, where transitions between trappable and untrappable magnetic levels present a fundamental limit for miniaturization. Ohmic losses and nonlocal (ballistic) transport produce characteristic signatures in the magnetic noise spectrum, which can be directly addressed in measurements of the lifetime of trapped atoms. We found that the magnetic field noise at distances smaller than an electronic mean free path is less intense than predicted previously, if ballistic charge transport in a conductor is included in the model. The effect occurs similarly in doped semiconductors, metals, and superconductors and has its origin in Thomas-Fermi screening of magnetic fields. This parallels the screening of electric fields by surface charges, which makes the electric surface response largely material-independent in conductors. Magnetic field fluctuations in the extreme near field of a body were also found to be more coherent than anticipated from work on electric fields, with the magnetic correlation length directly connected to the electronic mean free path. In a complementary discussion of electromagnetic field noise, we identified electric patch potentials on the surface (due to trapped charges or adsorbates) as a relevant source of noise in quantum computing applications with trapped Rydberg states that puts a limit to coherence. They have, for the moment, less impact on the magnetic trap life times of atom chips.

The investigation of the magnetic dipole contributions to the van der Waals-Casimir-

Polder potential between atoms and a conducting surface in Chapter 4 underlined the role of ohmic losses. Compared with electric dipole transitions of isolated atoms, magnetic transitions have much lower frequencies so that the thermal occupation of field modes becomes relevant. We found in fact a strong impact of temperature on the magnetic dispersion interaction: Depending on the setting (superconductor or normal metal), the magnetic dipole-coupling contribution can be either enhanced or strongly suppressed, as compared to zero temperature. This behavior is unexpected from the electric dipole coupling but parallels closely effects known from the Casimir interaction between metallic mirrors. Magnetic atom-surface interactions might therefore provide an alternative setting to investigate open questions in the temperature dependence of the Casimir interaction. The large magnetic dipole moments of Rydberg states and spectroscopic techniques will be of help here.

In Chapter 5, the MQED treatment of atom-surface interactions was complemented by an alternative approach based on time-dependent perturbation theory. We studied the evolution of an atom after a nonadiabatic change of a system parameter. It is common to attribute these dynamics to the adaption of a cloud of virtual photons that surrounds the atom, known as *(partial) atomic dressing*. We generalized previous work limited to ideally reflecting boundaries to general materials and found that surface-mode excitations can give a dominant contribution to the transient forces acting on an atom during the dressing.

Surface plasmons play also an important role in the Casimir interaction between two conducting plates. While isolated surfaces feature a single plasmon mode, the degeneracy is lifted in a cavity, leading to a more complex mode structure. At distances well below a plasma wavelength, the Casimir interaction can actually be attributed completely to the electrostatic interaction between the surface plasmons. We confirmed in Chapter 6 that this result holds at arbitrary temperature and obtained asymptotes for thermodynamic potentials in different regimes of distance and temperature. The impact of plasmonic modes is not restricted to the near field. Selective excitations of surface plasmons to nonequilibrium states, e.g. by frustrated internal reflection of laser light, can be used to tune the total force between the plates and even to switch it from attraction to repulsion. This may have applications in the mitigation of stiction in microelectromechanical systems.

In the different aspects of fluctuation-induced physics considered in this thesis, a number of concepts have been recurring. For instance, we have seen how nonequilibrium effects give rise to rich physics whenever initial excitations are present in a system. Special cases are the nonequilibrium two-body interaction of Chapter 2 or the Casimir cavity formed by plates of different temperature considered in Chapter 6. In such setups, the investigation of energy flux provides interesting perspectives for future work. In fact, much effort has recently been made to model and measure the near-field heat transfer between two surfaces, e.g. [Volokitin and Persson, 2007; Rousseau et al., 2009]. Superconductors have been another recurring topic of this thesis. Both in magnetic microtraps for cold atomic gases and in interactions of the Casimir/vdWCP type, the unique ability to

control Johnson noise (ohmic losses) makes superconductors highly interesting for fundamental physics and applications. Because of the strong technological relevance, future work should head towards the study of residual magnetic flux in inhomogeneous (type-II) superconductors outside the Meißner regime.

Today, microfabrication of solid structures has reached the mesoscopic lengthscales comparable to the wavelengths of the light emitted and absorbed by the matter they are made of. Here, interesting perspectives are opened by the precise control over optical properties and the dominating role of the surface modes, in the field of nanoplasmonics, with broad applications, e.g. in the near-field spectroscopy of biomolecules [Willets and Van Duyne, 2007]. Surface-mode control has been used to enhance near-field heat flux [van Zwol et al., 2012; Guérout et al., 2012]. In contrast, the Casimir force is significantly reduced if a grating structure is used [Intravaia et al., 2012]. Similarly, polaritonic mode contributions could create a repulsive regime in a cavity made of a metamaterial, even in thermal equilibrium.

From all this, we can expect that, beyond the topics touched in this thesis, the study of mesoscale systems, where classical and quantum effects meet, will keep bringing about new insights into fundamental physics as well as surprising new technology.

Appendix A

Response Functions of Nonequilibrium QFT

This appendix contains material presented in *Feynman diagrams for dispersion interactions out of equilibrium* by H. R. Haakh, J. Schiefele, and Henkel, *International Journal of Modern Physics Conference Series* **14**, 347 (2012). Appendix A.4 is adapted from the article *Temperature dependence of the magnetic Casimir-Polder interaction* by H. R. Haakh, F. Intravaia, C. Henkel, S. Spagnolo, R. Passante, B. Power, and F. Sols, *Physical Review A* **80**, 062905 (2009).

The framework of molecular quantum electrodynamics has been presented in Chapter 2. This and the following appendix give explicit expressions for correlation functions in leading order and discuss some of their properties.

A.1 Atom Fields and Propagators

We consider a set of two-level atoms, distinguishable by an index $N = A, B, \ldots$. The starting point of the perturbation theory is the interaction Hamiltonian (2.3),

$$
\begin{aligned}
H_{AF}^{\mathrm{el}} &= -\sum_N \left[E_i(\boldsymbol{r}_N) d_i^{egN} \psi^{eN} \psi^{gN\dagger} + E_i(\boldsymbol{r}_N) d_i^{geN} \psi^{eN}(\boldsymbol{r}) \psi^{eN\dagger} \right] \\
&= \sum_N
\end{aligned}
$$

We removed all atomic mode functions, which is reasonable for immobile and sharply localized atoms[1]. Any position dependence is, therefore, carried by the electromagnetic field.

The atoms are characterized by their internal two-level structure of energies $\epsilon_{g,e}^N$ of the ground state and excited state (index g, e, respectively). The results will only depend on the Bohr frequencies $\omega_N \equiv \epsilon_e^N - \epsilon_g^N$. For a single transition, the superscripts ^{eg} of the matrix elements $\boldsymbol{d}^{egN} = \boldsymbol{d}^{geN*}$ can be omitted. The annihilation operator $\psi^{aN}(t)$ evolves in the interaction picture proportional to $\exp(-\mathrm{i}\epsilon_a^N t)$ with $a = g, e$. The bare

[1] This limits our description to single atoms. Spatially extended wave packets play a role, e.g. in BECs described by macroscopic wave functions [Schiefele and Henkel, 2010a,b; Schiefele, 2011], see also [Rzazewski and Zakowicz, 1992].

(leading order) propagator for a ground-state atom N is given by

$$g_{11}^N(t',t) = -\mathrm{i}\langle\psi^{gN}(t')\psi^{gN\dagger}(t)\rangle\theta(t'-t) = \int\frac{d\omega}{2\pi}\,\frac{e^{-\mathrm{i}\omega(t'-t)}}{\omega-\epsilon_g^N+\mathrm{i}\,0^+}\,. \tag{A.1}$$

For an excited atom, e_{11} is obtained using ϵ_e in place of ϵ_g. The step function $\theta(t'-t)$ arises because in this nonrelativistic theory, there are no antiparticles. In the frequency representation, we thus have the Feynman rules

$$g_{11}^N(\omega) = \frac{1}{\omega-\epsilon_g^N+\mathrm{i}\,0^+} = \quad\longrightarrow\quad , \quad e_{11}^N(\omega) = \frac{1}{\omega-\epsilon_e^N+\mathrm{i}\,0^+} = \quad\dashrightarrow\quad . \tag{A.2}$$

A.2 Atomic Polarizabilities

It is also useful to consider the atomic polarization operator for atom N

$$\boldsymbol{P}^N(t) \equiv \boldsymbol{d}^N\psi^e(t)\psi^{g\dagger}(t) + \boldsymbol{d}^{N*}\psi^g(t)\psi^{e\dagger}(t)\,,$$

that appears in the dipole interaction (2.3). The general correlation functions for an atom N in state a are the Keldysh polarizabilities, where Greek indices $\alpha,\beta = 1,2$ denote the branches of the Keldysh-Schwinger contour (Fig. 2.1.)

$$\alpha_{\alpha\beta,ij}^{aN}(t',t) = \frac{\mathrm{i}}{\hbar}\langle T_c\{P_{\alpha,i}^N(t')P_{\beta,j}^N(t)\}\rangle_a = \frac{d_i^N d_j^{N*}}{\hbar}\tilde{\alpha}_{\alpha\beta}^{aN}(t',t)\,. \tag{A.3}$$

In the second step the spatial tensor structure (latin indices) has been separated for brevity. This may be used to contract the spatial tensor structure early in calculations, leading to simpler scalar expressions. Among the different Keldysh correlation functions, the Feynman polarizability is the most important, for our purposes:

$$\tilde{\alpha}_{11}^{eN}(t',t) = -\big(\langle e|\psi_e^{N\dagger}(t')\psi_e^N(t)|e\rangle g_{11}^N(t',t) + t'\leftrightarrow t\big) \tag{A.4}$$

$$= -\int\frac{d\omega}{2\pi}\,e^{-\mathrm{i}\omega(t'-t)}\left(\frac{1}{\omega_N+\omega+\mathrm{i}\,0^+}+\frac{1}{\omega_N-\omega+\mathrm{i}\,0^+}\right). \tag{A.5}$$

For an excited atom N, the Feynman polarizability $\alpha_{11}^{eN}(\omega)$ has a pole in the upper right quadrant of the ω-plane which leads to a residue ('resonant' contribution) when contour techniques are used to move integrations to the positive imaginary axis. The nonequilibrium ('off-diagonal') Keldysh functions gives only a resonant (or 'on-shell') contribution

$$\tilde{\alpha}_{12}^{eN}(t',t) = \langle e|\psi_e^{N\dagger}(t)\psi_g^N(t)\psi_e^N(t')\psi_g^{N\dagger}(t')|e\rangle \quad = \int\frac{d\omega}{2\pi}\,e^{-\mathrm{i}\omega(t'-t)}\,2\pi\mathrm{i}\,\delta(\omega-\omega_N)\,. \tag{A.6}$$

To illustrate the link to the retarded polarizability, we form the combination

$$\tilde{\alpha}_{11}^{eN}(t',t) - \tilde{\alpha}_{12}^{eN}(t',t) = -\int \frac{d\omega}{2\pi} e^{-\mathrm{i}\omega(t'-t)} \left(\frac{1}{\omega_N + \omega + \mathrm{i}\,0^+} + \frac{1}{\omega_N - \omega - \mathrm{i}\,0^+} \right)$$
$$= \int \frac{d\omega}{2\pi} e^{-\mathrm{i}\omega(t'-t)} \tilde{\alpha}_{\mathrm{R}}^{e}(\omega) \;, \tag{A.7}$$

which has poles in the lower half-plane only, as it should. Note the analogy with Eqs. (2.12) and (2.13). For ground-state atoms, replace $\omega_N \leftrightarrow -\omega_N$ in these expressions, cf. Eq. (2.20) for α_{11}^{gN}. Note finally, that in a diagrammatic representation it is possible to draw polarization lines (α) rather than atomic propagators (g, e), cf. [Janowicz et al., 2003; Sherkunov, 2005, 2007]. This reduces the number of contributing diagrams even further and leads to a higher symmetry between photon and atomic fields. However, – in our opinion – this comes at the cost of physical intuition.

A.3 Response Functions of the Electromagnetic Field

We use the following Keldysh–Green's functions for the photon field, and allow for a thermal state at a temperature T, so that the fluctuation-dissipation theorem applies, cf. Sec. 2.1.4 and [Callen and Welton, 1951; Agarwal, 1975b; van Leeuwen et al., 2006]. Then

$$\boldsymbol{G}_{11}(x',x) = \mathrm{i}\langle T\big\{\boldsymbol{E}(x')\boldsymbol{E}(x)\big\}\rangle_T = \int \frac{d\omega}{2\pi} e^{-\mathrm{i}\omega(t'-t)} \boldsymbol{G}_{11}(\boldsymbol{r}',\boldsymbol{r},\omega) \;, \tag{A.8}$$

$$\boldsymbol{G}_{12}(x',x) = \mathrm{i}\langle \boldsymbol{E}(x)\boldsymbol{E}(x')\rangle_T = \mathrm{i}\int \frac{d\omega}{2\pi} e^{-\mathrm{i}\omega(t'-t)}\; 2\bar{n}(\omega)\; \mathrm{Im}[\boldsymbol{\mathcal{G}}(\boldsymbol{r}',\boldsymbol{r},\omega)] \;, \tag{A.9}$$

$$\boldsymbol{G}_{21}(x',x) = \mathrm{i}\langle \boldsymbol{E}(x')\boldsymbol{E}(x)\rangle_T = -\,\mathrm{i}\int \frac{d\omega}{2\pi} e^{-\mathrm{i}\omega(t'-t)} 2\bar{n}(-\omega)\, \mathrm{Im}[\boldsymbol{\mathcal{G}}(\boldsymbol{r}',\boldsymbol{r},\omega)] \;. \tag{A.10}$$

Here, spatial tensors are only indicated by bold symbols and we abbreviate space time arguments by $x = (\boldsymbol{r}, t)$.

Note that the thermal occupation number becomes $n(\pm\omega) \to \mp\theta(\mp\omega)$ at zero temperature. The Fourier transforms $\boldsymbol{G}_{12}(\omega)$ and $\boldsymbol{G}_{21}(\omega)$ are then only supported by negative / positive frequencies, respectively. The link to the retarded Green's function $\boldsymbol{\mathcal{G}}$ is provided by the relations

$$\boldsymbol{\mathcal{G}} = \boldsymbol{G}_{11} - \boldsymbol{G}_{12}, \qquad \boldsymbol{\mathcal{G}}^* = \boldsymbol{G}_{11} - \boldsymbol{G}_{21} \;, \tag{A.11}$$

which parallel Eq. A.7 and Eqs. (2.12), (2.13). Note that at real frequencies, $\boldsymbol{\mathcal{G}}^*(\omega)$ is the advanced Green's function.

From the relations (A.8)- (A.11) , the Feynman propagator in the frequency domain (diagrammatic photon line) can be expressed in the form

$$\boldsymbol{G}_{11}(\boldsymbol{r}',\boldsymbol{r},\omega) = \quad \sim\!\sim\!\sim \quad = \mathrm{Re}[\boldsymbol{\mathcal{G}}(\boldsymbol{r}',\boldsymbol{r},\omega)] + \mathrm{i}\coth(\beta\omega/2)\,\mathrm{Im}[\boldsymbol{\mathcal{G}}(\boldsymbol{r}',\boldsymbol{r},\omega)] \,. \quad \text{(A.12)}$$

Of course, $\boldsymbol{\mathcal{G}}$ is just the classical retarded Green's tensor, forms of which are given in App. B.1 for free space and App. B.2 in the presence of a surface.

A.4 Magnetic Matrix Elements

This section gives the magnetic transition matrix elements used in the calculations of magnetic polarizabilities. The simplest approach used is the spin-$1/2$ system (two-level atom) with states $|m_S\rangle = |\pm\tfrac{1}{2}\rangle$. The dipole operator is $\boldsymbol{\mu} = \mu_B\hbar g_S \boldsymbol{S}$.

In a surface mounted trap, the quantization axis of the *trap basis* may be tilted by an angle θ with respect to the z-axis (surface normal), as shown in Fig. 3.1. We need, however, components of μ in the cartesian *surface basis*, connected to the trap basis by the relations [Henkel et al., 1999]

$$\begin{aligned}
S_x|m_S\rangle &= \tfrac{1}{2}\cos(\theta)|-m_S\rangle + \sin(\theta)m_S|m_S\rangle \,, && \text{(A.13)}\\
S_y|m_S\rangle &= \mathrm{i}m_S|-m_S\rangle \,, && \text{(A.14)}\\
S_z|m_S\rangle &= \tfrac{1}{2}\sin(\theta)|-m_S\rangle + \cos(\theta)m_S|m_S\rangle \,. && \text{(A.15)}
\end{aligned}$$

Since all magnetic polarizabilities are proportional to the transition frequency [see App. A.2 or, e.g., Eqs. (4.3), (4.7)], the S_z elements connecting identical states do not contribute. We need only the off-diagonal elements

$$\langle -\tfrac{1}{2}|S_x|\tfrac{1}{2}\rangle = \tfrac{1}{2}\cos(\theta)\,, \langle -\tfrac{1}{2}|S_y|\tfrac{1}{2}\rangle = \tfrac{\mathrm{i}}{2}\,, \langle -\tfrac{1}{2}|S_z|\tfrac{1}{2}\rangle = -\tfrac{1}{2}\sin(\theta)\,, \quad \text{(A.16)}$$

already given in Eq. (3.6). In the case $\theta = 0$ the previous matrix elements give Eq. (4.18).

Finally, we outline the calculation of matrix elements for an atom prepared in a particular hyperfine s-state, e.g. the $^{87}\mathrm{Rb}$ considered in Sec. 4.4.2. Here, we have orbital momentum $L = 0$, nuclear spin $I = 3/2$, and a single valence electron, hence the total electronic angular momentum $J = S = 1/2$. For an angle $\theta = 0$, the trap basis and the surface basis coincide and

$$\mu_i^{ab} = \langle a|\mu_i|b\rangle = \langle F, m_F|\mu_i|F', m_F'\rangle \,. \quad \text{(A.17)}$$

The dipole operator $\boldsymbol{\mu} = \mu_B\hbar(g_S\boldsymbol{S} + g_L\boldsymbol{L} + g_I\boldsymbol{I}) \approx \mu_B\hbar g_S\boldsymbol{S}$, because of the small value of the nuclear Landé g-factor $g_I \sim m_e/m_p$. We express the states $|a\rangle, |b\rangle$ in the uncoupled basis of the spin and nuclear spin momenta with the help of the Clebsch-Gordan coefficients

$$|F, m_F\rangle = \sum_{m_I, m_S} C_{F,m_F}^{m_I,m_S}|m_I, m_S\rangle \,, \quad \text{(A.18)}$$

where the action of the components of the spin operator on an electronic spin state is known [Eqs. (A.13-A.15)]. Hence, we find ($\theta = 0$)

$$\mu_x^{ab} = g_S \mu_B \sum_{m_I, m_S} \tfrac{1}{2} C_{F',m'_F}^{m_I,-m_S} C_{F,m_F}^{m_I,m_S} , \tag{A.19}$$

$$\mu_y^{ab} = -i g_S \mu_B \sum_{m_I, m_S} m_S C_{F',m'_F}^{m_I,-m_S} C_{F,m_F}^{m_I,m_S} , \tag{A.20}$$

$$\mu_z^{ab} = -g_S \mu_B \sum_{m_I, m_S} m_S C_{F',m'_F}^{m_I,m_S} C_{F,m_F}^{m_I,m_S} . \tag{A.21}$$

Appendix B

Electromagnetic Response

This appendix is based on material from the articles *Temperature dependence of the magnetic Casimir-Polder interaction* by H. R. Haakh, F. Intravaia, C. Henkel, S. Spagnolo, R. Passante, B. Power, and F. Sols, *Physical Review A* **80**, 062905 (2009), and *Magnetic near fields as a probe of charge transport in spatially dispersive conductors* by H. R. Haakh and C. Henkel, *European Physical Journal B* **85**, 46 (2012).

B.1 Green's Tensor in a Homogeneous Medium

The retarded electric Green's tensor describes the electric field

$$E_i(\boldsymbol{r},\omega) = \mathcal{G}_{ij}(\boldsymbol{r},\boldsymbol{r}',\omega)d_j(\omega) \tag{B.1}$$

radiated by a point-like fictitious dipole test-source $\boldsymbol{d}$ placed in $\boldsymbol{r}'$. The retarded Green tensor in a linear and isotropic medium depends only on the difference $\boldsymbol{r}'-\boldsymbol{r}$ and is given by

$$\begin{aligned}\boldsymbol{\mathcal{G}}^{\mathrm{free}}(\boldsymbol{r},\boldsymbol{0},\omega) &= \frac{\omega^2}{c^2}\frac{e^{\mathrm{i}kr}}{4\pi\varepsilon_0 r}\left[\left(1+\frac{\mathrm{i}}{kr}-\frac{1}{k^2r^2}\right)\mathbb{1}-\left(1+\frac{3\mathrm{i}}{kr}-\frac{3}{k^2r^2}\right)\hat{\boldsymbol{r}}\otimes\hat{\boldsymbol{r}}\right] \\ &\quad +\frac{1}{3\varepsilon_0}\delta(r)\mathbb{1}\,, \end{aligned}\tag{B.2}$$

where $\hat{\boldsymbol{r}} = \boldsymbol{r}/|r|$, and $k = \sqrt{\varepsilon(\omega)\mu(\omega)}\omega/c$ ($\mathrm{Im}[k] > 0$) is the wave vector in the medium. Obviously, $[\boldsymbol{\mathcal{G}}(\boldsymbol{r},\boldsymbol{0},\omega)]^2$ oscillates at half the medium wavelength, while $|\boldsymbol{\mathcal{G}}(\boldsymbol{r},\boldsymbol{0},\omega)|^2$ does not. This is the origin of the spatially oscillating and nonoscillating results discussed in Sec. 2.2.4.

Along the same lines, an oscillating magnetic dipole is connected to the magnetic fields by the magnetic Green's tensor

$$\boldsymbol{\mathcal{H}}^{\mathrm{free}} = c^{-2}\boldsymbol{\mathcal{G}}^{\mathrm{free}}\,. \tag{B.3}$$

For coinciding spatial arguments, the finite imaginary part of the free space Green's tensor reads

$$c^{-2}\,\mathrm{Im}\,\mathcal{G}_{ij}^{\mathrm{free}}(\boldsymbol{r},\boldsymbol{r},\omega) = \mathrm{Im}\,\mathcal{H}_{ij}^{\mathrm{free}}(\boldsymbol{r},\boldsymbol{r},\omega) = \frac{\mu_0\omega^3}{6\pi c^3}\delta_{ij}\,. \tag{B.4}$$

A detailed discussion including regularization procedures for the divergent real part can be found in [de Vries et al., 1998; Cohen-Tannoudji et al., 1987].

B.2 Green's Tensor Near a Surface

Near a single surface, this field consists of a free-space part and a reflected contribution (cf. Sec. 2.3), and therefore $\boldsymbol{\mathcal{H}} = \boldsymbol{\mathcal{H}}^{\mathrm{free}} + \boldsymbol{\mathcal{H}}^{\mathrm{refl}}$. The general expression for the reflected magnetic (retarded) Green's tensor can be conveniently expressed in the Weyl basis of transverse[1] s- and p-polarized waves, also known as TE- and TM-polarization, respectively. (Labels refer to the geometry of electric field components, see Fig. 3.1 (left), hence the tensor symbols below.) Here, we have [Sipe, 1981]

$$\boldsymbol{\mathcal{H}}^{\mathrm{refl}}(\boldsymbol{r},\boldsymbol{r'},\omega) \;=\; \frac{\mu_0}{4\pi}\int_0^\infty \frac{pdp}{\kappa} e^{-\kappa|z+z'|}\left[r_{\mathrm{s}}(\omega,p)\boldsymbol{P} + r_{\mathrm{p}}(\omega,p)\boldsymbol{S}\right], \tag{B.5}$$

where $\kappa = \sqrt{p^2-\omega^2/c^2}$ ($\mathrm{Re}\,\kappa \geq 0,\ \mathrm{Im}\,\kappa \leq 0$ for $\omega > 0$) is the propagation constant. The quantities r_{s} and r_{p} are the reflection coefficients for s- and p-polarized waves and the tensor structure is included in

$$\boldsymbol{P} \;=\; \begin{pmatrix} \kappa^2\left(J_0(px) - \frac{J_1(px)}{px}\right) & 0 & -p\kappa J_1(px) \\ 0 & \kappa^2\frac{J_1(px)}{px} & 0 \\ p\kappa J_1(px) & 0 & p^2 J_0(px) \end{pmatrix} \tag{B.6}$$

$$\boldsymbol{S} \;=\; \frac{\omega^2}{c^2}\begin{pmatrix} \frac{J_1(px)}{px} & 0 & 0 \\ 0 & J_0(px) - \frac{J_1(px)}{px} & 0 \\ 0 & 0 & 0 \end{pmatrix}, \tag{B.7}$$

where $J_n(x)$ indicate Bessel functions of the first kind. The relative separation along the surface has length $x = [|\boldsymbol{r}-\boldsymbol{r'}|^2 - |z-z'|^2]^{1/2}$ and points in the direction of the x-axis, as shown in Fig. 3.1 (right). In the limit $\boldsymbol{r} \to \boldsymbol{r'}$, we obtain the one-point reflected Green's tensor of Eq. (3.5)

$$\begin{aligned}\mathcal{H}^{\mathrm{refl}}_{ij}(z,\omega) = \frac{\mu_0}{8\pi}\int_0^\infty dp\, p\kappa\, e^{-2\kappa z}\times \\ \times\left[\left(r_{\mathrm{s}}(\omega,p) + \frac{\omega^2}{c^2\kappa^2}r_{\mathrm{p}}(\omega,p)\right)[\delta_{ij} - \hat{z}_i\hat{z}_j] + 2\frac{p^2}{\kappa^2}r_{\mathrm{s}}(\omega,p)\hat{z}_i\hat{z}_j\right],\end{aligned}$$

that depends only on the distance from the surface [Sipe, 1981].

From the geometry of electromagnetic waves in free space and the continuity conditions at a surface, the magnetic reflected Green's tensor can be obtained from the electric one $\boldsymbol{\mathcal{G}}$ by swapping the reflection coefficients [Henkel et al., 1999]

$$\boldsymbol{\mathcal{H}}^{\mathrm{refl}} \equiv c^{-2}\boldsymbol{\mathcal{G}}^{\mathrm{refl}}(r_{\mathrm{s}} \leftrightarrow r_{\mathrm{p}})\,. \tag{B.8}$$

[1] It is an interesting observation, that even though the tensor describes the full dipole response including static fields, there are no longitudinal components. This is due to cancellations under the wave-vector integral [Sipe, 1981; Pieplow et al., 2012].

B.3 Reflection Coefficients

For s-, p-polarized incident waves, reflectivities are given by [Ford and Weber, 1984]

$$r_{\mathrm{p}} = \frac{Z_{\mathrm{p}}^0 - Z_{\mathrm{p}}}{Z_{\mathrm{p}}^0 + Z_{\mathrm{p}}}, \qquad r_{\mathrm{s}} = \frac{Z_{\mathrm{s}} - Z_{\mathrm{s}}^0}{Z_{\mathrm{s}} + Z_{\mathrm{s}}^0}\,, \tag{B.9}$$

where the surface impedances $Z_{\mathrm{s}}, Z_{\mathrm{p}}$ are made dimensionless by normalizing to the impedance of free space, $\tilde{Z}_0 = \sqrt{\mu_0/\varepsilon_0} \approx 377\,\Omega$. The well-known results for a local isotropic, nonmagnetic [$\mu(\omega) = 1$] bulk medium are [Jackson, 1975; Dressel and Grüner, 2002]

$$Z_{\mathrm{p}}^{\mathrm{loc}} = \frac{\sqrt{\varepsilon(\omega)\omega^2/c^2 - p^2}}{\varepsilon(\omega)\omega/c}, \qquad Z_{\mathrm{s}}^{\mathrm{loc}} = \frac{\omega/c}{\sqrt{\varepsilon(\omega)\omega^2/c^2 - p^2}}\,, \tag{B.10}$$

where $\varepsilon(\omega)$ is the dielectric function, $p = |\boldsymbol{p}|$ is the in-plane wave vector, and the square roots have positive imaginary parts. The surface impedance on the vacuum side, $Z_{\mathrm{p}}^0, Z_{\mathrm{s}}^0$, is obtained by setting $\varepsilon(\omega) = 1$.

It is convenient to use the propagation constants $\kappa = \sqrt{p^2 - \omega^2/c^2}$ in vacuum and $\kappa_m = \sqrt{p^2 - \varepsilon(\omega)\omega^2/c^2}$ in the medium (roots with $\mathrm{Re}\,\kappa \geq 0, \mathrm{Im}\,\kappa \leq 0$) to express the reflectivities (B.9) for a local isotropic, nonmagnetic bulk medium. This recovers the Fresnel formulas of Eq. (3.20)

$$r_{\mathrm{s}}(\omega, p) = \frac{\kappa - \kappa_m}{\kappa + \kappa_m}, \quad r_{\mathrm{p}}(\omega, p) = \frac{\varepsilon(\omega)\kappa - \kappa_m}{\varepsilon(\omega)\kappa + \kappa_m}\,.$$

For good conductors, where $|\varepsilon(\omega)| \gg 1$, asymptotic expansions for different regimes of the wave vector are given in Table 3.1.

B.4 Reflection from a Nonlocal Metal

B.4.1 Impedances for specular and diffuse scattering

We now give details the surface response in a nonlocal metal used in Ch. 3. In these materials, ballistic charge transport leads to a wave vector dependence of the bulk response. In this case, the solution of Maxwell's equations at the surface requires additional boundary conditions or a description of the underlying scattering problem for charges at the metal-vacuum interface [Reuter and Sondheimer, 1948; Kliewer and Fuchs, 1968; Ford and Weber, 1984; Flores and García-Moliner, 1979].

The additional boundary condition that charge carriers undergo specular reflection at the inner metal surface can be exploited to extend the conducting half-space into a fictitious homogeneous medium, using a similar symmetry for the fields [Reuter and

Sondheimer, 1948; Kliewer and Fuchs, 1968; Ford and Weber, 1984]. The resulting impedances are

$$Z_{\rm s}^{\rm spec}(\omega,p) = \frac{2{\rm i}\omega}{c\pi}\int_0^\infty dq \frac{1}{\varepsilon_t(\omega,\boldsymbol{k})\omega^2/c^2-k^2} \tag{B.11}$$

$$Z_{\rm p}^{\rm spec}(\omega,p) = \frac{2{\rm i}\omega}{c\pi}\int_0^\infty \frac{dq}{k^2}\left[\frac{p^2}{\varepsilon_l(\omega,\boldsymbol{k})\omega^2/c^2}+\frac{q^2}{\varepsilon_t(\omega,\boldsymbol{k})\omega^2/c^2-k^2}\right], \tag{B.12}$$

where the medium wave vector is $k^2=p^2+q^2$. If the medium is local, $\varepsilon_{t,l}$ do not depend on k, and a direct calculation of the integrals brings us back to the Fresnel impedances (B.10).

The diffuse reflection of conduction electrons at the surface has been considered by Reuter and Sondheimer [1948]; Kliewer and Fuchs [1970]; Foley and Devaney [1975]; Halevi and Fuchs [1984], but only for the propagating sector $p<\omega/c$. We have used the s-polarized impedance obtained by Foley and Devaney [1975] where the additional boundary condition is implemented via the so-called dielectric approximation. This means that in the basic linear current-field relation [Eq. (3.1)], the volume integral is restricted to the medium-filled half-space alone. Solving a Wiener-Hopf equation that follows from the Maxwell equations, one gets an impedance

$$Z_{\rm s}^{\rm diff}(\omega,p) = \frac{{\rm i}\pi\omega}{c}\left(\int_0^\infty {\rm d}q\,\ln\left[\frac{q^2}{k^2-\varepsilon_t(\omega,\boldsymbol{k})\omega^2/c^2}\right]\right)^{-1}. \tag{B.13}$$

This recovers correctly the local limit at all values of p. However, this is not true for the p-polarized impedance given in the same work and used in the numerical evaluation in Fig. 3.3. This is related to the violation of charge conservation at the surface in the dielectric approximation that has been discussed by Flores and García-Moliner [1977, 1979]; Foley and Devaney [1975]. We continue here with the specular boundary condition.

B.4.2 Limiting behavior of the reflectivities

For a metal with specular reflection of charge carriers, we change the variable in the q-integral in Eq. (B.11) according to $q=p\sqrt{t^2-1}$, so that the medium wave vector is $k=pt$. In the treatment of nonlocal metals, our focus is on low frequencies where in the local limit, $\varepsilon(\omega)\omega^2/c^2\approx 2{\rm i}/\delta^2(\omega)$ in terms of the skin depth (3.8), and on the sub-wavelength limit $p\gg\omega/c$. Here, the nonlocal dielectric function of the Boltzmann-Mermin model is expressed through the transverse Lindhard function and the skin depth, see Eqs. (3.8) and (3.10), respectively,

$$\frac{\omega^2}{c^2}\varepsilon_t(\omega,\boldsymbol{k}) \approx \frac{2{\rm i}f_t(0,{\rm i}/k\ell)}{\delta^2(\omega)}\,. \tag{B.14}$$

For simplicity, we drop in the following the frequency arguments and the redundant argument of the Lindhard function f_t. We are left with the integral

$$\begin{aligned} Z_{\rm s}^{\rm spec}(p) &= -\frac{2{\rm i}\omega}{\pi c}\int_1^\infty dt \frac{1}{\sqrt{t^2-1}\,pt\,[1-2{\rm i}f_t({\rm i}/p\ell t)/(p\delta t)^2]} \\ &\approx -\frac{2{\rm i}\omega}{\pi c}\int_1^\infty dt \frac{1+2{\rm i}f_t({\rm i}/p\ell t)/(p\delta t)^2}{\sqrt{t^2-1}\,pt} = -\frac{{\rm i}\omega}{cp}+\frac{2\omega/c}{p^4\delta^2\ell}\,. \end{aligned} \quad \text{(B.15)}$$

We expanded the denominator in the nonlocal regime ($p \gg 1/\delta, 1/\ell$) and replaced, in the last step, the transverse Lindhard function [Eq. (3.12)] by its asymptote for large $p\ell$:

$$f_t({\rm i}/p\ell t) = \frac{3\pi}{4p\ell t} + \mathcal{O}[(p\ell t)^{-2}]\,. \quad \text{(B.16)}$$

This result complies with a similar calculation by Esquivel and Svetovoy [2004]. The first term in Eq.(B.15) corresponds to the free-space surface impedance $Z_{\rm s}^0$ in the subwavelength limit ($p \gg \omega/c$). The reflection amplitude (B.9) therefore becomes

$$r_{\rm s}^{\rm spec}(p) \approx \frac{Z_{\rm s}^{\rm spec}(p)+{\rm i}\omega/(cp)}{Z_{\rm s}^{\rm spec}(p)-{\rm i}\omega/(cp)} \approx \frac{\rm i}{p^3\delta^2\ell} \quad \text{(B.17)}$$

which gives Eq. (3.16), and clearly differs from the $1/p^2$-dependence in the local case [cf. Table 3.1 and Fig. 3.3a)].

In the scenario where charge carriers are reflected diffusely rather than specularly, we start from Eq. (B.13). The same substitution of the integration variable gives

$$Z_{\rm s}^{\rm diff}(p) = \frac{{\rm i}\pi\omega/(cp)}{\displaystyle\int_1^\infty \frac{dt\,t}{\sqrt{t^2-1}}\ln\left[\frac{t^2-1}{t^2-2{\rm i}f_t({\rm i}/p\ell t)/(p\delta t)^2}\right]}\,. \quad \text{(B.18)}$$

The integrand is expanded in $1/(p\delta)^2$, and the integration can be performed explicitly

$$\begin{aligned} &\int_1^\infty \frac{dt\,t}{\sqrt{t^2-1}}\ln\left[\frac{t^2-1}{t^2-2{\rm i}(p\delta t)^{-2}f_t({\rm i}/p\ell t)}\right] \\ \approx\ &\int_1^\infty \frac{dt\,t}{\sqrt{t^2-1}}\left\{\ln\left[\frac{t^2-1}{t^2}\right]+\frac{2{\rm i}f_t({\rm i}/p\ell t)}{(p\delta t)^2}\right\} \\ =\ &-\pi+\frac{3\pi{\rm i}}{2p^3\delta^2\ell} \qquad \text{if } p\ell \gg 1\,. \end{aligned} \quad \text{(B.19)}$$

The resulting impedance reads

$$Z_{\rm s}^{\rm diff}(p) \approx -\frac{{\rm i}\omega}{cp}+\frac{3\omega/c}{2p^4\delta^2\ell}\,. \quad \text{(B.20)}$$

This differs from Eq. (B.15) only by a factor $3/4$ in the second term, so that the reflection amplitude is smaller by this number compared to the specular boundary condition, Eq. (B.17).

Appendix C

Models for Superconductors

C.1 BCS Conductivity with Nonlocal Transport

In this appendix, we give some details on the optical response functions of superconductors, based on the microscopic theory of Bardeen, Cooper, and Schrieffer [1957]. All calculations of optical conductivities in BCS superconductors build on the work by Mattis and Bardeen [1958]. There, closed forms were given only in the extremely anomalous ('dirty' and local) limit. Note that it was pointed out in previous work on electromagnetic noise near the superconducting surfaces [Hohenester et al., 2007] that this limit predicts too high a *coherence peak*, i.e. a maximum of $\mathrm{Re}\,\sigma$ as a function of temperature, and that the theory of Eliashberg [1960] may be better suited to describe experimental data.

For the numerical work in Chapter 3, we used a form of the optical BCS conductivity given by Pöpel [1989]. This model provides a nonlocal response function valid at arbitrary mean free paths ℓ and impurity scattering rates γ, and recovers the Lindhard model in the normally conducting state ($\Delta \to 0$). The local limit $p\ell \to 0$ agrees with the results of Zimmermann et al. [1991]; Berlinsky et al. [1993].

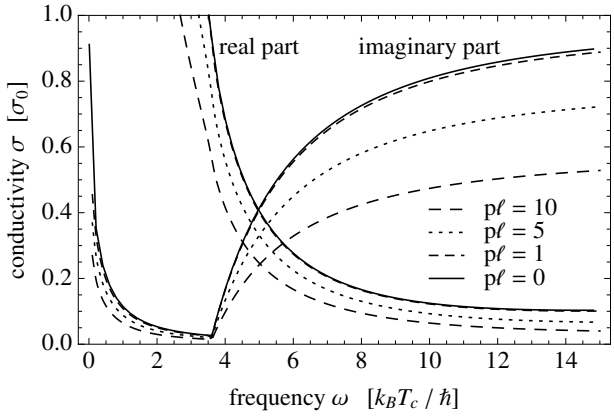

Figure C.1: Real and imaginary part of the BCS conductivity for different values of $p\ell$. Parameters for niobium taken from [Ashcroft and Mermin, 1987]. The limit $p\ell \to 0$ recovers the local limit of Zimmermann et al. [1991]; Berlinsky et al. [1993].

For convenience, we reproduce here expressions for the real and imaginary part [Pöpel, 1989, Eqs. (13) and (14)]:

$$\begin{aligned}\text{Re }\sigma(\omega,p) =& \frac{3\sigma_0}{\hbar\omega pl}\times \qquad \text{(C.1)}\\ &\times\Bigg[-\int_{\Delta}^{\infty} d\epsilon[f(\epsilon+\hbar\omega)-f(\epsilon)][(g(\epsilon)+1)R(a_-,b)+[g(\epsilon)-1]R(a_+,b)]+\\ &+\frac{1}{2}\theta(\hbar\omega-2\Delta)\int_{\Delta-\hbar\omega}^{-\Delta} d\epsilon[1-2f(\epsilon+\hbar\omega)][(g(\epsilon)+1)R(a_-,b)+(g(\epsilon)-1)R(a_+,b)]\Bigg]\end{aligned}$$

$$\begin{aligned}\text{Im }\sigma(\omega,p) =& \frac{3\sigma_0}{\hbar\omega pl}\times \qquad \text{(C.2)}\\ &\times\Bigg[-\int_{\Delta}^{\infty} d\epsilon[f(\epsilon+\hbar\omega)-f(\epsilon)](g(\epsilon)+1)S(a_-,b)-\\ &\quad-\int_{\Delta}^{\infty} d\epsilon[1-f(\epsilon)-f(\epsilon+\hbar\omega)][(g(\epsilon)-1)S(a_+,b)+\\ &+\frac{1}{2}\theta(\hbar\omega-2\Delta)\int_{\Delta-\hbar\omega}^{-\Delta} d\epsilon[1-2f(\epsilon+\hbar\omega)][(g(\epsilon)+1)S(a_-,b)+(g(\epsilon)-1)S(a_+,b)]+\\ &\quad+\int_{\max\{-\Delta,\Delta-\hbar\omega\}}^{\Delta} d\epsilon[1-2f(\epsilon+\hbar\omega)][(\tilde{g}(\epsilon)R(a_2,b+|a_1|)+S(a_2,b+|a_1|)]\Bigg]\,.\end{aligned}$$

Here, σ_0 is the static conductivity of the normal state and $f(\epsilon)=[\exp(\epsilon/k_BT)+1]^{-1}$ is the Fermi-Dirac distribution. The BCS gap function $\Delta=\Delta(T)$ can be approximated by closed expressions [Thouless, 1960; Townsend and Sutton, 1962]. Besides,

$$g(\epsilon)=\frac{\epsilon^2+\hbar\omega\epsilon+\Delta^2}{E_1E_2}\,, \qquad \tilde{g}(\epsilon)=\frac{\epsilon^2+\hbar\omega\epsilon+\Delta^2}{|E_1|E_2}\,, \qquad \text{(C.3)}$$

$$E_1=\sqrt{\epsilon^2-\Delta^2}\,, \qquad E_2=\sqrt{(\epsilon+\hbar\omega)^2-\Delta^2}\,, \qquad \text{(C.4)}$$

$$a_1=\frac{E_1}{p\ell\hbar\gamma}\,, \qquad a_2=\frac{E_2}{p\ell\hbar\gamma}\,, \qquad a_\pm=a_2\pm a_1\,, \qquad b=\frac{1}{p\ell}\,. \qquad \text{(C.5)}$$

The dimensionless functions R and S read

$$R(a,b)= -\tfrac{b}{2}+\tfrac{ab}{4}\ln\left(\tfrac{b^2+(1+a)^2}{b^2+(1-a^2)}\right)+\tfrac{1+b^2-a^2}{4}\left[\arctan\left(\tfrac{2b}{a^2+b^2-1}\right)+\pi\theta(1-a^2-b^2)\right] \qquad \text{(C.6)}$$

$$S(a,b)= \tfrac{a}{2}-\tfrac{1+b^2-a^2}{8}\ln\left(\tfrac{b^2+(1+a)^2}{b^2+(1-a^2)}\right)-\tfrac{ab}{2}\left[\arctan\left(\tfrac{2b}{a^2+b^2-1}\right)+\pi\theta(1-a^2-b^2)\right]\,. \qquad \text{(C.7)}$$

A numerical evaluation of the conductivity based on Eqs. (C.1) and (C.2) is plotted in Fig. C.1.

C.2 Analytical Continuation of the Local BCS Conductivity

This section contains material from *Optical BCS conductivity at imaginary frequencies and dispersion energies of superconductors* by G. Bimonte, H. R. Haakh, F. Intravaia, and C. Henkel, *Journal of Physics A* **43**, 145304 (2010)[1].

For calculations of dispersion interactions, such as the atom-surface interactions of Secs. 4.1.1 and 5.2.1), it is convenient to evaluate optical response functions in the complex frequency plane. From the BCS theory, the optical conductivity is known at real frequencies. In the case of a local BCS conductor with arbitrary scattering rates, expressions were given by Zimmermann et al. [1991]; Berlinsky et al. [1993], in full agreement with the local limit $p\ell \ll 1$ of the model of Sec. C.1 (solid curve in Fig. C.1).

It is common to perform an analytical continuation to complex frequencies through a Kramers-Kronig integral relation, cf. [Bimonte et al., 2005]. This approach is, however, inefficient for numerical calculations. In a recent publication [Bimonte et al., 2010], we have obtained a closed form of the optical conductivity at complex frequencies z ($\mathrm{Im}\, z > 0$), which we reproduce here. It turns out that a normal metal (Drude) contribution can be separated from the optical conductivity

$$\sigma(z) = \frac{\sigma_0}{1 - \mathrm{i}z/\gamma} + \delta_{\mathrm{BCS}}(z)\,. \tag{C.8}$$

The BCS correction is given by

$$\delta_{\mathrm{BCS}}(z) = \mathrm{i}\frac{\sigma_0\gamma}{2z}\int_{-\infty}^{\infty}\frac{d\epsilon}{E}[1-2f(\epsilon)]\left[g_+(z,\epsilon)+g_-(z,\epsilon)\right]\,, \tag{C.9}$$

$$g_\pm(z,\epsilon) = \frac{\epsilon^2 Q_\pm + [Q_\pm + \mathrm{i}\hbar\gamma]A_\pm}{Q_\pm[\epsilon^2 - (Q_\pm + \mathrm{i}\hbar\gamma)^2]}\,, \tag{C.10}$$

with the static conductivity of the normal state σ_0, the BCS gap function $\Delta = \Delta(T)$, and the Fermi-Dirac distribution $f(\epsilon) = [\exp(\epsilon/k_BT)+1]^{-1}$. Besides,

$$E = \sqrt{\epsilon^2+\Delta^2}\,, \quad A_\pm = E(E+\hbar z) + \Delta^2\,, \quad Q_\pm^2 = (E\pm\hbar z)^2 - \Delta^2\,. \tag{C.11}$$

It is straightforward to check that at real frequencies $z = \omega \in \mathbb{R}$, this recovers the expressions of Zimmermann et al. [1991], see [Bimonte et al., 2010, App. B]. At purely imaginary frequencies $z = \mathrm{i}\xi$ ($\xi \in \mathbb{R}$), parity arguments can be used to obtain

$$\delta_{\mathrm{BCS}}(\mathrm{i}\xi) = \frac{\sigma_0\gamma}{\xi}\int_{-\infty}^{\infty}\frac{d\epsilon}{E}[1-2f(\epsilon)]\,\mathrm{Re}\left[g_+(i\xi,\epsilon)\right]\,. \tag{C.12}$$

In the normal conductor limit ($\Delta \to 0$), $g_+(\mathrm{i}\xi,\epsilon)$ becomes purely imaginary, so that the BCS correction $\delta_{\mathrm{BCS}}(i\xi)$ vanishes, leaving only the Drude term in Eq. (C.8).

Eq. (C.12) was used in the numerical calculation of the atomic interaction with a local superconductor in Sec. 4.3.3. A calculation of the Casimir energy in a superconducting cavity based on this model was presented in [Bimonte et al., 2010].

[1] A partial previous presentation in my diploma thesis [Haakh, 2009] is acknowledged.

Bibliography

J. R. Ackerhalt and P. W. Milonni, 1984. *J. Opt. Soc. Am. B* **1**, 116.

G. S. Agarwal, 1975a. *Phys. Rev. A* **11**, 230.

G. S. Agarwal, 1975b. *Phys. Rev. A* **11**, 243.

E. Altewischer, M. van Exter, and J. Woerdman, 2002. *Nature* **418**, 304.

W. R. Anderson, J. R. Veale, and T. F. Gallagher, 1998. *Phys. Rev. Lett.* **80**, 249.

D. L. Andrews, 1989. *Chem. Phys.* **135**, 195.

D. L. Andrews and A. A. Demidov, 1999. *Resonance energy transfer*. Wiley, New York.

M. Antezza, L. P. Pitaevskii, and S. Stringari, 2004. *Phys. Rev. A* **70**, 053619.

M. Antezza, L. P. Pitaevskii, and S. Stringari, 2005. *Phys. Rev. Lett.*, **95**, 113202.

M. Antezza, L. P. Pitaevskii, S. Stringari, and V. B. Svetovoy, 2008. *Phys. Rev. A*, **77**, 022901.

N. W. Ashcroft and N. D. Mermin, 1987. *Solid state physics*. Holt, Rinehart and Winston, New York.

A. Aspect and J. Dalibard, 2003. *Prog. Math. Phys.* **30**, 93.

V. S. Bagnato, G. P. Lafyatis, A. G. Martin, E. L. Raab, R. N. Ahmad-Bitar, and D. E. Pritchard, 1987. *Phys. Rev. Lett.* **58**, 2194.

R. Balian and B. Duplantier, 1977. *Ann. Phys. (N. Y.)* **104**, 300.

R. Balian and B. Duplantier, 1978. *Ann. Phys. (N. Y.)* **112**, 165.

J. Bardeen, L. N. Cooper, and J. R. Schrieffer, 1957. *Phys. Rev.* **108**, 1175.

G. Barton, 1972. *Phys. Rev. A* **5**, 468.

G. Barton, 1979. *Rep. Prog. Phys.* **42**, 963.

G. Barton, 2012. *Lecture notes of the Casimir Physics School - Workshop at Lorentz-Center Leiden*.

D. Bedeaux and J. Vlieger, 2004. *Optical properties of surfaces*. World Scientific, Singapore.

R. Behunin, F. Intravaia, D. A. R. Dalvit, P. Maia Neto, and S. Reynaud, 2012. *Phys. Rev. A* **85**, 012504.

P. Ben-Abdallah and K. Joulain, 2010. *Phys. Rev. B* **82**, 121419(R).

H. Bender, P. W. Courteille, C. Marzok, C. Zimmermann, and S. Slama, 2010. *Phys. Rev. Lett.* **104**, 083201.

O. G. Berg and P. H. von Hippel, 1985. *Ann. Rev. Biophys. Biophys. Chem.* **14**, 131.

D. J. Bergman and M. I. Stockman, 2003. *Phys. Rev. Lett.* **90**, 027402.

A. J. Berlinsky, C. Kallin, G. Rose, and A.-C. Shi, 1993. *Phys. Rev. B* **48**, 4074.

P. R. Berman, R. W. Boyd, and P. W. Milonni, 2006. *Phys. Rev. A* **74**, 053816.

H. A. Bethe, 1947. *Phys. Rev.* **72**, 339.

V. B. Bezerra, G. L. Klimchitskaya, and V. M. Mostepanenko, 2002a. *Phys. Rev. A* **65**, 052113.

V. B. Bezerra, G. L. Klimchitskaya, and V. M. Mostepanenko, 2002b. *Phys. Rev. A* **66**, 062112.

V. B. Bezerra, G. L. Klimchitskaya, V. M. Mostepanenko, and C. Romero, 2004. *Phys. Rev. A* **69**, 022119.

V. B. Bezerra, G. L. Klimchitskaya, V. M. Mostepanenko, and C. Romero, 2008. *Phys. Rev. A* **78**, 042901.

S.-A. Biehs, E. Rousseau, and J.-J. Greffet, 2010. *Phys. Rev. Lett.* **105**, 234301.

G. Bimonte, 2008. *Phys. Rev. A* **78**, 062101.

G. Bimonte, 2009. *Phys. Rev. A* **79**, 042107.

G. Bimonte, E. Calloni, G. Esposito, and L. Rosa, 2005. *Nucl. Phys. B* **726**, 441.

G. Bimonte, G. L. Klimchitskaya, and V. M. Mostepanenko, 2009. *Phys. Rev. A* **79**, 042906.

G. Bimonte, H. R. Haakh, C. Henkel, and F. Intravaia, 2010. *J. Phys A* **43**, 145304.

A. Blais, R.-S. Huang, A. Wallraff, S. M. Girvin, and R. J. Schoelkopf, 2004. *Phys. Rev. A* **69**, 062320.

D. Bloch and M. Ducloy, 2005. *Adv. At. Mol. Opt. Phys.* **50**, 91.

K. Blomstedt, T. Setälä, and A. T. Friberg, 2007. *Phys. Rev. E* **75**, 026610.

J. Blum and G. Wurm, 2008. *Ann. Rev. Astron. Astrophys.* **46**, 21.

M. Bordag, 2006. *J. Phys. A* **39**, 6173.

M. Boström and B. E. Sernelius, 2000. *Phys. Rev. Lett.* **84**, 4757.

M. Boström and B. E. Sernelius, 2004. *Physica A* **339**, 53.

S. E. Boustani, P. R. Buenzli, and P. Martin, 2006. *Phys. Rev. E* **73**, 036113.

B. Bouvier, T. Gustavsson, D. Markovitsi, and P. Millié, 2002. *Chem. Phys.* **275**, 75.

T. H. Boyer, 1974. *Phys. Rev. A* **9**, 2078.

I. Brevik, S. Å. Ellingsen, and K. A. Milton, 2006. *New J. Phys.* **8**, 236.

M. L. Brongersma and P. G. Kik (eds.), 2007. *Surface plasmon nanophotonics*. Springer, Berlin.

P. R. Buenzli and P. A. Martin, 2005. *Europhys. Lett.* **72**, 42.

S. Y. Buhmann and S. Scheel, 2008. *Phys. Rev. Lett.* **100**, 253201.

S. Y. Buhmann and D.-G. Welsch, 2007. *Progr. Quant. Electron.* **31**, 51.

S. Y. Buhmann, M. R. Tarbutt, S. Scheel, and E. A. Hinds, 2008. *Phys. Rev. A* **78**, 052901.

E. Buks and M. L. Roukes, 2001. *Phys. Rev. B* **63**, 033402.

H. B. Callen and T. A. Welton, 1951. *Phys. Rev.* **83**, 34.

D. Cano, B. Kasch, H. Hattermann, R. Kleiner, C. Zimmermann, D. Koelle, and J. Fortágh, 2008. *Phys. Rev. Lett.* **101**, 183006.

F. Capasso and J. Munday, 2011. In [Dalvit et al., 2011], pages 249–286.

R. Carminati and J.-J. Greffet, 1999. *Phys. Rev. Lett.* **82**, 1660.

C. K. Carniglia and L. Mandel, 1971. *Phys. Rev. D* **3**, 280.

J. D. Carter and J. D. D. Martin, 2011. *Phy. Rev. A* **83**, 032902.

H. B. Casimir, 1948. *Indag. Math.* **10**, 261.

H. B. Casimir and D. Polder, 1948. *Phys. Rev.* **73**, 360.

L. S. Cederbaum, 1975. *J. Phys. B* **8**, 290.

R. G. Chambers, 1952. *Proc. Roy. Soc. A* **215**, 481.

H. B. Chan, V. A. Aksyuk, R. N. Kleiman, D. J. Bishop, and F. Capasso, 2001. *Science* **291**,

1941.

P. O. Chapuis, M. Laroche, S. Volz, and J.-J. Greffet, 2008a. *Phys. Rev. B* **77**, 12.

P. O. Chapuis, S. Volz, C. Henkel, K. Joulain, and J.-J. Greffet, 2008b. *Phys. Rev. B* **77**, 35431.

F. Chen, G. L. Klimchitskaya, V. M. Mostepanenko, and U. Mohideen, 2007. *Phys. Rev. B* **76**, 035338.

C. C. Cheng and M. G. Raymer, 1999. *Phys. Rev. Lett.* **82**, 4807.

D. B. Chklovskii and P. A. Lee, 1992. *Phys. Rev. B* **45**, 5240.

A. E. Cohen and S. Mukamel, 2003a. *Phys. Rev. Lett.* **91**, 233202.

A. E. Cohen and S. Mukamel, 2003b. *J. Phys. Chem. A* **107**, 3633.

C. Cohen-Tannoudji, J. Dupont-Roc, and G. Grynberg, 1987. *Photons and atoms*. Intereditions, Paris.

G. Compagno, G. M. Palma, R. Passante, and F. Persico, 1995a. *J. Phys. B* **28**, 1105.

G. Compagno, R. Passante, and F. Persico, 1995b. *Atom-field interactions and dressed atoms*. Cambridge University Press, Cambridge.

A. M. Contreras-Reyes and W. L. Mochan, 2005. *Phys. Rev. A* **72**, 034102.

J.-Y. Courtois, J.-M. Courty, and J. C. Mertz, 1996. *Phys. Rev. A* **53**, 1862.

D. Craig and T. Thirunamachandran, 1998. *Molecular quantum electrodynamics*. Dover Publications, Mineola.

R. A. Craig, 1968. *J. Math. Phys.* **9**, 605.

J. A. Crosse, S. Å. Ellingsen, K. Clements, S. Y. Buhmann, and S. Scheel, 2010. *Phys. Rev. A* **82**, 010901.

J. C. da Silva, A. M. Neto, H. Q. Plácido, M. Revzen, and A. E. Santana, 2001. *Physica A* **292**, 411.

R. R. Dagastine, D. C. Prieve, and L. R. White, 2000. *J. Coll. Interf. Sci.* **231**, 351.

J. Dalibard, J. Dupont-Roc, C. Cohen-Tannoudji, et al., 1982. *J. Physique* **43**, 1617.

D. A. R. Dalvit and S. K. Lamoreaux, 2008. *Phys. Rev. Lett.*, **101**, 163203.

D. A. R. Dalvit, P. W. Milonni, D. C. Roberts, and F. S. S. da Rosa (eds.), 2011. *Casimir physics*. Springer, Heidelberg.

P. Danielewicz, 1984. *Ann. Phys. (N.Y.)* **152**, 239.

T. David, Y. Japha, V. Dikovsky, R. Salem, C. Henkel, and R. Folman, 2008. *Eur. Phys. J. D* **48**, 321.

P. de Vries, D. van Coevorden, and A. Lagendijk, 1998. *Rev. Mod. Phys.* **70**, 447.

R. Decca, D. Lopez, E. Fischbach, G. Klimchitskaya, D. Krause, and V. Mostepanenko, 2005. *Ann. Phys. (N.Y.)* **318**, 37.

R. Decca, V. Aksyuk, and D. López, 2011. In [Dalvit et al., 2011], pages 287–309.

M. DeKieviet, U. Jentschura, and G. Lach, 2011. In [Dalvit et al., 2011], pages 393–418.

A. A. Deniz, S. Mukhopadhyay, and E. A. Lemke, 2008. *J. R. Soc. Interface* **5**, 15.

B. V. Derjaguin and L. D. Landau, 1941. *Zh. Eksp. Teor. Fiz* **11**, 802.

B. V. Derjaguin, V. M. Muller, and Y. P. Toporov, 1975. *J. Coll. Interf. Sci.* **53**, 314.

M.-C. Desjonquères and D. Spanjaard, 1996. *Concepts in surface physics*. Springer, Berlin, 2nd edition.

L. Deslauriers, S. Olmschenk, D. Stick, W. K. Hensinger, J. Sterk, and C. Monroe, 2006. *Phys. Rev. Lett.* **97**, 103007.

V. Dikovsky, V. Sokolovsky, B. Zhang, C. Henkel, and R. Folman, 2009. *Eur. Phys. J. D* **51**, 247.

R. B. Dingle, 1953. *Physica* **19**, 311.

J. F. Dobson and T. Gould, 2012. *J. Phys. C* **24**, 073201.

V. V. Dodonov, 2010. *Physica Scripta* **82**, 038105.

V. V. Dodonov and A. V. Dodonov, 2006. *J. Phys. B* **39**, S749.

I. A. Dorofeyev, 1998. *J. Phys. A* **31**, 4369.

I. A. Dorofeyev and E. A. Vinogradov, 2011. *Phys. Rep.* **504**, 75.

I. A. Dorofeyev, H. Fuchs, and J. Jersch, 2002. *Phys. Rev. E* **65**, 026610.

M. Dressel and G. Grüner, 2002. *Electrodynamics of solids*. Cambridge University Press, New York.

V. Druzhinina and M. DeKieviet, 2003. *Phys. Rev. Lett.* **91**, 193202.

S. Du, M. B. Squires, Y. Imai, L. Czaia, R. A. Saravanan, V. Bright, J. Reichel, T. W. Hänsch, and D. Z. Anderson, 2004. *Phys. Rev. A* **70**, 053606.

R. Dubessy, T. Coudreau, and L. Guidoni, 2009. *Phys. Rev. A* **80**, 031402.

H. T. Dung, L. Knöll, and D.-G. Welsch, 1998. *Phys. Rev. A* **57**, 3931.

F. J. Dyson, 1949. *Phys. Rev.* **75**, 1736.

D. Dzsotjan, A. S. Sørensen, and M. Fleischhauer, 2010. *Phys. Rev. B* **82**, 075427.

I. E. Dzyaloshinskii, E. M. Lifshitz, and L. P. Pitaevskii, 1961. *Adv. Phys.* **10**, 165.

J. Earman and D. Fraser, 2006. *Erkenntnis* **64**, 305.

C. Eberlein and D. Robaschik, 2004. *Phys. Rev. Lett.* **92**, 233602.

W. Eckhardt, 1984. *Physica A* **128**, 467.

E. N. Economou, 1969. *Phys. Rev.* **182**, 539.

A. Einstein, 1905. *Ann. Phys.* **322**, 132.

A. Einstein and O. Stern, 1913. *Ann. Phys.* **345**, 551.

R. Eisenschitz and F. London, 1930. *Z. Phys. A* **60**, 491.

G. M. Eliashberg, 1960. *Sov. Phys. JETP* **11**, 696.

S. Å. Ellingsen, I. Brevik, J. S. Hoye, and K. A. Milton, 2009a. *J. Phys.: Conf. Series* **161**, 012010.

S. Å. Ellingsen, S. Buhmann, and S. Scheel, 2009b. *Phys. Rev. A* **80**, 22901.

S. Å. Ellingsen, S. Y. Buhmann, and S. Scheel, 2009c. *Phys. Rev. A* **79**, 052903.

S. Å. Ellingsen, S. Y. Buhmann, and S. Scheel, 2010. *Phys. Rev. Lett.* **104**, 223003.

S. Å. Ellingsen, S. Y. Buhmann, and S. Scheel, 2011. *Phys. Rev. A* **84**, 060501.

T. Emig, N. Graham, R. L. Jaffe, and M. Kardar, 2007. *Phys. Rev. Lett.* **99**, 170403.

A. Emmert, A. Lupaşcu, G. Nogues, M. Brune, J. Raimond, and S. Haroche, 2009. *Eur. Phys. J. D* **51**, 173.

R. J. Epstein, S. Seidelin, D. Leibfried, J. H. Wesenberg, J. J. Bollinger, J. M. Amini, R. B. Blakestad, J. Britton, J. P. Home, W. M. Itano, et al., 2007. *Phys. Rev. A* **76**, 033411.

R. Esquivel and V. B. Svetovoy, 2004. *Phys. Rev. A* **69**, 062102.

R. Esquivel-Sirvent, C. Villarreal, W. L. Mochán, A. M. Contreras-Reyes, and V. B. Svetovoy, 2006. *J. Phys. A* **39**, 6323.

H. Failache, S. Saltiel, M. Fichet, D. Bloch, and M. Ducloy, 1999. *Phys. Rev. Lett.* **83**, 5467.

H. Failache, S. Saltiel, A. Fischer, D. Bloch, and M. Ducloy, 2002. *Phys. Rev. Lett.* **88**, 243603.

D. Farias and K.-H. Rieder, 1998. *Rep. Prog. Phys.* **61**, 1575.

S. Fasel, F. Robin, E. Moreno, D. Erni, N. Gisin, and H. Zbinden, 2005. *Phys. Rev. Lett.* **94**, 110501.

H. Fearn, R. J. Cook, and P. W. Milonni, 1995. *Phys. Rev. Lett.* **74**, 1327.

P. J. Feibelman, 1982. *Prog. Surf. Sci.* **12**, 287.

J. Feinberg, A. Mann, and M. Revzen, 2001. *Ann. Phys. (N.Y.)* **288**, 103.

R. Fermani, S. Scheel, and P. L. Knight, 2006. *Acta Phys. Hung. A* **26**, 55.

D. K. Ferry, 2012. *Science* **335**, 45.

A. L. Fetter and J. D. Walecka, 2003. *Quantum theory of many-particle systems*. Dover Publications, Mineola.

R. P. Feynman, 1961. In *Solvay Institute Proceedings*, page 76. Wiley Interscience, New York.

F. Flores and F. García-Moliner, 1977. *J. Physique* **38**, 863.

F. Flores and F. García-Moliner, 1979. *Introduction to the theory of solid surfaces*. Cambridge University Press, New York.

J. T. Foley and A. J. Devaney, 1975. *Phys. Rev. B* **12**, 3104.

R. Folman, P. Krüger, J. Schmiedmayer, J. Denschlag, and C. Henkel, 2002. *Adv. At. Mol. Opt. Phy.* **48**, 263.

G. W. Ford and W. H. Weber, 1984. *Phys. Rep.* **113**, 195.

T. Förster, 1949. *Z. Naturforsch. A* **4**, 321.

J. Fortágh and C. Zimmermann, 2005. *Science* **307**, 860.

J. Fortágh and C. Zimmermann, 2007. *Rev. Mod. Phys.* **79**, 235.

J. Fortágh, S. Kraft, A. Günther, C. Trück, P. Wicke, and C. Zimmermann, 2004. *Opt. Comm.* **243**, 45.

H. Fröhlich, 1970. *Nature* **228**, 1093.

H. Fröhlich, 1975. *Proc. Nat. Acad. Sci. USA* **72**, 4211.

M. Fuechsle, J. A. Miwa, S. Mahapatra, H. Ryu, S. Lee, O. Warschkow, L. C. L. Hollenberg, G. Klimeck, and M. Y. Simmons, 2012. *Nature Nanotech.* in press.

A. Gaëtan, Y. Miroshnychenko, T. Wilk, A. Chotia, M. Viteau, D. Comparat, P. Pillet, A. Browaeys, and P. Grangier, 2009. *Nature Phys.* **5**, 115.

T. F. Gallagher, 1988. *Rep. Prog. Phys.* **51**, 143.

T. F. Gallagher, 1994. *Rydberg atoms*. Cambridge University Press, New York.

F. García-Moliner and F. Flores, 1977. *J. Physique* **38**, 851.

F. J. Garcia-Vidal, L. Martin-Moreno, T. W. Ebbesen, and L. Kuipers, 2010. *Rev. Mod. Phys.* **82**, 729.

A. Geier and G. Schön, 1982. *J. Low Temp. Phys.* **46**, 151.

E. Gerlach, 1971. *Phys. Rev. B* **4**, 393.

B. Geyer, G. L. Klimchitskaya, and V. M. Mostepanenko, 2010. *Phys. Rev. B* **81**, 104101.

M. Gierling, P. Schneeweiss, G. Visanescu, P. Federsel, M. Häffner, D. P. Kern, T. E. Judd, A. Günther, and J. Fortágh, 2011. *Nature Nanotech.* **6**, 446.

V. L. Ginzburg and L. D. Landau, 1956. *Sov. Phys. JETP* **2**, 589.

R. Golestanian, 2005. *Phys. Rev. Lett.* **95**, 230601.

F. Gori, D. Ambrosini, and V. Bagini, 1994. *Opt. Comm.* **107**, 331.

M. P. Gorza and M. Ducloy, 2006. *Eur. Phys. J. D* **40**, 343.

Y. V. Gott, M. S. Ioffe, and V. G. Telkovskii, 1962. *Nucl. Fusion Suppl.* **3**, 1045.

P. Goy, J. M. Raimond, M. Gross, and S. Haroche, 1983. *Phys. Rev. Lett.* **50**, 1903.

J.-J. Greffet and C. Henkel, 2007. *Contemp. Phys.* **48**, 183.

J.-J. Greffet, R. Carminati, K. Joulain, J.-P. Mulet, S. Mainguy, and Y. Chen, 2002. *Nature* **416**, 61.

E. Gross and R. Dreizler, 1995. *Density functional theory*. Springer, Berlin.

R. Guérout, J. Lussange, F. S. S. Rosa, J.-P. Hugonin, D. A. R. Dalvit, J.-J. Greffet, A. Lambrecht, and S. Reynaud, 2012. *ArXiv: 1203.1496*.

R. Haag, 1955. *Kgl. Danske Vidensk. Selsk. Mat. Fys. Medd.* **29**, 1.

H. R. Haakh, 2009. *Cavity QED with superconductors and its application to the Casimir effect*. Diploma thesis, Universität Potsdam. http://opus.kobv.de/ubp/volltexte/2009/3256/.

H. R. Haakh, F. Intravaia, C. Henkel, S. Spagnolo, R. Passante, B. Power, and F. Sols, 2009. *Phys. Rev. A* **80**, 062905.

H. R. Haakh, F. Intravaia, and C. Henkel, 2010. In M. Bordag and K. Milton (eds.), *Quantum Field Theory under the Influence of External Conditions (Proceedings of QFExt '09)*, pages 194–198. World Scientific, Singapore.

P. Halevi and R. Fuchs, 1984. *J. Phys. C* **17**, 3889.

W. Hänsel, J. Reichel, P. Hommelhoff, and T. W. Hänsch, 2001. *Phys. Rev. Lett.* **86**, 608.

D. M. Harber, J. M. McGuirk, J. M. Obrecht, and E. A. Cornell, 2003. *J. Low Temp. Phys.* **133**, 229.

D. M. Harber, J. M. Obrecht, J. M. McGuirk, and E. A. Cornell, 2005. *Phys. Rev. A* **72**, 33610.

C. Henkel, 2005. *Eur. Phys. J. D* **35**, 59.

C. Henkel and B. Horovitz, 2008. *Phys. Rev. A* **78**, 42902.

C. Henkel and F. Intravaia, 2010. *Int. J. Mod. Phys. A* **25**, 2328.

C. Henkel and K. Joulain, 2005. *Europhys. Lett.* **72**, 929.

C. Henkel and K. Joulain, 2006. *Appl. Phys. B* **84**, 61.

C. Henkel and M. Wilkens, 1999. *Europhys. Lett.* **47**, 414.

C. Henkel, S. Pötting, and M. Wilkens, 1999. *Appl. Phys. B* **69**, 379.

C. Henkel, K. Joulain, R. Carminati, and J. J. Greffet, 2000. *Opt. Comm.* **186**, 57.

C. Henkel, K. Joulain, J.-P. Mulet, and J.-J. Greffet, 2002. *J. Opt. A* **4**, S109.

C. Henkel, P. Krüger, R. Folman, and J. Schmiedmayer, 2003. *Appl. Phys. B* **76**, 173.

C. Henkel, B. Power, and F. Sols, 2005. *J. Phys.: Conf. Series* **19**, 34.

G. Hétet, L. Slodička, M. Hennrich, and R. Blatt, 2011. *Phys. Rev. Lett.* **107**, 133002.

A. Hillisch, M. Lorenz, and S. Diekmann, 2001. *Curr. Opin. Struct. Biol.* **11**, 201.

E. A. Hinds and V. Sandoghdar, 1991. *Phys. Rev. A* **43**, 398.

U. Hohenester, A. Eiguren, S. Scheel, and E. A. Hinds, 2007. *Phys. Rev. A*, **76**, 033618.

B. Horovitz, 2011. Personal communication.

C. Hufnagel, T. Mukai, and F. Shimizu, 2009. *Phys. Rev. A*, **79**, 053641.

P. Hyafil, J. Mozley, A. Perrin, J. Tailleur, G. Nogues, M. Brune, J. Raimond, and S. Haroche, 2004. *Phys. Rev. Lett.* **93**, 103001.

D. Iannuzzi, M. Lisanti, and F. Capasso, 2004. *Proc. Nat. Acad. Sci. USA* **101**, 4019.

F. Intravaia, 2005. *Effet Casimir et interaction entre plasmons de surface*. Doctoral dissertation, Université Paris 6. http://tel.archives-ouvertes.fr/docs/00/04/82/54/PDF/tel-00009755.pdf.

F. Intravaia and C. Henkel, 2008. *J. Phys. A* **41**, 164018.

F. Intravaia and C. Henkel, 2009. *Phys. Rev. Lett.*, **103**, 130405.

F. Intravaia and A. Lambrecht, 2005. *Phys. Rev. Lett.* **94**, 110404.

F. Intravaia, C. Henkel, and A. Lambrecht, 2007. *Phys. Rev. A* **76**, 033820.

F. Intravaia, S. Å. Ellingsen, and C. Henkel, 2010. *Phys. Rev. A* **82**, 032504.

F. Intravaia, C. Henkel, and M. Antezza, 2011. In [Dalvit et al., 2011], pages 345–391.

F. Intravaia, S. Koev, I. W. Jung, A. A. Talin, P. S. Davids, R. S. Decca, V. A. Aksyuk, D. A. R. Dalvit, and D. Lopez, 2012. *Arxiv: 1202.6356*.

J. Israelachvili, 1992. *Intermolecular and surface forces*. Academic, London, 2nd edition.

J. D. Jackson, 1975. *Classical electrodynamics*. John Wiley and Sons Inc., New York.

M. T. Jaekel and S. Reynaud, 1991. *J. Physique I* **1**, 1395.

R. L. Jaffe, 2005. *Phys. Rev. D* **72**, 21301.

B. Jancovici, 2006. *Phys. Rev. E* **74**, 052103.

B. Jancovici and L. Samaj, 2005. *Europhys. Lett.* **72**, 35.

M. Janowicz, D. Reddig, and M. Holthaus, 2003. *Phys. Rev. A* **68**, 043823.

Y. Japha and Y. B. Band, 2002. *J. Phys. B* **35**, 2383.

K. L. Johnson, K. Kendall, and A. D. Roberts, 1971. *Proc. Roy. Soc. A* **324**, 301.

S. Johnson, 2011. In [Dalvit et al., 2011], pages 175–218.

M. P. A. Jones, C. J. Vale, D. Sahagun, B. V. Hall, and E. A. Hinds, 2003. *Phys. Rev. Lett.* **91**, 80401.

P. Jordan, 1939. *Z. Phys. A*, **113**, 431.

K. Joulain, R. Carminati, J. P. Mulet, and J.-J. Greffet, 2003. *Phys. Rev. B* **68**, 245405.

K. Joulain, J.-P. Mulet, F. Marquier, R. Carminati, and J.-J. Greffet, 2005. *Surf. Science Rep.* **57**, 59.

T. E. Judd, R. G. Scott, A. M. Martin, B. Kaczmarek, and T. M. Fromhold, 2011. *New J. Phys.* **13**, 083020.

L. Kadanoff and G. Baym, 1962. *Quantum statistical mechanics*. Benjamin, New York.

C. R. Kagan, C. B. Murray, M. Nirmal, and M. G. Bawendi, 1996. *Phys. Rev. Lett.* **76**, 1517.

J. C. Karam, M. Boustimi, J. Baudon, M. Ducloy, F. Perales, J. Reinhardt, V. Bocvarski, C. Mainos, F. Levron, and J. Robert, 2002. *Europhys. Lett.* **60**, 207.

J.-C. Karam, J. Grucker, M. Boustimi, F. Perales, V. Bocvarski, J. Baudon, G. Vassilev, J. Robert, and M. Ducloy, 2006. *Europhys. Lett.* **74**, 36.

B. Kasch, H. Hattermann, D. Cano, T. E. Judd, S. Scheel, C. Zimmermann, R. Kleiner, D. Koelle,

and J. Fortágh, 2010. *New J. Phys.* **12**, 065024.

L. V. Keldysh, 1964. *Zh. Eksp. Teor. Fiz* **47**, 151.

O. Kenneth and I. Klich, 2006. *Phys. Rev. Lett.* **97**, 160401.

W. Ketterle and D. E. Pritchard, 1992. *Appl. Phys. B* **54**, 403.

J. B. Ketterson and S. N. Song, 1999. *Superconductivity*. Cambridge University Press, Cambridge.

K. L. Kliewer and R. Fuchs, 1968. *Phys. Rev.* **172**, 607.

K. L. Kliewer and R. Fuchs, 1969. *Phys. Rev.* **181**, 552.

K. L. Kliewer and R. Fuchs, 1970. *Phys. Rev. B* **2**, 2923.

G. L. Klimchitskaya, U. Mohideen, and V. M. Mostepanenko, 2009. *Rev. Mod. Phys.* **81**, 1827.

L. Knöll, S. Scheel, and D. Welsch, 2001. In J. Perina (ed.), *Coherence and Statistics of Photons and Atoms*. Wiley, New York.

W. Kohn, 1961. *Phys. Rev.* **123**, 1242.

W. Kohn and L. J. Sham, 1965. *Phys. Rev.* **140**, A1133.

F. H. L. Koppens, D. E. Chang, and F. J. García de Abajo, 2011. *Nano Lett.* **11**, 3370.

G.-i. Kweon and N. M. Lawandy, 1993. *Phys. Rev. A* **47**, 4513.

J. Labaziewicz, Y. Ge, D. R. Leibrandt, S. X. Wang, R. Shewmon, and I. L. Chuang, 2008. *Phys. Rev. Lett.* **101**, 180602.

A. Lambrecht and I. G. Pirozhenko, 2008. *Phys. Rev. A* **78**, 062102.

A. Lambrecht, A. Canaguier-Durand, R. Guérout, and S. Reynaud, 2011. In [Dalvit et al., 2011], pages 97–127.

S. K. Lamoreaux, 1997. *Phys. Rev. Lett.* **78**, 5.

S. K. Lamoreaux, 2011. In [Dalvit et al., 2011], pages 219–248.

L. D. Landau and E. M. Lifshitz, 1960. *Course of theoretical physics, Vol. VIII: Electrodynamics of continuous media*. Pergamon Press, Oxford.

L. D. Landau, E. M. Lifshitz, and L. P. Pitaevskij, 1981. *Course of theoretical physics, Vol. X: Physical kinetics.* Pergamon Press, Oxford.

A. Landragin, J. Y. Courtois, G. Labeyrie, N. Vansteenkiste, C. I. Westbrook, and A. Aspect, 1996. *Phys. Rev. Lett.* **77**, 1464.

I. A. Larkin, M. I. Stockman, M. Achermann, and V. I. Klimov, 2004. *Phys. Rev. B* **69**, 121403.

W. T. Lau, J. T. Shen, G. Veronis, and S. Fan, 2007. *Phys. Rev. E* **76**, 016601.

D. A. LaVan, T. McGuire, and R. Langer, 2003. *Nature Biotech.* **21**, 1184.

D. Leibrandt, B. Yurke, and R. Slusher, 2007. *Quant. Inf. Comp.* **7**, 52.

Z. Lenac, 2006. *Phys. Rev. Lett.* **96**, 218901.

J. E. Lennard-Jones, 1932. *Trans. Faraday Soc.* **28**, 333.

M. Lewenstein and L. You, 1996. *Adv. At. Mol. Opt. Phys.* **36**, 221.

M. Lewenstein, L. You, J. Cooper, and K. Burnett, 1994. *Phys. Rev. A* **50**, 2207.

W. Li, I. Mourachko, M. W. Noel, and T. F. Gallagher, 2003. *Phys. Rev. A* **67**, 052502.

E. M. Lifshitz, 1956. *Sov. Phys. JETP* **2**, 73.

Y.-j. Lin, I. Teper, C. Chin, and V. Vuletić, 2004. *Phys. Rev. Lett.* **92**, 050404.

J. Lindhard, 1954. *Kgl. Danske Vidensk. Selsk. Mat. Fys. Medd.* **28**, 1.

M. Lisanti, D. Iannuzzi, and F. Capasso, 2005. *Proc. Nat. Acad. Sci. USA* **102**, 11989.

F. London, 1930. *Z. Phys. A* **63**, 245.

F. London, 1937. *Phys. Rev.* **51**, 678.

F. London and H. London, 1935. *Proc. Roy. Soc. A* **149**, 71.

C.-J. Lorenzen and K. Niemax, 1983. *Physica Scripta* **27**, 300.

J. Maciejko, 2007. *An Introduction to nonequilibrium many-body theory*. http://www.stanford.edu/~maciejko/nonequilibrium.pdf.

J. Mahanty and B. Ninham, 1976. *Dispersion forces*. Academic Press, London.

S. A. Maier, 2007. *Plasmonics: Fundamentals and applications*. Springer, Berlin.

E. Majorana, 1932. *Nuovo Cimento* **9**, 43.

V. M. Mal'nev and S. I. Pekar, 1970. *Sov. Phys. JETP* **31**, 597.

L. Mandel and E. Wolf, 1995. *Optical coherence and quantum optics*. Cambridge University Press, New York.

H. Margenau and N. Kestner, 1971. *Theory of intermolecular forces*. Pergamon Press, Oxford, 2nd edition.

T. Matsubara, 1955. *Prog. Theor. Phys.* **14**, 351.

D. C. Mattis and J. Bardeen, 1958. *Phys. Rev.* **111**, 412.

J. M. McGuirk, D. M. Harber, J. M. Obrecht, and E. A. Cornell, 2004. *Phys. Rev. A* **72**, 033610.

A. D. McLachlan, 1963. *Proc. Roy. Soc. A* **271**, 387.

R. R. McLone and E. A. Power, 1965. *Proc. Roy. Soc. A* **286**, 573.

D. Melrose and R. McPhedran, 1991. *Electromagnetic processes in dispersive media*. Cambridge University Press, Cambridge.

N. D. Mermin, 1970. *Phys. Rev. B* **1**, 2362.

R. Messina, R. Vasile, and R. Passante, 2010. *Phys. Rev. A* **82**, 062501.

M. O. Mewes, M. R. Andrews, N. J. Van Druten, D. M. Kurn, D. S. Durfee, and W. Ketterle, 1996. *Phys. Rev. Lett.* **77**, 416.

A. L. Migdall, J. V. Prodan, W. D. Phillips, T. H. Bergeman, and H. J. Metcalf, 1985. *Phys. Rev. Lett.* **54**, 2596.

P. B. Miller, 1960. *Phys. Rev.* **118**, 928.

R. Mills, 1969. *Propagators for many-particle systems*. Taylor and Francis, London.

P. W. Milonni, 1976. *Phys. Rep.* **25**, 1.

P. W. Milonni, 1994. *The quantum vacuum*. Academic Press, Boston.

P. W. Milonni and R. W. Boyd, 2004. *Phys. Rev. A* **69**, 023814.

P. W. Milonni and M.-L. Shih, 1992. *Phys. Rev. A* **45**, 4241.

P. W. Milonni, R. J. Cook, and M. E. Goggin, 1988. *Phys. Rev. A* **38**, 1621.

K. A. Milton, 2001. *The Casimir effect*. World Scientific, Singapore.

K. A. Milton, 2009. *J. Phys.: Conf. Series* **161**, 012001.

K. A. Milton and J. Wagner, 2008. *J. Phys. A* **41**, 155402.

V. M. Mostepanenko and N. N. Trunov, 1997. *The Casimir effect and its applications*. Clarendon, Oxford.

I. Mourachko, D. Comparat, F. de Tomasi, A. Fioretti, P. Nosbaum, V. M. Akulin, and P. Pillet,

1998. *Phys. Rev. Lett.* **80**, 253.

M. Müller, H. Haakh, T. Calarco, C. Koch, and C. Henkel, 2011. *Quant. Inf. Proc.* **10**, 771.

T. Müller, B. Zhang, R. Fermani, K. S. Chan, Z. W. Wang, C. B. Zhang, M. J. Lim, and R. Dumke, 2010. *New J. Phys.* **12**, 043016.

J. N. Munday, F. Capasso, and V. A. Parsegian, 2009. *Nature* **457**, 170.

C. Muschik, H. Krauter, K. Hammerer, and E. Polzik, 2011. *Quant. Inf. Proc.* **10**, 839.

A. Negretti, P. Treutlein, and T. Calarco, 2011. *Quant. Inf. Proc.* **10**, 721.

J. Nenonen, J. Montonen, and T. Katila, 1996. *Rev. Sci. Instr.* **67**, 2397.

M. A. Nielsen and I. L. Chuang, 2011. *Quantum computation and quantum information*. Cambridge University Press, Cambridge.

T. Nirrengarten, A. Qarry, C. Roux, A. Emmert, G. Nogues, M. Brune, J. M. Raimond, and S. Haroche, 2006. *Phys. Rev. Lett.* **97**, 200405.

G. Nogues, C. Roux, T. Nirrengarten, A. Lupascu, A. Emmert, M. Brune, J.-M. Raimond, S. Haroche, B. Placais, and J.-J. Greffet, 2009. *Europhys. Lett.* **87**, 13002.

A. Norrman, T. Setälä, and A. T. Friberg, 2011. *J. Opt. Soc. Am. A* **28**, 391.

L. Novotny and C. Henkel, 2008. *Opt. Lett.* **33**, 1029.

H. Nussenzveig, 1972. *Causality and dispersion relations*. Academic Press, New York.

R. Nyman, S. Scheel, and E. Hinds, 2011. *Quant. Inf. Proc.* **10**, 941.

J. M. Obrecht, R. J. Wild, M. Antezza, L. P. Pitaevskii, S. Stringari, and E. A. Cornell, 2007. *Phys. Rev. Lett.*, **98**, 063201.

Y. B. Ovchinnikov, 2000. *Opt. Comm.* **182**, 35.

V. A. Parsegian, 2006. *Van der Waals forces*. Cambridge University Press, New York.

R. Passante and F. Persico, 2003. *Phys. Lett. A* **312**, 319.

R. Passante and N. Vinci, 1996. *Phys. Lett. A* **213**, 119.

W. Paul, 1990. *Angew. Chem. Int. Ed.* **29**, 739.

L. Pauling and M. Delbrück, 1940. *Science* **92**, 77.

M. R. Philpott, 1966. *Proc. Phys. Soc.* **87**, 619.

G. Pieplow, H. R. Haakh, and C. Henkel, 2012. In *Proceedings of QFExt '11. ArXiv: 1111.3748*.

A. B. Pippard, 1947. *Proc. Roy. Soc. A* **191**, 385.

L. P. Pitaevskii, 2005. *J. Phys. A* **39**, 6665.

L. P. Pitaevskii, 2010. *Int. J. Mod. Phys. A* **25**, 2313.

L. P. Pitaevskii, 2011. In [Dalvit et al., 2011], pages 23–37.

L. P. Pitaevskii and S. Stringari, 2003. *Bose-Einstein condensation*. Clarendon Press, Oxford.

M. Planck, 1901. *Ann. Phys.* **309**, 553.

M. Planck, 1912. *Ann. Phys.* **342**, 642.

R. Podgornik, G. Cevc, and B. B. Žekš, 1987. *J. Chem. Phys.* **87**, 5957.

D. B. Poker and C. E. Klabunde, 1982. *Phys. Rev. B* **26**, 7012.

V. G. Polevoi and S. M. Rytov, 1975. *Theor. Math. Phys.* **25**, 1096.

S. A. Ponomarenko and E. Wolf, 2001. *Phys. Rev. E* **65**, 016602.

R. Pöpel, 1989. *J. Appl. Phys.* **66**, 5950.

M. L. Povinelli, M. Loncar, M. Ibanescu, E. J. Smythe, S. G. Johnson, F. Capasso, and J. D. Joannopoulos, 2005. *Opt. Lett.* **30**, 3042.

E. A. Power, 1966. *Am. J. Phys.* **34**, 516.

E. A. Power and T. Thirunamachandran, 1983. *Phys. Rev. A* **28**, 2671.

E. A. Power and T. Thirunamachandran, 1993. *Phys. Rev. A* **47**, 2539.

E. A. Power and T. Thirunamachandran, 1995. *Phys. Rev. A* **51**, 3660.

E. A. Power and S. Zienau, 1957. *Nuovo Cimento* **6**, 7.

E. A. Power and S. Zienau, 1959. *Proc. Roy. Soc. A* **251**, 427.

J. Preto and M. Pettini, 2012. *ArXiv: 1201.5187*.

J. Preto, E. Floriani, I. Nardecchia, P. Ferrier, and M. Pettini, 2012. *ArXiv: 1201.2607*.

D. E. Pritchard, 1983. *Phys. Rev. Lett.* **51**, 1336.

E. M. Purcell, 1946. *Phys. Rev.* **69**, 674.

H. Raether, 1988. *Surface plasmons on smooth and rough surfaces and on gratings*. Springer, Berlin.

S. Rahi, T. Emig, and R. Jaffe, 2011. In [Dalvit et al., 2011], pages 129–174.

J. Rammer, 2007. *Quantum field theory of non-equilibrium states*. Cambridge University Press, Cambridge.

J. Reichel and V. Vuletic (eds.), 2011. *Atom chips*. Wiley-VCH, Weinheim.

F. Reil, U. Hohenester, J. R. Krenn, and A. Leitner, 2008. *Nano Lett.* **8**, 4128.

P. K. Rekdal, S. Scheel, P. L. Knight, and E. A. Hinds, 2004. *Phys. Rev. A* **70**, 013811.

J. Renger, R. Quidant, N. van Hulst, S. Palomba, and L. Novotny, 2009. *Phys. Rev. Lett.* **103**, 266802.

G. E. H. Reuter and E. H. Sondheimer, 1948. *Proc. Roy. Soc. A* **195**, 336.

G. Rickayzen, 1959. *Phys. Rev.* **115**, 795.

E. Rousseau, A. Siria, G. Jourdan, S. Volz, F. Comin, J. Chevrier, and J.-J. Greffet, 2009. *Nature Photon.* **3**, 514.

S. Rytov, A. Kravtsov Yu, and V. Tatarskii, 1989. *Principles of statistical radiophysics, Vols. 3, 4*. Springer, Berlin.

K. Rzazewski and W. Zakowicz, 1992. *J. Phys. B* **25**, L319.

H. Safari, S. Y. Buhmann, D. Welsch, and H. T. Dung, 2006. *Phys. Rev. A* **74**, 042101.

A. Salam, 2005. *J. Chem. Phys.*, **122**, 044112.

A. Salam, 2009. *Molecular quantum electrodynamics: Long-range intermolecular interactions*. Wiley, Hoboken (NJ).

L. Samaj and B. Jancovici, 2008. *Phys. Rev. E* **78**, 051119.

V. Sandoghdar, C. I. Sukenik, E. A. Hinds, and S. Haroche, 1992. *Phys. Rev. Lett.* **68**, 3432.

S. Scheel and S. Y. Buhmann, 2008. *Acta Phys. Slov.* **58**, 675.

S. Scheel, P. K. Rekdal, P. L. Knight, and E. A. Hinds, 2005. *Phys. Rev. A* **72**, 42901.

J. Schiefele, 2011. *Casimir-Polder Interaction in Second Quantization*. Doctoral dissertation, Universität Potsdam. http://opus.kobv.de/ubp/volltexte/2011/5417/.

J. Schiefele and C. Henkel, 2010a. *Phys. Rev. A* **82**, 023605.

J. Schiefele and C. Henkel, 2010b. *Phys. Lett. A* **475**, 680.

J. Schmiedmayer, R. Folman, and T. Calarco, 2002. *J. Mod. Opt.* **49**, 1375.

K. Schram, 1973. *Phys. Lett. A* **43**, 282.

J. Schrieffer, 1999. *Theory of superconductivity*. Perseus Books, Reading.

T. Schumm, S. Hofferberth, L. Andersson, S. Wildermuth, S. Groth, I. Bar-Joseph, J. Schmiedmayer, and P. Krüger, 2005. *Nature Phys.* **1**, 57.

J. Schwinger, 1960. *Ann. Phys. (N.Y.)* **9**, 169.

J. Schwinger, 1992. *Proc. Nat. Acad. Sci. USA* **89**, 4091.

B. E. Sernelius, 2005. *Phys. Rev. B* **71**, 235114.

B. E. Sernelius, 2006. *J. Phys. A* **39**, 6741.

Y. Sherkunov, 2005. *Phys. Rev. A* **72**, 052703.

Y. Sherkunov, 2007. *Opt. Spectrosc.* **103**, 388.

Y. Sherkunov, 2009. *J. Phys.: Conf. Series* **161**, 012041.

F. Shimizu, 2001. *Phys. Rev. Lett.* **86**, 987.

S. Shresta, B. L. Hu, and N. G. Phillips, 2003. *Phys. Rev. A* **68**, 062101.

J. A. Sidles, J. L. Garbini, W. M. Dougherty, and S. H. Chao, 2003. *Proc. IEEE* **91**, 799.

J. E. Sipe, 1981. *Surf. Science* **105**, 489.

B.-S. Skagerstam, U. Hohenester, A. Eiguren, and P. K. Rekdal, 2006. *Phys. Rev. Lett.* **97**, 70401.

B.-S. Skagerstam, P. K. Rekdal, and A. H. Vaskinn, 2009. *Phys. Rev. A* **80**, 022902.

F. Sols and F. Flores, 1982. *Solid State Comm.* **42**, 687.

S. Spagnolo, 2009. *Quantum Electrodynamics with Boundary Conditions and Casimir-Polder Forces*. Doctoral dissertation, Università degli Studi di Palermo.

M. J. Sparnaay, 1957. *Nature* **180**, 334.

C. Stehle, H. Bender, C. Zimmermann, D. Kern, M. Fleischer, and S. Slama, 2011. *Nature Photon.* **5**, 494.

C. I. Sukenik, M. G. Boshier, D. Cho, V. Sandoghdar, and E. A. Hinds, 1993. *Phys. Rev. Lett.* **70**, 560.

A. O. Sushkov, W. J. Kim, D. A. R. Dalvit, and S. K. Lamoreaux, 2011. *Nature Phys.* **7**, 230.

A. Suter, E. Morenzoni, R. Khasanov, H. Luetkens, T. Prokscha, and N. Garifianov, 2004. *Phys. Rev. Lett.* **92**, 87001.

V. B. Svetovoy, 2007. *Phys. Rev. A*, **76**, 062102.

V. B. Svetovoy and R. Esquivel, 2005. *Phys. Rev. E*, **72**, 036113.

A. Tauschinsky, R. M. T. Thijssen, S. Whitlock, H. B. L. van den Heuvell, and R. J. C. Spreeuw, 2010. *Phys. Rev. A* **81**, 063411.

C. E. Theodosiou, 1984. *Phys. Rev. A* **30**, 2881.

D. J. Thouless, 1960. *Phys. Rev.* **117**, 1256.

M. Tinkham, 2004. *Introduction to superconductivity*. Dover Publications, Mineola.

J. Tisler, R. Reuter, A. Lämmle, F. Jelezko, G. Balasubramanian, P. R. Hemmer, F. Reinhard, and J. Wrachtrup, 2011. *ACS nano* **5**, 7893.

F. Toigo, A. Marvin, V. Celli, and N. R. Hill, 1977. *Phys. Rev. B* **15**, 5618.

P. Townsend and J. Sutton, 1962. *Phys. Rev.* **128**, 591.

P. Treutlein, P. Hommelhoff, T. Steinmetz, T. W. Hänsch, and J. Reichel, 2004. *Phys. Rev. Lett.* **92**,

203005.

P. Treutlein, A. Negretti, and T. Calarco, 2011. In [Reichel and Vuletic, 2011], pages 283–308.

Q. A. Turchette, B. E. King, D. Leibfried, D. M. Meekhof, C. J. Myatt, M. A. Rowe, C. A. Sackett, C. S. Wood, W. M. Itano, C. Monroe, et al., 2000. *Phys. Rev. A* **61**, 063418.

J. D. Van der Waals, 1873. *Over de continuiteit van den gas en vloeistoftoestand*. Doctoral dissertation, Universiteit Leiden.

N. G. Van Kampen, B. R. A. Nijboer, and K. Schram, 1968. *Phys. Lett. A* **26**, 307.

H.-J. Van Leeuwen, 1921. *J. Phys. Radium* **2**, 361.

R. van Leeuwen, N. E. Dahlen, G. Stefanucci, C.-O. Almbladh, and U. von Barth, 2006. In M. Marques (ed.), *Time dependent density functional theory*, pages 33–59. Springer, Berlin.

P. van Zwol, V. Svetovoy, and G. Palasantzas, 2011. In [Dalvit et al., 2011], pages 311–343.

P. J. van Zwol, L. Ranno, and J. Chevrier, 2012. *ArXiv: 1201.4992*.

T. Varpula and T. Poutanen, 1984. *J. Appl. Phys.* **55**, 4015.

R. Vasile and R. Passante, 2008. *Phys. Rev. A* **78**, 032108.

E. J. W. Verwey and J. T. G. Overbeek, 1946. *Trans. Faraday Soc.* **42**, B117.

A. I. Volokitin and B. N. J. Persson, 2007. *Rev. Mod. Phys.* **79**, 1291.

T. G. Walker and M. Saffman, 2005. *J. Phys. B* **38**, S309.

B. Weber, S. Mahapatra, H. Ryu, S. Lee, A. Fuhrer, T. C. G. Reusch, D. L. Thompson, W. C. T. Lee, G. Klimeck, L. C. L. Hollenberg, et al., 2012. *Science* **335**, 64.

L. Weber and E. Gmelin, 1991. *Appl. Phys. A* **53**, 136.

G. C. Wick, 1950. *Phys. Rev.* **80**, 268.

K. A. Willets and R. P. Van Duyne, 2007. *Ann. Rev. Phys. Chem.* **58**, 267.

C. M. Wilson, G. Johansson, A. Pourkabirian, M. Simoen, J. R. Johansson, T. Duty, F. Nori, and P. Delsing, 2011. *Nature* **479**, 376.

W. H. Wing, 1984. *Progr. Quant. Electr.* **8**, 181.

P. G. Wu and L. Brand, 1994. *Anal. Biochem.* **218**, 1.

J. M. Wylie and J. E. Sipe, 1984. *Phys. Rev. A* **30**, 1185.

J. M. Wylie and J. E. Sipe, 1985. *Phys. Rev. A* **32**, 2030.

E. Yablonovitch, 1989. *Phys. Rev. Lett.* **62**, 1742.

Y. Zakrevskyy, M. Richter, S. Zakrevska, N. Lomadze, R. von Klitzing, and S. Santer, 2012. *Submitted to Adv. Funct. Mat.*

A. Zangwill, 1988. *Physics at surfaces*. Cambridge University Press, Cambridge.

E. Zaremba and W. Kohn, 1976. *Phys. Rev. B* **13**, 2270.

B. Zhang, 2008. *Magnetic Fields near Microstructured Surfaces: Application to Atom Chips*. Doctoral dissertation, Universität Potsdam. http://opus.kobv.de/ubp/volltexte/2009/2898.

B. Zhang, C. Henkel, E. Haller, S. Wildermuth, S. Hofferberth, P. Krüger, and J. Schmiedmayer, 2005. *Eur. Phys. J. D* **35**, 97.

W. Zhang and D. F. Walls, 1994. *Phys. Rev. A* **49**, 3799.

W. Zimmermann, E. H. Brandt, M. Bauer, E. Seider, and L. Genzel, 1991. *Physica C* **183**, 99.

J. R. Zurita-Sánchez and C. Henkel, 2012. *Europhys. Lett.* **97**, 43002.